UNIVERSITY OF MESSINA

Department of Chemical, Biological, Pharmaceutical and Environmental Sciences

Ph.D. course in Chemical Sciences

XXXV cycle

SYNTHESIS AND CHARACTERIZATION OF PHOTOACTIVE NANOSTRUCTURED MATERIALS FOR SENSING AND BIOMEDICAL APPLICATIONS

S.S.D. (Settore Scientifico Disciplinare): CHIM/02 – CHIM/03

Giuseppe Nocito

SUPERVISOR: *Prof. Francesco Nastasi*

CO-SUPERVISOR: *Prof. Sabrina Conoci*

COORDINATOR: *Prof. Concetta De Stefano*

AA. (Anno Accademico): 2021/2022

Dottorati FSE XXXV ciclo UniMe - Bando PO FSE 2014-2020, Avviso n.2/2019 per il finanziamento di borse regionali di dottorato di ricerca in Sicilia A.A. 2019/2020 – D.D.G. n.6242 del 31/10/2019

TABLE OF CONTENTS

SECTION ONE

INTRODUCTION

1. NANOMATERIALS

In the last decades, nanotechnology is having relevant impact in many fields of research such as biomedicine [1], pharmaceutics [2], optoelectronics [3], environmental care [4] and energetics [5]. The scientific literature is more and more dominated by words beginning with "*nano*". Nanomaterials are, in opinion of the most, the actual answer to many of a researcher's questions thanks to the surprizing properties of the matter when it is nano-sized [6].

Nanomaterials are structures in which at least one dimension is less than 100 nm, organic or inorganic, with many different shapes and high surface area. These characteristics, highly and easily tunable originate a peculiar physical and chemical behaviour useful for many purposes [6, 7]. In biomedical field nanoparticles (NPs) are exploited for example for imaging [8], drug delivery [9], photodynamic [10] and photothermal [11] therapy, scaffolds for regenerative medicine [12, 13], smart biomaterials [14], sensing and so on. Metal nanoparticles (MNPs) are the first and most studied example, especially noble metal NPs (AuNPs, AgNPs, PtNPs, PdNPs, etc). In the last decades, carbon-based nanomaterials like fullerenes, graphene and graphene oxide (GO), carbon nanotubes (CNTs) and Carbon dots (CDs) are receiving great attention [15].

Nanomaterials, although identical chemical composition from bulk, reached the success because of extraordinary different physical and chemical properties. The key point of this difference lies precisely in the dimension. Since the theorization of quantum mechanics, we have become accustomed to thinking that the behaviour of matter changes going down to the ultra-small. Macroscopic materials (bulk) behaviour can be explained with traditional physics, the interaction between molecules, macromolecules and complex systems with the chemistry of low interactions (supramolecular chemistry), molecular properties with conventional chemistry, in the atomic scale classical and quantum physics are used to understand them. Nanomaterials are in a middle-earth between atoms/molecules and bulk materials. Their nanometric size (and also shape) on the interaction with the electromagnetic radiation returns peculiar properties that are explainable by quantum mechanics, in particular by the quantum size effect. The possibility to control

chemical and physical properties of materials without the alteration of chemical composition but only tuning size and shape has opened a new and intriguing area of research in remarkable hype since decades: nanochemistry and nanotechnology. [16]

1.1 CLASSIFICATION

Since their discovery, many nanostructures have been identified in natural productions such as volcanoes activities, combustion processes, inorganic compounds or biological activities (biovesicles). [16] Many others have been synthetized in a multitude of laboratory. In a long and spread research activity a large volume of nanoparticles is known, and of course need a classification. The most common categorization is per size and dimension, four different families are recognized: zero dimensional (0D), one dimensional (1D), bidimensional (2D) and three-dimensional (3D). Inside these groups nanoparticles can exist in various shapes and morphologies such as atomic clusters, filamentary structures, single, fused, aggregated structures of globular, tubular, ellipsoidal, irregular, layered nanoparticles. [17, 18]

- Zero dimensional (0D) – Structures wherein all the three dimensions are below 100 nm. As said before under every class are included nanoparticles from the most diverse morphologies. This class contains the largest group of diversity from spherical to the fanciest shape and they can be crystalline, polycrystalline or amorphous. Clusters, dendrimers, rings, fullerenes, quantum dots, metallic nanoparticles are members.
- One dimensional (1D) – Particles in which only two dimensions are below 100 nm, the other is over this limit. As it can be possible to imagine the commonest shape is the filamentary. Carbon nanotubes (CNTs), metals or metal oxides wires, nanofibers are representative for the class.
- Bidimensional (2D) – Particles in which only one dimension is below 100 nm. Graphene, graphene oxide (GO), transition metal dichalcogenides (TMDCs) are examples. Generally, the first dimension relies on the atomic scale, and they result as a thin sheet.

- Three-dimensional (3D) - Particles that are not in the nanoscale, such as bulk materials. They are included in nanomaterials classification due to many examples of nanocrystalline structures of reasonably small size, in many cases aggregates of nanoparticles, that feature nanoscale properties.

1.2 PHYSICAL AND CHEMICAL PROPERTIES

The dimension in nanomaterials strictly affect their physical and chemical properties, by means of two main effects: scalable surface effects, related to the fraction of the atoms at the surface, and quantum effects, related to the electronic confinement. The first explains the reactivity of nanoparticles to the interacting environment, some mechanical properties and thermodynamic parameters. [19] The second was theorized at the beginning of 1980s by Brus et al [20] that introduced the so-called "quantum size effect" to explain the different electronic spectra of CdS nanoparticles from bulk materials, even though the composition and the chemical bonding were the same. Quantum effects are used to explain nanoparticles optical, electrical, and magnetic properties. Since this milestone interpretation a new era in research started and many researchers were applied on this intriguing way to modify the matter.

1.2.1 Surface effects

Nanomaterials due to ultra-small size possess high surface area over volume ratio which leads to a major reactivity to the environment compared to bulk materials [17]. The reason of this increased reactivity is for a great number of surface atoms that have different properties from the inner. Interior atoms, as for bulk conditions, are more "coordinated" than surface atoms, they form more bonds because they have more neighbours, and their reactivity is lower. Surface atoms are freer to interact with the environment, considering a model cubic nanostructure the order of reactivity is corner, edge and in-plane atoms. Mechanic and thermodynamic properties of nanomaterials such as cohesive energy and phase transitions are so explained. For example, the Gibbs-Thomson equation describes that the melting point scales inversely with the radius of a particle. Surface atoms melt before than

inner atoms, and in general phase transitions in nanoparticles are not well defined due to a reduced number of atoms. [19]

1.2.2 Energy band gap and density of states in bulk materials

Molecules are an ordered collection of atoms that answer to the laws of quantum mechanics. Chemical bonds and electronic transitions occur through the involvement of quantum entities that are called orbitals in which electrons are ordered into quantized levels of energy. Electronic transitions occur from a lower to a higher energy state only when is administered the correct quantum of energy (photon) equal to the energy gap between the two states. In normal conditions, according to frontier orbitals theory, from a ground state, the highest occupied molecular orbital (HOMO), to the first excited state, the lowest unoccupied molecular orbital (LUMO).

The behaviour of solid-state systems, or bulk materials, such as metals, semiconductors or insulators is similar to molecules. Instead of molecular orbital the ordered sum of atomic orbitals is called “band”. The density of states (DOS) within a band is proportionally to the numbers of atoms of an ensemble with an extended band-like state [19]. HOMO take the name of the valence band (VB), LUMO the conduction band (CB). The magnitude of the energy gap between VB and CB defines if a material is a metal, a semiconductor, or an insulator. In a metal the gap is so little that electron promotion occurs with a slight energy expenditure. In a semiconductor the energy band is appreciable and measurable, in insulators the gap is so high that electron promotion to conduction band does not take place unless harsh conditions. In a semiconductor during the photogenerated excited state the electron that is promoted to the conduction band leaves behind it a vacancy (hole) in the valence band. The electron-hole pair is called the exciton, it is quantized too, and it is described by wavefunctions, probability distribution and permitted energy.

1.2.3 Quantum confinement

Quantum confinement is the theoretical explanation of optical, electrical, and magnetic properties of nanomaterials and has evolved on the evidence of surface effects. Classical mechanics continues to explain the aforementioned, but as soon as the size decreases also the electronic

behaviour begins to be altered, which implies the introduction of quantum mechanics models. Surface atoms, that in nanomaterials are predominantly, possess exotic electronic states responsible of peculiar transitions on the interaction with the electromagnetic radiation.

In quantum mechanics, the characteristic radius of an electron is defined as Bohr radius. The exciton, the electron-hole pair, is a quantum mechanical system too and possess its own wavefunction and a Bohr exciton radius. When the size of a particle becomes too small or comparable with the Bohr exciton radius, quantum confinement effect can happen. Electrons and excitons are confined in a restricted area of the space that make energy levels discrete and consequently band gap energy will increase or widen. The more the size decrease the more the energy gap increase blue-shifting UV/Vis absorption and luminescence emission of nanoparticles. [21]

1.3 NANOMATERIALS FOR SENSING APPLICATIONS

Industrialization, urbanization, economic wellness, extension of life expectancy, excessive consumption of raw materials, pollution and inattention towards waste management characterized and continue to be joy and sorrows of our contemporary society. Fortunately, in the last decades there is increasing attention towards circular economy, environmental care, and renewable energy sources. On this scenario, the chemical community is increasingly striving to find new “green” methods of production and fast, reliable, cheap, and accurate analytical methods to detect more and more new pollutants, drugs, gases and biomolecular species related to disease detection. These changes require the development of novel and modern sensors. Actually, the realization of micro and nano sensing platforms is the way that researchers have found to reduce production costs and increase sensitivity and versatility.

A sensor is a device that transforms information about the physical and chemical properties of a system into analytically useful signal. The interaction between the analyte, the surrounding medium (the system) and the device leads to the change of a physical parameter that is instrumentally measurable giving unique information about the analytical specie. [22] In the best scenario

for a chemical sensor, the chemical information may originate from a chemical reaction that should be selective but reversible, those interactions include non-covalent (ion-dipole, van der Waals forces, …), covalent and supramolecular interactions (ion-ion, hydrogen and halogen bonding, hydrophobic, π- π, H- π, cations/anions- π interactions). [23] Sensors can be divided into several classes. They can be classified on the base of the constituent material (metal oxides, , carbon nanomaterial, class of molecules, class of metallic complex, …), on the base of the measured physical parameter (mechanical stress, heat, magnetic force, …), on the base of the detected chemical specie (gases, molecules in solution, biological macromolecules, …) or also on the base of the output information/detection parameter (optical – colorimetric, luminescent – conductometric, resistive, electrochemical, or in base of the spectroscopic technique).

The basic parameters that are calculated to characterize the efficiency of a sensor are: response, response time, recovery time, operating temperature, selectivity, limit of detection, stability, and repeatability. Both response and recovery time are affected by temperature, pressure or concentration of the analyte, binding (adsorption) and dissociation (desorption) kinetics of the analyte with the device, construction of the device and its material constitution. [24]

- Response – Is the ratio between the signal coming from the analysed physical parameter (resistance, conductance, photoluminescence, optical absorption, …) before and after the treatment with the analyte. The sensor response (S) is expressed by the formula $S = {\Delta R}/{R_0}$ where ΔR is the difference between the response at the time 0 (before the analyte interaction) and at the time 1 (after the interaction with the analyte). [24]
- Response time – The time that a sensor requires, during the exposure with the analyte, to change its signal from the initial state to the final state (in general 90 % of the final value). [24]
- Recovery time – The time to return from the final state, the maximum of the response toward the analyte, to the

background signal (in general 90 % of the baseline value). Some sensors are irreversible, so the recovery time cannot be calculated. [24]

- Operating temperature – Is dependent from the final application, material and device type. For some sensors such as gas sensors is a key parameter because controls the sensing mechanism, the gas adsorption/desorption kinetics and the radical reactions occurring on the surface of the device. [24]
- Selectivity – Is the measurement of the response of the sensor towards the target analyte under the contemporary presence of other analytes that could be interfering or not. $Selectivity = {S_i}/{S_t}$ where S_i is the sensitivity of the sensor toward interface species and S_t toward the target. [24]
- Limit of detection – Is the minimum concentration of the target specie which can be detected by a sensor under certain conditions. [24]
- Stability and repeatability – Determines the performance of the sensor on the possibility to be reused many times (multiple recoveries) without signal drifting. [24]

In comparison with the existing technologies, devices that are based on nanomaterials have so many advantages that the current research on sensors is more often focused on nano-platforms. Nanomaterials in fact, have unique physical and chemical properties such as good surface reactivity and catalytic efficiency, electrical conductivity, optical absorption, the possibility of photoluminescence emission and magnetic properties. All of those are different from bulk materials and related to the nanometric dimension (quantum confinement and surface effects) of nanomaterials. In terms of sensing applications, the unique and variegated physical and chemical properties of nanomaterials can be exploited as measurable parameters for the final output of sensing, but the major reason of their success is due to the high surface area. The more the surface area is the more the reactive sites will be present, improving so on selectivity, sensitivity, response, and response time of the sensor. A greater amount of interacting sites will give a greater

output, an increase of the signal intensity, even with very low concentration of the analyte allowing the detection for trace amounts of species. [25] Moreover, the actual knowledge on nanotechnology gives the opportunity to fabricate using cheap, green and facile methods a vast amount of different nanomaterials. The sensitivity to the analytes may be for nanomaterials dependent from synthetic and post-synthetic conditions thanks to the tunable chemical versatility in terms of surface and core constitution.

1.3.1 Gas sensing

As said in the previous paragraph, excessive consumption of raw materials and massive industrialization have been left their scars on our delicate ecological balance. The detection of pollutants and in particular toxic gases that are a risk for human health and for climate change (ozone hole, greenhouse effect, …) is an important task for industry, science, and ecology. The pollutant gases that are commonly monitored are sulphur oxides (SO_x), nitrogen oxides (NO_x), volatile organic compounds (VOC_s), carbon monoxide (CO) and carbon dioxide (CO_2). Nowadays, the main commercially available gas sensors are based on semiconductor metal oxides. The principal mechanism of detection is based on the resistance, conductance or in general electrical variation of the device response before and after gas adsorption. Their performance is affected by morphology, structure, and fabrication of the sensor. In addition, they often suffer of long-term loss of selectivity for structural modifications that are dependent from stoichiometry changes and coalescence of crystallites together with the high operating temperature and the continuous gases exposure. The fabrication of nanostructured devices for gas sensing replacing the bulk metal oxides with their equivalent nano-form, may overcome these issues for their greater surface area, better stoichiometry, and higher degree of crystallinity. The major metal oxides nanostructures that are currently studied for the fabrication of gas sensing devices are ZnO, TiO_2, SnO_2. [24]

1.3.1.1 Mechanisms of gas sensing

The commonly recognized mechanism of gas detection by metal oxides is based on Red-Ox reactions occurring on the surface of the device. The leading phenomenon is the high operating temperature that promotes the

Red-Ox and radical processes according to the semiconductive behaviour of the system. This explanation is based on the use of devices in which the output signal is based on the registration of electrical variation (resistance, conductance, ...).

Working on synthetic or ambient air below and over 150 °C (the common operating temperature of gas sensor devices) oxygen is pushed to interact with the surface of the device. On the moment of the interaction a surface state is created and an electron from the device surface is transferred to oxygen forming the instable anions such as O_2^- (superoxide) and O^-. Those species modify the electronic distribution on the surface of the semiconductor material increasing the Schottky barrier and the overall electrical resistance of the device. Increasing the temperature, the thermally generated electrons will decrease resistance favouring the desorption of oxygen anions, together with their trapped electrons, and the final interaction with the analyte gas. Contemporary, the ubiquitous present vapour water plays another role on sensor response. Water adsorption can modify the reactivity and the electrical response of the sensor, but as it was demonstrated it is eliminated over 200 °C. [24, 26]

1.3.2 Optical sensors

Optical sensors are devices in which the interaction between the system analyte/surrounding medium and the sensor leads to the change of an optical property that can be spectroscopically measured and interpreted [23].

According to the 1991 IUPAC classification of chemical sensors [22] those may be classified according to the operating principle of the output measure, the optical property used for sensing. The following are distinguished: i) absorbance, measured in a transparent medium it is caused by the absorbance of the analyte itself or by a reaction with a suitable indicator; ii) reflectance, measured in a non-transparent media usually using an immobilized indicator; iii) chemiluminescence, it is based on the measurement of the emission of light as a result of a chemical reaction occurring in the system; iv) photoluminescence, measurement of the emission of light caused by light irradiation; v) refractive index, resulting from changes in the solution composition; vi) photothermal effect, based on the

measurement of heat produced by light irradiation of the sample; vii) light scattering, based on the effect caused by particles of definite size present in the sample. [23]

Most of the optical sensors are based on the measurement of a phenomenon occurring in solution using appropriate spectroscopic methods such as UV/Vis and luminescence spectroscopies. In that way, the sensitivity of the analytical method is affected by physical and chemical parameters of solutions such as temperature, pH, ionic strength, solvent polarity and refractive index and analyte concentration. [23]

1.3.2.1 Optical sensors design

As said before, for an efficient chemical sensing it may occur a selective but reversible chemical interaction via non-covalent or covalent binding of the analyte to the analytical system. The chemical information will be then transformed into a measurable physical parameter. There are two main approaches to design an optical sensor: the first is based on the direct binding of the analyte to the system and the second to the competitive binding of the analyte to the system. [23]

The receptor-transducer system, usually named receptor-spacer-reporter in the case of sensors based on molecular systems, exemplifies the direct binding approach. On the fundamental design, the sensor is constituted by two main parts. The first is the receptor that is designed for the selective recognition of a specific analyte. For molecules it may be a certain chemical fragment, scaffold or functional group moiety recognized or properly designed for the analyte selective binding. In parallel for nanomaterials it may be a definite surface functional group, a peculiar physical and chemical interaction or a molecular scaffold previously installed on the surface of the nanomaterial. The second fundamental constituent of the sensor is the transducer that is defined as “a moiety that transforms the perturbed properties of the receptor into an observable analytical signal output” [27]. For nanomaterials it is usually exploited one of their peculiar physical and chemical property, for example the modification of the surface states generating a different UV/Vis absorption spectrum, or a modification of the luminescence related to the quantum confinement effect. For example, for

gold nanoparticles any modifications on their structure will be recognized by the change of their Localized Surface Plasmon Resonance (LSPR) band on the UV/Vis spectrum. [23]

The second main approach to design an optical sensor, particularly valid for colorimetric and luminescent sensors, is the indicator displacement assay. The fundamental scheme is not sensibly different from the first, the receptor and the transducer are assumed to exist, but there is a different mechanism of interaction between the analyte and the receptor. This method uses the competition between the analyte and an indicator for the receptor binding, importantly the two binding constants should be comparable. On the device, the receptor is usually occupied by the indicator, its displacement, operated by the analyte recognition, will lead to the change of optical parameters such as shifting in UV/Vis absorption spectrum resulting also, in the better case, to the change of the colour of the solution. For luminescence ON-OFF sensors the indicator may be a quenched fluorophore when bound to the sensor and free to emit photons in the moment of the displacement. [23]

Another more complex design of luminescence sensors exploits the Förster Resonance Energy Transfer (FRET) process. FRET is a non-radiative dipole-dipole energy transfer that occurs when a luminescent donor molecule and an acceptor molecule possess compatible absorption and emission spectra [28]. The acceptor is chosen to have a good overlapping integral of its absorption spectrum with the emission spectrum of the donor emissive specie. Under conditions of spatial proximity, the dipole generated by the light excitation of the donor fluorophore may resonate with the induced dipole on the acceptor occurring in an energy transfer. If the acceptor is a fluorophore too the fluorescence of the donor will appear. In any case, no emission from donor is found. In other words, if the recognition of the analyte will occur for spatial proximity with the receptor-transducer part of the sensor (the donor emissive specie) the FRET mechanism will happen, and it will be measurable thanks to the disappearing of the donor emission signal. When the analyte is not recognized the emission of the donor will be restored.

1.3.3 Biosensors

Successful optical sensors have been realized for selective and easy recognition of metals, heavy metals, pollutants, drugs, and various classes of small molecules. Electrochemical and electrical sensors are extensively utilized as alternative to optical sensors and for gas sensing. Sensors have been also developed for biomedical applications; in fact, the largest share of the market is for these applications. The attraction on the research on sensors for biomedical applications is on the possibility of producing miniaturized and versatile devices, suitable for the use in many environments, which can give easily qualitative and quantitative information with the least economic expenditure. Point-of-need and point-of-care devices are the most new and attractive for the market since they require the minimum use of reagents, processing steps, and manipulations. Moreover, most of them are realized to be disposable giving the opportunity to ensure sterility and hygiene and to overcome cross-contamination. [29, 30]

Biosensors are analytical devices for the detection of biological samples. Their design follows that of optical chemical sensors, the receptor-transducer model. The receptor is a biological moiety designed for the recognition of a complementary entity that is associated with a transducer unit converting the biological response into a quantifiable signal. They are used for a rapid and low-cost understanding of the bio-composition, structure, and function of biological samples in order to replace traditional testing procedures that are often more laborious and expensive. [30-31]

Considering these principles, transducer unities are designed for easy, affordable, and precise detection. Among the possible, optical sensors are the most utilized because of simplicity, diffusion, and consolidation of optical spectroscopy techniques. Traditionally, transducers are thus organic chromophores or fluorophores that transform the biological response of the receptor into a variation of UV/Vis absorbance or luminescence ensuring ultrasensitive detection. The explosion of nanotechnology changed the whole scenario because gave the opportunity to exploit unprecedented physical and chemical properties for the realization of cheaper and more versatile biosensors. The interaction of nanomaterials with biological entities, such as

proteins, enzymes, nucleic acids, oligonucleotides has emerged as a new field known as “nanobiotechnology”, which refers to the methodological approaches used for the bio-combination of nanomaterials to create tools for the investigation of biological systems. The integration of nanomaterials onto biosensors results on the enhancement of sensitivity, stability, and detectability even in small sample volumes, in comparison with conventional systems. In addition, thanks to the miniaturization techniques developed by the semiconductor industry, nanomaterials stimulated the research and development of miniaturized microfluidic tools for multiple detection. [32-33]

1.3.3.1 Classification

Biosensors may be classified in three ways: i) according to the signal transduction method (optical, mechanical, electrochemical); ii) according to the receptor type, catalytic biosensors if the receptor is an enzyme, affinity-bases biosensors for antibodies, aptamers, nucleic acids as receptors; iii) according to the assay type, direct or indirect (competitive). [30]

Considering the signal transduction method biosensors can be optical, mechanical (piezo-electric, acoustic, …) and electrochemical. For optical biosensors various techniques have been exploited for the purpose: chemiluminescence, electrochemiluminescence (ECL), luminescence, UV/Vis light absorption, light scattering, reflectance and surface plasmon resonance (SPR). The first three techniques are grouped into the label-based category, the others into the label-free category. Label-free approaches are the simplest to realize, they are based on light refraction index changes on the solution, and they allow quantitative and kinetic measurement. Label-based approach, instead, are more sensitive (for chemiluminescent or ECL sensors detectability down to attomoles can be reached when they are used in immunoassays or gene probe assays [29]) but they cannot be easily exploited for quantitative measurements. [31]

According to the receptor type, enzyme-based receptors are generally used for the detection of small molecules or small metabolites related to pathological conditions, one of the commonest are the sensors for glucose for diabetes management. Affinity-based receptors are principally constituted by antibodies, other macromolecules such as non-antidoby-binding proteins

(NABPs), nucleic acids, protein nucleic acids (PNA) are often used for this purpose. Affinity-based receptors are the most versatile and used for biosensing. They take advantage of the interaction between antigens and antibodies that naturally occur in biological systems and used for cellular recognition and communication. After understanding the language of the biological communication, used among other by the immune system, researchers have developed a new discipline, biotechnology, to realize new drugs, sensors, diagnostical agents and technologically advanced agents used for example as stationary phases for immuno-chromatographic separations. Antibody can be engineered to have a predictable binding physics to antigens in way of specificity and binding force. Dissociation of antigens from antibodies can be induced by the change of pH or ionic strength of the environmental aqueous solution. In order to enhance the stability of antigen-receptor complex non-antigen-binding proteins (NABPs) have been realized, they are stable proteins motif derived from conserved loop of fold from paratope-like complementarity determining region (CDR), a portion of the antibody deputed to antigen recognition. Antigen-NABPs complex is much more stable across pH, temperature and over the time, moreover NABPs can be produced from bacterial fermentation using biotechnological methods instead from animal sources as it is done for antibodies. Linear nucleic acids, aptamers and their synthetic analogues (protein nucleic acids – PNA) are used for complementary base pairing sequence recognition to a certain genome. [30]

1.4 NANOMATERIALS FOR BIOMEDICAL APPLICATIONS

With the tremendous technological progress, globalization, constant and generalized economic growth of the XX and XXI centuries, achieving an optimal level of public health is a common duty, especially for researchers who are called upon to provide innovative answers to new or ancient problems. According to the United Nations (UN) World Health Organization (WHO) the 2020-2030 must be a “decade of action” for health investments and it listed 13 urgent global health challenges that would be an investment in terms of saved life, support to most vulnerable counties and consequently future saved money by the health care systems. [34] Among these challenges

great attention is paid on the development and capitalization on technological advancements to realize even more numerous, cheap and quality drugs, medical devices, diagnostical kits and innovative therapeutical approaches. These goal could be based on the regularization and monitorization of digital technologies and synthetic biology and on the treatment of antibiotic resistance. [35]

Nanomaterials could be an extremely appealing and versatile answer to the great part of WHO challenges due to their peculiar physical and chemical properties that are dependent from size (quantum confinement) and from surface effects such as high surface area, luminescence, plasmonic properties, superparamagnetism and so on. [36]. Moreover, the research on those systems continues to be emerging and actual since the last 20-30 years and many of the synthetic procedures and properties are now quite established. Nanomaterials, in fact, have appealed a vast number of researchers in the last decades to find increasingly useful and original application, and great efforts have been paid for biomedical applications with the aim of quality life improvement. Is not surprising that the nature of the biochemical interaction between cells and within living organisms is in fact based on the nanoscale. Sub-cellular organelles, vesicles of various kind (endosomes, exosomes), viruses, plasmatic proteins, receptor complexes and many other biological functional structures are in effect in the range of tens of nanometers. The ability to produce tailored nanomaterials in size, shape and functionalities "would offer researchers unprecedented opportunities to probe, influence and even rewire cellular behaviours". [36]

Over the years, nanomaterials have been produced for a multitude of biomedical applications, so many that a new discipline, nanomedicine, has been created. Nanomedicine investigates all the nanomaterials, created thanks to nanotechnology, that are used "for the diagnosis, prevention, and treatment of disease and to gain increased understanding of the complex underlying physiopathology of disease. Moreover, the aim of nanomedicine may be broadly defined as the comprehensive monitoring, repair, and improvement of all human biological systems, working from the molecular level using engineered devices and nanostructures to achieve medical

benefits. The focus of nanomedicine is always on nano-interactions within a framework of a larger device or biologically with a sub-cellular (or cellular) system." (European Science Foundation – ESF – definition, 2004 [37]). In other words, the ESF definition explain and synthetize the concept that the potential of nanomedicine is the creation of tailored systems on the scale of the common cellular, sub-cellular and complex biochemical interactions of the human body in way to mimic and modify them with the aim to improve the quality of life. On the ESF definition, nanomaterials for biomedical or nanomedicine application are carrier agents for drug delivery purposes, analytical tools for nanobioimaging and novel therapeutics for theranostic applications.

1.4.1 EPR effect

In 1986 Matsumura and Maeda [38] have opened a new way in nanotechnology several years before it became widely known. They studied the *in vivo* behaviour of systemic administered macromolecules such as polymers and proteins conjugated with anticancer drugs or dyes founding their abnormal accumulation in the tumoral tissues of mice. They speculated that the "tumoritropic accumulation resulted because of the hypervasculature, an enhanced permeability to even macromolecules, and little recovery through either blood vessels or lymphatic vessels" [38] and consequently coined the Enhanced Permeability and Retention (EPR) effect. It was not long that this concept passed from a speculation to a widely demonstrated fact in the years to come.

The discovery of tumoral accumulation of macromolecules was successfully extended to nanoparticles and subsequently limited to 0D, or in some cases 1D, nanomaterials of specific size and shape. It has been also assessed that EPR effect occurs only in solid tumours accordingly to their physiopathology that modifies the dimension of the fenestrations of the vasculature that surround and sustain the tumour and allows the extravasation of nanoparticles.

Since the discovery of the EPR effect and thanks to the technological improvements appeared from the late '80s of the twentieth century, a large volume of research has been dedicated to nanotechnology for therapeutical

purposes, rechristened nanomedicine. In other words, EPR effect is one of the milestones of nanomedicine. It allowed researchers exploiting the extraordinary properties of nanomaterials inside the human body for therapeutical purposes. Theoretically, the realization of tailored nanospecies interacting with the complex human biochemical systems, exposed in the European Science Foundation (ESF) definition of 2004 [37], is something extraordinary that could has remained only a proof of concept without overcoming one of the most critical issues related to this new approach: how to get nanomaterials into the desired area? Additionally, how to exclude or limit the interaction with normo-functional systems, thus reducing the risk of side effects and toxicological related issues? The discovery of the EPR effect gave a reassuring answer to these questions, as it showed how systemic administered nanomaterials are preferentially accumulated, for physio pathological reasons, in tumour or inflamed districts limiting the interaction with sane tissues.

1.4.1.1 Mechanisms of EPR effect

The rapid growth of a tumoral mass implies an increase in energy needs that has to be sustained with the equally rapid production of blood vessels. A massive and rapid neovascularization produces abnormal blood vessels with deficient basement membrane and increased fenestrations. In parallel, the increase of the tumoral mass causes the reduction of the lymphatic vessels production and the increase of the inflammation levels. [39]

Irregularities on the basal membrane of vessels and lack of efficient drainage systems are the major cause of the retention of the nanoparticles into the tumoral area. Increased fenestration in blood vessels together with efficient transendothelial pathways guarantee nanoparticles extravasation, their retention is guaranteed by the reduced lymphatic activity. With the continuous increase of the tumoral mass solid tumour stress and increase on the interstitial fluid pressure will occur. They limit EPR effect due to reduced delivery of nanoparticles on the centre of the tumour, but the delivery on the peripheral area continues to be unmodified sustaining the anticancer effect. [39]

1.4.1.2 Criticisms on the EPR effect on humans and how to enhance

After the extensive demonstration of the therapeutical, imaging and theranostic effects of nanomaterials, that in many cases improved the classical therapeutical approaches based on small molecules, EPR effect guaranteed the passage from in vitro cell culture and animal experimentation to clinical trials on humans. Although the colossal advancements performed in the last decades, clinical scalability of nanomedicine based on EPR effect was non satisfactory as hoped due to several limitations that have been discovered over the practice such as, first and foremost, a reduced intensity of EPR effect in humans compared to animal models. Something that has been observed as remarkable in rodents (the most used animal models for *in vivo* pre-clinical studies) has not been comparable to the results on human experimentation. However, these results did not discourage the researchers, also prompting them to understand what the critical issues were and how to overcome them to improve the EPR effect on humans. [39]

The reduction of the EPR effect has been whereby attributed to the different physiopathology of a human solid tumour and on the different human physiology. For example, blood flow in humans is 800-fold higher than in rodents that means higher shear force in blood vessels and quicker wash off. Only this explanation could be satisfactory to justify the reduced intensity of EPR effect on humans, but also differences on tumour type, location, individual factors and tumoral microenvironment contribute to it. [39]

Considering the above-mentioned factors, the realization of efficient nanomedicine agents against cancer needs to be weighted on the specific purpose. Although the general effect may remain limited, there are some strategies to improve the EPR effect on humans: i) for macromolecular agents their weight must be below 40 KDa; ii) the optimal size of nanoparticles might be around 100-200 nm to prevent liver or spleen filtration and subsequent elimination; iii) to improve plasmatic half-life the surface charge should be neutral or negative; iv) nanoparticles might be preferentially constituted by biodegradables materials to improve nanodrug tolerability; v) preferential shape should be cylindrical, worm-like, discoidal or ellipsoidal; vi)

coadministration with permeability enhancers such as nitric oxide, anti-VEGF (Vascular Endothelial Growth Factor) agents, photodynamic and photothermal agents or radiotherapy. [39]

1.4.2 Drug delivery

Most of the efforts on the biomedical application of nanomaterials have been directed towards realization of drug carriers and onto their natural evolution, the smart carriers responsive to external stimuli (pH, heat, light, hypoxia, etc). [36] The discovery of the abnormal accumulation of systemic administered nanomaterials into tumoral districts significantly boosted medicinal research and in particular medicinal technologies. Exploiting the EPR effect for drug delivery purposes was the natural evolution of the research on this field and now, fortunately, nanodrugs for the controlled release of active drugs (mainly small molecules) are in medical practice. Thousands and thousands of different nanodrugs have been created, published, and used to improve the properties of hundreds of already available drugs.

Nanocarriers are designed to deliver and stabilize drugs preventing their interaction with everything that is not the final target reducing, in the less possible, the uptake from sane tissues. In other words, nanocarriers are used to improve pharmacokinetic of the delivered drug that can be also an association of two or more. The drug can be covalently or non-covalently attached to the surface or dispersed inside the matrix of nanomaterial, in the latter case the nanomaterial serves as reservoir system. [36, 40, 41]

In terms of pharmacokinetic, nanocarriers improve the solubility of drugs allowing, for example, the use of highly lipophilic molecules that could not be easily absorbed using conventional routes of administration. Similarly, molecules that are not stable to the metabolic system (hepatic microsomal systems, plasma non-specific esterases, gastric low pH, …) could be protected from the encapsulation on the nanocarrier by reaching almost unaltered to the final target. Drugs that have a narrow therapeutic window, or better, drugs whose therapeutic dose is very close to the toxic dose, such as most of the anticancer chemotherapeutics, can be delivered using a nanocarrier only on the correct site lowering their dose reducing in this manner side effects

and systemic toxicity. Nanocarriers are also used for extending the circulation time of drug on the plasma in way to increase bioavailability and the possibility to reach the target tissues. [40]

The real versatility on the use of nanomaterials as drug carriers stays on the large possibility of surface functionalization. Indeed, surface functionalization controls the targeting capability of the nanocarriers promoting their cellular uptake. In reality, EPR effect has a poor control on the final targeting because depends only on size, shape and charge of nanoparticles according to the dimension of endothelium vessel fenestration and trans-endothelial pathways efficacy. Broadly speaking, the EPR effect grossly does most of the work by bringing the nanoparticles inside or in the tumoral peripheral area, while surface functionalization finely completes the job controlling a punctual targeting in the desired tissue and promoting cellular uptake. In this way, nanocarriers may be functionalized with ligands able to address them to specific cell lines or sub-cellular organelles enhancing their uptake and reducing once more side effects and overall toxicity. The choice of the correct ligands is subject to in-depth biochemical knowledge of the cellular molecular machine in physiological and pathological conditions. Tumoral cell lines present or overexpress some receptors that must be selected for specificity in order to have a selective targeting. There are many examples on ligand-based targeting exploiting ligands such as adenosine, folate, glucose, aminoacids. Their action is based on the massive proliferative activity of cancer cells that require appropriate levels of nutrients, regulating factors and nucleotides. For this reason, cancer cells overexpress the receptors for those ligands significantly increasing the possibility of drug uptake. Apart the ligand-based targeting the surface of the nanocarriers have been successfully functionalized with several proteins and glycoproteins (ferritin, antibodies), oligonucleotides, DNA aptamers, siRNA and so on. [40]

Thanks to the continuous and fervent research on this field, it has been possible to combine the natural drug carrier ability of nanosystems with the latest findings in terms of nanotechnology obtaining smart devices that are stimuli responsive. The era of the controlled release is born. Nanocarriers can release drugs for example only in a specific pH, we observe for instance the

emergence of gastro-resistant formulations up to the most recent systems that are triggered by the acidic pH of tumour microenvironment. Connected to the peculiar characteristic of tumour microenvironment, there are some nanocarriers that activate their drug release only under hypoxic condition that is typical of solid tumours. There are many examples of photoactive drug carriers, for example near-infrared (NIR) absorbing nanoparticles that can release their content only under light irradiation on these energies. In most of the cases they use a combined therapeutical approach to enhance efficacy overcoming multi-drug resistance (MDR). They achieve this by carrying both a conventional anticancer drug and a photosensitizer for photodynamic therapy or an agent for photothermal therapy that possess high light-to-heat efficiency coefficient. Temperature, light and pH are not the only stimuli for the activation of smart nanomaterials for nanomedical purposes, in literature examples of nanomaterials that are responsive to magnetic, electrochemical, red-ox, enzymatic stimuli or to specific chemicals or biological environment are numerous demonstrating the vast interest of the scientific community. [40, 42]

1.4.3 Bioimaging

The early diagnosis is a crucial part of the clinical practice, in complex diseases such as cancer time is always a good ally for the best therapeutic response, clinical outcome and patient compliance. Imaging techniques often play a pivotal role on the identification and classification of diseases, those are in fact the gold standard on diagnosis. The technological progress offers increasingly sophisticated and accurate instruments refining even more the actual techniques, but to improve lesion detection very often more than one imaging modality is combined and the discovery of new contrast agents is continuously needed. Currently used contrast agents are, for the great part, conventional small molecules with non-specific distribution, fast metabolism, and negligible toxicity. Imaging modalities in current use are: ultrasound, fluorescence imaging, magnetic resonance imaging (MRI), computed tomography (CT), X-Ray radiography, positron emission tomography (PET) and single photon emission computed tomography (SPECT). [43]

Recently, nanomaterials have attracted researchers that are focused on the biomedical imaging for their unique physical and chemical properties to realize even more sensitive contrast agents. As was done in the previous section for the research on drug delivery, nanomaterials advantages compared to conventional small molecules approach are summarized below. [43]

- Tunable and enhanced targeting – Nanomaterials for the enhanced permeation and retention (EPR) effect possess unique passive targeting in tumours, having a preferential accumulation in cancerous over sane tissues. Moreover, for their high surface area and reactivity they can be easily functionalized with specific ligands (molecules, proteins, oligonucleotides, …) to active target receptors on the lesions that are wanted to show increasing the image contrast (lesion to background). [43]
- Tunable dimensions – It have been demonstrated that size, shape and surface charge of nanomaterials used in nanomedicine control their fate in the organism in terms of distribution and permeation, those are in fact the parameters on which the magnitude of the EPR effect depends. They can be manipulated to optimize the loading of imaging compounds or their physical and chemical properties to meet specific clinical needs. For example, nanomaterials that are below 10 nm are rapidly excreted by renal filtration and may be potentially used to image this system. Nanoparticles that are over 100 nm are easily identified and sequestered by the mononuclear phagocyte system (MPS) in organs such as lymph nodes, liver and spleen. [43]
- Prolonged bioavailability – Nanomaterials have a prolonged blood circulation time (bioavailability) for their intrinsic characteristics. Bioavailability can be enhanced by surface functionalization with polyethylene glycol (PEG) that reduces the clearance operated by macrophage opsonization. [43]

- Real time imaging – Nanomaterials offer the possibility of real time functional visualization and monitoring of biological processes. [43]
- Smart control– Stimuli responsive nanomaterials (pH, heat, hypoxia, red-ox potential, light, …) successfully used for controlled chemotherapeutical drug release can be used also for the release of contrast agents. The punctual release only on the desired area increases the bioimaging contrast. [43]
- Multimodality – The proper choice of surface functionalization or intrinsic material constitution of nanoparticles offer the possibility to have in the same object the contemporary presence of two or more properties that can be used by different imaging modalities. For example, a nanosystem based on ^{64}Cu-Fe-RGD-PEG-MNPs nanoparticles [44] was used for contemporary photoacoustic, PET and MR imaging. Melanin nanoparticles (MNPs), good photoacoustic contrast agents and melanoma targeting agents, naturally complex $^{64}Cu^{2+}$ and Fe^{3+} ions bringing their MRI and PET contrast capabilities and PEG functionalization/covering enhance the blood circulation of the system. [43]

1.4.3.1 Imaging techniques characteristics

- Ultrasound – Ultrasound imaging is one of the most widely used diagnostic imaging technique due to its high spatial resolution, low cost, real-time operability, portability and non-invasiveness. Nanoparticles used as contrast agent for ultrasound imaging are needed to be between hundreds of nanometres in size (usually about 200 nm). [43]
- Fluorescence – Fluorescence imaging can provide the best spatial resolution on the microscopic level compared to the other available techniques. It is frequently utilized to guide interventions on real time, staining tumoral tissues and controlling that all the tumoral area has been completely resected. Using near-infrared light to stimulate

photoluminescence emission an advantage on deeper tissue penetration and less non-specific tissue autofluorescence is reached. The common designs of nanoparticles for this purpose are three: i) nanomaterials are used as carriers for surface-labelled fluorophores; ii) core-shell structure on which the fluorophore is embedded on the core and antibodies or ligands for active targeting on the shell; iii) smart nanosystems in which there is a luminescence quenching under normal conditions and a luminescence turning on only into the desired area for in situ enzymatic degradation. [43]

- Magnetic resonance – Magnetic resonance imaging has high spatial resolution, three-dimensionality, soft-tissue contrast and is completely harmless. MRI contrast agents can be divided onto three categories: T_1-weighted positive contrasts, T_2-weighted negative contrasts and mixed T_1-T_2-weighted contrasts. The first encompasses Gd^{3+} complexes and typically paramagnetic materials that shorten the T_1 relaxation time of protons, the second superparamagnetic materials such as iron oxides nanoparticles that shorten T_2 relaxation time of protons, the last family of the mixed contrast agents includes for example gadolinium oxide (Gd_2O_3) nanoparticles. Nanoparticles design for MRI imaging retraces the previously exposed for fluorescence imaging. Nanoparticles decorated on the surface with MRI contrast agents and core-shell superparamagnetic iron oxide nanostructures reported. For the smart materials family combination of two or more properties are installed into a single nanoparticle for multimodal detection techniques. [43]
- Computed tomography – Computed tomography imaging is the natural evolution of conventional X-Ray radiography because offer with fast examination speed, improved efficiency and higher spatial resolution cross-sectional images of the detected area that are used to reconstruct 3D images. Conventional CT contrast agents are based on iodine that suffer of rapid

clearance, potential renal toxicity and some other potential side effects. Moreover, compared to conventional radiography there is higher exposure to ionizing radiations. Nanoparticle-based contrast agents are designed to lower the toxicity of the conventional one enhancing the X-Ray attenuation effect and the overall contrast. Metals nanoparticles containing gold, zirconium or tantalum have been produced, it was even demonstrated that gold has a greater X-Ray absorption efficiency and a better toxicity profile than iodine-based agents. [43]

- PET/SPECT – Positron emission tomography and single photon emission computed tomography are powerful imaging techniques with high tissue penetration and the possibility of the real time detection of the extent of a metabolic or specific biochemical processes as a function of the contrast agent selection. Those technique suffers from the high cost and from the potential high radioactive exposure of the patient. The use of nanoparticles can reduce the amount of the administered radionuclide. [43]

2. CARBON DOTS

Carbon dots (CDs) is a generic term used for photoluminescent carbon 0D nanomaterials. They are quasi-spherical in shape and their size is generally less than 10 nm, in some cases also ≈ 60 nm carbon dots were reported. [45]

CDs are constituted by carbonaceous sp^2/sp^3 core, the extent of graphitic or amorphous allotropy influences their final physicochemical properties. CDs surface, typically made of sp^3 amorphous carbon, is abundantly functionalized with oxygenated groups in various oxidation states, from -OH (hydroxyls) to -C=O (carbonyls, ketones, or aldehydes) and HO-C=O (carboxylates, carboxylic acid). Amines or amides are often present. Collectively, they impart exceptional water dispersibility to the nanomaterial that make them addressable for biological applications. These functional groups are also particularly useful for post-synthetic functionalization with a multitude of chemical species such as small molecules, polymers and biological macromolecules which divert their chemical and physical behaviour and reactivity towards selected entities useful for analytical and sensing purposes. [45, 46]

Functional groups, the choice of the precursor and the synthetic procedure together with the nanometric size and the extended π core domains control carbon dots optical behaviour. CDs are universally recognized for excellent photostability, excitation wavelength dependent photoluminescence, Red-Ox reactivity of the excited states and multicolour UV/Vis absorption. The optical behaviour of CDs is dependent from its precursor that can be molecular, polymeric or inorganic which in turn influences the choice of the synthetic procedure, top-down or bottom-up approaches. The produced nanomaterial could result different in size, functionalization rate, graphitization degree and some of the structural features of the precursor can be retained in the nanoparticles, which allows some degree of predictability. Carbon dots so on can be all the quasi-spherical carbon nanomaterials which includes those with molecular-like behaviour or delocalized electronic structure and all those that range between them. [47]

2.1 CLASSIFICATION

Since their discovery, carbon dots have been extensively produced and studied. They have been prepared starting from so many precursors whose the only limit is the imagination, for example natural compounds, microorganisms, food, wastes, pure chemicals and so on. A lot of different carbon dots have been characterized and the actual deep knowledge on the system allowed a retrospective analysis on the already published. Now we know that all the carbon dots family possess some common features, but slightly different morphologies or uncommon optical properties were used to start classifying them. However, it is still a challenge to properly classify carbon dots in a specific subfamily, because tedious and expensive characterization are necessary and sometimes these go beyond the scope of application or basic research that is not a niche.

Carbon dots can be classified for morphological features, for the heteroatom doping or for a functional classification. The latter is the most common. For morphology they can be amorphous carbon dots (a-CDs), graphitic carbon dots (g-CDs) or single-layer graphitic carbon dots (slg-CDs). If carbon dots have been doped, during or after the synthesis, the atomic symbol of the heteroatom is used as a prefix to CDs acronym (N-CDs, P-CDs, S-CDs).

2.1.1 Functional classification

Functional classification of carbon dots is based on physicochemical (shape and crystallinity) and photophysical properties. Subfamilies were created reflecting the four kinds of photoluminescence mechanisms of carbon dots that have been reported: quantum confinement effect, defect states, molecular states, and crosslink-enhanced emission states. These mechanisms have led to a classification of CDs as graphene quantum dots (GQDs), carbon quantum dots (CQDs), carbon nanodots (CNDs) and carbonized polymer dots (CPDs). [47]

- GQDs – Layers of graphene nanosheets that are packed together to form discoidal shaped dots. During High Resolution Transmission Electron Microscopy (HR-TEM)

analysis it is possible to find graphene lattice on the core, generally with the typical interlayer distance of 0.24 nm associated with the C(100) in-plane lattice spacing. The surface of the nanoparticle is fully decorated with functional groups. They show photoluminescence mainly due to quantum confinement effect related to their overall nanometric size or to the confined space of excitons from conjugated π domains.

- CQDs – Quasi-spherical in size and show visible crystallinity from core graphene-like domains. Like GQDs their emissive phenomena are related in majority due to quantum confinement.
- CNDs – Also this group is formed by quasi-spherical dots that are in this case mainly constituted by amorphous carbon phase. Their luminescence is related to defect states and eventual molecular-like states.
- CPDs – They possess a hybrid polymer-carbon based quasi spherical core, in some case polymer-like surface is distinguishable next to the traditional plethora of polar functional groups.

2.2 SYNTHETIC METHODS

Carbon dots can be prepared in different ways. Their success in many fields of research also comes from their affordability, easy manipulation and relatively simple synthetic methods that have attracted many translational researchers. CDs were serendipitously discovered in 2004 as side products of carbon nanotubes synthesis. During the electrophoretic purification of the reaction mixture, Xu and co-workers [48] found a brilliant emissive fraction and wrote something that was rapidly recognized as pioneering. As usual in research time and practice are required for optimization, in fact in the earlier examples something that now are considered harsh methods were employed for CDs preparation. In instance physical cracking methods of bulk materials were only feasible. They continue to be matchless for industrial production, but the need of expensive and field instrumentations relegated them on a niche. The situation has been quickly reversed when thermal decomposition

methods appeared in 2007 (Liu et al [49]). Now carbon dots are commonly prepared using solvothermal methods that are cheap, easy, versatile, and available to the most. Relying on the large volume of knowledge now available it is possible to classify all the reported methods in two large families: top-down and bottom-up approaches. [47]

2.2.1 Top-down approaches

This family encompasses in the timeline the earliest synthetic approaches of carbon dots. All of them use bulk carbon materials such as graphite as carbon dots precursors. They are physically fragmented to nanoscale and the kinetic energy is provided by different sources such as electricity or light.

According to Royal Society of Chemistry (RSC) Chemical Methods Ontology (CHMO) definition (ID: CMO:0002240), arc discharged method is "a method for the synthesis of carbon nanotubes where a direct-current arc voltage is applied across two graphite electrodes immersed in an inert gas such as He". In extension, this was the first used for carbon dots synthesis. Xu et al [48] in fact discovered CDs during an arc discharged synthesis of carbon nanotubes, the method has been widely used [50] but generally production yields are low, high voltages and temperatures are required and purification is difficult [51].

Laser ablation, electrochemical exfoliation, ultrasonic fragmentation, and chemical oxidation are the other family members. It is possible to obtain large quantities of material and tuning physical conditions it is also possible to have monodispersity. Working on physical parameters give the advantage of industrial scalability of the process that compensate some of the disadvantages of these methods. Laser ablation lacks on product uniformity in size and in high luminescence quantum yield, chemical oxidation can be time consuming for multi-step reactions and may leads to more defects on CDs surface cause of blue shifted luminescence [47], ultrasonic fragmentation could not produce monodispersity and electrochemical exfoliation could be also longer than the other techniques but it can be still optimized. [51]

2.2.2 Bottom-up approaches

Subsequent in the timeline, these approaches have achieved success for a major versatility of the starting material selection and synthetic procedures. Unlike the previous group, carbon precursors are organic molecules or polymers that are forced to dehydrate and condensate to dimensional nanostructures by chemical or physical forces. Generally, these procedures are simpler and more convenient than top-down approaches and lead to a final product that is tunable in physical and chemical properties. It often happens that the chemical behaviour of the molecular precursor is retained on the product. In this way, choosing the correct precursor to predictable reactions it has been possible to start elucidating the chemistry behind carbon dots synthesis. Nowadays in fact, there are more and more examples of Near-Infrared (NIR) emissive CDs exceptionally useful for biomedical and technological applications that could be also scalable for large productions.

This family encompasses the following methods: combustion, template, solvothermal/hydrothermal and other recent and "exotic". Historically, the combustion (or pyrolytic) method was the first example of bottom-up synthesis of CDs, as reported by Liu et al in 2007 [49]. They prepared CDs from the combustion soot of candles that was oxidated with nitric acid (HNO_3) and subsequently purified. [46] Actually, the method requires first of all the pyrolysis of the molecular precursor with the aid of a muffle furnace, than the carbon-based powder is chemically oxidated in reflux with a proper oxidizing agent (generally HNO_3) followed by purification via centrifugation, dialysis or chromatography.

Template synthesis of carbon dots is essentially a multi-step process in which is possible to control the morphology of the final product. Zeolites or mesoporous silica are employed as host templating nanomaterials for the controlled growth of carbon dots that are finally released from the support via chemical etching. CDs with exceptional uniformity in size can be obtained, but long and expensive procedures are needed and low luminescence QY is generally reached. Sometimes etching is not quantitative and purification procedures could be difficult. [51]

Solvothermal techniques are the most versatile and utilized for CDs preparation. The carbon precursor is solubilized in a high boiling solvent in the presence of an eventual catalyst or co-reactant. The mixture is placed in a closed vessel that generally is a Teflon-line sealed stainless-steel autoclave heated at a temperature higher than solvent boiling point for 8-20 hours. When water is the solvent, the procedure is called “hydrothermal synthesis”. The process take place also with microwave irradiation, and many examples of faster reactions are reported. The complex pattern of reactions as dehydration, coupling, polymerization and condensations involved in carbon dots synthesis are dependent from the starting material, reaction time, temperature, catalyst or co-reactant, solvent polarity. With this technique surface oxidation degree and core crystallinity/graphitization of the final product are manageable. Moreover, incomplete carbonization of small molecules (mainly for polycyclic aromatic hydrocarbons) and polymers could lead to polymer-like carbon dots surface that may retain molecular like optical behaviour.[47]

Recent bottom-up methods in literature are rapid plasma [52], localized heat generation from Fano resonance of AuNPs [53], in situ solvent free carbonization [54] or rapid magnetic hyperthermia [55].

2.3 ELECTRONIC PROPERTIES

The electronic properties of carbon dots are influenced by the sum of different physical and chemical phenomena. Due to nanometric size they are subjected to quantum confinement effect and their chemical state as functionalization rate or heteroatom surface doping can strongly modulate the conjugation.

It can be assumed that carbon dots are constituted by a condensed reticulum of sp^2/sp^3 carbon that can be ordered or non. Carbon on CDs core is mainly bonded to itself or sometimes with hydrogen, while on the surface hydrogen, oxygen or other heteroatoms can bind to it. On this assumption, the frontiers orbitals have a significant π character and the most probable transitions are the π-π^* and the n-π^*. The energy gap between LUMO and HOMO orbitals, usually quite high for hydrocarbons, can be modulated or

lowered by the above-described phenomena. In the past years in silico models and experimental data from different research groups theorized and demonstrated the influence of these parameters on the electronic properties of carbon dots. They control the physical and chemical properties of CDs such as photostability, inertness, biocompatibility, water dispersibility, easy functionalization and photoluminescence tunability. [45]

In 2012 Mandal et al [56], theorized, using a self-consistent-charge density-functional tight-binding (SCC-DFTB) method, that quantum confinement effectively modulates the energy gap between the frontier orbitals tightening it as the size of carbon dots increases and enlarging it as the size decreases. The effect thus affects both orbitals, for example as the size of carbon dots decrease the energy of LUMO is decreased and the energy of HOMO is increased. They recognized that quantum confinement effect is prominent on the control of energy gap magnitude, while the contribution of functional groups modulates only the energy of the orbitals and not the energy gap between them. This result is based on the classification on electron-donating and electron-withdrawing groups. The former perturbate frontiers orbitals by increasing the energy of both, while the latter decreasing it. In other words, if we compare two groups of carbon dots with the same size but with different functional groups, these will maintain the same energy barrier between HOMO and LUMO but the electronic transition of the one functionalized with electron-withdrawing groups will occur at lower energies.

In 2015 Li et al [57], improved this model combining density functional theory (DFT), GW approximation (Green function G and Coulomb interaction W), and Bethe-Salpeter equation (BSE). They focused on the effect of functional groups, adding that the electronic structure of CDs is characterized by the competition and cooperation between hybridization of frontier orbitals with the functional groups and charge transfer therebetween [45]. The theoretical model considers also the influence of functional groups on the magnitude of HOMO-LUMO energy barrier. Hybridization between the core-related π orbitals and the orbitals of functional groups results on the decrease of the energy gap, while charge transfer processes between them increase it. They found in fact that C=O (carbonyl) containing (aldehyde, ketone and

carboxyl) functional groups are more effective on tailoring electronic and optical properties of CDs, while another common functional group of CDs, the amino group (-NH_2), has a weaker influence. C=O containing groups, that are electron-withdrawing, will low both frontier orbitals energy, as reported in the previous theory, but they will be more favourable for LUMO. C=O in fact is better conjugated or hybridized with LUMO. On the contrary, NH_2 groups have a better charge transfer capability than conjugation and they will be less effective on tightening the HOMO-LUMO barrier.

At the same time, the doping of the surface of carbon dots with heteroatoms such as P, S, N and B can significantly modify their electronic structure. Heteroatoms introduce new energy levels, new orbitals, between the π orbitals of CDs. This can adjust CDs photophysical properties, tuning for example their photoluminescence. New energy levels can lead to the population of new excited states with a slightly different radiative decay to the fundamental state. Complex emission bands with low energy contributions or red-shifted band can be observed. The most common doping agent is nitrogen, but many and many examples on S, B and P have been reported. In some cases, the introduced photophysical properties are related to the parent heteroatom, for example phosphorous doping could lead to long living excited states.

2.4 PHOTOLUMINESCENCE

Despite all the efforts to understand the exact mechanism of photoluminescence emission of carbon dots, this still remains the subject of a fervent scientific debate. The nature of these controversial issue is probably to be found on the influence of many complex factors arising from CDs as a single entity and as a population in colloidal dispersion. Photoluminescence can be affected by size, shape, surface and core defects, crystallinity, functional groups, oxidation state, and heteroatom doping of the single CDs. In addition, colloidal dispersion of CDs often suffers of heterogeneity, polydispersity and in some cases lacks reproducibility. Fragments of molecules, oligomers, polymers free or adsorbed on the surface are always together with CDs in colloidal dispersion. Moreover, photoluminescence properties vary significantly depending on the precursor and on the

preparation method. [45] Classical molecular structure-property relationships cannot be easily applied. Therefore, it can be understood that the rationalization of this multifactorial emission phenomenon remains a challenge. [58]

Four different mechanisms of photoluminescence for carbon dots are reported: quantum confinement effect, defect states, molecular states, and crosslink-enhanced emission states. These helped to classify carbon dots into as many groups (vide Par. 1.5.1). Among them, the surface state derived photoluminescence has been recently considered as the universal photophysical model to explain CDs emission phenomena. This model includes and correlates all the above-mentioned factors but remains an ambiguous concept for the uncertain identification of these states. The key factor determining surface state derived photoluminescence are: i) particle size, related to quantum confinement effect; ii) surface defects, related to carbon surface defects, functional groups and eventually embedded molecules or polymers on the surface; iii) heteroatom doping. Generally, the surface states come from the synergistic hybridization of the π electrons of carbon core with an external electronic influence. New orbitals coming from functional groups (oxygen- or nitrogen-related), heteroatoms (such as N, S, P, B, F) or from sp^2/sp^3 carbon imperfections on the surface perturb the extended π conjugation of the core serving as exciton traps. [58]

The surface of carbon dots, due to heterogeneity and abundant functionalization, is usually rich of this “defects” resulting in a peculiar photoluminescence which is easily distinguishable from molecular. Usually, photoluminescence quantum yield (QY) may decrease with the increase of surface defects that are directly related to oxidation state, type and amount of functional groups and therefore on the fabrication method and surface chemistry. The more the emissive traps are present the more the radiative decay from the excited states to the fundamental may be not favoured. Sometimes is accompanied also with the red shift of emission bands. Luminescence lifetimes often results in a bi-exponential function and the extracted parameters are in the order of nanoseconds. Frequently, emission spectra are excitation wavelength dependent. In other words, changing the

excitation wavelength a complete emission spectrum is reported in which the emission maximum redshifts as the red shift of the excitation wavelength. In addition, these are broad and full width half maximum (FWHM) can be from dozen to hundreds of nanometres. These effects can be explained again with the surface defects model. Many defects and many emissive traps create a variegated profile of very similar emissive states, the sum of which contribute to a broad spectrum sum of different colours. The energies of these emissive states are numerous, so every time always different states can be populated as a function of the excitation energy. Finally, photoluminescence intensity can be also susceptible to the surrounding environment such as pH, solvents, salts, and so on. [58]

Another interpretation of the emission mechanism of carbon dots was reported by Wang et al [59] using femtosecond transient absorption spectroscopy. They considered the core of CDs as an optical antenna responsible of the initial photon absorption, subsequently an exciton is created which is rapidly transferred on the surface where is trapped and modified in energy. Finally, the radiative recombination of the electron-hole pair releases a photon. This model, despite good accordance with the surface state defect derived emission model was endorsed by many authors but still can't find convincing experimental evidence. Considering the surface state model, the theory of the core as an antenna can explain the greater weight of the particle size parameter above the others on the initial generation of the emission phenomenon. Excitation wavelength dependent luminescence, red shifts on the visible and broad emission spectra depending on the functionalization rate, heteroatom doping and so on are controlled by surface effects and then again in accordance with the surface state model by the amount of surface defects. [60]

2.4.1 Particle size

Quantum confinement effect modifies the electronic structure of carbon dots by means of the magnitude of the energy gap between HOMO/Valence band and LUMO/Conduction band and the energy of the states themselves. [58] In terms of photoluminescence, the larger the nanoparticles are and the lower the energy of the emitted photons will be.

This concept may be misunderstood considering only the overall size of the nanoparticle. Recent interpretations suggested that quantum confinement must be extended to the dimension of π electron systems. The previous statement should therefore be improved with "the larger is the π-system and the smaller the energy gap within the frontier states will be". As a confirm, many DFT computational studies suggested that CDs luminescence is mainly centred on the core conjugated π domains. By the way, this effect may be the leading actor only when CDs are considered as "only-carbon" sphere. Coupling interactions between extended π core orbitals and orbitals from functional groups, heteroatoms and defects normally occur in these systems. At this point, the surface defect related model gives a trustworthy explanation of CDs photoluminescence. In light of this, particle size may be considered only one of the parameters that influences CDs luminescence.

2.4.2 Surface defects

The sp^2 conjugated carbon domains of CDs are usually accompanied by many imperfections that come from various sources. Those imperfections are usually localized on the surface of the nanoparticle and serve as energetic traps for excitons. Consequently, surface defects are responsible for the peculiar photophysics of carbon dots such as excitation wavelength dependent photoluminescence. [58] The different types of defects are summarized above:

- sp^3 Carbon – σ and σ* states of the sp^3 carbon couple with the π and π* states of sp^2 carbon resulting in a modified electron-hole pairs recombination. Weak ultraviolet absorption and strong visible emission are a consequence.
- Oxygen-containing functional groups – Carbon dots surface is abundantly functionalized with polar groups that confer excellent aqueous dispersibility. The majority of them contains oxygen in various states of oxidation, -OH, C=O, and HO-C=O. Their introduction modifies the electronic configuration of π-extended core system by adding different populable energy states. It was recognized that hydroxylic groups introduce new n-π* gaps responsible of excitation wavelength-dependent

photoluminescence. Moreover, quantum yield of CDs seems to be strictly related to carbonyls groups content.

- Nitrogen-containing groups – When nitrogen-containing groups are present in form of surface functional groups they modify the electronic structure of carbon dots due to coupling interactions between their orbitals and the extended π-system of CDs core. Generally, coupling is mostly driven by charge transfer processes and so the extent of the electronic modification on the emissive properties is lower than oxygen containing groups in which coupling is principally driven by orbital hybridization. However, different reports found significant QY improvement and red shifts in absorbance and emission even with the only amino functionalization.
- Others – A large group of organic molecules, macromolecules and polymers can interact with the carbon dots surface via noncovalent interactions based on polarity or π-stacking. In the case of polymers, the correct choice of their structure and chemical functionalities allows a stable but noncovalent interaction with carbon dots surface such that are called passivation agents. They improve the optical behaviour of carbon dots enhancing the surface defects derived effects resulting in QY enhancement or in emission spectra modifications. Many other molecules, metal cations or polymers can act on the opposite resulting in a photoluminescence quenching.

2.4.3 Heteroatom doping

The introduction of heteroatoms on the surface or embedded into the core of carbon dots imply the interruption of the extended π electronic conjugation. Heteroatoms orbitals possess additional energy levels that result in defect states. Those defects usually produce red shifts of emission and on the UV/Vis absorption spectra or additional photophysical effects related to the parent heteroatom. Nitrogen, Sulfur, Phosphorus, Boron, Fluorine and other non-metals elements were used for CDs doping.

Among the most popular, nitrogen is one of the most utilized for tuning CDs optical behaviour. The atomic radius and the electronic structure of nitrogen is similar to carbon, so its incorporation onto the carbon matrix is reasonably efficient even more than in the form of a functional group. Sulfur possesses similar electronegativity but larger atomic radius than carbon, has six valence electrons instead of the four of carbon and the electronic transitions on sulfur are easier than that of carbon.

2.5 APPLICATIONS

Carbon dots have been widely used as fluorescent probes for detecting various analytes in solution even in the biological environment. Their large use as analytical probes is due to remarkable versatility for the plentiful presence of functional groups that can be tuned by synthetic or post-synthetic conditions to be specific for a determined chemical specie. As nanoparticles carbon dots possess large surface area of interaction and for their carbonaceous nature, they are quite inert to the environment and to biological systems. In addition, the preparation of carbon dots is simple and low cost, and, in most cases, it is possible to predict the final reactivity choosing the correct starting material whose properties the carbon dots will retain. CDs have a good luminescence quantum yield, excellent photostability and a quick response on the quenching or the enhancement of photoluminescence on the interaction with analytes, and they are quite sensitive to the surrounding environment such as pH, ionic strength, solvents, and temperature. The postulated mechanisms of interaction and modification of their luminescence include photoinduced electron transfer, fluorescence resonance energy transfer (FRET) and inner filter effect. [61]

2.5.1 Sensing applications

CDs have been used to detect various metal cations, small molecules, macromolecules, and in some examples also negative ions such as SCN^- or S_2^-. Normal or tumoral living cells and bacteria were also detected by the interaction with properly functionalized, passivated or CDs synthesized for purpose possessing specific ligands. The detection sensitivity for ions is usually very high and, in some cases, can be in the femtomolar order. CDs are also used in ratiometric sensor taking advantage of the simultaneous

detection of two emission peaks that increase the sensitivity of the system considering the intensity ratio between the two. [60-61]

2.5.2 Biomedical applications

CDs are one of the most promising nanomaterials for biomedical applications due to peculiar photoluminescence, physical and chemical properties and excellent biocompatibility, the latter demonstrated in numerous in vitro studies. CDs quickly enter cells passing the membrane by not defined mechanisms, it seems that they can use all the known, and subsequently distribute into the organelles in a manner that is dependent from CDs properties. In vivo studies demonstrated that CDs are rapidly excreted via the hepatobiliary system and presented no inflammation-related signs from biochemical, histological and haematological analyses on rats. [61] After the demonstration of biocompatibility, a large volume of science was made on exploiting the photoluminescence properties of CDs for the realization of smart nanomedicine tools for theranostic, bioimaging, phototherapy, drug delivery.

Bioimaging is a non-invasive microscopy technique for the real-time visualization of biological events via probes and detectors. Due to peculiar photoluminescence CDs were amply utilized as probes for real-time fluorescence imaging. Most organic dyes utilized for fluorescence microscopy require cell fixation and only few are available for living cells. Living cells can be treated in fact with CDs and directly analysed without the pre-treatments required for conventional staining that can't allow to visualize a living cell. Tailoring the surface and dimensions of CDs it is possible to divert cellular uptake and distribution to organelles realizing specific luminescent probes that can be employed for studying the related biochemistry or to punctual deliver drugs, the theranostic purpose. The specific uptake can be realized also with the functionalization of carbon dots with targeting ligands for nucleus or mitochondria. [61]

Covalent functionalization or non-covalent surface adsorption of anticancer drugs, photosensitizers for photodynamic therapy, aptamers, oligonucleotides or biotechnological drugs are developed for targeted delivery purposes. In this way, drugs with a narrow therapeutic window, poor

solubility or bioavailability can be simply utilised, delivered on the desired body site (for example tumoral lesions) carrying out their therapeutical actions with a significant reduction in the dose. In some cases, CDs per se exhibit pharmacological effect. [61-62]. Shereema et al found antiangiogenic effect of CDs prepared from carbon soot from burned styrene that downregulated the expression of the growing factors VEGF and FGF [63]. It is known antibacterial effect but surprisingly it was observed also antiviral effect against novoviruses [64] and herpes simplex 1 virus [65]. Their effect can be photoactivated or not [61].

Carbon dots, naked, functionalized or nanohybridized with other photoactive nanoparticles (TiO_2, AgNPs – Silver nanoparticles, or AuNPs – Gold nanoparticles) have been employed as active agents for phototherapy. Phototherapy incudes photodynamic therapy (PDT) and photothermal therapy (PTT), they can be used alone or in combination with surgery, conventional chemotherapy, or ionizing radiations to eliminate cancerous cells, fungal infections, or other skin-related diseases. Conventional PDT agents are organic molecules – prodrugs – that are inactive until their photoactivation, they are photosensitizers whose excited states react with oxygen converting it into reactive oxygen species (ROS) such as $^1O_2$, $O_2^{-\cdot}$ and $^{\cdot}OH$ that induce cell death by apoptosis. Photothermal therapy agents can be also small molecules that during photoexcitation promote non-radiative decay to the fundamental state discharging the energy excess with the release of heat. For many side effects and the poor light to heat conversion efficiency during the time they have been substituted by metallic nanoparticles such as gold nanoparticles that enormously increase the light to heat conversion efficiency for the localized surface plasmon effect. For their extraordinary photostability, the large potential of tuning the electronic structure and the photoproduced excited states, carbon dots were successful employed as PDT and PTT agents. For example, Zheng et al [66] prepared a carbon dots-carbon nitride (C_3N_4) nanohybrid in which protoporphyrin IV was non covalently adsorbed. Carbon nitride improved red light absorption and catalyses the water splitting reaction with O_2 production. Hypoxia in tumoral tissues was overcome and the photogenerated oxygen could be used by protoporphyrin

photosensitizer for $^1O_2$ production. Similar effect was found for Mn-doped CDs [67]. A photothermal efficiency of 50 % was achieved with a Red/NIR emitting CPDs prepared from citric acid, urea, polythiophene and diphenyl diselenide, superior also to some gold nanoparticle based PTT agent [68].

3. NOBLE METALS NANOPARTICLES (AUNPS AND AGNPS)

Noble metals are a group of elements of the periodic table that are resistant to oxidation and corrosion, the reason of their curious epithet is connected to the limited reactivity. Ru, Rd, Pd, Ag, Os, Ir, Pt and Au are listed in this group. Among all, silver and gold are the most studied, they are known since prehistory, they have been largely utilized for ornamental, status symbol and economic purposes, without forgetting the ancient and wide use in medicine. Nowadays, the attention on noble metals has shifted from the bulk to the nano level. Milestone concepts such as size dependence of the physical and chemical properties of materials have been discovered thanks to noble metals nanoparticles, laying the foundations for modern nanotechnology. Again, nano-structuration of silver and gold is the most studied, synthetic routes for Au and Ag nanoparticles are well established, physical, chemical, and therapeutical properties are consolidated and the safety profile for the environment and for the human health is one of the best for the nano-world. [69]

3.1 Plasmon resonance

Noble metal nanomaterials have fascinated researchers because of their unique optical properties. Their nano-sized dimensions make them addressable for biological applications, because of their similarity in size with the biochemical machinery of the living organisms. The interesting optical features of noble metals nanoparticles, in particular gold and silver, arises from the so-called localized surface plasmon resonance (LSPR) effect. LSPR effect occurs when the oscillating wave of light induces a coherent oscillation of the metal free electrons respect to the positive metallic lattice. When photons, for the quantum confinement effect, are confined to the small size of nanoparticles it is induced an intense electric field around those resulting in light absorption, scattering and non-radiative decay with heat production. Compared to molecular chromophores or fluorophores, metal nanoparticles in the range of 10-100 nm, that are subjected to the LSPR effect, present 5 order of magnitude of enhancement of the optical cross-sections. In this way,

the interaction of light with a single nanoparticle could be similar to up to a million of molecular dyes behaviour. [70]

Noble metals nanoparticles are photostable, the common photobleaching effect, in first instance for fluorophores and for chromophores in second instance, that most of molecular dyes presents does not occurs with metal nanoparticles. Higher excitation energies and time are allowed probing the enhancement of sensitivity and of the radiative and non-radiative decay effects of light excitation. [70]

3.1.1 Tunable properties

Localized surface plasmon resonance effect has a strong dependence on the size, shape and composition of nanoparticles. For gold, silver, and copper nanoparticles the LSPR occurs in the visible or near infrared (NIR) region of the electromagnetic spectrum, those nanoparticles are clearly visible because of their characteristic colours ranging from yellow (AgNPs) to red, purple, or blue (AuNPs). The optical behaviour of this type of nanomaterials is studied by UV/Vis absorption spectrophotometry, luminescence spectroscopy (only for some of these) and light scattering techniques. Colloidal dispersions (or even in solid dispersion) of noble metals nanomaterials present a characteristic LSPR band elucidating in many cases the morphology of nanoparticles, their chemical status, many physical and chemical properties, and their interaction with the external environment. [70]

Apart from elemental composition, the size of nanoparticles plays a key role on the definition of LSPR band maximum position. Without considering differences in shape and for spherical monodispersed nanoparticles, 10 nm AgNPs present the LSPR maximum around 390 nm, AuNPs around 520 nm. The LSPR band maximum red shifts as a function of the increase of nanosphere size. However, this effect is limited only to a restricted range of size, basically from 10 to 90 nm, and results in the external limit of red shift around 600 nm in plasmon resonance band maximum position. For 40 nm AuNPs LSPR maximum is around 530 nm. [11, 70]

The more efficient red shift of the LSPR band maximum is obtained modifying the shape of noble metals nanomaterials. This phenomenon is

extensively studied on gold nanoparticles. Rod-shaped AuNPs present two plasmon bands, one for the electron resonances on the short axis that retraces the conventional resonance of spherical gold nanoparticles around 520-540 nm and a second band related to the electron resonances on the long axis that is normally on the red od NIR region of the spectrum. Bizarre-shaped gold nanomaterials such as nanoprisms or nanoflowers usually possess the second plasmon band on the NIR region and they could be easily exploited for photothermal applications. The realization of core-shell structures is another way to red shifts the LSPR band position. [70-71]

3.2 Sensing and biomedical applications

3.2.1 Noble metals nanomaterials for optical sensing applications

The LSPR effect occurring in colloidal dispersions of noble metals nanomaterials (in particular gold and silver) is frequently exploited for sensing purposes. After choosing the correct nanomaterial for composition and shape set to be non-variable parameters, the sensing strategy is based on the recognition of modification in morphology and chemical status of the nano-system identifiable by the shift of the maximum of the LSPR band. Gold or silver nanoparticles functionalized with ligands are placed to react with their complementary species (receptors), the distance variation induced by the selective recognition causes LSPR band shifts by means of light scattering or refractive index changes. This expedient is widely used for DNA detection, the successful interaction between gold nanoparticles functionalized with oligonucleotides, designed for the specific hybridization with complementary regions of DNA, and the targeted genetic material causes a semi-aggregation of the colloidal system that results on the size increase and on the red shift of the LSPR band maximum. Sometimes, on commercially available colorimetric kits the LSPR band maximum shift is so large that the positive reaction is recognizable by colour change from red to purple. [70, 72]

Apart from the above cited LSPR band shifts other sensing strategies have been reported. Assays based on luminescence quenching, gold staining or surface enhanced Raman scattering have been realized.

The fluorescence of many fluorophores is quenched when they are close to noble metals nanoparticles surface, in particular gold surface. In proximity of noble and "heavy" metals the energy decay from the fluorophore excited states to the fundamental state is prevalently shifted to the non-radiative pattern. Many sensors have been realized on the base of competitive displacement assays, on the commonest approach without the analyte there will be no fluorescence, otherwise the analyte recognition causes the displacement of the fluorophore from the god nanoparticle surface causing its fluorescence restoring. [72]

Raman spectroscopy is based on the inelastic light scattering of an incident wavelength operated by molecules or chemical bonds resulting on characteristic spectra. Raman scattering efficiency depends on the intensity and on the wavelength of the incident light, the resulting signals are usually weak. Raman scattering is dramatically enhanced if the species are close to the surface of noble metals nanoparticles, such as gold nanoparticles, due to the strong enhancement of the electric field caused by the LSPR effect. The more the localized electric field is the more the probability of light scattering and of the resulting signal intensity. On this approach, molecules that possess complex Raman spectra can be easily recognized by their Raman signal enhancement operated by gold nanoparticles. Very sensitive analytical tools have been realized. [72]

Gold nanoparticles have been used to substitute expensive fluorophores or chromophores for the read out of the ELISA (enzyme linked immunosorbent assays) results. [72]

3.2.2 Therapeutic efficacy of noble metals nanomaterials

Noble metals nanomaterials have been extensively studied for therapeutical applications. On the large volume of knowledge currently available, the therapeutic efficiency of noble metals nanomaterials has been found both *per se* and under electromagnetic irradiation (mainly light).

Some types of AuNPs and AgNPs have been recognized for *per se* antimicrobial and anti-angiogenic activity, have been used as drug carriers, as X-ray contrast agents and for bio-imaging purposes. Other types presented

antitumoral activity under light, X-ray or γ irradiation for the photogeneration of reactive oxygen species (ROS). Light or electromagnetic irradiation could be used as a trigger for the release of covalently or non-covalently attached drugs. Some types of nanomaterials are tailored to have high light-to-heat efficiency conversion realizing photostable tools for photothermal therapy (PTT). [69]

Cellular internalization of gold and silver nanoparticles has been extensively studied and discussed and until now the results are still ambiguous. However, it is recognized that surface charge, size, shape, and surface chemistry are involved on the internalization process. Positive charged nanoparticles can easily pass through the cellular membrane via electrostatic interactions (cellular membrane is negatively charged), but internalization was observed also for negative charged nanoparticles via passive targeting (EPR effect). On the moment of the cellular internalization noble metals nanoparticles can fulfil their task as drug carriers or antitumoral agents for *per se* and photo-stimulated activity, but in many cases – as it was explained in the previous sections on the EPR effect and on the therapeutical applications of nanomaterials (vide section 1.4) – cellular internalization is not pivotal because even the only peritumoral accumulation of nanoparticles is sufficient to express their activity.

SECTION TWO

EXPERIMENTAL PART

4. AIM OF THE THESIS

The aim of the experimental work of this PhD thesis was the synthesis and characterization of nanomaterials of photochemical interest for sensing and biomedical applications.

4.1 INTRODUCTION

In the last decades, nanomaterials have been largely utilized for sensing and biomedical purposes. Driven by the need to find new, cheaper, more versatile, and easy-to-use tools that could be available for the largest share of users, researchers designed a large volume of analytical devices based on nanomaterials. The unique physical and chemical properties of nanomaterials, combined with the established synthetic and characterization protocols provided by nanotechnology offered the possibility to realize tailored devices for almost any purpose. Moreover, nanomaterials are realized from abundant starting materials that are generally cheap and readily available. Those are engineered to the nanoscale, the order of magnitude in which biological and biochemical interactions normally occur. This principle has laid the foundation for the use of nanomaterials for biomedical and therapeutical approaches. The idea was to dialogue with the biological matter using the same language, to compete on equal footing and in contemporary learning from the nature how to modify itself acting on orders of magnitude hitherto little explored. Nanomaterials are used as drug carriers, for bioimaging or to develop unconventional therapeutical approaches. The aim is to solve one of the more actual problems of the clinical practice, the prominent multi drug resistance of some cancer types or pathogenic microorganisms. In this scenario, the great efforts made by frontier researchers have produced a new class of nanomaterials, the “smart nanomaterials”, that might be simply defined as the natural evolution of conventional nanomaterials with controllable activity and activatable upon request maybe from an external stimulus. Among the possible, light is one of the most elegant triggers. Light possesses high spatio-temporal resolution, photons can be simply produced, controlled, and administered. The study of the interaction with light and matter represent one of the simplest, the more intriguing and affordable spectroscopies unrevealing the secrets behind the

fascinating mechanisms of photophysics. The possibility of realizing and controlling endergonic processes with the conversion of the energy enclosed onto light photons into chemical energy is one of the “life motif” of the photochemist in attempt to replicate the more complex, elegant, and efficient processes realized by the nature.

4.2 WORK DESCRIPTION

With such promises the experimental activity during the PhD period was mainly focused on understanding the behaviour of an emerging class of 0D carbon nanomaterials with interesting photophysical, physical and chemical properties: carbon dots (CDs). Carbon dots were prepared via a bottom-up approach from a natural source recycling the waste produced during the olive oil production. The produced CDs were used for chemical sensing and biomedical purposes. Interestingly, although the incredibly vast knowledge of chemical sensors based on carbon dots, little was known about their gas sensing capability, in particular as sensing layers onto conductometric devices. We found high performance sensing activity of carbon dots produced from olive solid wastes coming from the Mediterranean region Puglia (Italy) towards NO_2. Carbon dots prepared from another Mediterranean region Calabria (Italy) showed instead sensitivity towards NO. The different physical and chemical properties of the two CDs types, mainly dependent from the surface functionalization rate, in addition with the abundantly demonstrated cytocompatibility in the scientific literature of CDs inspired us to test their antibacterial activity. We found high antibacterial activity vs *S. Aureus* and a lower activity against *P. Aeruginosa*, moreover carbon dots coming from Puglia olive solid wastes showed lower activity compared to Calabria CDs. The variegated surface functional groups of carbon dots, mainly -OH, $-COO^-$, and $-NH_2$ that are responsible of their physical and chemical properties were exploited as complexing moieties for Eu(III) cations. A novel CDs-Eu(III) complex was realized in which carbon dots are utilized as light harvesting antennae inducing an energy transfer onto europium nuclei sensitizing their peculiar, sharp and intense emission in the red region of the electromagnetic spectrum. This red emitting complex, useful as potential biosensor because of the lack of interfering optical phenomena

such as tissue autofluorescence or non-specific scattering, was tested as a ratiometric luminescent pH sensor on the acidic range. We continued exploring the surface reactivity and the reactivity of the excited states of CDs realizing a CDs-Au nanohybrid useful for photothermal applications. CDs were functionalized with ethylenediamine to enhance Au(III) complexing and Au(0) binding capabilities. CDs-ethylenediamine excited states, generated by blue light irradiation, served as reducing agent for Au(III) salt to Au(0). In contemporary, CDs-ethylenediamine served as capping agent for the forming gold nanohybrid.

As complementary activity on noble metals nanomaterials it was also produced a new Mg-hydroxyapatite (Mg-HA) functionalized with silver nanoparticles. The nanofunctionalization was realized in situ, on the surface of the scaffold, via a photochemical reduction of Ag(I) to Ag(0). Results showed exceptional antibacterial activity against *E. coli* and *S. Aureus* but also cytotoxicity on human adipose derived stem cells probably for dysregulated increase of Reactive Oxygen Species (ROS).

During the visiting PhD period at the Laboratory of Nanochemistry of the Institute of Supramolecular Science and Engineering (ISIS) at the University of Strasbourg/CNRS (Strasbourg, France), carried out from January to June 2022 and under the supervision of Dr. Stefania Vitale and Prof. Paolo Samorì, the scientific activity was focused on the discovery of new nanomaterials starting from unexplored sources. Under this idea, there were produced, by liquid phase exfoliation methods, nanostructured materials from light volcanic rocks that are called “lapilli” that are produced during the explosive activity of Mount Etna (Sicily, Italy).

4.3 WORK EXPOSURE

The scientific activities, summarized in the above section, are divided in 5 chapters. The structure of each chapter reflects that of an original paper. The published papers are reproduced/adapted from the original before asking permissions to the editor. Anyway, also the non-published results and experiments are organized in form of a paper.

4.3.1 Chapters and author contribution

- Chapter 5 – CDs conductometric sensor for NOx gas sensing
  - 5.1 – NO_2 sensing

    Sawalha, S.[1, 2, *]; Moulaee, K.[3, *]; Nocito, G.[4]; Silvestri, A.[5]; Petralia, S.[6]; Prato, M.[5, 7, 8, 9]; Bettini, S.[2]; Valli, L.[10]; Conoci, S.[4, 11, 12]; Neri, G.[3], Carbon-dots conductometric sensor for high performance gas sensing. *Carbon Trends* **2021**, *5*, 100105

    [1] *Department of Chemical Engineering, An-Najah National University, Nablus, Palestine*
    [2] *Dipartimento di Ingegneria dell'Innovazione, Università del Salento, Lecce, Via Monteroni 73100, Italy*
    [3] *Dipartimento di Ingegneria, Università di Messina, Contrada Di Dio, Messina 98186, Italy*
    [4] *Dipartimento di Scienze Chimiche, Biologiche, Farmaceutiche ed Ambientali (ChiBioFarAm), Università di Messina, Viale F. Stagno d'Alcontres 31, Messina 98186, Italy*
    [5] *Center for Cooperative Research in Biomaterials (CIC biomaGUNE), Basque Research and Technology Alliance (BRTA), Paseo de Miramon 182, Donostia San Sebastián 20014, Spain*
    [6] *Dipartimento di Scienze del Farmaco e della Salute, Università di Catania, Viale Andrea Doria 6, Catania 95125, Italy*
    [7] *Consorzio Interuniversitario Nazionale per la Scienza e Tecnologia dei Materiali (INSTM), Via G. Giusti 9, Firenze 50121, Italy*
    [8] *Center of Excellence for Nanostructured Materials (CENMAT), Dip. Di Scienze Chimiche e Farmaceutiche, Università di Trieste, Via Giorgieri 1, Trieste 34127, Italy*
    [9] *Ikerbasque, Basque Foundation for Science, Plaza Euskadi 5, Bilbao 48009, Spain*
    [10] *Dipartimento di Scienze e Tecnologie Biologiche e Ambientali, Università del Salento, Via Monteroni, Lecce 73100, Italy*
    [11] *STMicroelectronics, Stradale Primosole 50, Catania 95121, Italy*
    [12] *Istituto per la Microelettronica e Microsistemi, Consiglio Nazionale delle Ricerche (CNR-IMM), Ottava strada n. 5, I-95121 Catania, Italy*

    [*] *These authors equally contributed to this work.*

    Contribution: Support on synthesis of CDs and on chemical tests.
  - 5.2 – NO sensing

    Development of a novel C-dots conductometric sensor for NO sensing. (Draft)

    Contribution: synthesis of CDs, characterization of CDs except for FT-IR and XPS analysis.

- Chapter 6 – CDs antibacterial activity

  Nocito, G.[1, *]; Sciuto, E.L.[1, *]; Franco, D.[1]; Nastasi, F.[1]; Pulvirenti, L.[2]; Petralia, S.[3]; Spinella, C.[4]; Calabrese, G.[1]; Guglielmino, S.[1]; Conoci, S.[1, 4, 5, 6] Physicochemical Characterization and Antibacterial Properties of Carbon Dots from Two Mediterranean Olive Solid Waste Cultivars. *Nanomaterials* **2022**, 12, 885.

  [1] Department of Chemical, Biological, Pharmaceutical and Environmental Sciences, University of Messina, Viale Ferdinando Stagno d'Alcontres, 31, 98168 Messina, Italy

[2] Department of Chemical Science, University of Catania, Viale A. Doria, 6, 95125 Catania, Italy
[3] Department of Drug Science and Health, University of Catania, Viale A. Doria, 6, 95125 Catania, Italy
[4] Istituto per la Microelettronica e Microsistemi, Consiglio Nazionale delle Ricerche (CNR-IMM) Zona Industriale, VIII Strada 5, 95121 Catania, Italy
[5] Department of Chemistry "Giacomo Ciamician", University of Bologna, Via Selmi 2, 40126 Bologna, Italy
[6] LabSense beyond Nano, URT Department of Physic, CNR Viale Ferdinando Stagno d'Alcontres, 31, 98168 Messina, Italy

* These authors contributed equally to the work

Contribution: methodology and writing

- Chapter 7 – CDs-Eu(III) as red emitting pH sensor

  Nocito, G.[1], Puntoriero, F.[1], Conoci, S.[1], Galletta, M.[1], Nastasi, F.[1] A New Carbon Dots-Eu(III) Complex as Red Emitting pH-Sensor. In: Di Francia, G., Di Natale, C. (eds) Sensors and Microsystems. AISEM 2021. Lecture Notes in Electrical Engineering, vol 918., Springer International Publishing (2023)

  [1] *Department of ChiBioFarAm, University of Messina, Viale F. Stagno d'Alcontres, 31, Messina, Italy*

  Contribution: methodology and writing

- Chapter 8 – CDs-Au nanohybrid

  Photochemical route to CDs-Au nanohybrid for photothermal applications (Draft)

  Contribution: methodology (except for TEM, SEM and Raman characterizations) and writing.

- Chapter 9 – Ag-nanostructured Mg-HA porous scaffold

  Calabrese, G.[1, *]; Petralia, S.[2, *]; Franco, D.[1]; Nocito, G.[1]; Fabbi, C.[3]; Forte, L.[3]; Guglielmino, S.[1]; Squarzoni, S.[4, 5]; Traina, F.[5, 6]; Conoci, S.[1, 7], A new Ag-nanostructured hydroxyapatite porous scaffold: Antibacterial effect and cytotoxicity study. *Materials Science and Engineering: C* **2021,** *118*, 111394.

  [1] *ChiBioFarAm Department, University of Messina, Messina, Italy*
  [2] *Department of Drug Science Department, University of Catania, Catania, Italy*
  [3] *Fin-Ceramica Faenza, 48018 Faenza, RA, Italy*
  [4] *CNR - Institute of Molecular Genetics "Luigi Luca Cavalli-Sforza", Bologna, Italy*
  [5] *IRCCS Istituto Ortopedico Rizzoli, Bologna, Italy*
  [6] *Biomorf Department, University of Messina, Messina, Italy*
  [7] *Distretto Tecnologico Micro e Nano Sistemi Sicilia, Catania, Italy*

  Contribution: support on the Ag-nanofunctionalization and on chemical tests

- Chapter 10 – Silicon nanoparticles from volcanic rocks (Draft)

  Contribution: methodology and writing

4.3.2 Experimental procedure utilized on this work for the preparation of carbon dots from olive solid wastes

Carbon dots were prepared according to the method reported in [73]. Olive solid wastes were washed several times with boiling deionized water until a clear solution appeared, dried overnight in oven, and pyrolyzed in a muffle furnace in the absence of air at 550-600 °C for 1 h. The resulting carbon-based material was finely grounded in a mortar and suspended in deionized water (10 mg/mL, 100 mL). The mixture was sonicated in ultrasonic bath for 10 min, 1 mL of hydrogen peroxide (H_2O_2 sol. 30 % (w/w) – Sigma-Aldrich) was added and then refluxed for 90 min under stirring. The reaction mixture was purified by centrifugation at 8000 rpm/6800 x g (RCF) for 20 min and the supernatant syringe-filtered (Sartorius Minisart RC 0.2 μm) obtaining the final CDs colloidal dispersion. A production yield from 2 to 4 % was estimated by weighting after solvent evaporation under reduced pressure and subsequent drying in oven. (See Fig. 1)

This procedure was applied on olive solid wastes collected from two southern Italian regions, Puglia and Calabria, obtaining carbon dots with different physical and chemical properties.

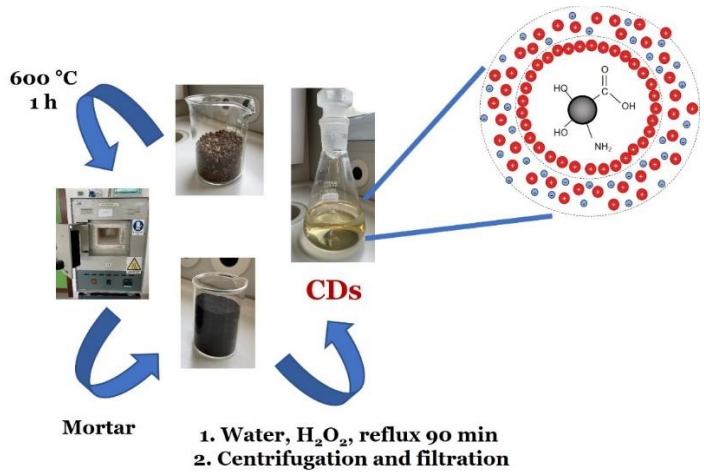

Fig. 1 Schematic representation of CDs preparation

5. CARBON DOTS CONDUCTOMETRIC SENSOR FOR NO_X GAS SENSING

5.1 NO_2 SENSING
"CARBON-DOTS CONDUCTOMETRIC SENSOR FOR HIGH PERFORMANCE GAS SENSING"

The content of this chapter is reprinted/adapted from Elsevier B.V., the author has the right to include it in a thesis [74]: Sawalha, S.; Moulaee, K.; Nocito, G.; Silvestri, A.; Petralia, S.; Prato, M.; Bettini, S.; Valli, L.; Conoci, S.; Neri, G., Carbon-dots conductometric sensor for high performance gas sensing. *Carbon Trends* **2021**, *5*, 100105

5.1.1 ABSTRACT

In this paper the first example of using C-dots (CDs) as sensing nanomaterial for monitoring low concentrations of NO_2 in ambient air is reported. In the logic to support a green circular economy, CDs were prepared from a natural low-cost precursor consisting in olive solid waste (OSW) by a simple pyrolysis process combined with chemical oxidation. Characterization data showed the formation of spherical CDs with dimensions in the narrow size range from 0.5 to 5 nm and charged with functional groups (COO- (carboxylate), C-O-C (epoxide) and C-OH (hydroxyl) imprinting excellent water colloidal dispersion. The nanomaterial was used to fabricate and test a conductometric gas sensor (CDs-sensor) that was found to exhibit excellent performances in terms of high and selective response to sub-ppm concentration of NO_2 at low temperature (150 °C), low limit of detection (LOD) of 50 ppb, good reproducibility and stability over use and aging. To the best of our knowledge, this is the first example reported in the literature of CDs high performances gas sensing material. Results here presented pave the way for a new class of a carbon nanomaterial for gas sensing to be applied in the field of environmental monitoring.

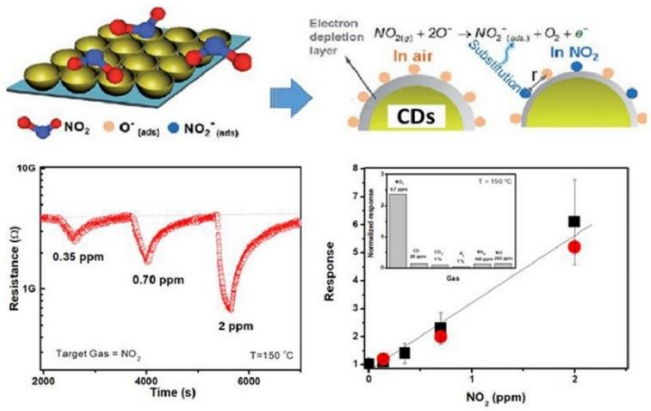

Fig. 2 Graphical abstract

5.1.2 INTRODUCTION

Carbon dots (CDs) represent one of the most promising nanomaterials for many advanced applications due to their multifunctional properties deriving from their unique quantum confinement and edge effects [75-76]. They also exhibit high chemical stability and good conductivity which, coupled with the very high surface area, can address effectively the use of CDs for sensing applications. In a recent review paper, the use of CDs for sensing towards several class of both organic and inorganic analytes has been extensively described [77]. However, most of the studies address sensing applications focusing on both CDs fluorescence and electrochemical properties as transduction detection method. Target analytes were mostly metal ions (Fe^{+3}, Cu^{2+}, Hg^{2+}, etc.) and electroactive (bio)molecules (H_2O_2, dopamine, glucose, etc.) [77].

Surprisingly, no particular attention has been given to CDs as material for gas sensing that is one of the most important applicative sectors for environmental sustainability. Limited study appeared only very recently. In one paper, a CDs-based quartz crystal microbalance sensor was used for the detection of gaseous formaldehyde [78]. In another work, Shauloff et al. fabricated an artificial nose based on CDs as the principle capacitance sensing determinant [79]. However, conductometric (resistive) sensors, which represents the most suitable, practical and cheaper gas sensing technology for monitoring a wide variety of gases [80], based on CDs are not reported so far.

In the environmental pollution, one of the most dangerous gas is nitrogen dioxide (NO_2) representing a relevant source of atmospheric pollution being a product of burning fossil fuel in industry, power plants, houses heating, and car engines. It relevantly contributes to particulate matter, photochemical smog and acid rain and it is very toxic for human health even at very low concentrations [81-84]. Therefore, sensitive, selective and easy to use sensors for NO_2 monitoring in both industrial and urban areas are strongly required and today no satisfactory solutions are present [85]. In this respect, only one study has been reported for optical detection (fluorescence) of NO_2 gas using a hybrid carbon nanodot functionalized aerogel (CDs/SiO_2,) tested in a pure nitrogen atmosphere [86]. Also, for the electrical detection, a single example describing a conductometric sensors uses a hybrid reduced graphene oxide-carbon dots (rGO–CD) sensing material has been described so far [87-88]. However, both above mentioned studies have practical limitations. Actually, CDs/SiO_2 fluorescence material has been demonstrated to work only in N_2 atmosphere, displaying a detection of limit of 250 ppb, which rule out its use for the low concentrations of NO_2 to be monitored in ambient air. In this respect, the Environmental Protection Agency (EPA) has settled one-hour exposure to NO_2 at the level of 100 ppb. Further, these work are based on sensing layer obtained by complex and multi-step synthetic procedures for the preparation.

In this work we present the first example of pure CDs sensing nanomaterial exhibiting excellent performances towards NO_2 monitoring in conductometric sensor architecture with selective and sensitive response up to sub-ppm concentrations of NO_2 in air.

The CDs here used were obtained from olive solid wastes (OSWs) raw material, an agricultural waste from the olive oil industry, highly appealing from an economical point of view due to its abundance and low cost [73]. Actually, OSWs are produced in massive quantities during olive oil production and represent a waste with high pollution potential. Therefore, providing to its re-use is within the logic of the circular economy. The transformation of OSWs in CDs here described leads to

carbon nanoparticles having very small particle size, which implies an extremely large surface-to-volume ratio and hence an elevated proportion of highly reactive sites. These features make these materials very appealing candidates for gas sensors material with high performance. Further, the easy processability of CDs enables the use of a facile integration on a variety of sensing platforms made in plastics, ceramics, or silicon, so offering different possibility for various practical applications. Finally, due the lack of investigation on CDs for gas sensing, this study can also represent a stimulus for further investigations on these nanomaterials in the environmental sensor field.

5.1.3 EXPERIMENTAL SECTION

5.1.3.1 Synthesis of carbon dots (CDs)

The CDs were prepared according to the method reported in [73] using olive solid wastes (OSWs) collected from Puglia – Italy (vide section 4.3.2).

5.1.3.2 Sensing tests

Devices for the sensing tests were fabricated by printing thick films of the C-dots powders dispersed in water on alumina substrates (6 mm × 3 mm) and provided by Pt interdigitated electrodes and a Pt heater located on the backside [83]. For the sensing tests, the sensors were introduced in a stainless-steel test chamber and after an initial time of stabilization at the fixed working temperature in flowing synthetic dry air (20 % O_2 in nitrogen), exposed to pulses of gas mixtures of selected composition.

Electrical measurements were collected through a data acquisition unit Agilent 34970A, while a dual channel power supplier instrument Agilent E3632A was employed to bias the built-in heater of the sensor. The concentration of NO_2 was varied from 140 ppb to 2.8 ppm. The gas response, S, is defined as $S = R/R_0$ for NO_2, where R is the electrical resistance of the sensor at different NO_2 concentrations and R_0 is the baseline resistance in dry synthetic air. Dynamic characteristics, such as response time, τ_{res}, defined as the time required for the sensor resistance to reach 90% of the equilibrium value after the target gas is injected and recovery time, τ_{rec},

taken as the time necessary for the sensor resistance to reach 90 % of the baseline value in air, were also evaluated.

5.1.4 RESULTS AND DISCUSSION

CDs was produced by using OSWs as starting material (see Fig. 3). First, the pyrolysis of OSWs at 600 °C for one hour has been carried to produce carbonized olive solid wastes (COSWs). The chemical oxidation of this intermediate material was employed to obtain CDs using H_2O_2 as an oxidizing agent. Optimization of H_2O_2 concentration (0.45 wt%) led to CDs of low diameter with a production yield of 10%. H_2O_2 is beneficial for breaking down the carbonaceous particles and extracting CDs with surfaces rich of oxygenated groups [73].

Fig. 3 Schematization of the synthesis process of CDs.

The morphology of the CDs obtained from OSWs has been investigated by TEM and AFM. The HR-TEM micrographs show well dispersed nanoparticles with good contrast and narrow size dispersion ranging from 1 to 4.5 nm as shown by the size distribution histogram drawn from TEM images and an average size of 2.8 ± 0.6 nm (Fig. 4a and b). Similar dimensions have been obtained by AFM for the height of the CDs with a range

of 0.5 to 5 nm having an average of 2.8 ± 0.9 nm, demonstrating that the particles have quasi-spherical morphology (Fig. 4c and d).

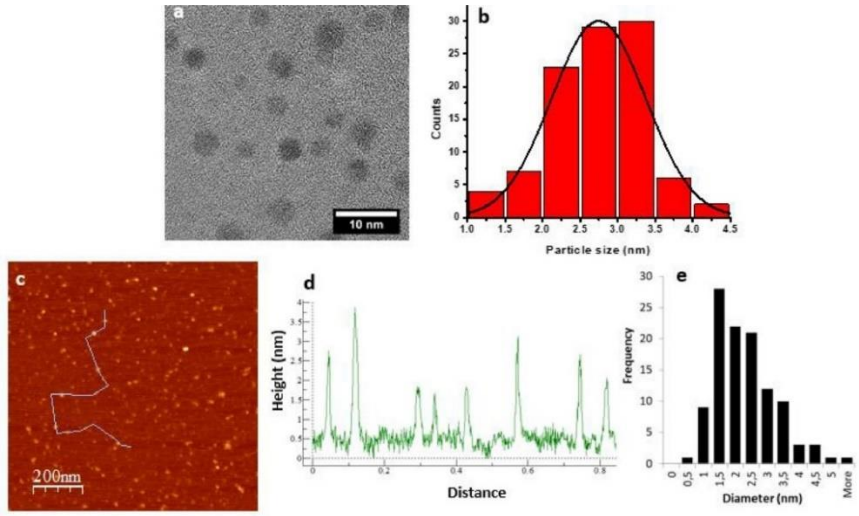

Fig. 4 Morphological characterization of CDs: (a) HR-TEM micrograph, (b) TEM size distribution histogram, (c) AFM height micrograph, (d) AFM height profile, (e) AFM height distribution histogram.

The functional surface groups were investigated using FT-IR spectroscopy (Fig. 5a). The peaks shown at 3424, 3236, 2923/2850, 1656, 1412, 1320 and 1116 and 1096 cm^{-1} are assigned to –OH, N-H, C-H, C=O (carbonyl), COO- (carboxylate), C-OH (hydroxyl) and C-O-C (epoxide) [89-90] groups, respectively. The presence of such functional groups implies that the synthesized CDs have excellent water-soluble colloidal dispersion [91]. It was also found that these dots are negatively charged with ζ-potential = - 32 mV in 10 mM PBS, the negative charge could be ascribed to the existence of oxygenated functional groups [92, 93-94].

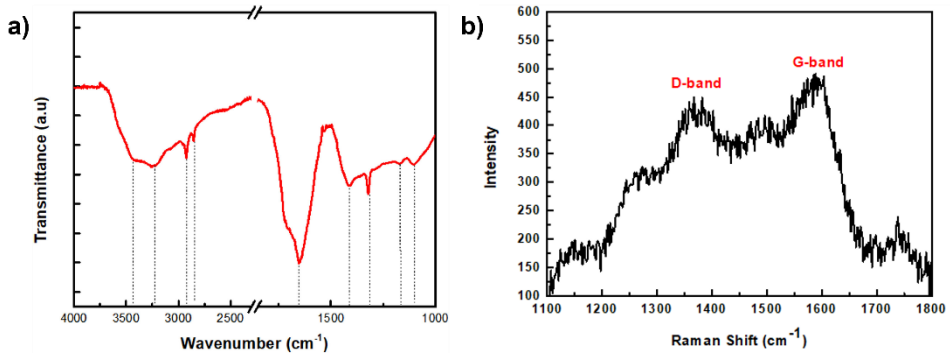

Fig. 5 a) FTIR spectrum of synthesized CDs; b) Raman spectrum of CDs sample.

Raman spectrum of the CDs sample is provided in the Fig. 5b. Weak D and G bands, at about 1370 and 1590 cm^{-1}, respectively, can been recognized in the Raman pattern. Further, a very high photoluminescence background is also presents, covering the Raman signals and hindering a deeper investigation. The photoluminescence background is likely due to the existence of chemical groups on the surface of carbon dots, such as C=O and -NH_2, and the presence of amorphous carbon.

In terms of conduction properties, the synthesized CDs evidence a semiconductor behavior with a band gap of 1.55 eV, estimated from the difference between LUMO (-4.24 eV) and HOMO (-5.79 eV) energy levels [95]. The HOMO – LUMO levels were calculated from oxidation and reduction onset resulted from the cyclic voltammogram (see Fig. 6a) using the following equations:

$$HOMO = -(E_{onset,OX} + 4.66\ eV)$$

$$LUMO = -(E_{onset,RED} + 4.66\ eV)$$

where $E_{onset,OX}$ and $E_{onset,RED}$ are the onset of the oxidation and reduction potentials respectively [96, 97].

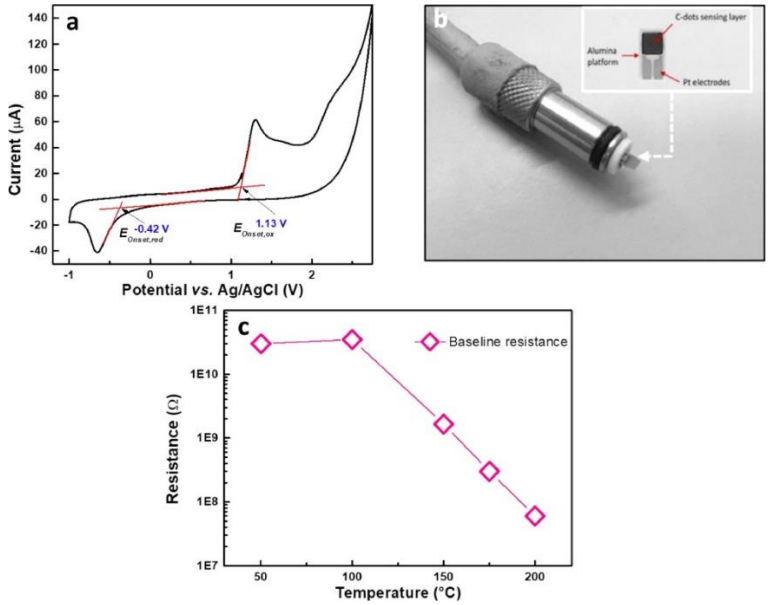

Fig. 6 a) Cyclic voltammogram versus Ag/AgCl reference electrode of synthesized CDs; b) picture of the conductometric sensor probe; in the inset is shown the sensor head; c) Baseline resistance vs. operating temperature trend.

The semiconductor behaviour has been confirmed by analysing the electrical resistance of thick films (around 10 μm) at different temperatures. The electrical measurements have been performed on the same platform used for the conductometric sensing tests (Fig. 6b), with the aim to acquire also direct information on the behaviour of CDs as a sensing layer in the practical device. In the inset of this Fig. 6b is noted CDs deposited as thick films by printing on the conductometric transduction device having a pair of interdigitated Pt electrodes on the ceramic substrate.

The range of temperature investigated was between 50 °C and 200 °C due to both the restrictions imposed by the very high resistance registered below 50 °C and the unstable and large baseline drift observed at temperatures higher than 200 °C. The trend of baseline resistance in this temperature range is reported in Fig. 6c. At near room temperature, the resistance is out of the range of measurement with our instrumentation. Increasing the temperature, the resistance decreases, as expected by a semiconductor material. This behaviour can be explained as follows: at low temperature, free electrons are trapped by O_2 molecules as ionized species

(O^- or O^{-2}), generating a depletion layer (Schottky potential barrier); further, the grain boundaries at the contact between the very small CDs might create additional potential barriers, increasing the electrical resistance. Increasing the operating temperature, thermally generated electrons give the main contribution to the resistance decrease. However, as an additional process due to the adsorbed O_2 molecules desorption from the CDTs surface upon increasing of the temperature, releases the trapped electrons and decreases the resistance.

On the basis of above described electrical characteristics that make CDs to be full compatibles for their use in conductometric platform for gas sensing, we have tested its performances in the monitoring of low NO_2 concentration in air. First, we evaluated the effect of operating temperature on the sensor response. Fig. 7a reports the variation of resistance for the CDs sensor subjected to pulses of NO_2 at the concentration of 2 ppm in dry air.

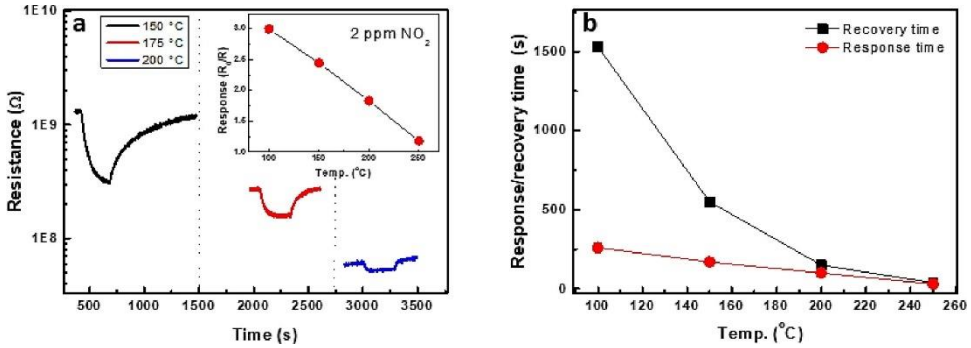

Fig. 7 a) Resistance variation at different temperatures of CDs sensor subjected to pulses NO_2 at the concentration of 2 ppm. Inset shows the trend of sensor response with temperature; b) Response/recovery time at different temperatures of the CDs sensor.

From the above reported data, it clearly appears that the CDs-based sensor is very sensitive to NO_2 gas exposure exhibiting a tendency to a response enhancement with the temperature decrease. However, by reducing the temperature, the recovery time becomes longer (see Fig. 7b) and this limits the practical application of the sensor. Therefore, the best balance between high response and faster dynamics can be settled at 150 °C. Fig. 8a reports the resistance variation for the CDs sensor, at the optimal

temperature of 150 °C, subjected to pulses of NO_2 at different concentration (from 140 ppb to 2 ppm) in dry air. The interaction among NO_2 molecules and CDs leads to a linear variation of the resistance with the nitrogen dioxide in the investigated concentration range, as highlighted in the calibration curve graph reported in Fig. 8b. It is noteworthy the good reproducibility of the two reported calibration curves, registered by two diverse sensors fabricated by using the same CDs. The resistance variations observed are well reversible; the response and recovery times are in the order of about 150 s and 315 s, respectively.

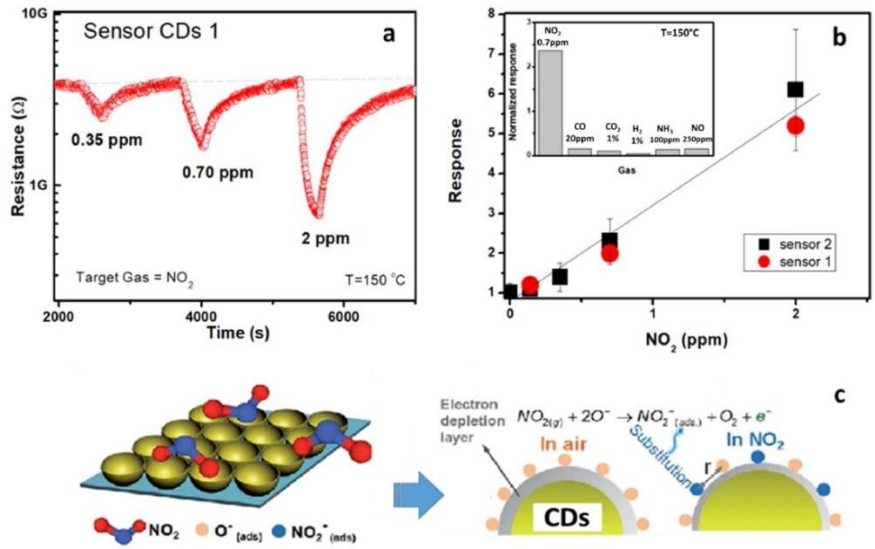

Fig. 8 a) Transient response towards different NO_2 concentrations for the CDs sensor; b) calibration curve towards NO_2, whereas the inset shows the response to different gases; c) schematization of the NO_2 proposed sensing mechanism on CDs-based conductometric sensor.

The interaction between the NO_2 molecule and CDs leads to a decrease of the resistance at all temperatures and NO_2 concentrations investigated, indicating that the CDs sensor has a p-type behaviour. This finding can be attributed to presence of electron withdrawing oxygen functional groups on the surface of CDs, as also suggested by some authors for other colloidal quantum dots [98].

The sensing mechanism can be described into the framework of general theory of p-type semiconducting gas sensors functioning [99]. However, the

true sensing mechanism of NO_2 on carbon materials is still not fully understood and only hypotheses could be formulated taking into account examples coming from CNTs and graphene as previous carbon nanostructures-based sensing material for NO_2 [100-103]. Here, we can suppose that the resistance of sensing layer decreases after adsorption of NO_2 gas molecule due to the direct adsorption/chemisorption of NO_2 on the CDs surface, which is covered of adsorbed O^- oxygen ions, the main surface oxygen species present at the operating temperature of 150 °C. NO_2 interacts with the chemisorbed oxygen ions on the surface and extracts electrons. Indeed, NO_2 as an electron acceptor consume electrons, resulting in the increase of hole concentration. The depletion layer becomes thinner (low electrical resistance, see Fig. 8c) and therefore, electrical resistance decreases, as experimentally observed.

Above explanation is in according with data reported for other carbon nanostuctures, such as CNTs, were Schottky barrier modulation is the main detection mechanism postulated for gas sensing [104].

However, other sensing mechanisms cannot be excluded and can be concurrently present, depending on many factors linked mainly to size of carbon nanostructures. Indeed, carrier transport through the electrode-carbon particles is influenced by the particle size and the width of the depletion region. In air, oxygen is adsorbed at the active carbon sites, accepting electrons from the conduction band and causing, depending on the size, a partial to fully depleted region devoided of mobile charge carriers. The conduction mechanism is then governed by Schottky barriers at the grain boundaries, and grain control mechanism, respectively.

For our CDs-based conductometric sensor, the sensing mechanism can be supposed to be related to limited charge transport across Schottky barriers. The conduction across Schottky barriers is regulated by thermoionic emission carrier transport, or less usually, by tunnelling. Relevant to gas sensing is however that the activation energy for conductance is a function of the barrier height, which is directly affected by the charge and fractional coverage of the surface species and, hence, a function of the composition of the gas surrounding the sensor.

Selectivity to target gas, response reproducibility and stability are also important parameters of a sensor for the practical use. From inset reported in Fig. 8b is noted a very low response toward reducing gases (CO, NH_3, CO_2, CH_4), which implies that the sensor is also highly selective towards NO_2. Experimental results have also demonstrated a good signal reproducibility. Fig. 9a shows the reproducibility test when the sensor was exposed to pulses of 2 ppm of NO_2 at 175 °C. A fairly stable response was observed for a period of approximatively three months (see Fig. 9b).

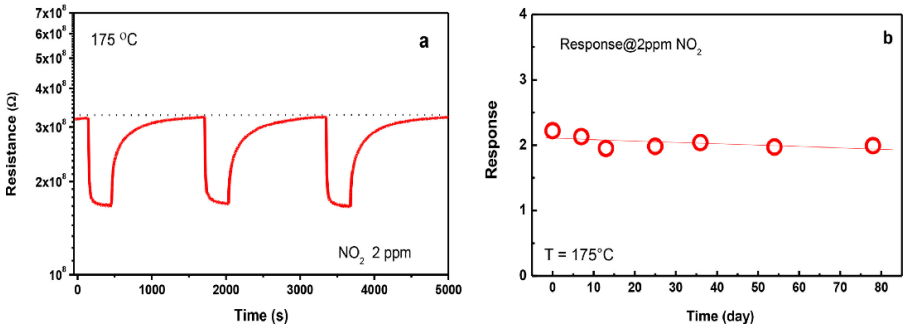

Fig. 9 (a) Response of the sensor to consecutive pulses of 2 ppm of NO_2; (b) Sensor response evaluated for a period of approximatively 3 months

The good sensing properties (sensitivity, selectivity, stability) of the sensor towards NO_2 can be then explained with the characteristics of CDs synthesized. First, the large specific surface area of the very small CDs provides many unsaturated sites with high reactivity, maximizing the interaction with the target gas. As regarding the excellent selectivity towards NO_2, it is associated to the surface state of CDs. Indeed, other than addressing the semiconducting behaviour, the chemical structure of the surface has the noticeable function to interact with the gases surrounding the sensor. In this way, depending on the chemical nature on the CDs surface and gaseous specie, the interaction will have a different strength and charge transfer. It seems then that the presence of the various organic groups on the CDs surface as indicated by FT-IR and XPS investigation can be relevant for NO_2 gas. In this perspective, it is interesting to note that it is possible to modulate the surface chemistry of the C-dots by introducing new ligands. These modifications can change the interaction of CDs with the gas molecules, modulating then the selectivity of the sensor versus different gases. At last,

the long term stability of the sensor can be related to mild temperature (150 °C) chosen for sensing tests. This aspect is fundamental in order to avoid thermal stress to sensing layer in general, and in particular in the case of CDs sensing layer, this mild temperature avoids to modify/degradate the labile surface groups on the surface of CDs.

Finally, the sensing performances of the developed CDs-based sensor were also compared with previously reported conductometric sensors based on other carbon nanomaterials (see Table 1).

Sensing material	LOD (ppb)	Response[1]/ concentration	Operating temp.	Measurement range (ppm)	UV light	Ref.
SWCNTs[2]	86	100/0.1 ppm	50 °C	0.1-10	No	[105]
Graphene oxide	0.21	10/1 ppm	150 °C	1-9	No	[106]
Aligned SWCNTs	-	7/0.5 ppm	RT[3]	0.5-10	Yes	[105]
S-doped graphene	-	0.2/500 ppt	RT	0.5-100	No	[107]
3D rGO[4]	186	0.1/1 ppm	22 °C	1-8	No	[108]
rGO	-	37/5 ppm	RT	5-100	No	[109]
CVD graphene	4	3/1 ppm	RT	1-20	Yes	[110]
C-Dots	50	140/0.7 ppm	150 °C	0.14-2	No	This work

1
Response (R) is defined as $R = 100 \times \frac{|R_g - R_a|}{R_a}$ where R_a and R_g are, respectively, the recorded signal in the absence and in presence of NO_2 at the indicated concentration.
2
Singled walled carbon nanotubes
3
Room temperature
4
Reduced graphene oxide

Table 1 Comparison of the NO_2 sensing performances of carbon conductometric sensors.

From this comparison, it is worthy to mention the outstanding sensitivity (3rd column in Table 1) of our nanomaterials. Further, this remarkable sensitivity and full and fast response/recovery of the signal is reached without the use of UV light. Once again, these comparative data confirm that the suitable carbon nanostructure obtained improve the performance of conductometric device for monitoring NO_2 at part-per-billion levels. However, we plan to further improve the performances of our materials by investigating in future studies both the effect of possible surface functionalization of C-dots and also the optimization of film structure and morphology.

5.1.5 CONCLUSIONS

In summary, CDs here reported were produced by a simple pyrolysis process combined with chemical oxidation from olive solid wastes, a cheap and readily available natural precursor. Morphological and microstructural characterization indicated that these nanometer CDs have a spherical shape with dimension ranging from 0.5 to 5 nm. Further, the presence of charged functional groups (COO- (carboxylate), C-O-C (epoxide) and C-OH (hydroxyl), which imprint excellent water colloidal dispersion properties, has been also highlighted.

NO_2 sensing properties of CDs has been investigated showing excellent performances in terms of sensitivity, selectivity, full recovery after exposure and stability. Noteworthy, this study represents the first evidence of using CDs sensing material for conductometric gas sensor. Therefore, we expect that this study will pave the way for a large family of CDs produced by different natural sources to be employed as highly sensitive sensors.

5.2 NO SENSING
"DEVELOPMENT OF A NOVEL C-DOTS CONDUCTOMETRIC SENSOR FOR NO SENSING"

The content of this chapter is a draft based on preliminary results during the experimental investigation of the PhD activity.

5.2.1 ABSTRACT

Carbon dots (CDs) obtained by waste generated during the production of Calabria olive oil have been investigated as a gas sensing material for the sensitive and selective detection of nitric oxide (NO) in air. The obtained CDs were characterized by X-ray Photoelectron, conventional and ATR FT-IR, Raman, UV/Vis and luminescence spectroscopies. CDs were deposited as a sensitive layer on a conductometric platform and tested for gas sensing, showing promising results for the selective monitoring of NO in air. The response of CDs composite to NO was 1.5 @ 1250 ppm and the response and recovery times were 90 and 200 s, respectively. The sensing behavior of CDs prepared by olive waste from a different geographic location (Puglia) was also reported and compared. It has been found that the sensing behavior of the two sensors investigated towards nitrogen oxides (NO and NO_2) was completely different. The first resulted selective to NO while the latter showed prominent selectivity towards NO_2. This behavior was attributed to the different functional groups present on the CDs surface. Data here presented indicate that hydroxyl group -OH address the response for NO, while C-O-C ether group promote the sensitivity and selectivity for NO_2.

5.2.2 INTRODUCTION

Gas detection using carbon nanomaterials, such as carbon nanotubes (CNTs), graphene (G) or graphene oxide (GO), has been largely pursued in the last decade [111]. Indeed, because of their small size, almost all atoms of the structure are located on the surface, so they can be highly sensitive to adsorbed gas molecules. This has subsequently enabled the development of conductometric sensors based on these 1-D or 2-D carbon nanomaterials, capable of detecting trace levels of gases [112]. In this regard, carbon dots (CDs) are 0-D carbon nanomaterials subjected to the "quantum size effect" showing interesting properties and promising applications in gas sensors [113].

CDs have quasi-spherical shape and the dimensions below 10 nm, consisting of an amorphous nucleus given by the sp^2 hybridized carbon and crystalline structures given by the sp^3 hybridized carbon. CDs can be synthesized following the "top-down" and "bottom-up" approaches. In the top-down approach, they are obtained from large carbon structures using characteristic methods to control their size, morphology, and purity, such as laser ablation, chemical and electrochemical oxidation, and ultrasound treatment. In the “bottom up”, the methods are simpler in which it is possible to control the size and obtain them with low cost using few solvents, such as microwave synthesis, thermal decomposition, and hydrothermal treatment [114]. In recent years there is a tendency to use organic waste materials, also defined biomass, to obtain carbon nanomaterials by exploiting simple and low-cost synthesis methods [115]. Carbon dots also can be produced from biomass, exhibiting different physical and chemical properties depending on the starting biomaterial and the preparation method adopted. So, carbon dots have attracted much attention due to their unique optical, chemical, and electronic properties enabling a wide range of applications. Further, CDs properties can be effectively adjusted through modifying their chemical composition.

The presence of -COOH, -OH and $-NH_2$ surface groups distinguish these nanomaterials, which give them excellent optical properties with wide continuous and absorption spectra, so contributing to their excellent fluorescent, photoluminescent and optoelectronic properties [116]. However, a major challenge remains in understanding the core and surface contributions to optical and electronic properties [61, 117].

Their electrochemical and optical properties were largely exploited for chemical sensing [118]. In fact, many studies on CDs focus on their fluorescence and electrochemical properties for the detection of various metal ions in water (Fe^{3+}, Cu^{2+}, Hg^{2+}, etc.) and biomolecules [76].

Given their properties, they could be also used as sensitive materials to develop sensors to detect gaseous environmental pollutants. However, on the contrary, few studies exist for the application of CDs in gas sensors. These reports deal with the use of CDs as a support for the sensing phase, usually a

metal oxide, and optical detection is the preferred transduction method [119-120].

In a previous introductory work, we reported the feasibility to develop a CDs-based conductometric sensor for NO_2 detection in air, demonstrating for the first time the use of pristine CDs in this typology of electrical solid-state device [74]. In this work we try to expand the possibility to use CDs obtained from olive solid waste to monitor nitrogen monoxide (NO) in air by a conductometric sensor. The main NO emissions in the atmosphere derive from the exhaust gases of cars, in which NO is the most common form of NO_x at around 93 %, around 100–2000 ppm. The Environmetal Protection Agency (EPA) sustains that these emissions cause environmental problems, causing an increase in the greenhouse effect as it has 310 times more impact than CO_2 and compromising human health through the onset of serious diseases related to the respiratory system. The minimum exposure value is 20 ppm. This outlines the importance of developing gas sensors that can detect NO in real time. However, the previous CDs-sensor was not able to detect NO [74]. So, we tested another CDs obtained by olive oil production solid waste coming from a different geographic origin (Calabria). This was motivated by fact that the surface composition of CDs produced may be very different if the raw material is changed.

Here we report the fabrication and characterization of a such conductometric sensor. Results demonstrate as the developed device allows the sensitive and selective detection of NO in air. Further, the comparison with the previous CDs sensor was also made, attempting to explain the different sensing behavior observed. At last, this study suggests the potential of this low-cost nanomaterial as promising active material in gas sensors for monitoring selectively the desired gases, by simply designing its surface composition.

5.2.3 EXPERIMENTAL SECTION

5.2.3.1 CDs synthesis

The CDs were prepared according to the method reported in [73] using olive solid wastes (OSWs) collected from Puglia – Italy (vide section 4.3.2).

5.2.3.2 Sensing tests

Sensor devices were prepared by printing thick films of CDs dispersed in water onto alumina substrates (6mm x 3mm) provided by Pt interdigitated electrodes and a Pt heater located on the backside. The sensing tests were carried out using the data acquisition instrument Agilent 34970A to monitor the resistance. A dual-channel power supply Agilent E3632A was used to bias the built-in heater of the sensor.

Sensing tests were performed using a homemade detection setup as follows; first, the sensor was inserted in a stainless-steel test chamber and was kept at a fixed temperature while a flow of synthetic dry air (O_2 + N_2) was passing over the sensing material to obtain a stable baseline resistance. Afterwards, the sensor was exposed to pulses of gas mixtures supplied from certified bottles from SOL company. The sensor response to target gas (R) is determined as the ratio of R_a (resistance of the gas sensor in dry synthetic air) to R_g (resistance of the injected gas sensor), $R = R_a/R_g$. The calculation of the response and recovery time, i.e., the variation of the sensor resistance over time until it reaches 90 % of equilibrium after the start and end of NO detection, allowed the study of sensor dynamics.

5.2.4 RESULTS AND DISCUSSION

5.2.4.1 Synthesis of carbon dots (CDs)

Carbon dots (CDs) were prepared from a natural precursor recycling the olive oil production discard, according to the method reported in our recent work [74], using olive solid waste from the Mediterranean region Calabria (Italy) (vide section 4.3.2). CDs final concentration was 0.4 mg/mL. C-CDs were prepared by pyrolysis from solid waste produced during the production of Calabria olive oil. We also investigated CDs prepared from Puglia origin olive solid waste; its sample code is P-CDs.

Carbon dots were obtained using a facile, low cost, and biofriendly route that starts with the pyrolysis of the natural precursor and continues with a green surface oxidation of the carbon-based nanostructured components. Hydrogen peroxide addition is crucial for the reaction because permits CDs surface oxidation and so on their functionalization with polar

groups, such as hydroxyls (-OH) and carboxyls/carboxylates (-COOH/-COO^-) [73]. These groups confer aqueous dispersibility and considering a different surface functionalization rate, in addition to different π domains extension in the carbon core, their peculiar optical properties and reactivity. These properties are recognized also as size dependent. [58]

5.2.4.2 Characterization of carbon dots (CDs)

5.2.4.2.1 Chemical composition

Carbon dots obtained from Calabria olive solid waste provenience (C-CDs) were exceptionally dispersible in water and the resulting dispersion was stable up to two months. According to Dynamic Light Scattering (DLS) technique, CDs surface was negatively charged, measured ζ-potential was -23 mV confirming the system stability.

As represented in Fig. 10 the XRD pattern of C-CDs included several peaks. The broad peak from 20 ° to 24 ° (2θ) and the sharp one at 2θ = 24.35 ° (3.7 Å d lattice spacing) are attributable to the amorphous carbon phase and to graphitic C(002) plane [121]. The graphitic nature of CDs is confirmed by the peaks around 40-45 ° and 53.80 ° (d-spacing 1.7 Å) assignable to C(100) and C(004) planes of graphitic carbon [122].

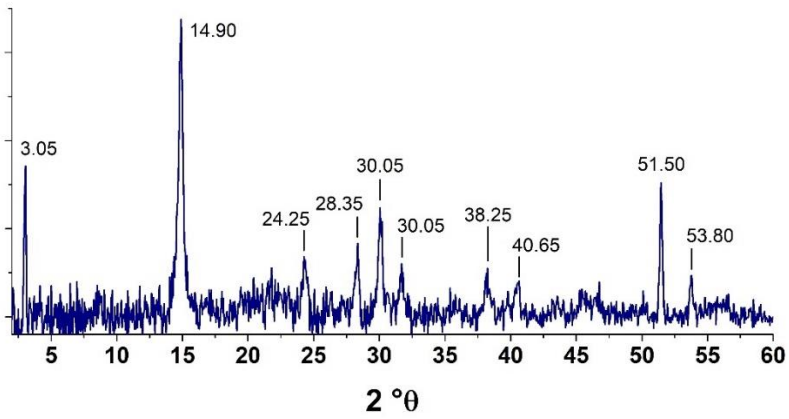

Fig. 10 XRD pattern of C-CDs

FT-IR analysis (see Fig. 11) revealed the extent of CDs surface functionalization. Different vibrational signatures, coming from surface groups can be seen, revealing the presence of –OH, C=O (carbonyl), COO^-

(carboxylate), C–OH (hydroxyl), and C–O–C (ether) groups. In particular, the wide band in the 3500-3000 cm^{-1} region is due to the stretching vibration of O-H groups. The strong feature around 1600 cm^{-1} can be associated to convolution to the signals due to C=O stretching of carboxylic (1660 cm^{-1}) of acids or amides, to the asymmetric stretching of carboxylate (1570 cm^{-1}) and to the bending of H_2O (1620 cm^{-1}). The other strong feature at about 1370 cm^{-1} correspond to convolution of the symmetric stretching of carboxylate groups (1450 cm^{-1}), the C-O stretches of carboxylic acids (1250 cm^{-1}) and the bending of OH groups (1350 cm^{-1}).

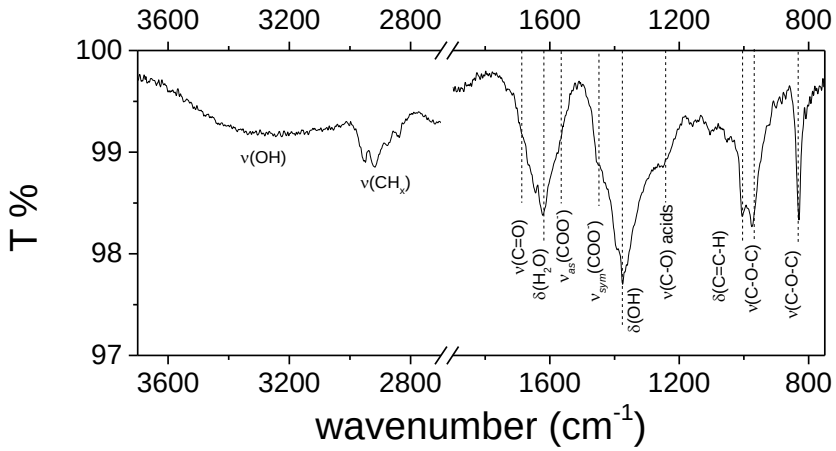

Fig. 11 FT-IR spectrum of CDs

HR-XPS spectra on the C1s, N1s and O1s regions are showed in Fig. 12. The complex shape of the C1s signal is mainly due to the presence of C-C, C-H signal at 285.0 eV and to the signal at 289.0 eV of carboxylic groups. A component around 287.3 eV must be added to account for the presence of carbons in carboxylates and amides groups. Note a small amount of K^+ is also present. The N1s band is mainly constituted by a peak at 400.4 eV that can be due to amines and amides (C-N containing groups). A small shoulder at about 399.0 eV could be also present due to the formation of imidic groups (-C=N-). The O1s peak position at 532.2 eV is typical of the oxygen in organic compounds.

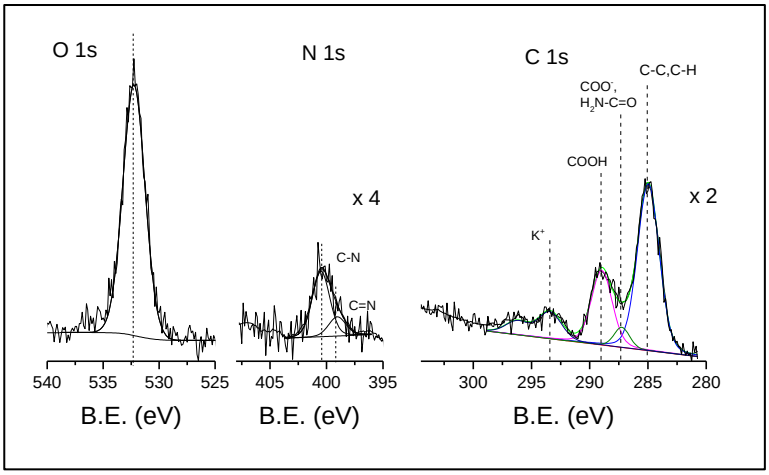

Fig. 12 HR-XPS analysis on C-CDs

In the Raman spectrum of C-CDs (Fig. 13) the D band at 1346 cm^{-1} and the G band at 1598 cm^{-1} were observed, the intensity ratio I_D/I_G was calculated to be 0.8. Another peak at 1444 cm^{-1} was assigned to C-C vibrations related to surface passivation with heteroatoms such as O, N and H. The typical Raman vibrational modes of carbon (D and G bands) and their intensity ratio revealed that carbon dots were constituted by sp^3/sp^2 carbon in which the graphitic nature is slightly higher than the disordered one.

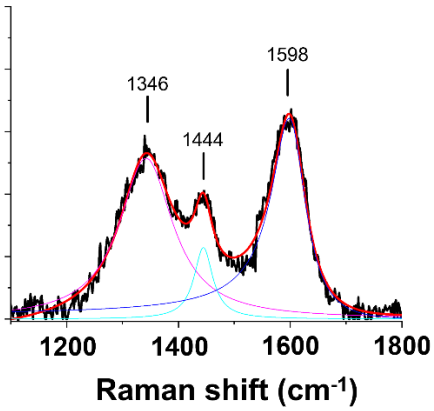

Fig. 13 Raman spectrum of C-CDs

5.2.4.2.2 Optical characterization

C-CDs colloidal dispersion in ultrapure water appears as pale yellow and presents blue/green luminescence under 365 nm lamp excitation. The

UV/Vis absorption spectrum in Fig. 14a exhibits broadband UV absorption with a quasi-asymptotic trend compatible with the light scattering operated by small nanoparticles. Under this band, there could be detected two peaks, confirmed by the photoluminescence excitation spectra in Fig. 14c, located around 280-290 nm and 340 nm attributed respectively to π-π* and n-π* transitions believably responsible for CDs emission phenomena [123, 124].

CDs show excitation wavelength-dependent photoluminescence, their emission bands move to lower energies as a function of the excitation wavelength. Emission spectra were recorded in the excitation wavelength interval between 250 and 450 nm as reported in Fig. 14b. Emission maximum is located around $\lambda_{emission}$ = 450 nm for $\lambda_{excitation}$ = 350 nm.

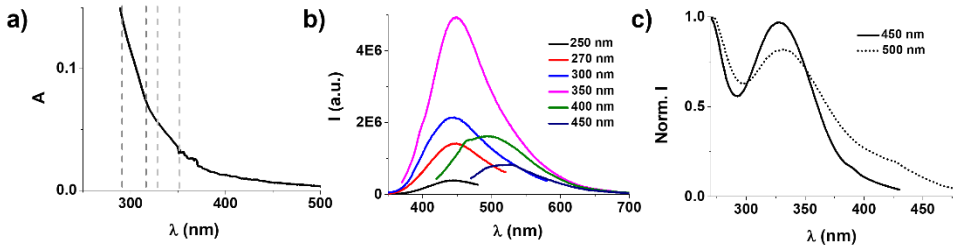

Fig. 14 Optical characterization of C-CDs sample: a) UV/Vis absorption spectrum; b) Photoluminescence emission spectra, excitation wavelengths in legend; c) Photoluminescence excitation spectra, emission wavelengths in legend

5.2.2.2.4 Thermogravimetric and Differential Scanning Calorimetry analysis

Thermogravimetric analysis (TGA) in air and nitrogen (Fig. 15 and Fig. 17a) shows that C-CDs are stable until 120 °C, 58-59 % of weight loss is experienced in two main steps.

Under nitrogen flow, 27 % of weight loss occurred on the first step at 175 °C and 16 % on the second at 450 °C. In synthetic air 21 % of weight loss is observed at 182 °C. The second step with an overall weight loss of 22 % is split into two sub-steps, the first at 434 °C with 8 % of loss and the second at 471 °C, as highlighted by the Differential Scanning Calorimetry (DSC) curve and the Differential Thermal Analysis (DTA) curve (see Fig. 16 and Fig. 17b).

The first decomposition stage can be attributed to the loss of water adsorbed on CDs surface, the loss of crystallization water, or the one released from dehydration processes [125]. The second may be associated with the loss of covalently linked species to CDs surface [126] or simpler to the loss of oxygen-containing groups such as -O-C=O and C=O [127, 128]. TGA confirms the empirical evidence that CDs in powder are particularly hygroscopic.

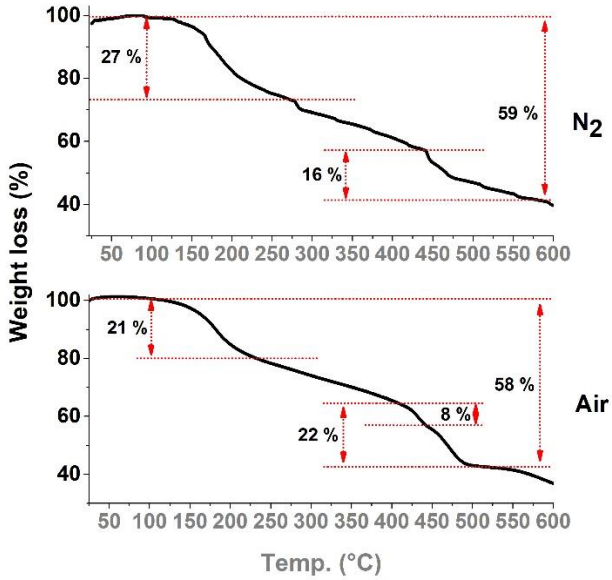

Fig. 15 TGA analyses in Nitrogen and synthetic air of Calabria carbon dots. Inside the graphs are reported the weight loss percentages per process.

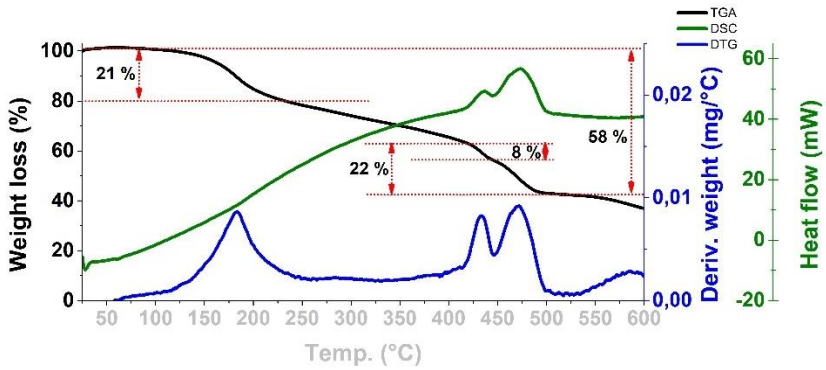

Fig. 16 TGA/DTG/DSC graphs in synthetic air atmosphere

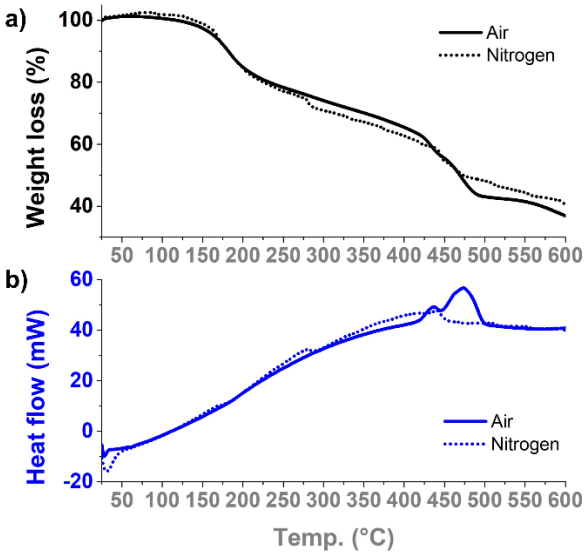

Fig. 17 a) TGA and b) DSC analyses in comparison between air and nitrogen atmospheres

5.2.4.3 CDs sensitivity to NO gas

The electrical resistance in dry air as a function of temperature for the C-CDs has been first investigated. The measurements were performed with the CDs sample deposited as a layer on the conductometric platform used for the successive sensing experiments, so the information obtained can be directly used for optimizing the performances. We noted as, starting from room temperature, the sample layer exhibits a very high resistance (Fig. 18). Increasing the temperature there is a sharp decrease of the resistance. CDs can be considered as p-type semiconductors, the decreasing of the observed resistance may be attributed to holes carriers which are activated for the conduction as the temperature increase. As they require a higher activation energy for the conduction, larger than for electrons, this explains the sharp decrease of resistance compared to that exhibited by n-type sensing materials such as metal oxides.

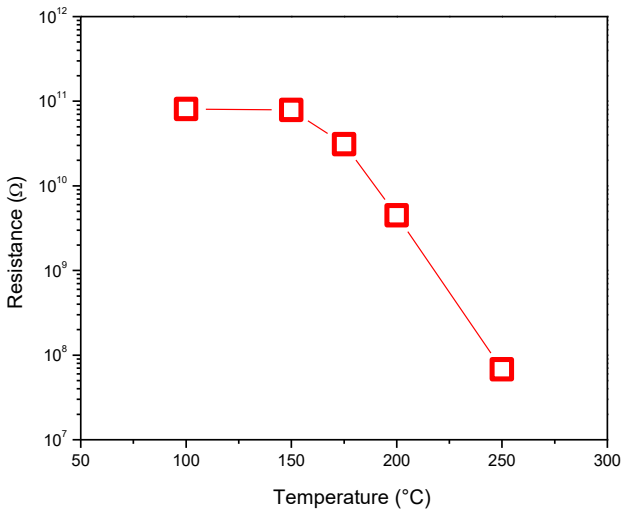

Fig. 18 Electrical resistance of C-CDs sensor as a function of the operating temperature

Then, we tested the sensing characteristics of the fabricated C-CDs sensor at the operating temperature from 100°C to 250°C. For these measurements, NO was selected as the target gas. The choice of this target gas derived by considering that carbon nanostructures are largely used for monitoring nitrogen oxides [129]. For performing the tests, a concentration of 2500 ppm NO was used. Results obtained are shown in Fig. 19. Starting from the temperature of 150 °C, the C-CDs-based sensor exhibits a reversible decrease of the resistance when NO pulse was injected in the sensor chamber. An increase in temperature allows the improvement of the reaction kinetics that occur on the surface of the material and then the response increase. The response reached a plateau at an operating temperature of 200°C.

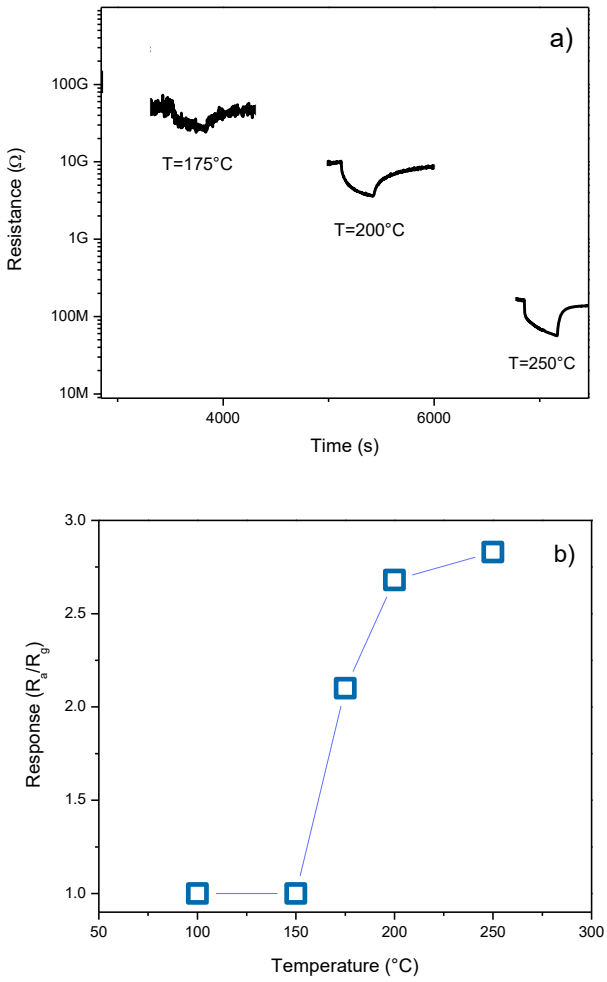

Fig. 19 a) Response at different temperature to 2500 ppm NO of the C-CDs sensor; b) Trend of the sensor response vs. temperature

NO behave as a strong π-acceptor, thus very likely a strong binding is established between NO and the carbon dots surface, decreasing the baseline resistance, as reported for other carbon nanomaterials [130]. We suppose that when the sensor is exposed to dry air, the oxygen molecules are adsorbed on the carbon dots surface to be ionized by electrons trapped by the semiconductor conduction band to produce oxygen ions such as O^{2-}, O^{-} or O_2^{-}, depending on the operating temperature. In the presence of target gas, the absorption and subsequent reaction of NO with adsorbed oxygen species,

causes a local doping effect and inherently leads to the observed resistance decrease.

Sensing tests were also carried out to verify the performance of the C-CDs sensor towards the gas target. Therefore, dynamic, sensitivity, reproducibility, stability over time and selectivity to the target gas in the presence of other interferent gases, were also investigated. The dynamic of the C-CDs sensor was verified by testing the sensor to a concentration of 1250 ppm of NO at the operating temperature of 200 °C, as shown in Fig. 20. The response and recovery time calculated are approximatively 90 s and 200 s, respectively.

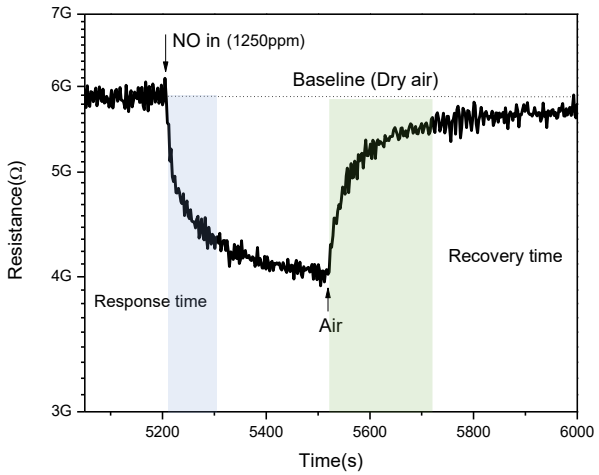

Fig. 20 Transient response of the C-Cdots sensor

In the subsequent tests we have verified the response of the sensor to different concentrations, from 125 to 4000 ppm, of NO (Fig. 5a). Further, in order to verify the presence of a memory effect, the sensor was tested at decreasing NO concentration (Fig. 5b). The response of the sensor is quite reproducible over time for the different concentrations, excluding the presence of any memory effect (Fig. 5c). Further, the signal reproducibility is quite good (Fig. 5d).

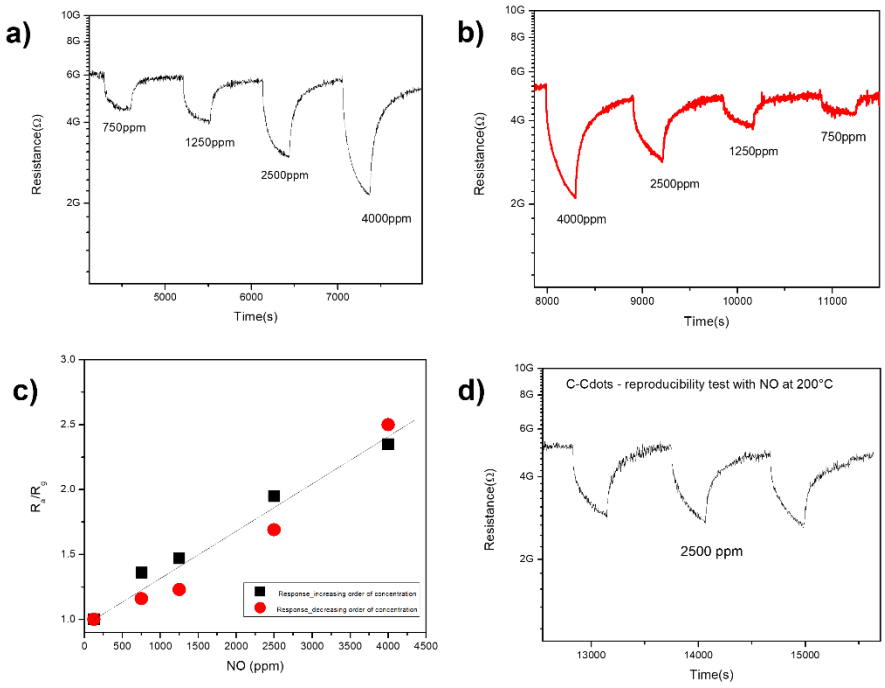

Fig. 21 Response of the C-CDs sensor at a) increasing and b) decreasing concentrations of NO; c) calibration curve; d) reproducibility of the signal over time at 2500 ppm of NO.

The selectivity of the sensor was verified by evaluating the response to different interferent gases, i.e. CO_2. NH_3, NO_2 and CO. The high selectivity of the C-CDs sensor for NO is clearly manifested looking at the bar graph in Fig. 22.

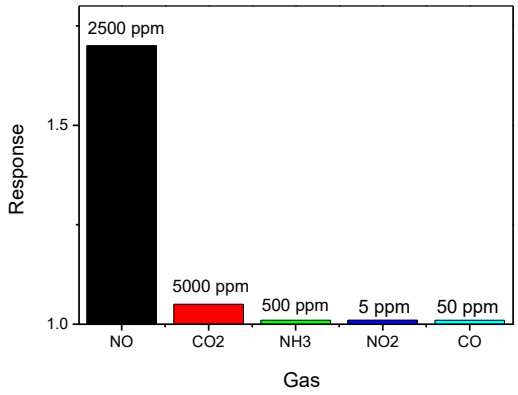

Fig. 22 Response of the C-CDs based sensor to different gases. The high response to NO, compared to the lower response to other gases, highlights the high selectivity of this sensor towards NO.

Table 2 shows the comparison of our CDs sensor material with some others found in the literature. The performances of our material, in terms of operating temperature, sensitivity, selectivity, and response/recovery time, are comparable with the state-of-the-art of others, proving it can be a promising alternative to existing ones.

Sensor material	Temp. (°C)	NO conc. (ppm)	Response time (s)	Recovery time (s)	Response	Ref.
CDs	200	1250	30	200	1.50 #	This work
GaN	35	100	280	2300	115%*	[131]
Bi-SnO_2	75	5	100	120	90	[132]
MoO_3	200	250	600	120	80	[133]
WO_3	300	500	63	88	37#	[134]
ZnO	28	10	135	130	1.7#	[135]

Ra/Rg or Rg/Ra;

* Ra-Rg/Ra or Rg-Ra/Ra where Ra and Rg represent the values of sensor resistance in presence of air and target gas, respectively.

Table 2 Comparison of NO sensing properties of different sensor materials

5.2.2.4 Mechanistic insight

Working on nanomaterials as sensing layers for conductometric gas sensors we discovered that carbon dots prepared from different olive solid waste provenience have different gas sensitivity. Above data demonstrated unambiguously that C-CDs sensor detect selectively NO. In a previous paper [74] we reported a study on the sensing characteristics of a conductometric sensor based on carbon dots prepared from olive oil production waste coming from a different geographic origin (Puglia, Italy). The two sensors exhibit a very different sensing behavior, presenting a large and different sensitivity and selectivity towards the nitrogen oxides, NO and NO_2. To explain this behavior, we focused our attention on the surface characteristics of the two C-dots. Surface characteristics are very important in gas sensing, because the interaction between the gas and the sensing layer surface is mediated by the surface groups. Indeed, the gas sensing mechanism of conductometric gas sensors is well known to be primary related to the adsorption/desorption and surface reaction of gases on surface groups [26, 136-137].

In this work we found that carbon dots prepared using olive solid waste collected from the Mediterranean region Calabria (Italy) (CDs_C) have high performance sensitivity to gaseous nitric oxide (NO). In our previous work carbon dots, prepared with the same unmodified procedure, using olive solid waste collected from the Mediterranean region Puglia (Italy) (CDs_P) presented high performance gas sensitivity to nitrogen dioxide (NO_2). By FT-IR investigation we acquired information on these surface groups. FT-IR analysis showed that C-CDs has a large signature attributed to presence hydroxyl groups, while the ether one prevails on P-CDs. Obviously, the band intensity it is expected to change with the temperature, which is related to the different thermal stability of the surface groups. Then, to investigate the sensor surface in the same conditions under which operate the sensor, we carried out an *in situ* ATR-FTIR investigation on the sensor platform (see Fig. 23).

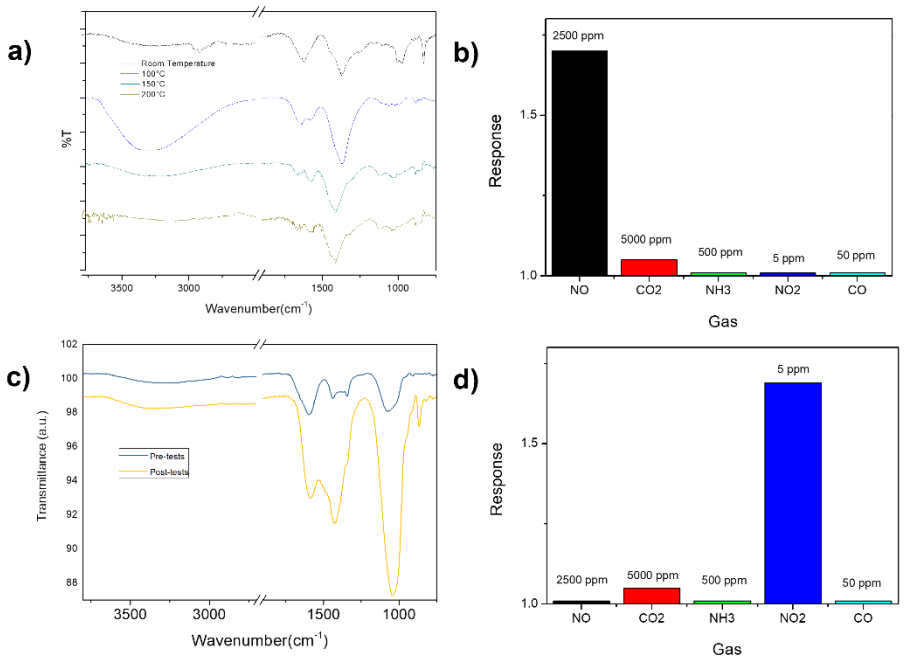

Fig. 23 a) ATR-FTIR spectra of C-CDs recorded at different temperatures; b) selectivity plot for the C-CDs sensor; c) ATR-FTIR spectra of P-CDs sensor before and after the gas sensing tests; d) selectivity plot for the P-CDs sensor.

Comparing the ATR-FTIR results collected at different temperature (from room temperature to 200 °C), it is confirmed that the two CDs samples investigated show different functional groups. Interestingly, it was noted that the differences noted at room temperature, remains also at the highest temperatures (max. 200 °C).

For a quantitative comparison about the sensing characteristics of the two sensors, we used the $S = R_{NO}/R_{NO2}$ ratio, where R_{NO} and R_{NO2} is the response to NO and NO_2, respectively, at the conc. of 2500 ppm for NO and 5 ppm for NO_2. For the C-CDs sensor, the above ratio is very high ($S > 23$), while for sample P-CDs is around 0.1. These values indicate clearly that C-CDs sensor is selective to NO, while P-CDs is selective to NO_2.

By characterization data before reported, it has been confirmed that ether and hydroxyl are the main functional groups presents on C-CDs and P-CDs, respectively.

The Raman pattern of C-CDs and P-CDs is similar (see Fig. 24). The D band is respectively for P-CDs and C-CDs at 1370 and 1346 cm^{-1} and G band in the same way at 1590 and 1598 cm^{-1}; the ratio I_D/I_G is also similar. Even in the P-CDs spectrum it can be recognized the presence of the third band attributed to surface passivation, that in this case is shifted of around 50 cm^{-1} compared to C-CDs.

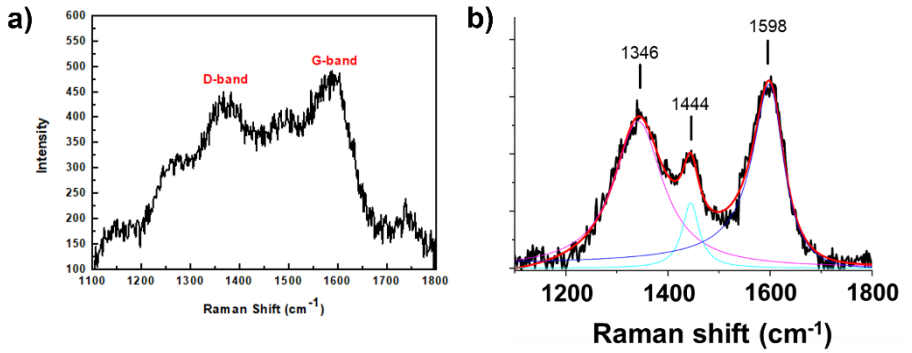

Fig. 24 Raman spectra of a) P-CDs and b) C-CDs

C-CDs and P-CDs presented similar UV/Vis absorption spectra, but thanks to photoluminescence excitation spectra we found that C-CDs bands are shifted to lower energies (Fig. 25). Peaks of C-CDs were around 270-280 nm and 300 nm, for C-CDs around 280-290 and 340 nm. This result was confirmed by the photoluminescence emission spectra, C-CDs emission maxima are shifted to lower energies starting from excitation wavelength (λ_{exc}) 250 nm to 400 nm. Both the samples, in fact, presented excitation wavelength-dependent luminescence (see Fig. 26).

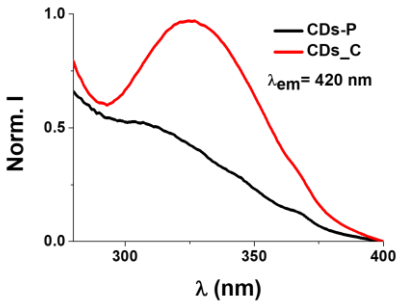

Fig. 25 Photoluminescence excitation spectra of P-CDs (black line) and C-CDs (red line) recorded with λ emission = 420 nm

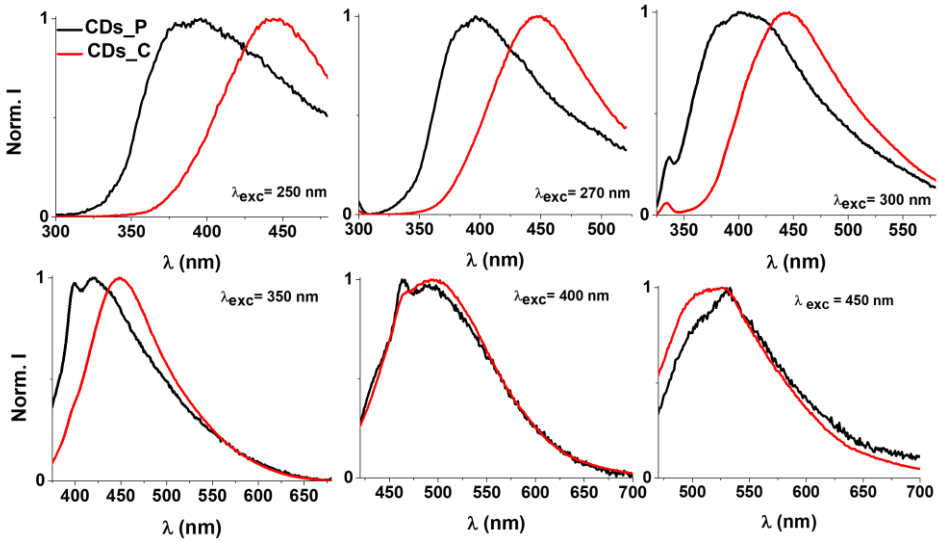

Fig. 26 Photoluminescence emission spectra of P-CDs (black line) and C-CDs (red line). In the legend the excitation wavelength.

The presence of ether and hydroxyl functional groups, that was confirmed in the two C-CDs and P-CDs samples, in other carbon nanomaterials such as CNT, graphene or GO provides the active defect sites for the adsorption of nitrogen oxides has been related to the improvement of the binding and charge-transfer properties [138]. In a computational study, Salih et al [139] investigated the interaction of nitrogen oxides with graphene nanoribbons differently functionalized on the surface. The results of this study indicate that ZGNR-OH is the most selective to NO gas. Instead, ZGNR-O-OH can be considered as promising gas sensors for NO_2. Tang et al. reported a density functional calculations study on the adsorption of nitrogen

oxides on graphene and graphene oxides [138]. These predictions agree with experimental data reported by us in the present study. In addition, Arunragsa reported computational calculations which confirmed the hypothesis that the -OH functional group was a major contributing factor to the NH_3 sensitivity and selectivity on graphene quantum dots (GQDs) modified via edge functionalization [140]. Another excellent example illustrating the structure-activity relationship of surface -OH groups during NO_2 reaction on TiO_2 and the generation of nitrogen-containing species, has been reported by Liu and collaborators [141]. Based on the above consideration, Fig. 27 shows a schematic representation of the gas sensing mechanism on CDs sensors.

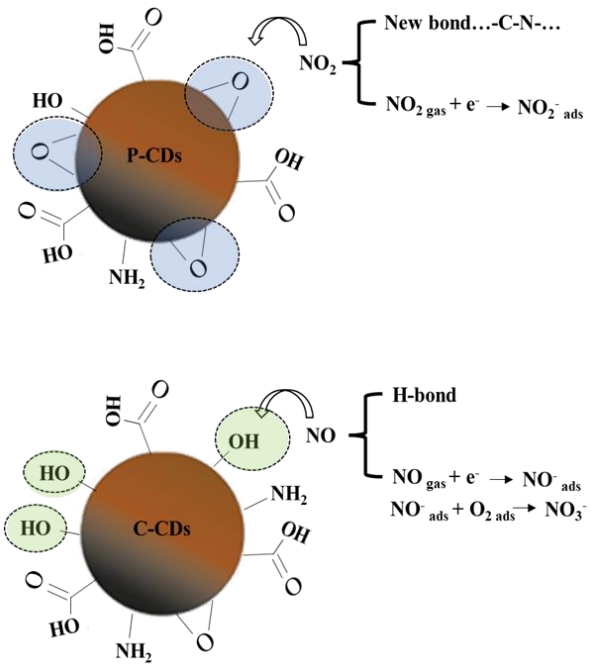

Fig. 27 Schematic representation of the NO and NO_2 sensing mechanism on CDs sensors

Gaseous molecules (NO or NO_2) are chemisorbed on CDs and interact with the surface groups. The interaction of nitrogen oxides with these functional groups results in the formation of different chemisorbed species. These intermediates can react further with the adsorbed oxygen species, explicating the transduction function. Based on the previous computational studies, the charge transfer per NO_2 increases as the number of hydroxyl

group decrease, suggesting that the P-CDs sensor will increase the sensor response to this gas, as observed experimentally. The opposite behavior noted on C-CDs sensor, leading to NO selectivity, agree with this view.

5.2.5 CONCLUSIONS AND FINAL REMARKS

In the present work, we focused our attention on sensing properties of conductometric platforms based on carbon dots as sensing layer for common pollutant gas molecules such as NO and NO_2. Comparing the sensing properties of CDs coming from olive waste of a different geographic origin, we observed a different sensitivity and selectivity towards these gases, which has been explained by the presence of different functional groups on the surface of these CDs. We believe that developing controllable synthetic/production methods, will greatly extend the application of CDs-based sensors for other target gases. However, some key scientific issues need to be addressed first. To establish relationships among the electrical property, morphology, and nanostructure of CDs, will help to better understand the gas sensing mechanism of CDs-based materials.

6. PHYSICOCHEMICAL CHARACTERIZATION AND ANTIBACTERIAL PROPERTIES OF CARBON DOTS FROM TWO MEDITERRANEAN OLIVE SOLID WASTE CULTIVARS

The content of this chapter is reprinted/adapted from MDPI [142] under open access permission: Nocito, G.; Sciuto, E.L.; Franco, D.; Nastasi, F.; Pulvirenti, L.; Petralia, S.; Spinella, C.; Calabrese, G.; Guglielmino, S.; Conoci, S. Physicochemical Characterization and Antibacterial Properties of Carbon Dots from Two Mediterranean Olive Solid Waste Cultivars. *Nanomaterials* **2022**, 12, 885.

6.1.1 ABSTRACT

Carbon nanomaterials have shown great potential in several fields, including biosensing, bioimaging, drug delivery, energy, catalysis, diagnostics, and nanomedicine. Recently, a new class of carbon nanomaterials, carbon dots (CDs), have attracted much attention due to their easy and inexpensive synthesis from a wide range of precursors and fascinating physical, chemical, and biological properties. In this work we have developed CDs derived from olive solid wastes of two Mediterranean regions, Puglia (CDs_P) and Calabria (CDs_C) and evaluated them in terms of their physicochemical properties and antibacterial activity against *Staphylococcus aureus* (*S. aureus*) and *Pseudomonas aeruginosa* (*P. aeruginosa*). Results show the nanosystems have a quasi-spherical shape of 12–18 nm in size for CDs_P and 15–20 nm in size for CDs_C. UV/Vis characterization indicates a broad absorption band with two main peaks at about 270 nm and 300 nm, respectively, attributed to the π-π* and n-π* transitions of the CDs, respectively. Both samples show photoluminescence (PL) spectra excitation-dependent with a maximum at λ_{em} = 420 nm (λ_{exc} = 300 nm) for CDs_P and a red-shifted at λ_{em} = 445 nm (λ_{exc} = 300 nm) for CDs_C. Band gaps values of ≈ 1.48 eV for CDs_P and ≈ 1.53 eV for CDs_C are in agreement with semiconductor behaviour. ζ potential measures show very negative values for CDs_C compared to CDs_P (three times higher, −38 mV vs. −18 mV at pH = 7). The evaluation of the antibacterial properties highlights that both CDs have higher antibacterial activity towards Gram-positive than to Gram-negative bacteria. In addition, CDs_C exhibit bactericidal behaviour at concentrations of 360, 240, and 120 μg/mL, while lesser activity was found for CDs_P (bacterial cell reduction of only 30 % at the highest concentration of 360 μg/mL). This finding was

correlated to the higher surface charge of CDs_C compared to CDs_P. Further investigations are in progress to confirm this hypothesis and to gain insight on the antibacterial mechanism of both cultivars.

6.1.2 INTRODUCTION

Since their serendipitous discovery as byproduct of the arc-discharged synthesis of single-walled carbon nanotubes [48], carbon dots (CDs) represent an emerging luminescent carbon-based nanomaterial. Simple synthetic procedure, wide precursors and fascinating physical and chemical properties have successfully stimulated researchers in the last years. In the spreading field of nanotechnology CDs have been utilized as promising tools for many applications [61] such as: optical sensors for ions and molecular species [143], photocatalysis [144], optoelectronics [145], biomaterials [146, 147], bio-imaging [148], cancer diagnosis and therapy [62], drug delivery in tumours [149, 97] and so on.

CDs are quasi spherical carbonaceous nanoparticles with sizes generally below 10 nm. They are mainly constituted by a crystalline sp2 core surrounded by sp3 imperfections and high oxygen content on their surface [150]. They are chemically stable, low toxic, biocompatible, good conductors/semiconductors and possess bright luminescence, high photostability and broadband UV absorption [151]. Their surface is mainly rich of hydroxyls (-OH) and carboxyl/carboxylates (-COOH/-COO^-). The latter contribute from 5 to 50 % (weight) of their oxygen content and impart excellent water colloidal dispersibility and subsequent easy functionalization or passivation with a great variety of chemical specie [152]. All these properties can be modulated by synthetic conditions that produce photo-physical behaviour, size and reactivity. CDs present emission bands shifts dependent from excitation wavelength modulated by precursor change, surface passivation or heteroatom doping [153]. The reason of this phenomenon is attributed to both (a) the nanometric size that in-duces quantum confinement effect and (b) the chemical composition referred to different surface functionalization groups and π-domain extension inducing many possible states slightly different in energy between the frontier's orbitals [58].

The synthetic strategies for CDs production could be broadly divided into top-down and bottom-up approaches. The first uses physical and chemical methods starting from a wide range of natural or chemical precursors that assembles to produce CDs such as pyrolysis, hydrothermal treatments, microwave irradiation, ultrasound. The second uses physical methods to nano fragmentate larger inorganic carbon pre-cursors (graphene, graphite, carbon nanotubes) such as laser ablation, arc discharge and electrochemistry. [62, 154, 155]. Recently great attention has been also paid to new synthetic methods in terms of green chemistry that address the production of CDs from biomass wastes, cheap or abundant, heterogeneous and biodegradable materials obtained from the manufacturing processes of food, forestry, energy, and many other industrial processes [117]. CDs derived from biomass are greenest and, in some case better than their chemical counterpart [156, 157] and have been produced using top-down approaches from a lot of precursors such as papaya [156], spent tea [100], lychee seeds [158], peanut shells [92], wool [159], strawberries [160], olive pit [161] and many others. Further, olive wastes management is one of the main ecological issues in the Mediterranean basin, due to the concentration more than 98% of global olive production and a market in hugely expansion over the last two decades

More specifically in the biomedical field, CDs gained a growing interest due to their excellent photoluminescence properties, diverse surface functions, good water solubility, low cytotoxicity, cellular uptake, biocompatibility, microbial adhesion, and theranostic properties [162, 163]. Among these properties, antibacterial activity is one of the most appealing features in the design of new biomaterials in which nanotechnology is giving fundamental contribution [12, 164, 165, 166]. In this context, the specific physicochemical properties of CDs (e.g. size and surface charge) make them promising tools for addressing antibacterial processes as drug resistance, biofilms, and intracellular active/latent bacteria [167, 168, 169, 170, 171].

In this context, we have developed CDs derived from olive solid wastes of two Mediterranean regions, Puglia (CDs_P) and Calabria (CDs_C) and evaluated them in terms of physicochemical properties and antibacterial

activity against *Staphylococcus aureus (S. aureus) and Pseudomonas aeruginosa (P. aeruginosa)*.

6.1.3 METHODS

6.1.3.1 Carbon dots preparation

CDs were prepared from olive solid wastes collected from two regions of the Southern Italy, Puglia (CDs_P) and Calabria (CDs_C), according to the method reported in [73] (vide section 4.3.2). CDs_P aqueous dispersion concentration was around 0.7 mg/mL, whereas CDs_C concentration was 1.4 mg/mL.

6.1.3.2 Bacterial assays

S. aureus (ATCC 29213) was purchased from American Type Culture Collection (LGC Promochem, Milan, Italy) and cultured in Tryptone Soya Broth (TSB, Sigma-Aldrich, Milan, Italy). *P. aeruginosa* (ATCC 27853) was purchased from American Type Culture Collection (LGC Promochem, Milan, Italy) and cultured in Luria-Bertani Broth (LB, Sigma-Aldrich, Milan, Italy).

Antibacterial tests were performed in Mueller Hinton Broth (MHB, Sigma-Aldrich, Milan, Italy), a culture medium susceptible to antibiotics.

To evaluate the Minimal Inhibitory Concentration (MIC) of both CDs colloidal dispersions the microplate inhibition assay was used. Specifically, semi-exponential cultures of bacterial strain at the final concentration of about 105 bacteria per mL were inoculated in MHB in presence of increasing concentration of CDs (60-360 μg/mL) in 96-well and incubated at 37 °C under shaking overnight. After incubation, the concentrations inhibiting at least 90 % and 99.9 % of bacteria, MIC_{90} and MIC_{99}, were determined compared to the untreated control.

To evaluate the bacterial cell viability, MTS assay (CellTiter 96® AQueous One Solution Cell Proliferation Assay, Promega, Milan, Italy) was performed. More in detail, bacterial cultures in presence of different concentrations of CDs were grown overnight at 37 °C in 96-well. After, MTS reagent was added to bacteria culture media, incubated for 2 hours at 37 °C in static condition, the plate shaked briefly and absorbance measured at 490 nm

by using a microtiter plate reader (Multiskan GO, Thermo Scientific, USA). Reduction of bacterial viability was evaluated in terms of percentage of MTS reduction (% MTSred), compared to the untreated control (CTR) by the following equation:

$$MTS_{red}\ (\%) = \frac{A}{B}\ X\ 100$$

where A e B are the OD_{490} from the MTS reduced formazan of condition with CDs and CTR. The samples were analysed in triplicate for each experimental condition.

6.1.3.3 Isoelectric point determination

The isoelectric points of CDs colloidal dispersions were estimated by ζ (Zeta) potential pH titration using the dynamic light scattering (DLS) technique with a Malvern Zetasizer Nano ZS90 instrument. pH was moved to 8, 10 and 2 by adding re-spectively NaOH 0.1 M (Sodium hydroxide – Sigma-Aldrich) and HCl 0.1 M solutions (Hydrochloric acid – Sigma-Aldrich). The isoelectric point was found plotting pH vs Zeta potential and intercepting the pH value when the ζ potential is zero.

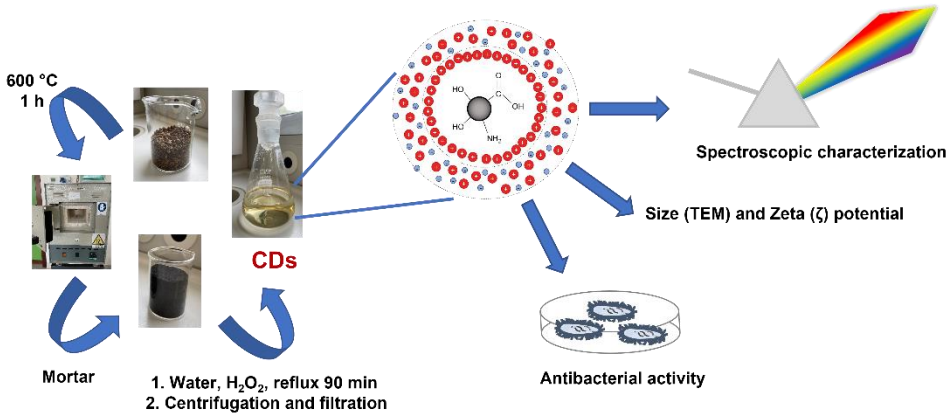

Fig. 28 Schematic representation of CD preparation, physico-chemical characterization, and bacterial testing.

6.1.4 RESULTS AND DISCUSSION

6.1.4.1 Physicochemical characterization of CDs

The optical properties of both synthesized CDs were characterized by UV-Vis absorbance and photoluminescence emission spectra displayed in Fig. 29. The absorption spectrum of CDs_P (Fig. 29a) exhibits broadband ultra-violet absorption, with a trend compatible with the light scattering operated by a small nanoparticles' colloidal dispersion. UV-Vis absorbance spectrum of CDs_P shows two detectable peaks as shoulders located around 270 nm and 300 nm attributed respectively to the π-π* transition of CDs and n-π* transitions of the functional groups present on CDs [123, 172]. These two absorption shoulders, probably suggest the existence of conjugated structures as well as the presence of functional groups containing oxygen in CDs [150, 151, 152]. Fig. 29b shows the PL spectra of CDs_P with the excitation wavelength in the interval between 300 nm and 450 nm. Emission maximum is around λ_{em} = 420 nm for λ_{exc} = 300 nm.

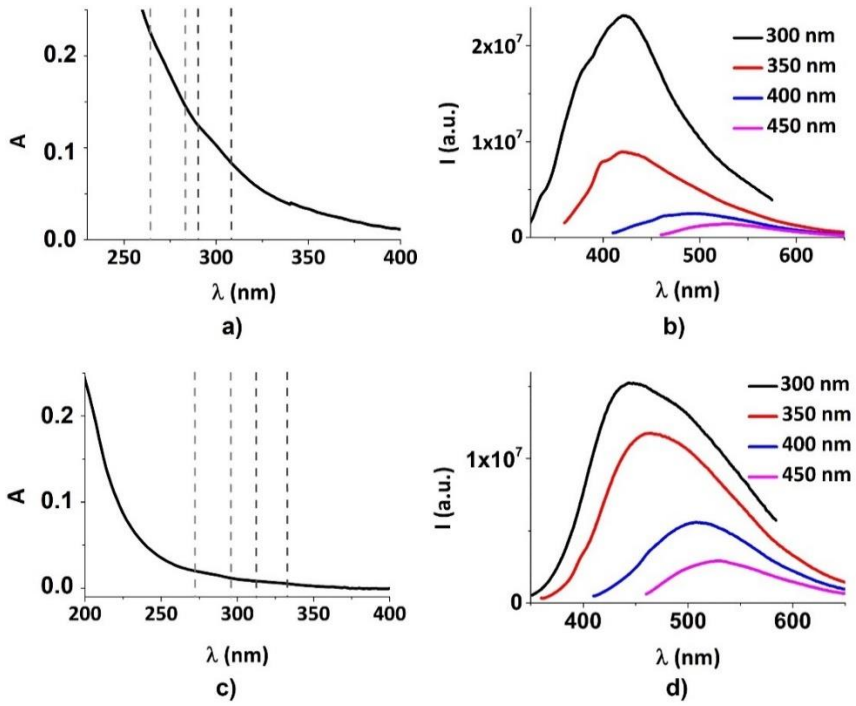

Fig. 29 Optical characterization of CDs: a) UV/Vis absorption spectrum of CDs_P; b) Photoluminescence spectra of CDs_P; c) UV/Vis absorption spectrum of CDs_C; d) Photoluminescence spectra of CDs_C

Although absorption spectrum of CDs_C showed a trend similar to that exhibited from CDs_P, some differences are present (Figure 2a-c). Firstly, the peaks detected as shoulders are shifted to lower energies founding them around 280 nm and 320 nm (Figure 2c). Secondly, although CDs_C show PL, the emission spectra -registered in the same excitation wavelength interval (300 - 450 nm) are red shifted with respect to CDs-P, as for the absorption bands [173]. Emission maximum is around λ_{em} = 445 nm for λ_{exc} = 300 nm (Figure 2d).

To further evaluate the difference between CDs derived from two different Mediterranean olive solid waste cultivars we calculated the respective band gaps from UV-Vis absorption spectra reported in Fig. 29a and Fig. 29c, using Tauc plot [174] with the formula [175]

$$(\alpha h\nu)^{\frac{1}{\gamma}} = B(h\nu - E_g)$$

Were α is the absorption coefficient ($\alpha = 2.303\, Acm^{-1}$), h is the Planck constant, ν is the frequency of the incident photon. The γ factor depends on the nature of the electronic transition, and in our case for permitted transition, it could be 0.5 for the indirect one and 2 for the direct one. B is a constant assumed to be 1, and E_g is the energy gap. E_g was calculated using $\gamma = \frac{1}{2}$ for direct electronic transition.

Plots are reported in Fig. 30. Band gaps values Fig. 30a of ≈ 1.48 eV for CDs_P and ≈ 1.53 eV for CDs_C, respectively, were found. These values are in agreement with a semiconductor behaviour, according to similar value found in [176, 96].

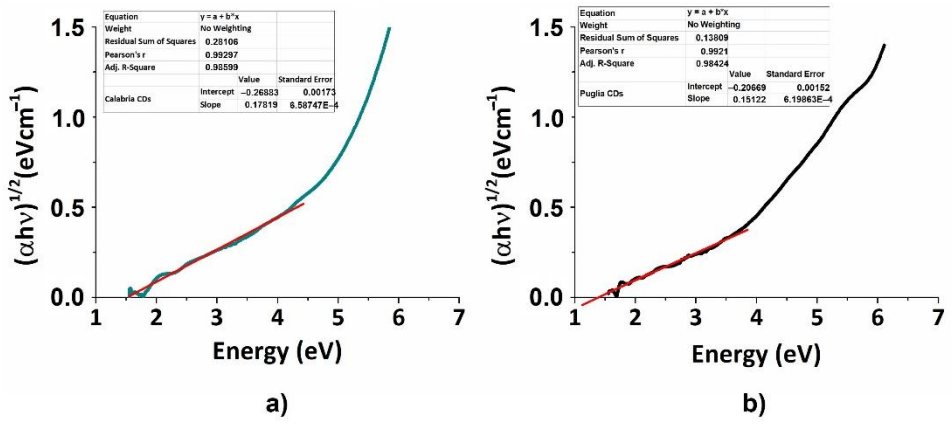

Fig. 30 a) Tauc plots for the optical energy band gap calculation: a) CDs_P; b) CDs_C

Concerning the chemical characterization, CDs_P, both FTIR and XPS analysis were reported in our previous works [73-74] and showed for FT-IR the following peaks: 3424, 3236, 2923/2850, 1656, 1412, 1320 and 1116 and 1096 cm−1, attributed to –OH, N-H, C-H, C=O (carbonyl), COO- (carboxylate), C-OH (hydroxyl) and C-O-C (epoxide) groups, respectively. XPS analysis showed peaks of C1s at 285 eV for C-C and 289 eV for O=C-O respectively. About CD_C, FT-IR analysis (see Fig. 31a) reveals the presence of –OH, C=O (carbonyl), COO- (carboxylate), C-OH (hydroxyl) and C-O-C (epoxide) groups, while XPS spectrum (see Fig. 31b) exhibits same C1s peaks of CDs_P at 285 eV for C-C and 289 eV for O=C-O respectively. The similarity of surface groups for both cultivars accounts also for similar values of band gap (see above).

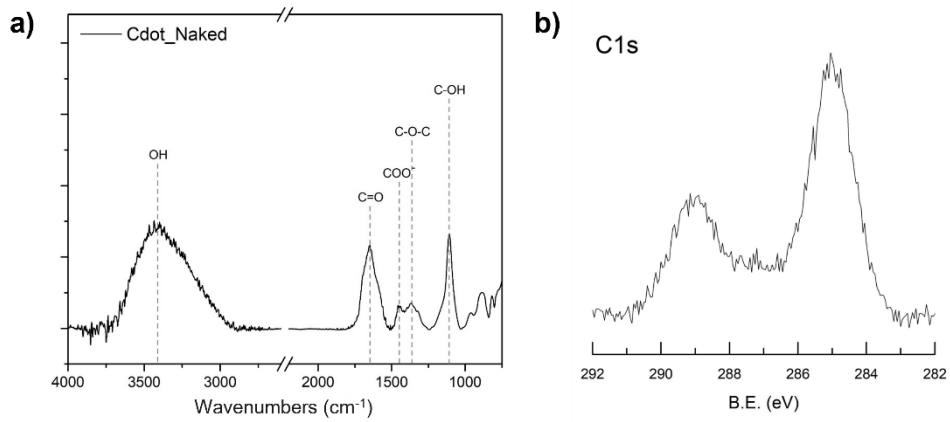

Fig. 31 a) FT-IR spectrum of CDs_C; b) XPS spectrum of CDs_C

Fig. 32 reports the plot of ζ potential values as a function of pH for both CDs_P and CDs_C. It can be noticed that both cultivars show negative surface charges, but CDs_P exhibits higher values of ζ potential respect to CDs_P. According to that, the values of the isoelectric point (pH value at 0 charge) correspond to pH ≈ 3 for CDs_P and pH ≈ 2.4 for CDs_C. More interesting, in the phisological conditions (pH ≈ 7), CDs_C are featured by a charge (ζ potential) about three times more negative than CDs_P (-32 mV *versus* -11 mV). This certainly can be a notable point for the antibacterial activity of the nanomaterials (*vide infra*).

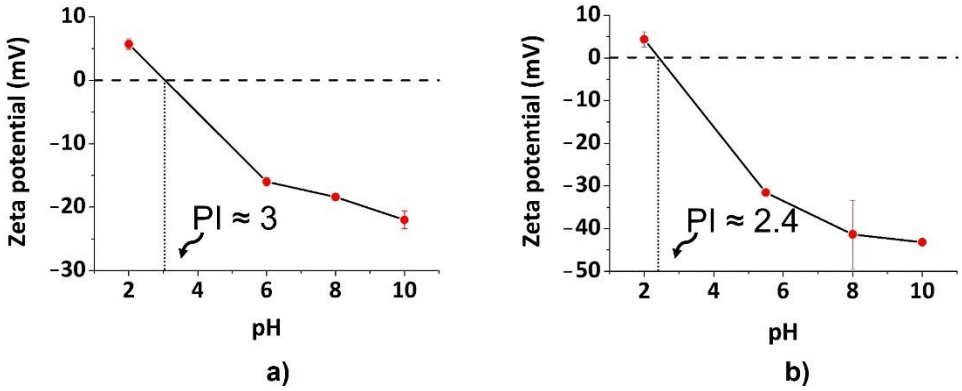

Fig. 32 Graphical representation of ζ potential as a function of pH titration: a) CDs_P; b) CDs-C

Morphological characteristics were also investigated by Transmission Electron Microscopy (TEM). Fig. 33 reports TEM images of the two different

cultivars. CDs_P displays dispersed quasi-spherical nanoparticles with particle size ranging between 12-18 nm, while CDs_C exhibits similar behaviour with mean size of 15-20 nm.

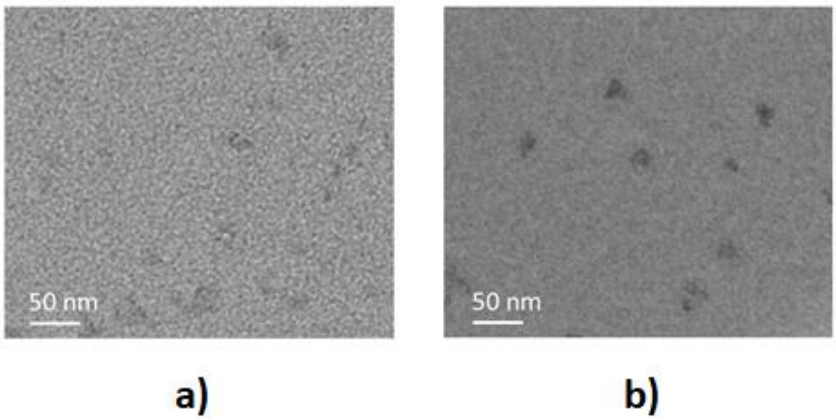

Fig. 33 Representative Transmission Electron Microscopy (TEM) images of: a) CDs_P; b) CDs_C

6.1.4.2 Antibacterial properties of Carbon dots

The bactericidal activity of both CDs dispersions was evaluated against both *S. aureus* (Gram-positive) and *P. aeruginosa* (Gram-negative), two of the most common pathogens involved in a wide range of infections. Firstly, values of MIC for both CDs types were determined by microplate inhibition assay up to the maximum concentration of 360 μg/mL. In table 1 are reported the MIC_{90} and MIC_{99} values (μg/mL) for both CDs.

Bacterial strain	CDs	MIC_{90}	MIC_{99}
S. Aureus	CDs_P	-	-
	CDs_C	120 μg/mL	360 μg/mL
P. Aeruginosa	CDs_P	-	-
	CDs_C	-	-
Dash (-) = No antibacterial activity up to the concentration of 360 μg/mL			

Table 3 MIC values (μg/mL) of S. Aureus and P. Aeruginosa strains in Mueller-Hinton broth (MH)

Our results showed that CDs_C exhibit *S. aureus* viability reduction of about 99.9 % (MIC_{99}) at 360 μg/mL and 90 % bacterial inhibition (MIC_{90}) at about 120 μg/mL, while no bacterial inhibition was observed against *P. aeruginosa*. On the contrary, no bacterial inhibition was observed for CDs_P at all used concentrations (ranging 60-360 μg/mL) against both bacterial strains.

To further evaluate the antibacterial proprerties of both CDs types we also performed MTS cell viability assay (Fig. 34 and Fig. 35).

MTS data showed that CDs_C dispersion reduces almost completely *S. aureus* viability at the higher concentrations (360, 240 and 120 μg/mL), while at the lowest concentration (60 μg/mL) it is reduced of about 50% compared to the control (untreated). On the contrary, MTS data of CDs_P indicated a bacterial cell reduction of only 30% at the highest concentration (360 μg/mL) showing very poor antibacterial activity. More in details, bacterial viability of CDs_C was found of 47.5 ± 2.37 % at 60 μg/mL, 4.75 ± 0.24 % at 120 μg/mL, 0.47 ± 0.005 % at 240 μg/mL, 0.05 ± 0.0005 % at 360 μg/mL; for CDs_P was 94.9 ± 4.74 % at 60 μg/mL, 92.6 ± 4.63 % at 120 μg/mL, 85.7 ± 4.28 % at 240 μg/mL, 68.4 ± 3.42% at 360 μg/mL. These data were in agreement with MIC results.

On the other hand, MTS data obtained against *P. aeruginosa* showed that only CDs_C at the higher concentration (360 μg/mL) exhibit a bacterial reduction of about 20%. In more detail, the bacterial viability of CDs_C was found to be 98.4 ± 1.17 % at 60 μg/mL, 95.75 ± 1.49 % at 120 μg/mL, 93.43 ± 1.12 % at 240 μg/mL, 83.81 ± 3.5 % at 360 μg/mL.

In addition to the above considerations, we also observe a different antibacterial activity between CDs_P and CDs_C, more evident in *S. aureus* than in *P. aeruginosa* probably due to the different cell wall composition. Several action mechanisms have been suggested to explain the antibacterial activity of CDs closely related to their physicochemical properties, including their dimensionalities, lateral size, shape, number of layers, surface charge, the presence and nature of surface functional groups, and doping [167, 168, 169, 170].

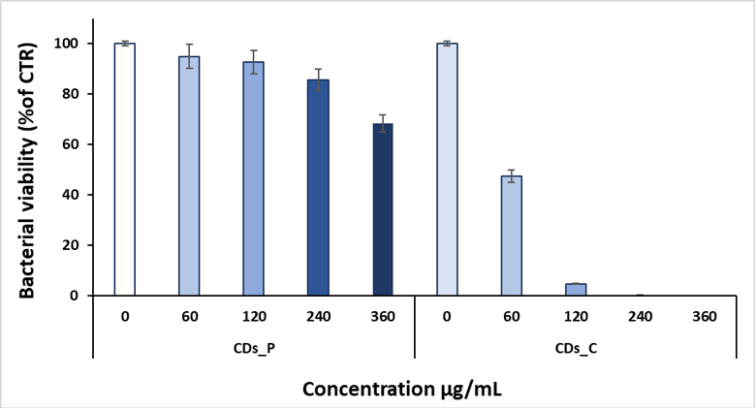

Fig. 34 MTS assay of CDs_C and CDs_P against S. Aureus strain. Data are presented as the mean ± SD from three independent experiments.

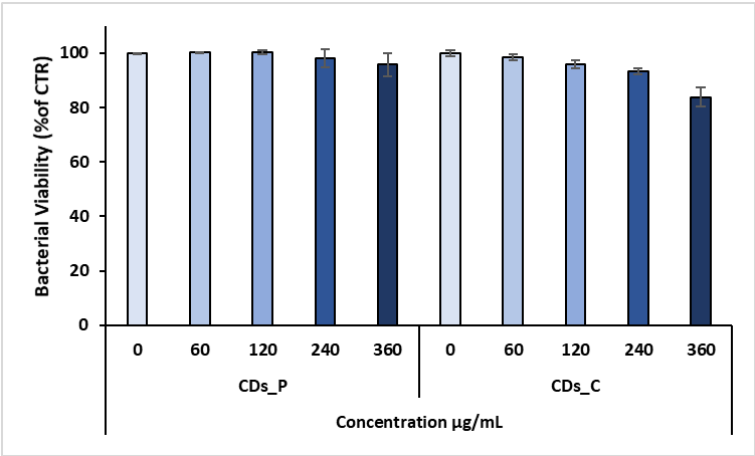

Fig. 35 MTS assay of CDs_C and CDs_P against P. Aeruginosa strain. Data are presented as the mean ± SD from three independent experiments.

A hypothesis to explain the dissimilar antibacterial behaviour of two CDs types could be due to the charge distribution and functional groups of CDs. Recently, some studies suggested that factors due to particle size and surface functionalization and charges can affect antibacterial effects [167, 177]. With specific focus on surface charge, Bing et al studied antibacterial capability of CDs with three different surface charges (uncharged, positive and negative) founding only positive- (spermine derived positive CDs, SC-dots) and negative-charged CDs (candle-soot derived negative CDs, CC-dots) exhibited signs of cell death on *E. coli* (gram negative), such as DNA fragmentation, extracellular exposure of phosphatidylserine, condensation of

the chromosome and loss of structural integrity, but the same effects not occurred with uncharged glucose Carbon Dots (GC-dots). Based on these considerations, our results could be compared with negatively charged candle-soot C-dots (CC-dots). Although similar results were obtained against *P. aeruginosa,* we found that *S. aureus* viability was almost totally and slightly reduced when treated with CDs_C and CDs_P, respectively. Since our systems CDs_C and CDs_P exibith similar size of nanoparticles and no surface functionalization was carried out, both factors are not relevant for the found data indicating that CDs_C show higher antibacterial activity respect to the CDs_P. These results suggest, rather, a different antibacterial mechanism for the two cultivars, probably attributable to the different surface charges and ζ potential. Although both CDs from the two cultivars exhibited negative surface charges, however CDs_C have much more negative charge respect to CDs_P (about -38 mV for CDs_C and -18 mV for CDs_P at pH = 7). Actually, during the bacterial growth, the medium pH decreases over time (0-8 hrs) reaching more acid values (from 7.2 to about 5.5) (See Fig. 36). By considering this aspect, we can observe that surface charge of both cultivars reaches about -32 mV (CDs_C) and -11 mV (CDs_P), respectively, at pH = 5.5 highlighting that CDs_C are featured by a negative surface charges 3 times higher than CDs_P. This is probably the reason of the increased antibacterial activity of CDs_C respect to CDs_P. Further studies are in progress to validate our hypotesis and gain insight on the understanding the active antibacterial mechanism.

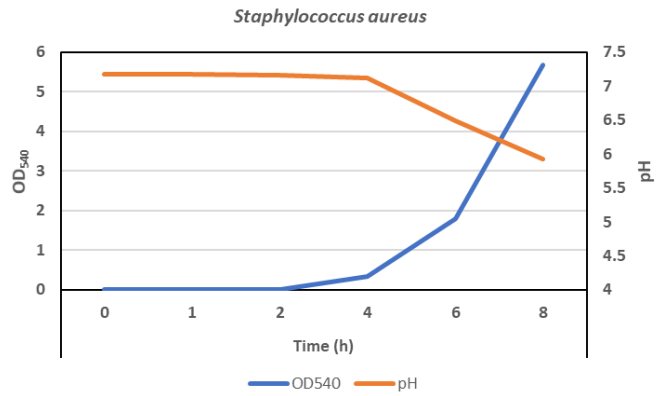

Fig. 36 pH changes during S. aureus bacterial growth (OD_{540}) (0-8 h)

6.1.5 CONCLUSIONS

In this paper, we report the development of CDs derived from olive solid wastes of two Mediterranean regions, Puglia (CDs_P) and Calabria (CDs_C) and their evaluation in terms of physicochemical properties and antibacterial activity against *S. aureus*. The UV-Vis characterization shows typical broad absorption band with two main peaks at about 270 nm and 300 nm, attributed to the π-π* and n-π* transitions of CDs, respectively. The PL spectra are excitation-dependent and CDs_P shows emission maximum at λ_{em} = 420 nm (λ_{exc} = 300 nm) while CDs_C has the emission maximum red-shifted at λ_{em} = 445 nm (λ_{exc} = 300 nm). Band gaps values of ≈ 1.48 eV for CDs_P and ≈ 1.53 eV for CDs_C, respectively, were found, in agreement with semiconductor behaviour. ζ potential values are negative for both cultivars. However, CDs_C are featured by more negative charge reaching three times more negative than CDs_P (-38 mV *versus* -18 mV at pH = 7). The TEM morphological inspection shows quasi-spherical nanoparticles 12-18 nm in size for CDs_P and 15-20 nm in size for CDs_C. The evaluation of antibacterial properties highlights that both CDs have higher antibacterial activity towards Gram-positive respect to Gram-negative. In addition, the evaluation of antibacterial properties towards *S. aureus* of both CDs types highlights that CDs_C exibiths antibacterial properties at concentrations of 360, 240 and 120 μg/mL, while CDs_P shows a bacterial cell reduction of 30 % at the highest concentration of 360 μg/mL. This finding was correlated to the highest surface charge of CDs_C than CDs_P that is still very negative also during the bacterial growth reaching acid pH of 5.5. Further investigations are in progress to confirm this hypothesis and gain insight on the antibacterial mechanism of both cultivars.

7. A NEW CARBON DOTS-EU(III) COMPLEX AS A RED EMITTING PH SENSOR

The content of this chapter is reprinted and adapted with permission from Springer Nature [178]: Nocito, G., Puntoriero, F., Conoci, S., Galletta, M., Nastasi, F. A New Carbon Dots-Eu(III) Complex as Red Emitting pH-Sensor. In: Di Francia, G., Di Natale, C. (eds) Sensors and Microsystems. AISEM 2021. Lecture Notes in Electrical Engineering, vol 918., Springer International Publishing (2023).

7.1 ABSTRACT

The intriguing photophysical properties and biocompatibility of carbon dots (CDs) have let them to become one of the most popular nanosystem for a multitude of applications. Generally, the interaction of external substrates such as metallic cations, small molecules or macromolecules with CDs surface leads to the change of CDs photoluminescence. In the better case it is possible to completely quench their emission and for this reason there is a large volume of knowledge on on/off luminescence sensors, based on carbon dots, for analytical purposes. Here we used CDs, prepared from natural precursor, as complexing and sensitizing agents for Eu(III) cations. In the CDs-Eu^{3+} adduct, CDs luminescence is quenched and shifted to higher energies. Great part of the energy absorbed by CDs is funnelled by energy transfer processes in the Eu(III) coordinated ions sensitizing their characteristic red luminescence (antenna effect). Lanthanide ions were complexed from -COO^- moieties on the surface of CDs that are pH sensitive. The CDs-Eu(III) complex was tested as a red emitting acidic pH sensor, reading the luminescence quenching at 700 nm operated by carboxylate protonation and consequent Eu^{3+} displacement. Red emission and particular sensitivity make this complex addressable also for bio-applications.

7.2 INTRODUCTION

Carbon dots (CDs) are quasi-spherical carbonaceous nanoparticles less than 20 nm to 60 nm with a sp^2-sp^3 core and an irregular surface rich of polar groups that confers aqueous dispersibility and intriguing optical properties [45]. CDs display fascinating excitation wavelength dependent luminescence mainly attributed to different surface states tunable by synthetic conditions [179]. Their preparation is simple and low cost. Due to these properties, there is spreading interest on carbon dots-based optical sensors, in fact the

interaction of analytes with CDs surface, favoured by polar groups, generally leads to the change of their fluorescence spectra. Current research on this field is aimed to control specificity and sensitivity for a wide range of substrates such as cells, biological molecules, small molecules, inorganic ions. [180] Moreover, systems capable of exhibiting the ability to switch an on/off luminescence signal in the presence of suitable substrates are widely studied for their interest in various application fields such as sensors and molecular logic gates. [181, 182, 183, 184, 185, 186, 187] In addition, CDs possess a well-known coordination ability for metal ions [118].

Generally, the absorption of carbon dots is limited to the UV region of the electromagnetic spectrum and their emissions lie with blue or green (400-550 nm) [188] narrowing their optical application to this spectral region. There are many examples in literature reporting on attempts to extend their emission to lower energies and they are mainly focused on surface modification such heteroatom doping [189], polymer passivation [190], or peculiar synthetic conditions [191].

In general, systems exhibiting red luminescence are of great interest for potential bio-applications because these wavelengths are not interested by interfering optical phenomena such as tissue autofluorescence or non-specific scattering. However, species capable of emitting in these regions, apart from exceptional cases, are characterised by low quantum yields, poor photostability, challenging synthetic steps and rather wide emission bands. [62]

Coordination of lanthanides ion, and their sensitization, could be a promising strategy to obtain emission in the red region characterized by long living excited states, large Stoke shifts and sharp emission bands that are located in the case of Eu(III) in the 600-750 nm range, as demonstrated in literature [192]. In fact, recently CDs have been covalently functionalized with lanthanides complexes, preserving the original morphology of CDs, demonstrating their sensitization power for the Vis-NIR emission. [193]

Lanthanides ions, due to 4fn electronic configuration, have very low molar absorption coefficients in the UV/Vis region and so sensitization from

proper coordinate chromophore is needed to sensitize their luminescence (antenna effect). Suitable chromophoric ligands may strongly coordinate lanthanide ions, replacing molecules from solvation sphere (that amplify, in particular for O-H containing solvents, non-radiative decay), and absorb light of higher energies than lanthanides excited state. The light absorbed by the ligand can be efficiently transferred, via energy transfer processes, to the luminescent lanthanide ions. [194]

Carbon dots surface [73] presents many polar groups such -COOH (Carboxyl), -OH (hydroxyl), $-NH_2$ (amine) so their emission could be tuned by the interaction with an external species. In particular, carboxylic groups can strongly coordinate lanthanides ions shielding metal ions from solvent. [195]

7.3 CARBON DOTS-EUROPIUM COORDINATION AND ITS pH TITRATION

In a typical experiment CDs aqueous dispersion was spectrophotometrically diluted ($A_{max} \approx 0.1$) in a final volume of 3 mL (2.4 μg/mL). Carbon dots were prepared according to the method from Sawalha et al [73] using olive solid waste from Calabria (Italy) (vide section 4.3.2). The final concentration of CDs aqueous colloidal dispersion was 0.36 mg/mL.

Titration was performed using a 0.22 mg/mL Europium chloride hexahydrate stock solution adding each time a little volume (10-20 μL) to CDs dispersion. Fluorescence emission spectra were recorded setting λ_{exc} = 300 nm with a 350 nm filter, the excitation spectra to λ_{em} = 700 nm with a 610 nm filter and to λ_{em} = 400 nm without any filter. Spectrofluorimetric pH titrations were executed adding a little volume (2-10 μL) of HCl and NaOH (0.1-1 M) solutions to a stirring dispersion of CDs-Eu(III) complex. Each time absorption and emission spectra (λ_{exc} = 300 nm, 350 nm filter) were recorded. pH was monitored with Metrohm 826 mobile pHmeter.

7.4 RESULTS AND DISCUSSION

7.4.1 CDs-Eu^{3+} coordination

We prepared sustainable CDs colloidal water dispersion from olive solid waste, as a coordination agent for Eu(III), according to the Sawalha et al

method [73]. The absorption spectrum in water and the emission (registered at 300 nm) are shown in Fig. 37a. As it can be seen, naked CDs emission band, exciting at 300 nm, extends from about 350 to 600 nm with the emission maximum at 466 nm and a less intense band tail up to 700 nm.

Upon addition of additive small volumes of $EuCl_3 \cdot 6H_2O$ aqueous solution (0.22 mg/mL) to a 3 mL of CDs (0.36 mg/mL), the luminescence of CDs is quenched and shifted to higher energies with the cooperative appearance of the characteristic Eu(III) luminescence bands located from green to red region at: 580 nm, 615 nm and 700 nm. This behavior can be rationalized by considering the formation of an adduct between CDs and Eu(III) ions. In this assembly part of the energy absorbed by the carbon dots is transferred to the Eu(III) coordinated ions, thus sensitizing their emission. This assumption is confirmed by the fact that sensitization of the Eu(III) luminescence relies on quasi-quantitative energy transfer from excited states centered on CDs that reach maximum efficiency at the ratio 1:1 (CDs/Eu, w/w) as highlighted in the Job Plot resumed in Fig. 37c.

Unambiguous confirmation of the energy transfer process is provided by the excitation spectrum shown in the Fig. 37d, recorded at 700 nm, which shows that the absorption of the carbon dots is responsible for the lanthanide emission.

The residual emission of carbon dots can be assigned to the deactivation from the excited state localized on the coordinated CDs the lies at higher energy because the coordination of metal cations influences the electronic state of their surfaces.

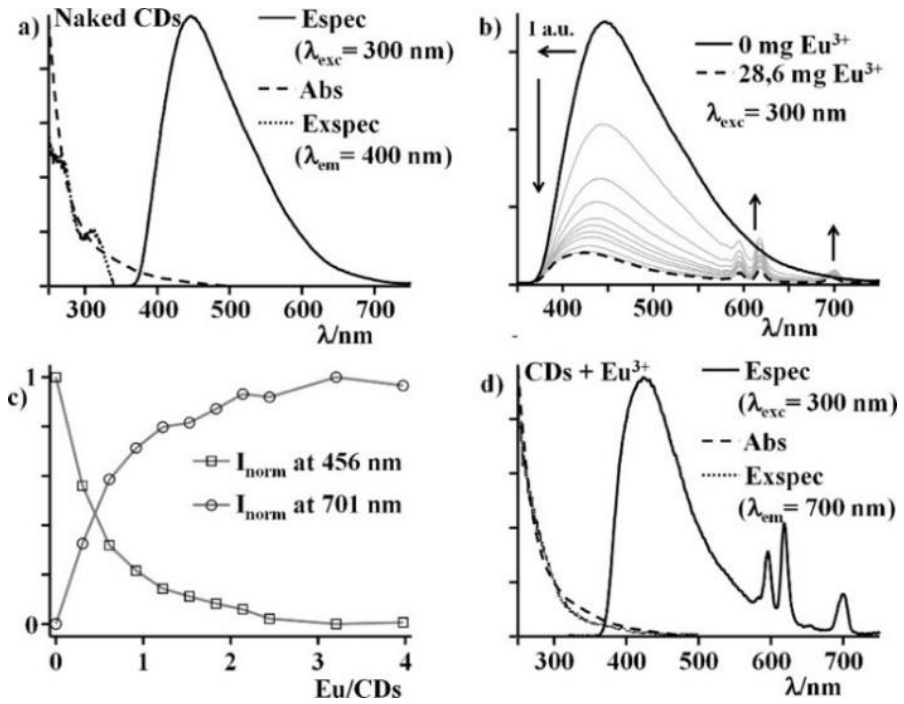

Fig. 37 a) Normalized emission (λ exc =300 nm), absorption and excitation (λ em =450 nm) spectra of naked CDs; b) Spectrofluorimetric titration of CDs-Eu(III) coordination; c) Job Plot on spectrofluorimetric titration: normalized emission intensities (701 nm for Eu-based emission and 456 nm for CDs based emission) versus Eu3+/CDs w/w ratios; d) Normalized emission (λ exc =300 nm), absorption and excitation (λ em =700 nm) spectra of CDs-Eu(III) complex.

7.4.2 CDs-Eu3+ complex as an acidic pH sensor

The main responsible are surface carboxylic groups, in aqueous neutral or alkaline media these are normally deprotonated in form of carboxylate (-COO^-) that are available for the coordination. Our idea was to test whether at different pH levels it is possible to modulate lanthanide coordination by protonating (at low pH) the sites responsible for coordination, and to test the reversibility of the process. The obtained aqueous solution of CDs-Eu3+ system have pH = 5.09. This was the starting point of a spectrofluorometric titration settled to test the responsivity of our system to pH changes (solid black line in Fig. 38). pH has been gradually turned towards low values observing the progressive quenching of Eu(III) based luminescence and a concomitant modification and shift to lower energies of the CDs fluorescence. Interestingly at pH = 2.15 only residual Eu(III) based emission is observed while CDs luminescence is dominant ($I_{700\ nm}/I_{420\ nm}$ = 0.25). This behavior is

most probably associated to the protonation of the carboxyl moieties engaged in the coordination so releasing in solution uncoordinated Eu^{3+} ions. No changes in UV/Vis absorption spectra during the process where found (data not shown). The trend of the titration curve (Fig. 38 insert) proceeds smoothly with an equivalence point around pH = 3.5 compatible with the commonest pKa of the carboxylic acids. The system is fully reversible as shown by the emission spectrum, see Fig. 2, obtained by returning the pH to 5.12. Titration towards basicity would lead to the competition between CDs and hydroxyls complexing ability for Eu(III) losing in specificity.

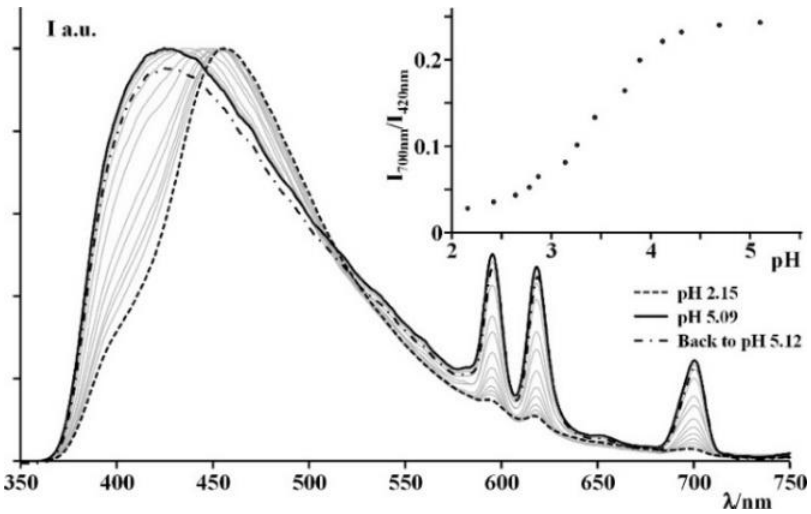

Fig. 38 Spectrofluorometric pH titration of the CDs-Eu^{3+} complex. Emissions are normalized to the maximum. In the insert the titration curve, in X-axis the pH and in the Y-axis the normalized emission intensity ratio 700 nm (Eu^{3+} complex band) over 420 nm (CDs band).

7.5 CONCLUSIONS

A new CDs-Eu^{3+} complex has been prepared starting from solid olive waste. The adduct emits in a wide range of wavelengths with the luminescence fingerprints of Eu(III) complexes.

The excited states of carbon dots, via energy transfer, serve as sensitizing agent for Eu^{3+} luminescence that is characterized by defined and shaped bands in the red region of the spectrum, which enhance the sensibility of the optical measurements.

Carbon dots coordinate the lanthanide thanks to carboxylic moieties that are pH sensitive, their protonation causes the displacement of the metal from the coordination site. The consequent emission quenching at 700 nm, range where common fluorescent dyes and indicators does not have characteristic signal, is proportional to pH. In particular the double reading at 456 nm and 700 nm could lead to a very sensitive optical application.

Further studies are ongoing to use this novel material for sensing application in the solid state.

8. PHOTOCHEMICAL ROUTE TO CDs-AU NANOHYBRID FOR PHOTOTHERMAL APPLICATIONS

The content of this chapter is a final and unpublished draft.

8.1 ABSTRACT

Gold nanoparticles (AuNPs) are the milestone of nanoscience and carbon dots, despite of their relative recent discovery, are one of the most studied members of carbon nanoparticles family. Efficient light-to-heat conversion, photostability and chemical versatility gave the successful application of AuNPs in many fields from biomedicine to photothermal applications. Intriguing photophysical properties, easy preparation and biocompatibility pushed researchers on extensive study of carbon dots. In this work we report a photochemical route to carbon dots-gold (CDs-Au) nanohybrid using CDs as both reducing and capping agent. According to green chemistry principles, precursors CDs (CDs) were prepared from olive solid waste and functionalized with ethylenediamine via amide bond formation (CDs-E). Actually, amine and amide groups are known for Au(III) complexing ability and amine to bind AuNPs surface. CDs and CDs-E were characterized via UV/Vis, steady-state and time-resolved luminescence, FT-IR, Raman, quantitative X-Ray Photoelectron spectroscopies and Transmission Electron Microscopy (TEM) imaging. CDs-E excited states, generated by blue light irradiation, served both as electron donors, for Au(III) reduction to Au(0), and acceptors for the counterpart. After the easy, green and one-step photochemical synthesis the resulting CDs-Au nanohybrid, exceptionally stable in aqueous dispersion, was characterized via UV/Vis, FT-IR, Raman, Energy-dispersive X-Ray spectroscopies and with TEM and SEM imaging. Its photothermal ability was also evaluated showing comparable light-to-heat energy conversion efficiency to the “gold standard” citrate-capped AuNPs by Turkevich.

8.2 INTRODUCTION

Gold nanoparticles (AuNPs) have intrigued most of the researchers due to their nanoscaled properties. They are subjected to quantum size effect that justifies Red-Ox activity and they feature surface plasmon resonance (SPR)

that explains the optical properties. [196] For example, AuNPs are photostable, possess high extinction coefficient and optical tunability. In fact, their Localized Surface Plasmon Resonance (LSPR) band in the UV/Vis absorption spectrum red-shifts as a function of particle diameter [197], shape [198], aggregation [199]. In addition they are known for efficient light-to-heat conversion, the reason why they are considered one of the most promising nanomaterials for photothermal applications [11]. However, in most of the synthetic procedures of AuNPs external reducing agents ($NaBH_4$, idrazine), sacrificial agents, capping layers (CTAB, PVP) are needed and, in some cases, they could be toxic for the environment or the human health [200]. Nowadays, according to green chemistry principles [201] the urgency of minimizing and valorising waste and to implement sustainable processes have pushed researchers to find alternative ways to metallic nanoparticles synthesis. [202]

In this concept, we decided to use carbon dots as both reducing and capping agent for AuNPs synthesis. We found that the two components, carbon and gold, are in intimate connection, so that we start calling it a carbon-gold (CDs-Au) nanohybrid.

Carbon dots (CDs) are the latest family of carbon-based nanomaterials [62], serendipitously discovered in 2004 during an electrophoretic purification of carbon nanotubes fragments [48]. Recently great attention has been paid to this nanomaterial, so much that according to Prato et al [203] classification the family now includes: Carbon NanoDots (CNDs), Carbon Quantum Dots (CQDs) and Graphene Quantum Dots (GQDs). It is still difficult to differentiate between the members, especially for CNDs and CQDs, so it is commonly accepted to refer to these as quasi-spherical carbonaceous nanoparticles with amorphous or crystalline core surrounded by polar groups as -OH (hydroxyls), $-COO^-$/-COOH (carboxylates/carboxylic acid) and amino groups responsible for their excellent water dispersibility [203]. The large volume of knowledge on CDs arises from their essential biocompatibility and interesting optical properties. They are photostable and present excitation-wavelength dependent photoluminescence [204]. There is a plethora of application of carbon dots: chemical and biological sensing [196], biomedicine [205], photosensitizers for solar-driven catalysis [206], optoelectronics [145],

cancer diagnosis and therapy [62], drug delivery in tumours [149] and so on. For the exceptional metal ions complexing ability [207], Red-Ox activity [208, 209, 210] and photophysical properties we decided to use carbon dots for CDs-Au nanohybrid formation. Moreover, other research groups confirmed CDs capping ability to gold nanoparticles, in fact AuNPs [209, 211], gold carbon dot core shell [212], gold-carbon nanoalloys [213], carbon-gold nanocomposites [214] were produced with carbon dots via thermal reduction. Another group produced a carbon-gold nanohybrid by the interaction of pre-formed carbon dots and gold nanoparticles [215].

Photochemical strategies to metallic nanoparticles, and in particular gold nanoparticles, synthesis are very appealing and well-suited for this purpose [216]. Photons, in fact, are considered green reactants, they are not expensive, and they can be easily modulated in terms of wavelength, intensity, duration and location [71]. Furthermore, there are many examples in literature in which free radicals, generated by UV light irradiation of organic molecules, can act as reducing agents for precise gold nanoparticles synthesis [217, 218, 219]. In this scenario, we developed a photochemical route to CDs-Au nanohybrid in which the excited states of ethylenediamine functionalized carbon dots (CDs-E), generated by blue light irradiation, served as both electron donors for the reduction of Au(III) to Au(0) and acceptors for the counterpart. Although the majority of the precedent works reports that hydroxyls on the surface of carbon dots are efficient anchoring groups for the rising gold nanoparticle, we found that amine and amide groups introduced with ethylenediamine functionalization are pivotal for the efficiency of the reduction and the final nanohybrid stability.

The resulting CDs-Au nanohybrid was tested for its photothermal ability. Efficient light-to-heat conversion of gold nanoparticles is related to the surface plasmon resonance (SPR) and illuminating wavelength. Light absorbed by AuNPs induces collective and coherent electron oscillation of the metal to the illuminating wavelength that is efficiently converted to heat for the surrounding fluid. [11, 220] With the powerful spatiotemporal and intensity control operated by light irradiation it is possible to generate punctual and

localized temperature increase in a determined site for example of the human body (photothermal therapy) or for technological applications.

8.3 SYNTHETIC PROCEDURES

8.3.1 Carbon dots-Ethylenediamine

8.3.1.1 EDC coupling

The procedure for carbon dots functionalization with ethylenediamine was optimized from different literature works [221, 222, 223]. Surface functional groups of CDs can be easily used for covalent functionalization with a plethora of molecules in well-established reactions as the EDC coupling [203]. In this case, carboxylic/carboxylate groups were exploited. These are very frequent on the carbon nanoparticle surface due to the oxidizing conditions of their preparation, in fact together with hydroxyl groups they impart polarity to the nanosystem and so on aqueous dispersibility [224].

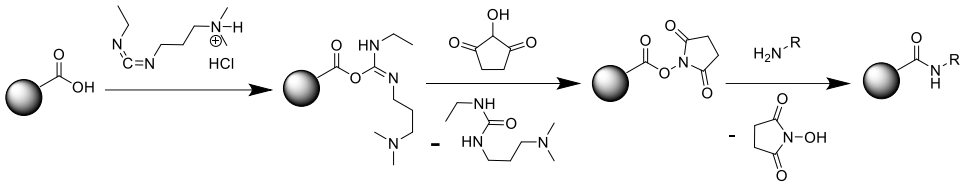

Fig. 39 EDC/NHS coupling mechanism

Carbodiimide coupling is a common synthetic strategy to form amide or ester bonds between a carboxylic moiety and a primary aminic or alcoholic moieties respectively. On the carboxylic acid the carbonyl carbon is not prone to acyl nucleophilic substitution because of the hydroxyl that is not a good leaving group. Carbodiimide coupling solves the problem installing a good and reasonably stable leaving group that allows the nucleophile attack. On the first step the carbodiimide derivative, in this case it was used *N*-(3-Dimethylaminopropyl)-*N′*-ethylcarbodiimide hydrochloride) - EDC hydrochloride – because of its water solubility, forms a O-acylisourea unstable intermediate with the carboxylic acid. On the second step N-hydroxysuccinimide reacts with the intermediate to form a more stable NHS-ester intermediate that can finally react with the nucleophile. The reaction

mechanism is summarized in Fig. 39 showing a primary amine as the nucleophile.

8.3.1.2 Naked carbon dots synthesis (CDs)

Naked carbon dots (CDs) were prepared from Sawalha et al [73] method (vide section 4.32.2) using olive solid waste from Calabria (Italy). Nanoparticle concentration, in colloidal dispersion, was 0.2 mg/mL.

8.2.1.3 Carbon dots-Ethylenediamine functionalization

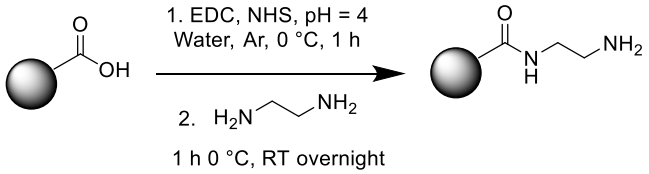

Fig. 40 CDs-Ethylenediamine reaction scheme

50 mL of 0.2 mg/mL naked carbon dots (CDs) aqueous colloidal dispersion were diluted with 50 mL of ultrapure water (HPLC Plus, Sigma-Aldrich) and degassed at 0 °C for 1 h with Ar flow in a two-neck round bottom flask, before pH was moved to 4 for HCl 0.1 M addition. After that 159.6 mg of *N*-(3-Dimethylaminopropyl)-*N′*-ethylcarbodiimide hydrochloride) - EDC hydrochloride - and subsequently 143.8 mg of N-hydroxysuccinimide were added. The reaction was magnetically stirred for 1 h in the ice bath. After that ethylenediamine (5.56 mL) was poured, and the reaction was continued for 1 h under ice and overnight in RT maintaining the inert atmosphere (Fig. 40). The reaction mixture was purified by dialysis (MWCO = 14 KDa) against deionized water for two days, changing the water every 2-8 h obtaining a light-yellow CDs-Ethylenediamine (CDs-E) dispersion of about 0.1 mg/mL. The concentration of CDs-E was quantified weighting the residue obtained from solvent evaporation.

SAMPLE	MW	mmol	eq.	mg	d	mL
CDs	12	0.833	1	10	-	50
EDC	191.7	0.833	1	159.6	-	-
NHS	115.09	1.25	1.5	143.8	-	-
Ethylenediamine	60.10	83.3	100	5	0.899	5.56

Table 4 CDs-Ethylenediamine reaction stoichiometry

8.3.2 Carbon dots-Au nanohybrid

A 4.77 · 10^{-3} M mother solution of tetrachloroauric(III) acid was prepared dissolving 16.2 mg of Gold(III) chloride hydrate ($HAuCl_4 \cdot xH_2O$) in 10 mL of ultrapure water (HPLC Plus, Sigma-Aldrich).

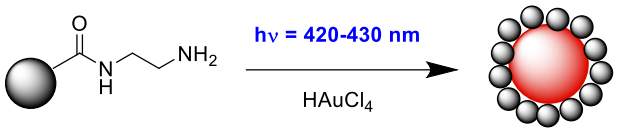

Fig. 41 CDs-Au nanohybrid reaction scheme

On a vigorously stirred aqueous dispersion of CDs-Ethylenediamine (100 mL, 0.1 mg/mL) $HAuCl_4$ mother solution was added until 2.5 · 10^{-4} mol/L. The mixture was irradiated with a blue (420-430 nm) LED for 310 min and left under overnight stirring in darkness. (Fig. 41) The crude was purified by filtration (fritted glass filter, porosity 4) to remove larger aggregates and subsequent centrifugation (1 h, 9000 rpm/8500 RCF). The supernatant was discarded, according to UV/Vis and fluorescence spectroscopies only unreacted CDs were contained, the precipitate was collected, washed two times with ultrapure water and sonicated for 2 h. CDs-Au nanohybrid was stored at RT in ultrapure water dispersion, appreciating at least 2 months stability, and was characterized without further purification. All the reaction steps and the reaction kinetic were monitored via UV/Vis absorption spectroscopy.

8.3.3 Gold nanoparticles

Spherical gold nanoparticles, used as a reference for photothermal measurements, were prepared using the Turkevich method [225]. Briefly, a solution of Gold(III) chloride hydrate ($HAuCl_4 \cdot xH_2O$ - 35 mL, 2.5 · 10^{-4} mol/L) was warmed up to 75 °C in a round-bottom flask under vigorously stirring. Then a solution of sodium citrate dihydrate (35 mL, 2.5 · 10^{-3} mol/L, 75 °C) was poured and the reaction was left for 30 min at 75 °C. Before 20 min the mixture changed from colourless to red/purple. After cooling to RT gold nanoparticles were directly characterized via UV/Vis absorption spectroscopy.

8.4 RESULTS AND DISCUSSION

8.4.1 Synthesis and characterization of naked CDs and CDs-Ethylenediamine

Naked carbon dots (CDs) were prepared recycling the biomass waste of olive oil production. Olive solid waste was collected from an oil mill in Calabria (Italy), pyrolyzed and grounded until a fine carbonaceous powder was obtained. CDs were produced with a modified hydrothermal method [73] using hydrogen peroxide as oxidizing agent, a recognized green chemical as its byproduct water [201, 226]. H_2O_2 addition provides CDs surface functionalization with polar groups such as hydroxyls (-OH) and carboxyls/carboxylates (-COOH/-COO^-) [73] that confer excellent aqueous dispersibility and hence stability to the colloidal dispersion. Exploiting carboxylic moieties and EDC coupling reaction it was possible to further functionalize the surface of CDs with amine and amide groups via ethylenediamine anchoring.

CDs-Ethylenediamine (CDs-E) and naked CDs (CDs) were characterized via UV/Vis absorption, steady-state and time-resolved luminescence, FT-IR, Raman and quantitative X-Ray Photoelectron spectroscopies. Nanoparticles surface charge was estimated by Zeta potential measurement via Dynamic Light Scattering (DLS) technique, nanoparticles size was obtained thanks to Transmission Electron Microscopy (TEM).

7.4.1.1. Optical characterization

In Fig. 42 and in Fig. 43 complete luminescence spectroscopy characterizations are reported, respectively for CDs and CDs-E.

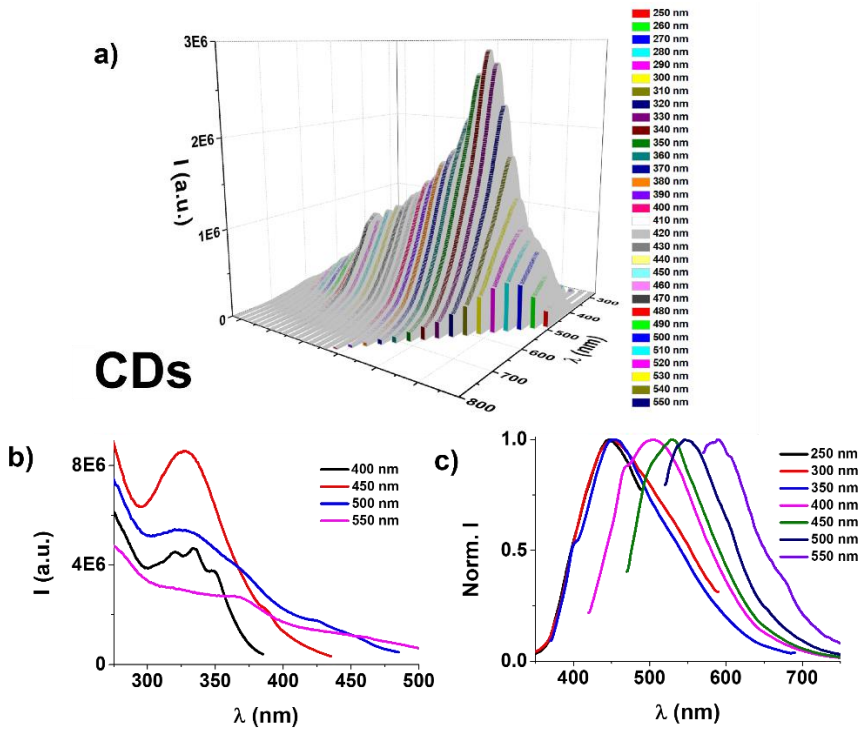

*Fig. 42 Optical characterization of **naked CDs (CDs)**: a) 3D profile of CDs luminescence emission spectra, excitation wavelength in legend; b) A selection of luminescence excitation spectra; c) A selection of normalized luminescence emission spectra ($\lambda_{excitation}$ = 250-550 nm)*

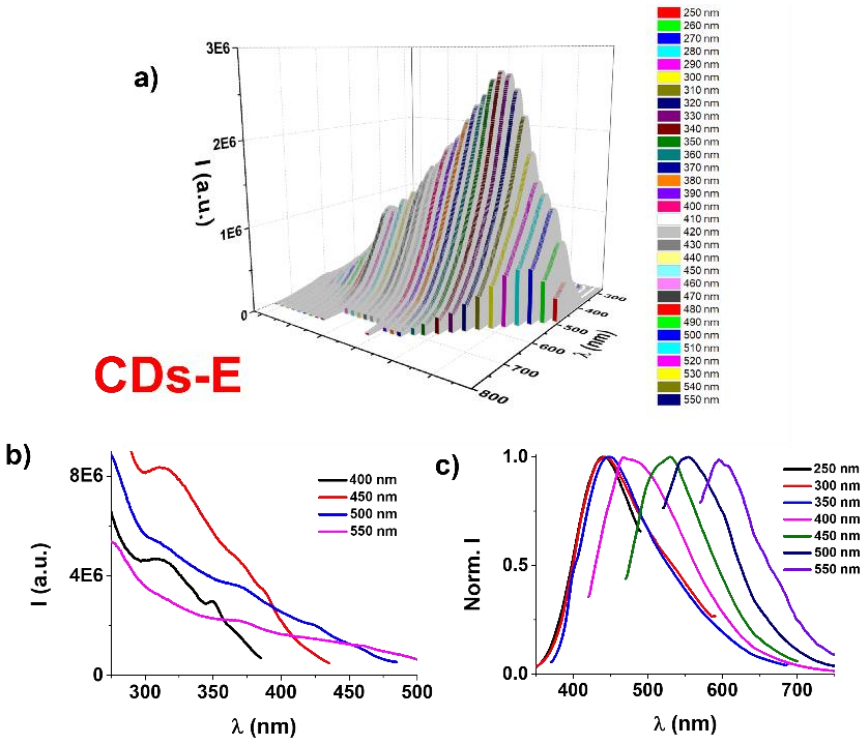

*Fig. 43 Optical characterization of **CDs-Ethylenediamine (CDs-E)**: a) 3D profile of CDs-E luminescence emission spectra, excitation wavelength in legend; b) A selection of luminescence excitation spectra; c) A selection of normalized luminescence emission spectra ($\lambda_{excitation}$ = 250-550 nm)*

CDs-E and CDs show broadband UV absorption compatible with the light scattering of small nanoparticles in colloidal dispersion (Fig. 44a). Despite of this trend it is still possible to differentiate two weak absorption bands around 300 and 340 nm attributable respectively to π-π^* and n-π^* transitions from core sp^2 domains and surface oxygen-containing groups believably responsible for the emission phenomena [227, 228, 123] as highlighted by luminescence excitation spectra in Fig. 44c and Fig. 44d.

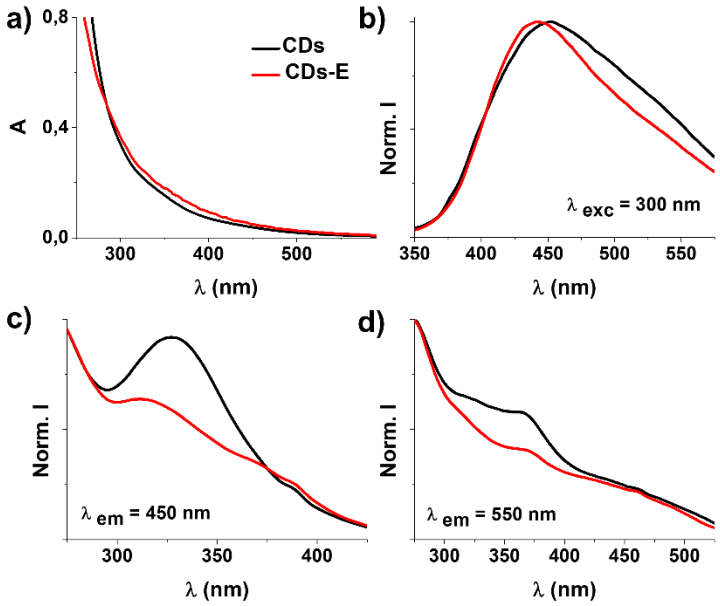

Fig. 44 Characterization of CDs naked (CDs, black line) and CDs-Ethylenediamine (CDs-E, red line): a) UV/Vis absorption spectra; b) Luminescence emission spectra (λ excitation = 300 nm); c) Luminescence excitation spectra (λ emission = 450 nm); d) Luminescence excitation spectra (λ emission = 550 nm)

Both the samples present excitation wavelength-dependent luminescence, in the excitation wavelength range of 250-550 nm (vide for complete luminescence spectroscopy characterizations Fig. 42 and Fig. 43). In Fig. 44b CDs and CDs-E emission spectra for $\lambda_{excitation}$ = 300 nm are reported. CDs-E emission maximum is slightly shifted to higher energies compared to CDs, altogether higher energies contributions in the emission spectra are similar while they differ for those at lower energies. CDs maximum emission intensity is at 451 nm for 340 nm excitation, for CDs-E is at 446 nm for 340 nm excitation.

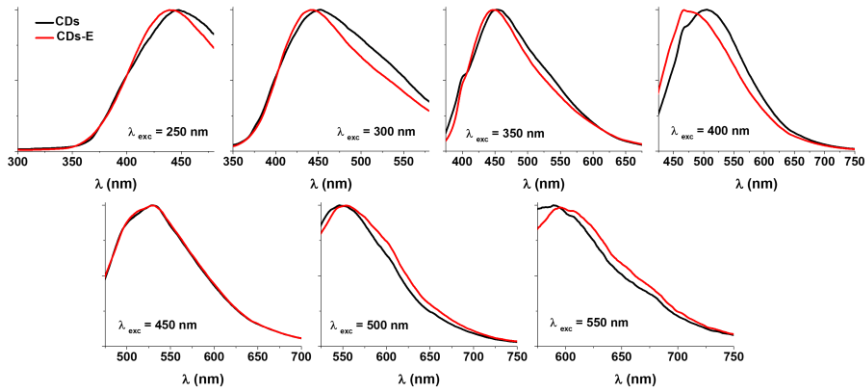

Fig. 45 Comparison of normalized luminescence emission spectra of CDs (black line) and CDs-E (red line). Excitation wavelengths: 250, 300, 350, 400, 450, 500 and 550 nm

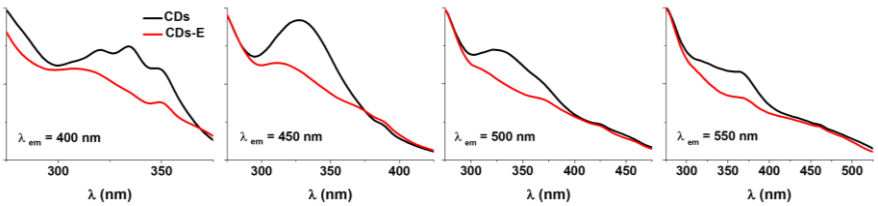

Fig. 46 Comparison of luminescence excitation spectra of CDs (black line) and CDs-E (red line). Emission wavelengths: 400, 450, 500, 550 nm.

According to steady-state emission spectra, time-resolved luminescence decays (Table 5 and Fig. 47, recording emission wavelength from 430 to 530 nm - Δ = 20 nm, 59 ps 408 nm pulsed laser) show two emissive populations with comparable lifetimes around 2 and 8 ns.

λ emission (nm)	**CDs-E**		**CDs**	
430	1.70 ns (62 %)	6.60 ns (38 %)	1.60 ns (69 %)	7.20 ns (31 %)
450	2.00 ns (57 %)	7.80 ns (43 %)	1.87 ns (57 %)	7.51 ns (43 %)
470	2.00 ns (52 %)	8.20 ns (48 %)	1.97 ns (52 %)	8.37 ns (48 %)
490	2.20 ns (48 %)	8.50 ns (52 %)	2.27 ns (45 %)	8.67 ns (55 %)
510	2.50 ns (49 %)	8.20 ns (51 %)	2.40 ns (42 %)	8.87 ns (58 %)
530	2.45 ns (45 %)	8.80 ns (54 %)	2.57 ns (43 %)	8.93 ns (57 %)

Table 5 Luminescence lifetimes of CDs-E and CDs. Samples were excited at 408 nm, luminescence lifetimes were recorded at different emission wavelengths.

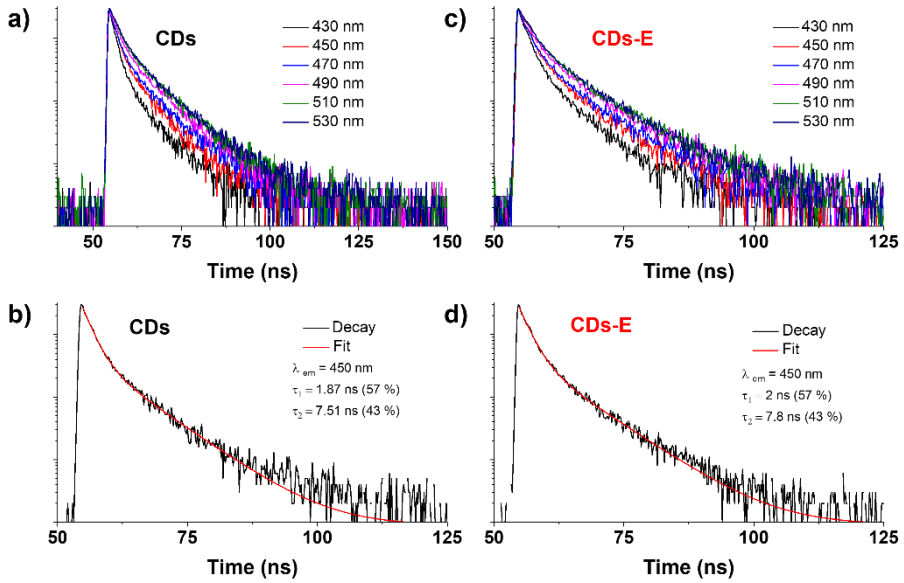

Fig. 47 Photoluminescence lifetimes of CDs and CDs_E: a) Decays recorded on different luminescence wavelengths of CDs; b) Lifetimes of CDs on λ_{em} = 450 nm; c) Decays recorded on different luminescence wavelengths of CDs-E; d) Lifetimes of CDs-E on λ_{em} = 450 nm

8.4.1.2 Chemical composition

Concerning chemical composition and the extent of naked carbon dots functionalization with ethylenediamine, analyses from quantitative X-Ray Photoelectron, FT-IR and Raman spectroscopies are reported. Quantitative XPS in Fig. 48 revealed that CDs and CDs-E are constituted by C, N, O, Na, Ca and P. N/C ratio is 1/16 for CDs-N and 1/10 for CDs-E.

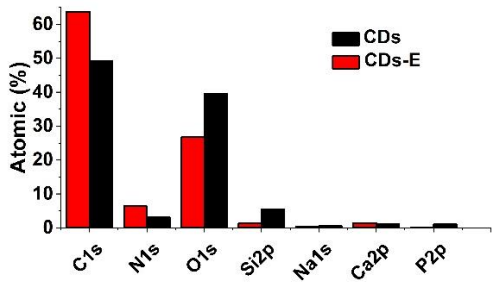

Fig. 48 Quantitative XPS analysis of CDs (black bar) and CDs-E (red bar).

FT-IR spectra in Fig. 49a clarify the extent of ethylenediamine functionalization of naked CDs. In CDs-E spectrum are more pronounced the

peaks at 3405, 3000-2900 and 1130 cm^{-1} attributable respectively to -NH stretching [229], -CH stretching [230] and amine -C-N stretching [230] introduced by ethylenediamine, instead in naked CDs spectrum are more intense peaks at 3200 and 1400 cm^{-1} of -OH stretching [230] and deformation [231]. Ethylenediamine covalent anchoring is recognizable by the presence of a doublet band from 1650 to 1550 cm^{-1} attributable to the overlapping of the secondary amide carbonyl stretching, -NH in plane vibrations and -C-N vibrations absorptions [230, 232]. Instead, carbonyl absorption band in naked CDs is broad and covered by the intense -OH bending vibrations from adsorbed water at 1645 cm^{-1} [233]. A shoulder around 1760 cm^{-1} is attributable to C=O stretching vibration of carboxylic/carboxylates moieties [230]. Another evidence of the ethylenediamine functionalization is given by the Raman CDs-E spectrum in Fig. 49b (red line). The intense band on the 2700-3200 cm^{-1} region, that is completely absent in CDs spectrum (black line), is addressable to -CH vibrations reasonably introduced by ethylenediamine, other characteristic vibrations are overlapping with the vibrational modes of carbon dots from 1150 to 1650 cm^{-1}.

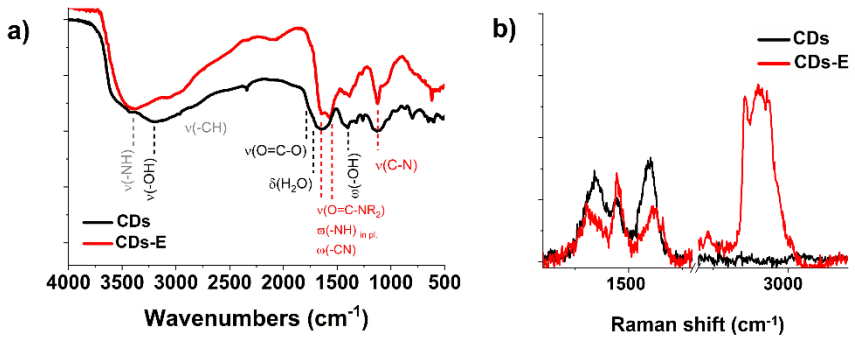

Fig. 49 Characterization of naked CDs (CDs, black line) and CDs-Ethylenediamine (CDs-E, red line): a) FT-IR spectra; b) Raman spectra

According to TEM in Fig. 50, CDs-E diameter was 2.3 ± 0.2 nm and their Zeta potential, according to DLS technique, was -32.7 ± 2.4 mV.

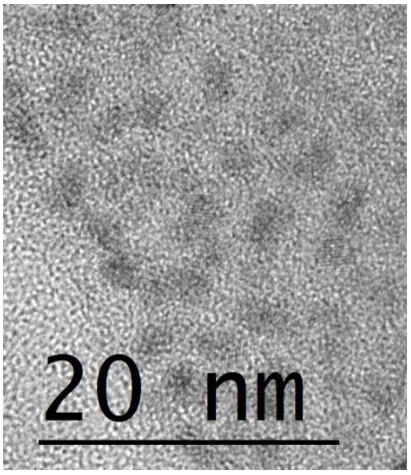

Fig. 50 TEM image of CDs-E

8.4.2 Synthesis and characterization of CDs-Au nanohybrid

8.4.2.1 CDs-Au nanohybrid synthesis

Carbon dots – Au (CDs-Au) nanohybrids were produced via visible light triggered reduction using ethylenediamine functionalized carbon dots (CDs-E) as reducing and capping agent.

Irradiation of CDs-E in the presence of $HAuCl_4$ (420-430 nm blue LED) resulted in the formation of the characteristic Localized Surface Plasmon Resonance (LSPR) band of gold nanoparticles centred at 543 nm, plateau was reached around 310 min (Fig. 51a). Reaction occurred in water with CDs-E and $HAuCl_4$ as the only reactants, no external reducing agent was added, and as reported in Fig. 52a only CDs-E absorbed 420-430 nm light.

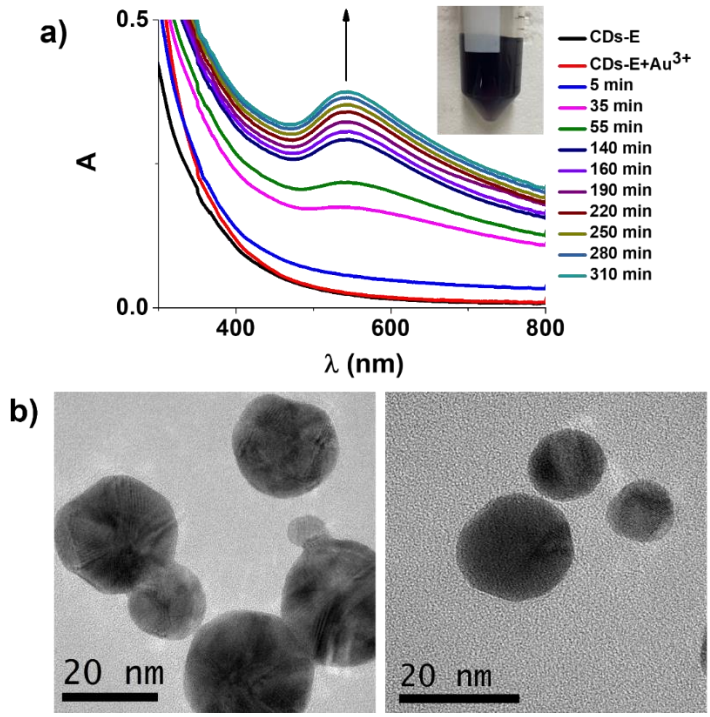

Fig. 51 a) Absorption spectral changes upon 420-430 nm irradiation, CDs-Au nanohybrid formation; b) TEM images of CDs-Au nanohybrid

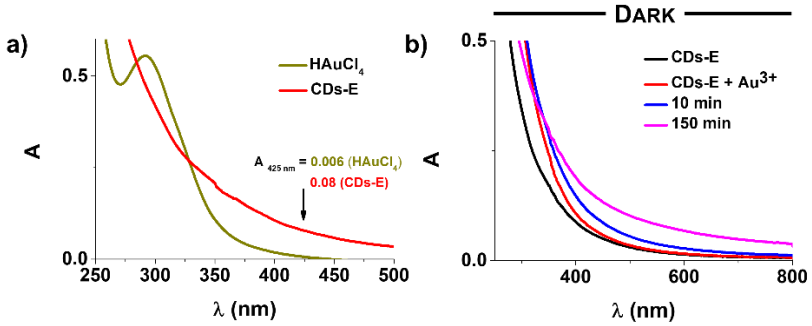

Fig. 52 a) UV/Vis absorption spectra of $HAuCl_4$ $2.5 \cdot 10^{-4}$ mol/L and CDs-E in ultrapure water; b) Control experiment of CDs-Au nanohybrid synthesis, absorption spectral changes in darkness conditions using CDs-E.

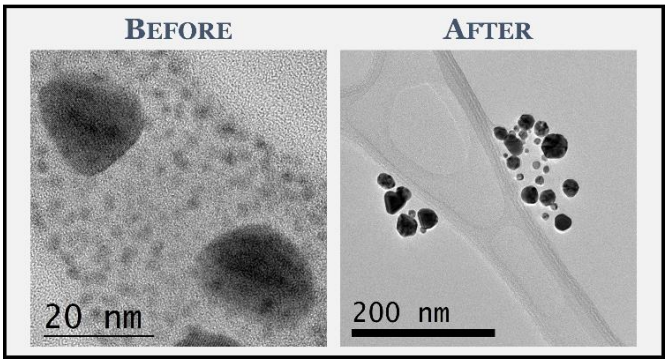

Fig. 53 TEM images of CDs-Au nanohybrid before and after purification.

Control experiment (Fig. 52b) executed in darkness showed that light irradiation is crucial for Au(III) reduction, in fact no LSPR band is detectable up to 150 min. These evidences suggest that CDs-E excited states, generated by blue light irradiation, served both as electron donors, for Au(III) reduction to Au(0), and acceptors for the counterpart. Transmission Electron Microscopy (TEM) analysis, in Fig. 51b and Fig. 53 images are reported, revealed that CDs-Au nanohybrids had a quasi-spherical shape and a mean diameter of 22.1 ± 6.1 nm. Z-potential of CDs-Au colloidal dispersion in water was -34.0 ± 1.0 mV. According to literature [234] the position of the maximum of the LSPR band of citrate-capped (Turkevich method [225]) gold nanoparticles is size dependant, for 21 nm nanoparticles is reported to be 521 nm. It is known that this effect is also capping layer dependant [235], our experimental results (22 nm size, 543 nm LSPR maximum) is not far from literature and advise the influence of CDs-E in the produced nanohybrid. Moreover, CDs-Au before and after purification were well dispersible and stable up to 2 months in ultrapure water. As it can be seen by TEM imaging in Fig. 53 in the reaction mixture before purification there were quasi-spherical nanoparticles around 20 nm and around 2-3 nm, respectively attributed to CDs-Au nanohybrid and unreacted CDs-E. After purification no residuals CDs-E were detected. In light of the aforementioned, it is reasonable to assume that CDs-E served also as capping layer in the synthetic process.

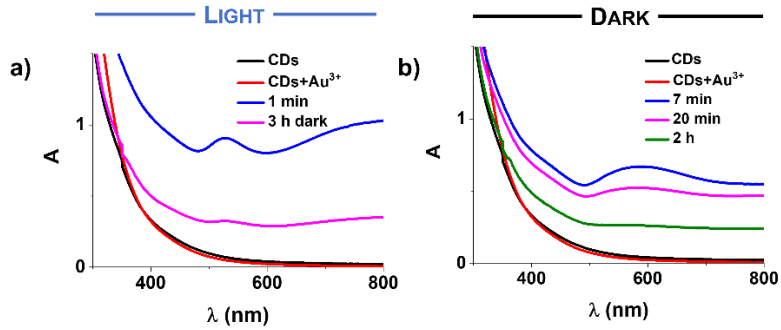

Fig. 54 Control experiment performed with naked CDs as reducing and capping agent: a) Blue (420-430 nm) light irradiated sample, b) Control in darkness condition

Control experiments substituting CDs-E with CDs as reducing and capping agents were performed (Fig. 54) showing that 1 min of blue light (420-430 LED) irradiation triggered a rapid and intense reduction of the gold salt. In the UV/Vis absorption spectrum in Fig. 54a two LSPR bands were detected: the first centred around 528 nm attributable to spherical nanoparticles, and the second in the NIR region attributable to complex nanostructures as nanoprisms or nanoflowers [236, 71]. After few hours the system collapsed to insoluble gold aggregates. Probably, the quasi-instantaneous reduction was not sustained by a powerful capping agent able to stabilize nanoparticles dispersion in water, that is index of the pivotal role of ethylenediamine functionalization of carbon dots. In fact, amine and amide groups are known for Au(III) complexing ability [237] and amine to bind AuNPs surface [238]. Control experiment with naked CDs in darkness was performed too (Fig. 54b), reduction was slower than in the light irradiated sample, a fine blush pink precipitate was formed and after two hours almost disappeared. This time no insoluble gold aggregates were produced, Red-Ox processes were in equilibrium probably because there were controlled by hydroxyl groups on CDs surface [211] and no stable gold nanoparticles were prepared.

8.4.2.2 Spectroscopic characterization of CDs-Au nanohybrid

CDs-Au UV/Vis absorption spectrum in Fig. 55a presented an LSPR band centred around 540 nm typical of gold nanostructures, and broadband UV absorption compatible with the sum of absorption and scattering operated

by carbon dots and gold nanostructures. CDs-Au nanohybrid is not luminescent as highlighted in Fig. 55. Black dash line spectra in Fig. 55a and Fig. 55b are referring to the supernatant of purification procedure in which only unreacted CDs-E were contained.

The elemental composition of CDs-Au nanohybrid, according to Energy-dispersive X-Ray spectroscopy (EDS) from Scanning Electron Microscopy imaging in Fig. 56 is: C, O, Au and Si (the latter for the background Si wafer). Carbon and gold amount is comparable. FT-IR and Raman analysis, in Fig. 55c and Fig. 55d respectively, show the presence of CDs-E absorption pattern in CDs-Au spectra. Luminescence of CDs-Au is quenched for small metal nanoparticles effect [239] and Raman signals are enhanced.

These evidence suggest that CDs-Au nanohybrid present CDs and AuNPs properties in contemporary.

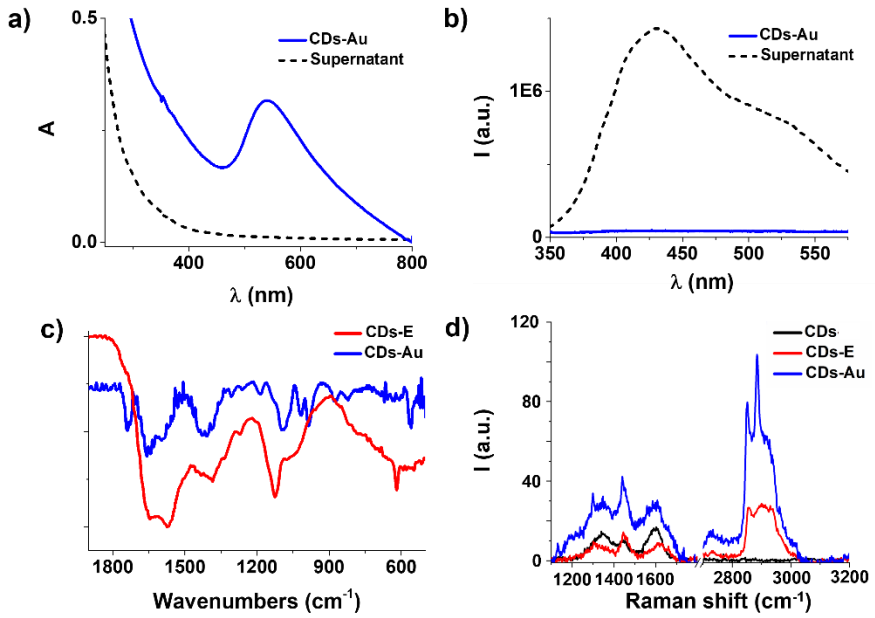

Fig. 55 Characterization of CDs-Au nanohybrid (blue line): a) UV/Vis absorption spectra of pure CDs-Au and the supernatant from purification (black dash line); b) Luminescence emission spectra ($\lambda_{excitation}$ = 300 nm) of pure CDs-Au and the supernatant from purification (black dash line); c) FT-IR spectra comparison of CDs-Au and CDs-E (red line); d) Raman spectra comparison of CDs-Au, CDs-E (red line) and CDs (black line).

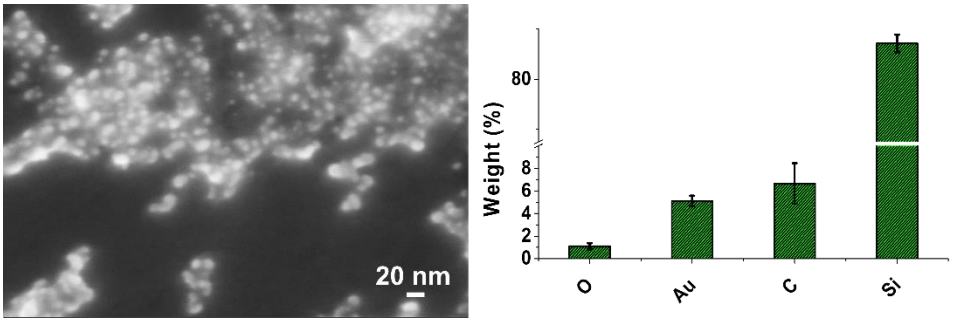

Fig. 56 SEM/EDS characterization of CDs-Au nanohybrid

8.4.3 Photothermal activity

8.4.3.1 Method

The experimental setup for photothermal measurements was reproduced from Jiang et al work [240] with little modifications.

1 mL of CDs-Au nanohybrid aqueous dispersion was placed in a 1 cm quartz cuvette which contained a magnetic stirring bar. Sample was kept under continuous stirring to avoid hotspot formation and non-homogeneous heat distribution. The dispersion was irradiated with a CW 532 nm laser, the incident light power was 30 μW for a 2 mm^2 illumination area. Sample dispersion was prepared to have $A_{532\ nm} \approx 1$, transmitted light power was 1 μW. Incident and transmitted light power were measured with a Newport model 843-R (Newport Co., CA – USA) power meter. Temperature profiles were acquired with a Vernier GoDirect (Vernier Software & Technology, OR - USA) digital thermometer equipped with a Pt_{100} resistance temperature detector (RTD) and digitalized using the Vernier LabQuest software. Each data point, recorded every 0.5 s (sensitivity ± 0.001 °C), represent an individual measurement. Laser beam direction was adjusted to be over the stirring bar and below the temperature sensor that was soaked in the upper part of the solution. In this way the laser beam could pass through the sample cell and be absorbed by the CDs-Au nanohybrid without any interference. In order to minimize heat loss from the cell surface to the external environment this was insulated with a 3 cm polystyrene coating with a 1 cm^2 opened window for the laser optical pass.

8.4.3.2 Results

CDs-Au nanohybrid photothermal ability was evaluated showing comparable light-to-heat energy conversion efficiency to the "gold standard" citrate-capped AuNPs by Turkevich. The temperature of the aqueous solution of CDs-Au and Turkevich AuNPs increased in a ten of minutes reaching plateau around 25 min and 23 °C starting from 22 °C (Table 6).

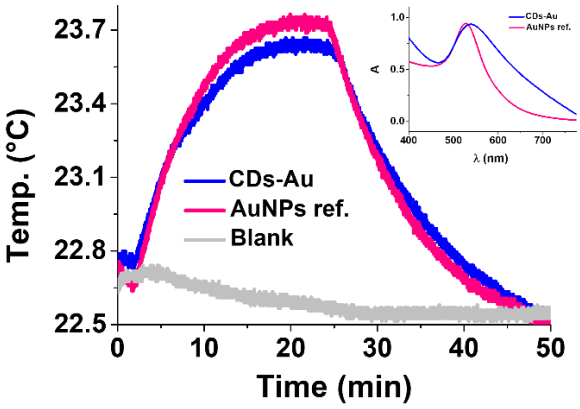

Fig. 57 Temperature changes upon 420-430 nm LED irradiation of CDs-Au (blue line) and AuNPs (Turkevich method) as reference (pink line). Gray line is referred to the temperature changes of 1 mL of water as blank experiment. On the insert: UV/Vis absorption spectra of CDs-Au and AuNPs Turkevich.

SAMPLE	TEMP. (°C)		ΔT (°C)
	Light ON	Light OFF	
CDs-Au	22.745 ± 0.001	23.657 ± 0.001	**0.912 ± 0.002**
AuNPs ref.	22.659 ± 0.001	23.753 ± 0.001	**1.094 ± 0.002**
Blank	22.713 ± 0.001	22.552 ± 0.001	**0.161 ± 0.002**

Table 6 Temperature values of photothermal experiments with CDs-Au

8.5 CONCLUSION

Stable and water dispersible CDs-Au nanohybrid were produced via a visible light (420-430 nm) triggered reduction of $HAuCl_4$ in the presence of ethylenediamine functionalized carbon dots (CDs-E) as contemporary reducing and capping agents. CDs-E excited states, produced by blue light irradiation, served both as electron donors, for Au(III) reduction to Au(0), and acceptors for the counterpart managing the Red-Ox process carbon and gold nano-structuration. Ethylenediamine functionalization of carbon dots is pivotal for Red-Ox and capping reactivity and was done exploiting carboxylic chemistry.

Naked carbon dots (CDs), ethylenediamine functionalized carbon dots (CDs-E) and CDs-Au nanohybrid were fully characterized via UV/Vis, steady state and time resolved luminescence, FT-IR, Raman, quantitative X-Ray Photoelectron, Energy-dispersive X-Ray spectroscopies. Particle morphology and surface charge were analysed by Transmission Electron Microscopy (TEM), Scanning Electron Microscopy (SEM) and Zeta potential with the Dynamic Light Scattering (DLS) technique respectively.

CDs-Au nanohybrid presented comparable light-to-heat conversion efficiency, with 532 nm irradiation, to “gold standard” citrate-capped gold nanoparticles firstly prepared by Turkevich. Further studies are on-going in order to test photothermal activity with different wavelengths and powers exploitable at example for therapeutic applications (Red, NIR).

9. A NEW AG-NANOSTRUCTURED HYDROXYAPATITE POROUS SCAFFOLD: ANTIBACTERIAL EFFECT AND CYTOTOXICITY STUDY

The content of this chapter is reprinted/adapted from Elsevier B.V., the author has the right to include it in a thesis [12]: Calabrese, G.; Petralia, S.; Franco, D.; Nocito, G.; Fabbi, C.; Forte, L.; Guglielmino, S.; Squarzoni, S.; Traina, F.; Conoci, S., A new Ag-nanostructured hydroxyapatite porous scaffold: Antibacterial effect and cytotoxicity study. *Materials Science and Engineering: C* **2021,** *118*, 111394.

9.1 ABSTRACT

We report a new chemical method for the functionalization of Mg-hydroxyapatite (Mg-HA) scaffold with Ag nanoparticles (Ag NPs) integrating in one step both the synthesis of the Ag NPs and their nano-structuring into the HA matrix (Ag-Mg-HA scaffold). This method exploits a green photochemical synthesis and allows the direct growth of Ag NPs on the Mg-HA surface. The surface structure of Ag-Mg-HA scaffold, investigated by scanning electron microscopy, shows no significant changes in the morphology upon Ag NPs incorporation. The presence of Ag was confirmed by EDX analysis. TEM and spectroscopic investigations show Ag NPs spherical shaped with a mean diameter of about 20 nm exhibiting the typical plasmon absorption band with maximum at 420 nm. The antibacterial properties of Ag-Mg-HA scaffolds were tested against two bacterial strains, *Escherichia coli* (*E. coli*) and *Staphylococcus aureus* (*S. aureus*). The results show excellent antibacterial properties achieving up to 99% and 100% reduction of colonies for both bacteria cultures after 24 h of incubation and 100% of reduction after 48 h of incubation. The cytotoxicity of Ag-Mg-HA was also in deep investigated assessing both cell proliferation and differentiation using hADSCs (human Adipose Derived Stem Cells) and testing data point at 0, 7, 14 and 24 days. The results show cytotoxic effect with cell proliferation decreasing up to 90% at 24 days and osteogenic differentiation inhibition. The observed cytotoxicity can be probable ascribed to the oxidative stress by ROS. Indeed, considering the effectiveness of the nanofunctionalization method and the excellent antibacterial properties showed by the Ag-Mg-HA scaffold, future works will be devoted to create nanofunctionalized scaffold satisfying both antimicrobial and osteo-regenerative properties.

9.2 INTRODUCTION

There are growing research interests on multifunctional innovative nanomaterials exhibiting antibacterial properties for bone tissue repair [241, 242, 243, 244, 245]. In this context, nanoscale materials play a key role providing new functionalities to biomaterial interacting with biological systems.

In bone regeneration, one of the most studied biomaterial is hydroxyapatite (HA), a calcium-phosphate ceramic ($Ca_{10}(PO4)_6(OH)_2$) exhibiting excellent biocompatibility, osteoconductivity, good cell adhesiveness, excellent biodegradability and non-inflammatory properties [246, 247]. However, this material fundamentally lacks of antibacterial property that is one of the unmet clinical needs in bone scaffolds and prosthetic coatings. The maintenance of bacteria-resistance, especially towards to the common pathogens present at surgical sites, represents a significant progress in the bone regeneration materials and bioactive coatings. Infections are events that can occur when the scaffold or the prosthesis are implanted in an environment rich of nutrients and favorable to bacteria proliferation. Therefore, the patient should be protected from infections as a result of both primary (up to 2% percentage of risk) and revision prosthetic implantations (greater than 10%). In the last case, the risk of infection is significantly higher, if the cause of the revision is the outbreak of a primary infection that must be eradicated.

Infections in implanted scaffolds and endoprostheses are mostly caused by *Staphylococcus aureus* (*S. aureus*), *Pseudomonas aeruginosa* (*P. aeruginosa*) or *Escherichia coli* (*E. coli*) due to their high virulence and an increase of antibiotic resistances. These events induce highly inflammatory processes leading to bone destruction and implant loss [248, 249]. Actually, the presence of the artificial surface of the implant favors the formation of bacterial biofilm making it more resistant to the immune system and antibiotic treatment [250]. It has been proven that treatments of bone infections with antibiotics offer poor results when not combined with

eradication of residual bacteria from the surgical site [251, 252]. Orthopedic implant infections are notoriously difficult to treat with antibiotics. Therefore, prevention and eventually eradication of residual bacteria from the surgical site is fundamental for the success of the implant.

In this context, new material design strategies based on nanostructured antibacterial coating offer unique properties of high specific surface area and topographies mimicking the microstructures of natural tissue with antibacterial properties at the same time [253]. Innovative nanomaterials exhibiting antibacterial properties for bone tissue repair are widely reported in literature including micro and nanostructured titania [254], titanium surface modification with Ag-, Sr- and Si micro-calcium phosphate coating [255], and red phosphorus/IR780/arginine-glycine-aspartic acid-cysteine coating on titanium implant [256], fluoridated hydroxyapatite coatings [257, 258] and calcium phosphate coatings on metallic implant [259]. Ag has been extensively studied because of its well know antimicrobial activities, against both gram-positive and gram-negative bacteria [260] and minimal bacterial resistance [261]. Additionally, Ag is an inorganic material and then it is not affected by degradation processes typical of organic molecules. For these reasons, it can be considered as one of the best material for antibacterial activity and has been widely used in several applicative fields including clinical and medical usage, personal care products, domestic, agriculture and industrial products [262]. Nanotechnology has improved physical, chemical and biological properties of Ag by transforming it into silver nanoparticles (Ag NPs). Several researchers studied the Ag-NPs antibacterial mechanism and their effect on osteogenic-related cells. An extensively review on antibacterial effect of Ag-NPs was published by Qing and coworkers [263]. They studied the effect of NPs concentration and dimension into the antibacterial property and cytotoxicity suggesting that Ag-NPs ≤10 μg/mL is a safe dose for osteogenesis-related cells. Castiglioni et al. [264] showed that Ag NPs cause cytotoxicity in different cell types in a dose-dependent manner. Khalandi et al. [265] in their review reported that Ag-NPs are able to anchor themselves to the bacterial cells wall and infiltrate them causing cell death. Recent evidences suggested that the released silver ions (Ag^+) from Ag NPs have a key role for the antibacterial activity [266]. Moreover, Pal et al. published the effect of NPs concentration

and shape on antibacterial properties, finding 50 μg of spherical shape NPs completely inhibits the grown of *E. coli* proliferation [267]. Martınez-Castanon et al. have investigated the antibacterial activity of Ag-NPs with dimension from 7 to 30 nm finding that the antibacterial effect decreases with an increase of the particle size [268]. Therefore, several are the parameters modulating the Ag-NPs properties towards the living cells offering a stimulating field of research.

The use of Ag NPs coating on scaffold and prosthesis can be a potential valuable strategy to be used to prevent infections in orthopedic application [269]. On that, both the method of Ag-NPs synthesis and the way of functionalization of the scaffold matrix play a key role in determining the final properties of the implantable system. The conventional methods reported in literature are mainly based on: i) bottom-up approach consisting on the loading of pre-formed Ag NPs on scaffold surface, resulting on unstable Ag decoration [270] and ii) in-situ Ag NPs formation mediated by reducing agents [271]. Versace et al. reported an alternative radical method for the in-situ formation of Ag NPs on microfibrous scaffold surface. They demonstrated the formation of a radical species on surface, which induces the Ag reduction. But this method is limited to the reactive surface able to form a radical species [272]. Therefore, all the state of art approaches includes several executive steps using organic agents with negative impact on both the production cost and the environment [273]. Therefore, the development of new nanofunctionalization methodologies of bone scaffold overcoming the above reported limitations represents an important challenge for regenerative biomaterials.

In the light of the above considerations, in this study we report a new chemical method for the functionalization of Mg-HA scaffold with Ag NPs, integrating in one step both the synthesis of the Ag NPs and their integration into the HA matrix. This method uses a green photochemical synthetic approach that has been already proved to be appealing for various technological applications [274, 275]. It is based on the reduction of Ag-acetylacetonate (Ag(acac)) precursor mediated by UV–Vis light offering the advantages of in-situ growth of Ag NPs on substrate surface without the need

of reducing agents. The obtained nanofunctionalized scaffold (Ag-Mg-HA scaffold) has been fully structurally characterized and in deep investigated towards (i) the antibacterial properties against two bacterial strains E. coli and S. aureus and (ii) cytotoxicity using hADSC cells.

9.3 EXPERIMENTAL

9.3.1 Chemicals

All chemicals were obtained from commercial sources at the highest possible purity and were used as received. All solvents used were spectrophotometric grade. Milli-Q-grade water was used in all preparations.

9.3.2 HA-based scaffold structure and Ag nano-functionalization

HA-based scaffolds have been provided by Fin-Ceramica Faenza SpA (Faenza-Italy) and produced according to the process described in [276, 277]. In brief, they consist in cylindrical shapes (8 mm diameter, 5 mm high) with a structure made of a mineralized blend of type I collagen (30%) and Mg-HA (70%), mimicking the bone extracellular matrix (ECM). The scaffolds were manufactured through a bio-inspired procedure, incorporating equine type-I collagen with bioactive Mg-doped hydroxyapatite (Mg-HA) nano-crystals and stabilizing the whole structure by an extremely reactive bis-epoxy (1,4-butanediol diglycidyl ether, BDDGE). The developed process leads to a very good combination between collagen (atelo-collagen isolated from equine tendon) and co-precipitated Mg-HA nanoparticles. Finally, the whole structure was freeze-dried with a controlled freezing and heating ramp from 25 °C to −35 °C and from −35 °C to 25 °C. The process was carried out over a period of 25 h under vacuum conditions (P = 0.29 mbar) and then samples were gamma-sterilized at 25 kGy.

Ag-Mg-HA was prepared dipping HA-based scaffold in 10 mL of Silver acetylacetonate (Ag(acac)) deaerated aqueous solution (concentration 4.5 mg/100 mL) in quartz tools. Then 100 μL of acetone was added to the reaction. After degassing with Ar for 15 min, the reaction was irradiated with 4 UV lamps (254 nm, 16 W) for 5 min in an home-made photoreactor. The

yellowish Ag-Mg-HA scaffold was rinsed with deionized water and dried by Nitrogen flow.

9.3.3 *In vitro* antibacterial procedure

S. aureus ATCC29213 and *E. coli* ATCC19138 were purchased from American Type Culture Collection (LGC Promochem, Milan, Italy) and cultured in Tryptone Soya Broth (TSB, Sigma-Aldrich, Milan, Italy) and Luria-Bertani Broth (LB, Sigma-Aldrich, Milan, Italy), respectively. All bacteria strains were maintained in 20% glycerol stocks at −80 °C. Ag-Mg-HA scaffolds were decontaminated by exposition to UV-light for 12 h.

Bactericidal activity was evaluated using a semi-exponential bacteria culture [278]. Briefly, a colony of *S. aureus* and *E. coli* from the overnight cultures in Tryptone Soya Agar (TSA) and Luria-Bertani Agar (LA), respectively, were inoculated in the corresponding medium, TSB and LB, and incubated for 6–8 h at 37 °C with 150 rpm speed shaking. After incubation period, bacteria were harvested by centrifugation and resulting pellet resuspended in Phosphate Saline Buffer (PBS), for two times. A final concentration of approximately 2.5×10^5 bacteria per mL was resuspended in TSB or LB.

Each bacteria suspension was aliquoted in 24-well plates (1 mL/well), containing pre-decontaminated scaffolds, and incubated under gentle shaking (100 rpm, orbital shaker KS-15, Edmund Bühler GmbH) at 37 °C. As positive control (CTR+) of normal bacterial growth, one well was evaluated without the scaffold.

Evaluation of the bactericidal effects were determined by Colony Forming Units (CFU) assay, comparing growths of bacteria tester strain in presence and absence of the scaffold after 24 and 48 h of incubation times. Specifically, 100 µL of bacterial suspension were serially diluted in 900 µL of PBS. From each dilution, 100 µl were spread on solid medium and incubated overnight at 37 °C. After incubation, colonies in the range 30–300 were considered to determine the number of CFU, which was calculated as follows:

CFU = (number of colonies)/(volume(0.1 mL)×dilution factor)

Number of adherent bacteria on the scaffold surface was also evaluated. Specifically, scaffolds after 24 and 48 h of incubation times, were aseptically removed, placed in a glass tube containing 1 mL of PBS and subjected to sonication in an ultrasonic bath (frequency 35 kHz) for 60 s. The detached bacteria were detected using the CFU assay, as described above. Simultaneously to CFU assay, Live/Dead BacLight bacterial viability kit was also performed. The procedure consists in the following: 6 µL of dye pre-mixed of SYTO 9 and propidium iodide (at 1:1 ratio) were added to 200 µl of culture from each condition and incubated for 15 min at 37 °C [279]. Then, the samples were visualized using a Leica DMRE epifluorescence microscope with Leica C Plan 63× objective, using a BP 515–560 nm excitation filter in combination with a LP 590 nm suppression filter.

9.3.4 *In vitro* study with hADSC

9.3.4.1 Cell culture

hADSC line used in this study was purchased from Thermo Fisher Scientific (NYSE: TMO) and cultured in MesenPRO RSTM medium (Thermo Fisher Scientific, NYSE: TMO) up to 70–80% confluence. The hADSCs at the second passage (P2) were used for the following experiments.

9.3.4.2 hADSCs cell adhesion and viability on Ag-Mg-HA scaffolds

1×10^6 hADSCs suspended in 50 µL of MesenPRO RSTM medium were slowly drop seeded onto the scaffold in 24-well culture plates and incubated at 37 °C for 4 h. Successively, the growth medium was added and the day after (day 0) replaced with StemPro™ osteogenesis differentiation medium (Thermo Fisher Scientific, NYSE: TMO). The osteogenic differentiation medium was completely replaced twice a week and hADSCs- Ag-Mg-HA scaffolds cultured for 24 days. hADSCs adhesion on Ag-Mg-HA scaffolds was evaluated by haematoxylin and eosin (H&E) staining. For H&E staining, hADSCs-Ag-Mg-HA scaffolds were fixed in 4% PFA, dehydrated, embedded in paraffin and cut into 5 µm-thick sections. Sections were mounted on slides and after de-paraffinization and rehydration, stained as described previously [280].

The cell viability of hADSCs on Ag-Mg-HA scaffolds was determined using DAPI staining. Briefly, for DAPI staining, hADSCs-Ag-Mg-HA scaffolds were fixed in 4% PFA, dehydrated, embedded in paraffin and cut into 5 μm-thick sections. After, the sections were permeabilized in 0.3% Triton X-100 for 10 min, washed in PBS and the nuclei stained with 4′,6-diamidino-2-phenylindole (DAPI) (1:5000) in PBS for 5 min. Finally, slides were mounted in fluorescent mounting medium (Permafluor, Thermo Scientific, Waltham, Massachusetts, USA), acquired using a Leica DMI4000B fluorescence microscope (three digital images/scaffold) and the nuclei counted by Fiji Image J recognition software.

9.3.5 hADSCs osteogenic differentiation on Ag-Mg-HA scaffolds

The extracellular matrix (ECM) mineralization of hADSCs cultured on Ag-Mg-HA scaffolds was tested by Alizarin Red staining. Alizarin Red S solution (Panreac, Castellar del Valles, Barcellona, Spain) was prepared according to the manufacturer protocol, added to the sections and incubated for 5 min. After, the sections were washed several times to remove the staining solution surplus and finally mounted. The stained sections were acquired by using a Leica DMI 4000B microscope (Leica Microsystems Srl, Milano, Italy) and optical density quantified using Fiji Image J software (three sections/scaffold).

9.3.6 Statistical analysis

Data were analyzed either as raw data or as mean ± standard error (SE), as appropriate. Differences between several time points of hADSCs- Ag-Mg-HA scaffolds were evaluated by using one-way ANOVA with post-hoc Holm test, where appropriate. $p < 0.05$ was considered to be significant.

9.4 RESULTS AND DISCUSSION

9.4.1 Ag-Mg-HA scaffolds preparation and characterization

The Ag-nanofunctionalized HA scaffold (Ag-Mg-HA) was prepared using a photochemical method based on reduction of Ag(acac) precursor dissolved in a water solution induced by ketyl radical formed by a photosensitizer upon UV-light absorption. A scheme of reaction steps is

reported in Fig. 58A. More in details, the acetone photosensitizer forms via Norrish type I reaction a ketyl radical upon 254 nm light absorption (reaction 1). This radical (ns typical lifetime [217]) reacts with Ag(acac) in solution inducing the formation of colloidal Ag^0 NPs and acaH byproduct (reaction 2). The mechanism of Ag NPs formation on the scaffold surface is probably driven by the formation of a coordination complex between the hydroxyl group (OH) present on Mg-HA surface with the Ag center of Ag(acac) precursor to form a bis-coordinated Ag complexes at the Mg-HA surface. The surface Ag-complex reacts with the ketyl radical present in the solution inducing the grown of Ag^0 NPs at surface (reaction 3). This mechanism is well supported by previous studies carried out on the formation of Ag NPs in aqueous media driven by light [281, 282].

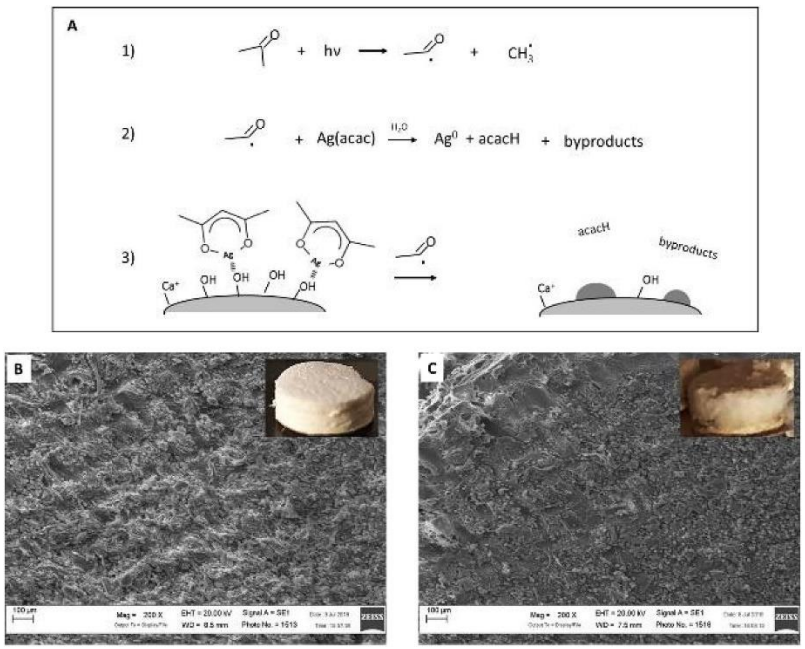

Fig. 58 A) Schematic reaction steps of the Mg-HA nano-functionalization with Ag NPs: Norrish-I type reaction for ketyl radical formation (reaction 1), Ag NPs formation in water solution (reaction 2) and Ag NPs formation at HA surface (reaction 3); B) SEM image of untreated Mg-HA; C) SEM image of Ag-Mg-HA The Insets are representative photos of Mg-HA and Ag-Mg-HA scaffolds.

The SEM analysis performed on untreated Mg-HA (Fig. 58B) and Ag-Mg-HA scaffold (Fig. 58C) indicates that the surface morphology does not undergo chemical changes by the photochemical treatment. The effectiveness

of Ag nanofunctionalization is also illustrated by the photos reported in the inset of Fig. 58 B and C clearly showing that the untreated scaffold has a white color, while the Ag-Mg-HA scaffold exhibits a yellowish color according to the Ag NPs plasmon absorption (*vide infra*). The presence of Ag NPs was confirmed by EDX measurements showing the Ag cluster diagnostic peaks at 3.15 ± 0.15 keV and P and Ca species peaks collected at 2.0 ± 0.1 keV and 3.85 ± 0.15 keV respectively. The EDX analysis gives an estimation of about 550 μg/scaffold of Ag NPs.

Further physico-chemical characterization allowed gaining insight into the Ag NPs formed during nanofunctionalization. In particular, TEM investigation carried out on colloidal Ag formed on the surfactant water solution shows the formation of NPs with diameters of about 20 nm (Fig. 59A). The UV–Vis spectrum confirms the effective Ag NPs formation showing a diagnostic plasmon band centered at 420 nm (Fig. 59B).

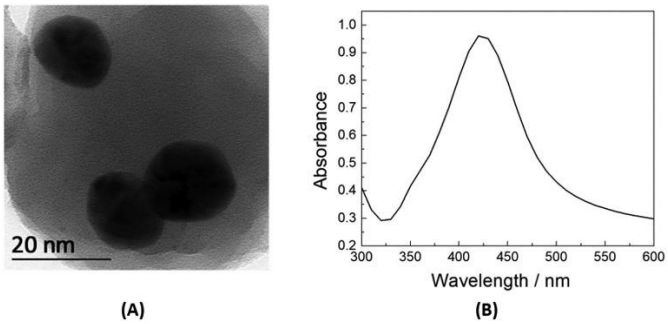

Fig. 59 A) Representative TEM image of Ag NPs; B) Ag NPs optical plasmon absorption spectrum on media reaction.

9.4.2 *In vitro* antibacterial study

The antibacterial properties of the Ag-Mg-HA scaffolds were firstly tested in suspension against two bacterial strains, E. coli and S. aureus. Fig. 60 shows the results obtained after 24 and 48 h of bacteria incubation on Ag-Mg-HA scaffold.

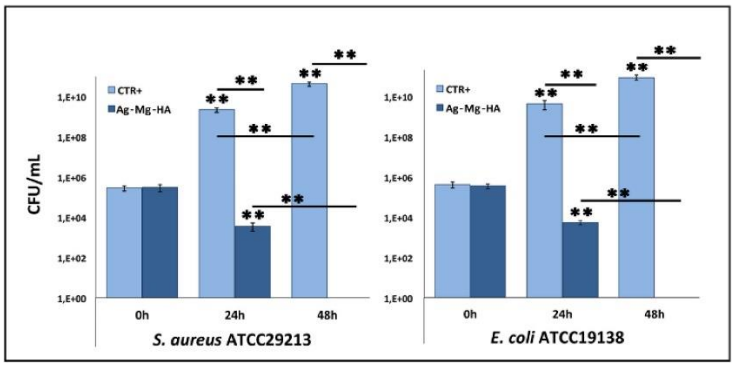

Fig. 60 Number of S. aureus ATCC29213 and E. coli ATCC19138 colonies after 24 and 48 h of incubation in presence/absence of Ag-Mg-HA. The values were obtained from the mean of three replicates and the error bars represent standard deviation.

Both bacteria showed a similar viability reduction in presence of functionalized Ag-Mg-HA scaffolds. In fact, *S. aureus* and *E. coli* cultures in the presence of Ag-Mg-HA scaffolds exhibited $3.57 \pm 1.5 \times 10^3$ and $4.2 \pm 1 \times 10^3$ CFU/mL, respectively. These values are about 6 logarithms lower than the control (cultures without Ag-Mg-HA scaffold), values that are $2.2 \pm 0.6 \times 10^9$ and $3.4 \pm 1.1 \times 10^9$ CFU/mL for *S. aureus* and *E. coli*, respectively. Similar results were obtained by evaluating adherent bacteria on scaffold surface after 24 and 48 h, respectively. More in details, we observed $6.1 \pm 2.2 \times 10^2$ CFU/ml for *S. aureus* and $1.3 \pm 0.4 \times 10^3$ CFU/ml for *E. coli* after 24 h, whereas no colonies were found after 48 h of incubation for both bacteria (Fig. 61A). Results were in agreement with the Live/Dead staining (Fig. 61B). It can be noticed that for both bacteria Ag-Mg-HA scaffold drastically reduced the number of live cells as highlighted by the red fluorescence due to dead cells (propidium iodide). On the contrary, the un-treated HA scaffold does not affect the bacterial viability showing high presence of live cells (green fluorescence due to Syto 9). Table 7 summarizes the above discussed antibacterial data collected for both methods (in suspension and in adhesion). These data correspond to 99 % and 100 % reduction of colonies for both bacteria cultures after 24 h of incubation and 100 % of reduction after 48 h of incubation.

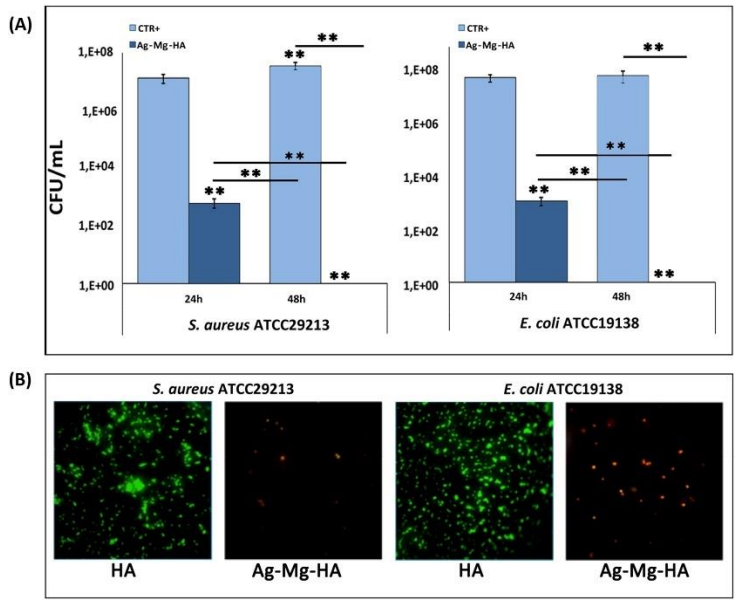

Fig. 61 (A) Number of S. aureus ATCC29213 and E. coli ATCC19138 colonies adhered to HA and Ag-Mg-HA after 24 and 48 h. The values were obtained from the mean of three replicates and the error bars represent standard deviation; (B) Live/Dead staining images of S. aureus ATCC29213 and E. coli ATCC19138 on HA and Ag-Mg-HA scaffolds.

	In suspension			In adhesion	
	0 h	24 h	48 h	24 h	48 h
S. Aureus ATCC 29231					
HA	$(2.8 \pm 0.7)10^5$	$(2.2 \pm 0.6)10^9$	$(4.2 \pm 0.8)10^{10}$	$(1.4 \pm 0.7)10^7$	$(3.6 \pm 0.9)10^7$
Ag-Mg-HA	$(3.1 \pm 0.9)10^5$	$(3.57 \pm 1.5)10^3$	No CFU	$(6.1 \pm 2.2)10^2$	No CFU
E. coli ATCC 29213					
HA	$(3.8 \pm 0.8)10^5$	$(3.4 \pm 1.1)10^9$	$(5.3 \pm 0.9)10^{10}$	$(6.4 \pm 1.0)10^7$	$(8.2 \pm 1.1)10^7$
Ag-Mg-HA	$(2.5 \pm 0.9)10^5$	$(4.2 \pm 1.0)10^3$	No CFU	$(1.3 \pm 0.4)10^3$	No CFU

Table 7 Number of S. aureus ATCC29213 and E. coli ATCC19138 colonies after 24 and 48 h of incubation on HA and Ag-Mg-HA for both "in suspension" and "in adhesion" cultures. The values were obtained from the mean of three replicates.

Since bacteria were suspended freely in bulk liquids before sticking to surfaces, they occupy one of the three regions of fluids: (1) bulk liquid, in which the cells do not undergo bactericidal effects from the specimen surface; (2) bulk liquid near the surface, where the cells can experience the bactericidal effects of the surface; and (3) constraint near the surface, in which the cells undergo to bactericidal effects, due to presence of Ag+ ions. Our experiments were carried out at low speed shaking and consequently, during incubation time, bacterial cultures were almost uniformly put in contact with the functionalized surface of specimens. Results at 24 h still

showed presence of live bacteria in suspension, although significantly reduced. This finding could indicate that some bacteria had no interaction with the sample surface. On the other hand, live adherent bacteria, although in contact with surface and consequently more subjects to bactericidal effects, were also present. This suggests that bactericidal effects require long contact time to killing all bacteria, as showed by the results after 48 h. In term of bactericidal mechanism, literature studies indicate possible pathways. Since bacteria cellular membrane has negative charge, essentially due to presence of phosphate and carboxyl groups, positive charge ions, such as Ag^+ are attracted on its surface [283]. The resulting electrostatic interactions can cause physical changes in the cellular membrane, damaging itself and promoting the ion infiltration inside cell [284]. Intracellularly, Ag^+ can cause protein denaturation, mainly those of the ribosomes, and/or high levels of reactive oxygen species (ROS). The latter, when in excess, inhibit cellular respiration, damage lipids and nucleic acids, also leading to an apoptosis-like response [263, 285].

These encouraging bactericide properties exhibited by Ag-Mg-HA scaffolds stimulate us to further in deep investigations on the specific antibacterial mechanism acting in the Ag-Mg-HA and testing against additional bacteria strains causing orthopedic infections (*i.e. P. aeruginosa*).

9.4.3 *In vitro* human adipose stem cells study

In order to investigate the cytotoxicity of the Ag-Mg-HA scaffolds with the host cells we seeded hADSCs on Ag-nanofunctionalized scaffolds and assessed their ability to adhere, penetrate and grow within them. Specifically, we cultured hADSCs cells in osteogenic medium for 24 days and performed H&E and DAPI staining's at four different differentiation time points (day 0, 7, 14 and 24). H&E results are reported in Fig. 62. Data indicated that hADSCs adhere and grow on the surfaces of scaffolds, showing a normal morphology and phenotype, but from day0 to day24 the cell amount that populate the scaffolds decreases significantly.

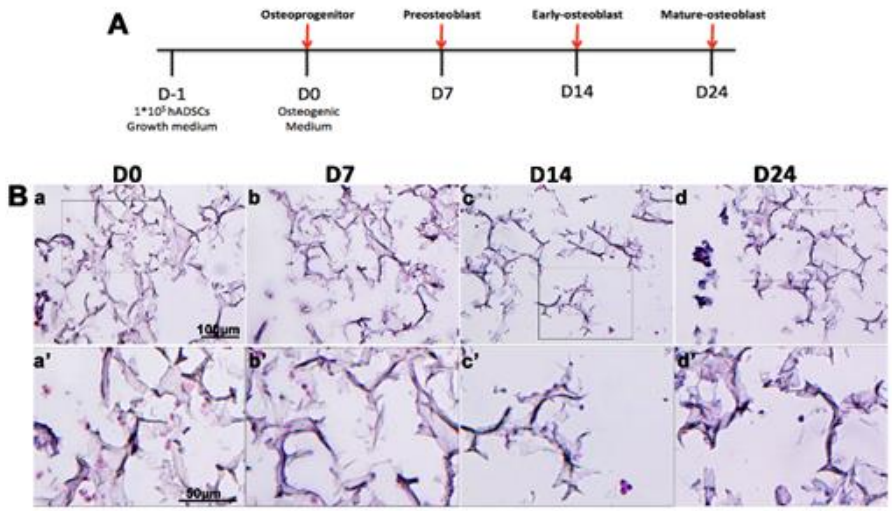

Fig. 62 A) hADSCs osteogenic differentiation schematic representation. B) Representative images of Ag nanofunctionalized scaffold sections, stained with H&E, after 0, 7, 14 and 24 days in osteogenic medium; a) Ag-Mg-HA scaffold at day 0 (D0), b) Ag-Mg-HA scaffold at day 7 (D7), c) Ag-Mg-HA scaffold at day 14 (D14), and d) Ag-Mg-HA scaffold at day 24 (D24); magnification 10× and scale bars 100 μm. A'-d') Images representing the magnifications of the rectangle indicated above. Scale bars: 50 μm.

To further investigate this result, we performed a quantitative measurement of cell number using DAPI stain. The data reported in Fig. 63 (first line of Fig. 63A and blue bars in Fig. 63B) confirm the findings obtained from H&E staining. It can be noted that the cell amount on day 7 is about 1.6-fold of that on day 0 (24 h after cells seeding). After 14 days of culture the cell number decreases almost 3.8-fold than day 0 and 2.3-fold than day 7. Finally, on day 24 the cell amount is reduced by 11.5, 7.14 and 3.04-fold compared to day 0, 7 and 14 respectively ($p < 0.01$). These data indicate that the Ag-Mg-HA scaffolds are toxic to hADSCs being unable to offer a biocompatible environment for hADSCs to propagate and grow.

To complete our cytotoxic investigation, we cultured the scaffolds with hADSC cells in presence of osteogenic differentiation medium and analyzing the Ag-Mg-HA scaffolds by Alizarin Red S (AR) staining at several time points (D0-D24). Fig. 63 (second line of Fig. 63A and orange bars in Fig. 63B) show that, at all the analyzed *time points*, the presence of calcium deposits is very low, although can be noted an increase at day 7 which decreases over time

until it returns to the level of day 0. This was quantitatively confirmed by the measurements of the AR optical densities (orange bars in Fig. 63B). Data show that even if after 7 days there is an increasing of cell differentiation of 4-folds respect to the starting point (0 day), this value decreases to 2-folds after 14 days and basically reaches the starting value after 24 days. This finding shows that Ag NPs inhibits the cell differentiation inducing a cytotoxic effect.

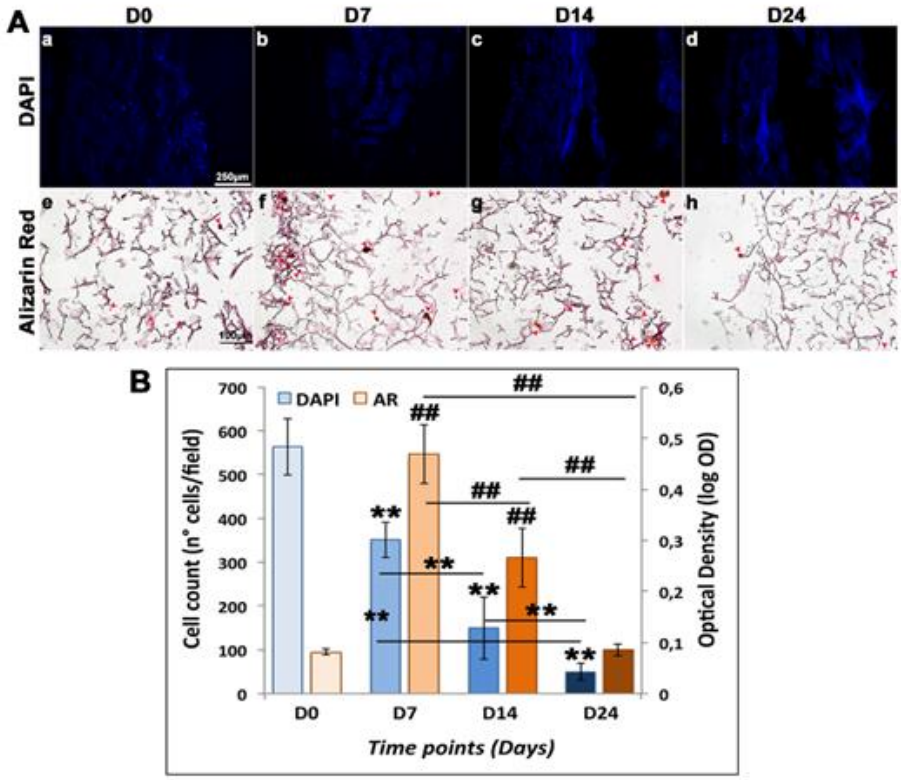

*Fig. 63 A) DAPI and Alizarin Red staining after 24 days of osteogenic differentiation on Ag nanofunctionalized scaffolds. Representative images of Ag nanofunctionalized scaffold sections, after 0, 7, 14 and 24 days. a) Ag-Mg-HA scaffold at day 0 (D0), b) Ag-Mg-HA scaffold at day 7 (D7), c) Ag-Mg-HA scaffold at day 14 (D14), and d) Ag-Mg-HA scaffold at day 24 (D24); scale bars 250 and 100 μm respectively. In Alizarin Red, the red arrows indicate the calcium deposits. B) Cell count of the DAPI positive nuclei/section and Optical densities quantification of Alizarin Red images. (Mean and standard deviation obtained on 3 sections/scaffold.) ANOVA test p value is indicated ($p < 0.0001$) and ** ($p < 0.01$) shows significant differences between the different time points as reported by the Holm post-hoc test. (For interpretation of the references to color in this figure legend, the reader is referred to the web version of this article.)*

Ag-Mg-HA	**Cell proliferation (DAPI) (n° cells/filed)**			
	Do	**D7**	**D14**	**D24**
	566 ± 65	552 ± 41	150 ± 71	50 ± 18
	Cell differentiation (AR) (LogOD)			
	Do	**D7**	**D14**	**D24**
	0.08 ± 0.005	0.47 ± 0.05	0.27 ± 0.05	0.08 ± 0.01

The values were obtained from the mean of three replicates.

Table 8 Cell proliferation and differentiation after 0 -24 days for Ag-Mg-HA.

Table 8 summarizes the above discussed data related to both cell proliferation (DAPI staining) and differentiation (AR staining) after 0-24 days.

The observed cytotoxicity can be probable ascribed to the oxidative stress by ROS, as already reported in previous *in-vitro* studies on human cell lines [286, 287]. Even if ROS are necessary for preserving normal physiological processes, an excess can lead to oxidative stress, disruption of ATP synthesis, antioxidant defense capacity damage, DNA damage and finally apoptosis [288]. Therefore, ROS interrupt the cellular respiratory chain and provoke cells dead. This process has been also observed in the bacteria cells (see above).

Together with cell dead mechanisms induced by Ag, another important aspect to be considered for the cytotoxicity observed in the Ag-Mg-HA scaffold regards the physiochemical properties of Ag-NPs (*i.e.* size, shape, concentration, and interaction with a biological system). These have been proved to imprint the specific cytotoxic effects to the material integrating the Ag-NPs [289].

Therefore, we can reasonably conclude that both (i) the cell dead mechanisms induced by Ag-NPs and (ii) their concentration play a key role in the observed cytotoxicity.

9.5 CONCLUSIONS

In this paper, we have presented a new chemical approach for nano-functionalization of Mg-hydroxyapatite (Mg-HA) scaffold with Ag NPs. It bases on a photochemical generation of ketyl radicals (Norrish type I reaction) as reducing agent of an Ag precursor (Ag (acac)). The method is fast (3 min), green (water solvent) and, most importantly, allow the direct grown of Ag-NPs direct on the whole Mg-HA scaffold without change the

morphology of the pristine HA scaffold. The size of the grown Ag NPs was observed to be about 20 nm. The nanofunctionalized Ag-Mg-HA scaffold exhibited excellent antibacterial properties against *E. coli* and *S. aureus*, with a reduction of CFU/mL up to 99% for *E. coli* and 100% for *S. aureus* after 24 h and 100% reduction after 48 h of incubation. The scaffold cytotoxicity was also in deep investigated. Results show cell proliferation decreasing up to 90% at 24 days and osteogenic differentiation inhibition. These data can be attributed to specific bactericidal and cytotoxic mechanism from Ag nanostructure. On that, literature studies describe several pathways involving Ag^+ release, ROS generation and NPs interaction with cells as function of dimensions, concentration and shape. Up to date, the bactericidal and cytotoxic mechanism of Ag-NP is not definitely identified. Therefore, in the light of that, due to the effectiveness of the nanofunctionalization method and the excellent antibacterial properties showed by the Ag-Mg-HA scaffold, our future works will be devoted to investigate the specific mechanism of toxicity of Ag NPs grown by the photochemical method towards hADSCs and the effect on the Ag-NPs concentration into the scaffold on both antibacterial properties and cytotoxicity. On that, an important point to be considered is that the respiratory chain on bacteria occurs in the cellular membrane, while in human eukaryotic cells it takes place in the mitochondria. This then significantly affects local concentration of Ag on the “killing site” (cell membrane for bacteria and mitochondria for human cell). Therefore, by playing with the Ag-NPs concentration into the scaffold and optimizing it, we will target the final goal to obtain nanofunctionalized scaffold satisfying both antimicrobial and osteoregenerative properties.

10. SILICON NANOPARTICLES FROM VOLCANIC ROCKS

The content of this chapter is a collection of experimental data obtained during the visiting PhD period on the laboratory of nanochemistry at the Institute of Supramolecular Science and Engineering (ISIS) (University of Strasbourg/CNRS) in Strasbourg, France.

10.1 INTRODUCTION

Within the research area of nanostructures for material science, the current focus of frontier research is the obtainment of new (nano)materials with versatile properties. Graphene and 2D materials have been amongst the milestones of nanoscience, material science, and condensed-matter physics, and still are extremely hot topics. In the last years their unique electrical, thermal, and optical properties allowed researchers to develop a large volume of knowledge. [290] Today, thanks to these efforts, we know that nanochemistry paraphernalia, in terms of nanostructures size and shape tunability or surface functionality, can support the demand for new materials with adjustable physical and chemical properties. It is also true that it is also needed to continue exploring new starting materials and nature is a continuous source of inspiration dear to researchers of any era. Following this lead, it was decided to explore the potential of an extremely abundant product, one of the basic constituents of our planet: volcanic rocks. The idea is to apply nanochemistry to volcanic rocks, forge of many elements entrapped in a complex silicate matrix, to produce new materials or new functional coatings.

As a starting material, it was decided to use “lapilli” which are one of the products of the volcanic activity of Mount Etna (Sicily, Italy). This volcano alternates effusive activity, with basaltic lava production, with explosive activity. The latter appears generally as a huge column made of gases, ashes, and “lapilli” from one of the volcano’s vents. Lapilli, that are small, light, and porous lava rocks, have been selected both for their abundance in eastern Sicily areas and for their facile mechanical processability.

Research state-of-art on lava products is generally focused on geological studies, for example to predict new eruptions or earthquakes, to understand the history of the volcano [291, 292] or for other fundamental

studies [293]. Little is known about lava nanostructures that could become a new and promising research niche for a plethora of applications in material science, chemistry, and nanomedicine. Some works were published in 2007-2008 in which volcanic ashes were used as catalysts for nanocarbons (carbon nanotubes and nanofibers) synthesis [294] and this complex as support for oxidative dehydrogenation reactions [295]. In 2016 Zhua used α-Fe_2O_3 nanoparticles-coated volcanic rock for Cd(II) removal from wastewater [296]. This work was born with the aim to explore nanomaterials coming from volcanic rocks that can be easily "extracted" instead of obtaining similar with long, expensive, and maybe also pollutant synthetic techniques. New nanoparticles with bizarre shapes, unusual compositions, and unrevealed physical and chemical properties within the framework of a complex silicate matrix can be an inert and bio-compatible basis to install new targeted functionalities and entrap molecules to become drug delivery agents. Their mechanical, thermal, and electrical properties can be also exploited for functional coatings in material science.

10.2 MATERIAL PREPARATION

Lapilli rocks, collected in the area of Zafferana Etnea (Catania, Italy), were grounded in a mortar until fine grey powder (Fig. 64).

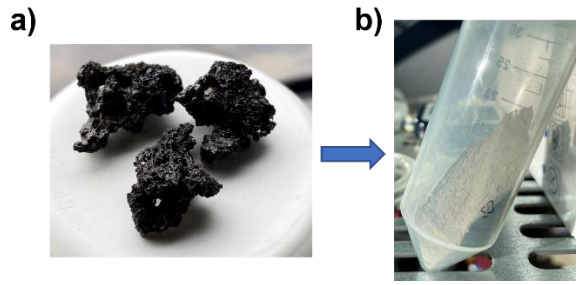

Fig. 64 Lapilli "lava" as collected (a) and after grounding (b)

The resultant powder was used for the liquid phase exfoliation experiments summarized in Table 9. Among the possible methods to fragment bulk layered materials into the nanoscale, liquid exfoliation represents a simple technique to obtain large quantities of nanomaterials like nanosheets, hybrids, composites, and others. There are several methods to do this that involve oxidation, ion intercalation/exchange, or surface passivation

by surfactants or solvents. [297] For this work it was decided to use the ion-exchange/intercalation method, in acidic and alkaline solutions, driven by ultrasonication that is a recognized procedure to decrease particle size until the nanometric scale [298]. It was also explored the surfactant-assisted method driven both by ultrasonication and conventional thermal procedure.

SAMPLE	SOLVENT	ADDITIVE	CONDITIONS
Lava exf. pH = 2 (LExA)	Water	HCl to pH = 2	Ultrasonication
Lava exf. Natural pH = 9.3		-	
Lava exf. pH = 13		NaOH to pH = 13	
Lava CTAB UW (LExC UW)	Ethanol	CTAB	
Lava CTAB Reflux (LExC reflux)			Thermal

Table 9 Experimental conditions of liquid phase lava exfoliation

10.2.1 Liquid phase exfoliation in water – Ultrasonication

Lapilli powder (500 mg) was suspended in 100 mL of ultrapure water (MilliQ-type). The pH of the solution was moved to 2 with 0.1 M hydrochloric acid (Merck, Darmstadt, Germany) addition or to 13 with 0.1 M NaOH addition (Merck, Darmstadt, Germany). The mixture was sonicated in a cup horn sonicator for 3 h at 20 °C, with 40 % of amplitude in a programmed pulse cycle of 3 s ON and 1 s OFF. The instrument was a QSonica cup horn Q700 sonicator (Qsonica L.L.C., Newton, CT – USA) (Max power: 700 W, 20 KHz) equipped with a ThermoCube Qsonica/Solid State Colling recirculating chiller (Solid State Cooling Systems, Wappinger Falls, NY – USA).

The product was then centrifuged at 550 rpm for 10 min to remove all the bigger fractions and unreacted constituents, collecting the supernatant. Only the pH = 2 exfoliated sample was centrifuged again in two different fractions: the first was treated at 4629 rcf (6000 rpm) for 30 min and the other at 15557 rcf (11000 rpm) for 30 min. All of them were split into other two fractions: one that was laid untreated and the second filtered with a 0.22 μm PES (Polyethersulfone) filter (Merck Millipore Millex-GP 0.22 μm, Merck, Darmstadt, Germany). Below the list of the samples, for a matter of simplicity,

it was chosen to short the name of lava exfoliated pH = 2 samples in LExA – *Lava Exfoliated Acid*.

- LExA 6000 rpm
- LExA 6000 rpm filt.
- LExA 11000 rpm
- LExA 11000 rpm filt.

10.2.2 Surfactant-assisted liquid phase exfoliation

Lapilli powder (500 mg) was suspended in 100 mL of absolute ethanol with Cetyltrimethyl Ammonium Bromide (CTAB) as a surfactant (1.823 g). CTAB critical micelle concentration (CMC) in ethanol is 0.24 M [299] compared to $9 \cdot 10^{-4}$ M in water. Using ethanol as a solvent could avoid micelle formation favouring surfactant interaction with the material to be exfoliated and providing a better solvent for laboratory manipulations. Ethanol is also recognized as a "green" solvent. To estimate lava powder molecular weight, it was decided to approximate using the one of SiO_2.

SAMPLE	MW	mmol	eq.	mg
Lapilli powder (SiO_2)	46	5	1	500
Cetyltrimethyl ammonium bromide (CTAB)	364.46	5	1	1823

Table 10 Reaction stoichiometry of CTAB-assisted lava exfoliation

This experiment was performed with ultrasonication, as for the liquid phase exfoliation in water, and with a thermal treatment.

- Ultrasonication

The mixture of lapilli powder and CTAB in EtOH was sonicated in a cup horn sonicator for 3 h at 10 °C, with 40 % of amplitude in a programmed pulse cycle of 3 s ON and 1 s OFF.

- Thermal exfoliation

The mixture of lapilli powder and CTAB in EtOH was left under stirring at 40 °C for 4 h and then under reflux for 61 h.

For both methods, the mixture was purified by centrifugation at 550 rpm for 10 min, followed by filtration of the supernatant with a sintered glass filter (porosity 4); such filtered product was washed many times with ethanol. Two products were collected: a grey solid precipitate named “coarse fraction” (already washed) and a “fine fraction” coming from the filtered dispersion. The latter was recovered as the precipitate of centrifugation made at 15557 rcf for 60 min of the filtered ethanolic dispersion.

10.3 LIQUID PHASE EXFOLIATION ON DIFFERENT PH

10.3.1 Optical microscopy

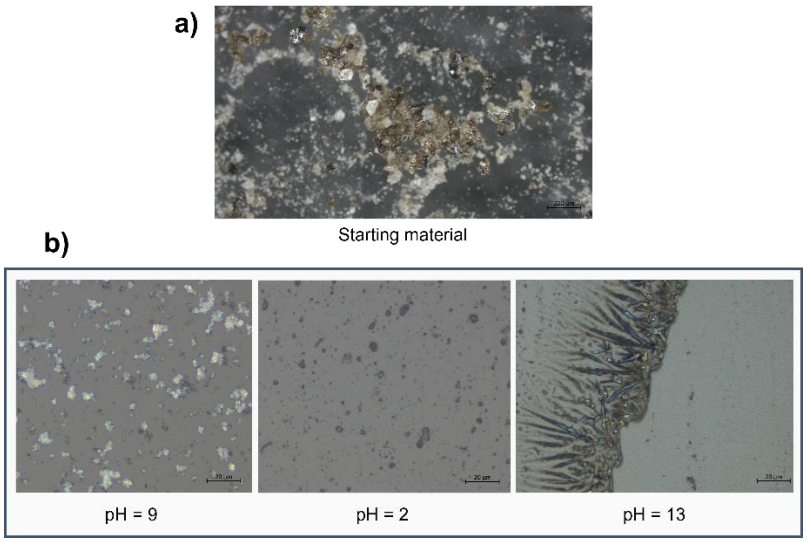

Fig. 65 Optical microscopy images of lava liquid phase exfoliation in water on different pH values

As is shown in Fig. 65a, starting material (the non-exfoliated lapilli powder) presented different types of crystals with heterogeneous shapes and size distribution. The images in Fig. 65b are referred to the ultrasound liquid phase exfoliation performed at different pH values. As the purpose of the work was to obtain materials on the nanometric scale, it was chosen to continue the experimental plan only on exfoliation at pH = 2 (LExA). This procedure in fact, according to optical microscopy images, seems that produced smaller particles compared to the other two. It can be deduced that Na^+ and OH^- as intercalating/exchanging ions were not efficient as H^+ and Cl^- coming from HCl dissociation. Protons, in particular, lead to the substitution

of the interlayer cations producing Si-OH at the layer edges which increases the general reactivity and ion binding [300, 301].

pH of the natural bare lava suspension was 9.23, according to carbonates dissolution, and became 8.4 after the process. Alkaline exfoliation was performed on pH = 13.15 and after the process was found equal to 12.65. LExA exfoliation started on pH = 2 and evolved to pH = 2.64.

10.3.2 SEM/EDS on starting material and LExA

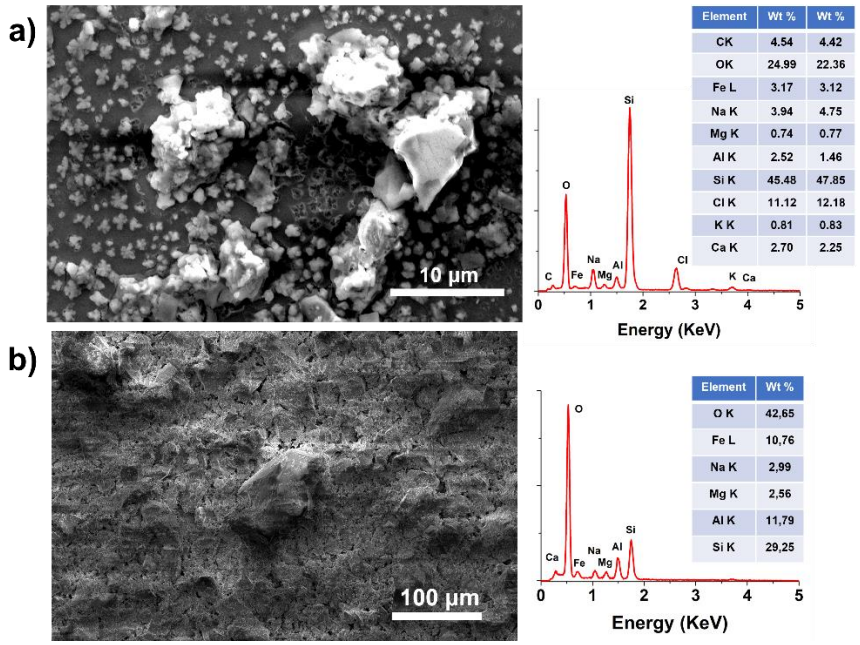

Fig. 66 SEM imaging and EDS characterization: a) LExA sample; b) Bare lava "lapilli" powder.

A 1/100 dilution of the product of "lava" powder exfoliation pH = 2 (LExA) was drop-casted on a Si/SiO_2 wafer and directly analysed on SEM, without metallic sputtering. Elemental composition, according to EDS spectroscopy, did not change as a function of material morphology. Quantitative analysis in Fig. 66a is reported on two different points of the sample, one related to the micrograph image shown and the second on a single particle (image not shown). As a comparison experiment (Fig. 66b) bare lapilli powder (the starting material) was attached to a Copper tape and directly analysed on SEM, without metallic sputtering. Elemental

composition, according to EDS spectroscopy, was: O, Fe, Na, Mg, Al, Si. Carbon, Chlorine, Potassium, and Calcium are missing, so it can be concluded that these elements were introduced or unmasked during the LExA process due to hydrochloric acid addition. Protons and Chlorides, in this way, reasonably served as intercalator/exchange ions favouring silicate exfoliation and their presence prove the effectiveness of the procedure. This, however, was not quantitative, as it is still possible to find multilayered crystals in the product mixture (Fig. 67).

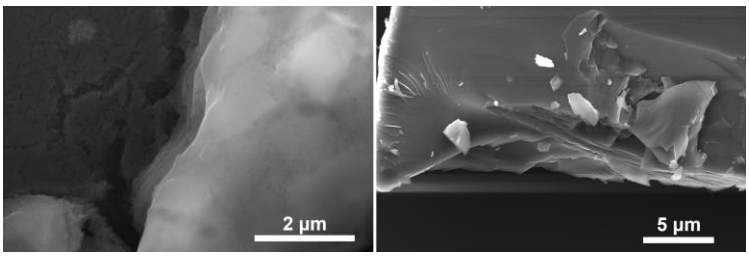

Fig. 67 SEM images on LExA sample: multi-layered crystals in the product mixture

10.3.3 Dimensional selection on LExA materials

As reported in the material preparation section (2.2.3), the product of lapilli powder acidic exfoliation was centrifuged to obtain nanometric scale materials attempt a size separation of nanometric fractions in dispersion. The LExA samples list is reported below.

- LExA 6000 rpm
- LExA 6000 rpm filtered 0.22 µm
- LExA 11000 rpm
- LExA 11000 rpm filtered 0.22 µm

10.3.3.1 UV/Vis and luminescence characterization

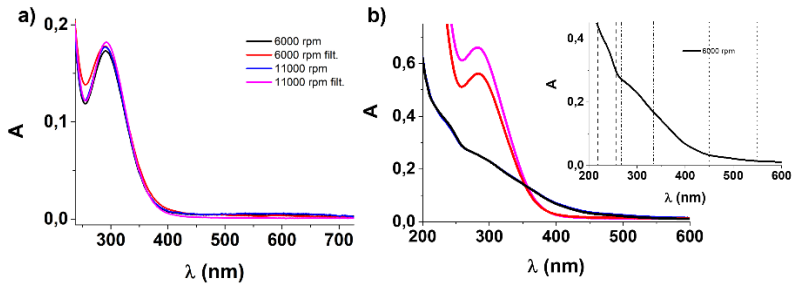

Fig. 68 UV/Vis absorption spectra: a) Spectra recorded right after sample preparation, b) Spectra recorded 2 weeks after preparation.

All the samples presented the same absorption spectrum right after the preparation (Fig. 68a), with one band from 250 to 350 nm (A_{max} = 292 nm). After two weeks (Fig. 68b) only the absorption spectra of the non-filtered samples changed, showing one band from 217 to 255 nm (A_{max} = 237 nm), another from 265 to 333 nm (A_{max} = 300 nm), and the last one from 450 to 550 nm (A_{max} = 495 nm) as highlighted in the insert of Fig. 68b.

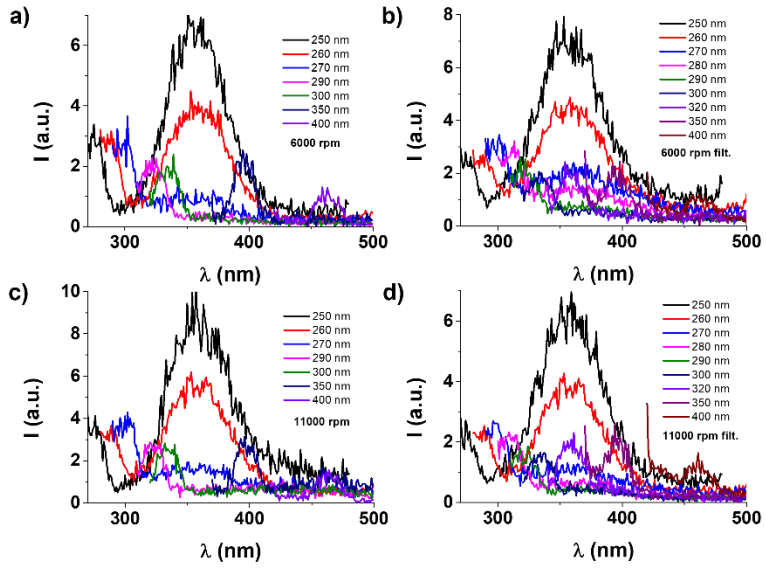

Fig. 69 Emission spectra: a) 6000 rpm, b) 6000 rpm filtered 0.22 µm, c) 11000 rpm, d) 11000 rpm filtered 0.22 µm

In Fig. 69 are reported emission spectra recorded right after the preparation, on the legend the excitation wavelengths. Even in this case, there

is no difference between the samples. It could be detected an emission band from 300 to 400 nm ($\lambda_{\text{emission max}}$ = 350 nm) with 250 nm excitation. The absorption band responsible for the emission phenomenon is attributed to the deep UV band from 200 to 250 nm as confirmed by the excitation spectra in Fig. 70a.

After two weeks of preparation, analysing 6000 rpm non-filtered sample, it can be seen a change also in the emission band that became larger (Fig. 70b).

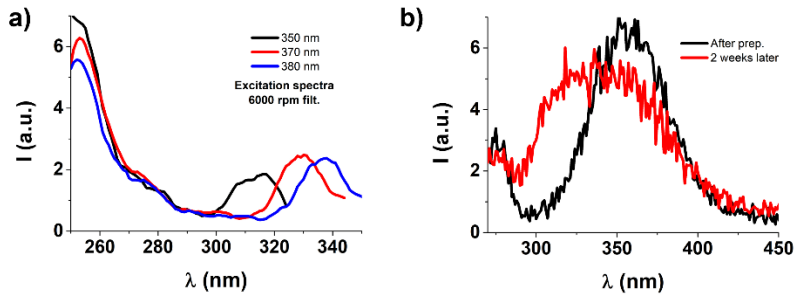

Fig. 70 a) Excitation spectra of 6000 rpm filtered sample; b) Emission spectra (λ_{exc} = 250 nm) right after the preparation and two weeks later

10.3.3.2 FT-IR characterization

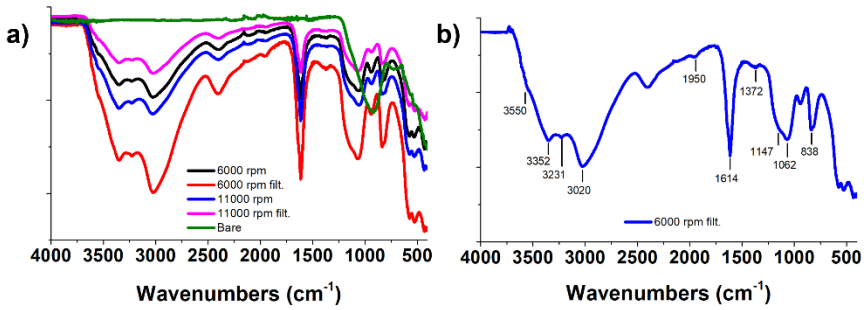

Fig. 71 FT-IR (ATR) spectra: a) Comparison between of LExA samples and bare lava; b) FT-IR spectrum of LExA 6000 rpm filt., as a reference for the others, with the selected peaks.

In Fig. 71a are reported FT-IR spectra of the different samples. It can be seen a dramatic change in the IR bands from the bare lava (non-exfoliated lapilli powder), that has one large band from 1250 to 763 cm^{-1} and a less intense band from 763 to 653 cm^{-1}, to the LExA samples. The latter presented the same IR absorptions. In Fig. 71b a single spectrum is reported with a selection of the peaks (cm^{-1}), which are listed in Table 11 and can be associated

to silicates [230]. Notably, the most important contribution is given by the Si-OH bond vibrations.

WAVENUMBERS (cm^{-1})	ATTRIBUTION
3550	-Si-OH
3352	-Si-NH-Si-; -NH
3231	-Si-OH
3020	-C=C-; sp^2 CH stretch
1950	
1614	Water; -C-C- arom. stretch
1372	
1147	-Si-NH-Si; -Si-O-Si-
1062	-Si-OH
940	-Si-NH-Si-
838	-Si-OH; -CH oop bend.

Table 11 FT-IR peaks attribution

In Table 12 are reported on the left the common IR absorption bands of silicates, on the right other bands associated with common vibration of carbon and nitrogen bonds that are reported in [230] and were used for spectrum interpretation.

GROUP	WAVENUMBERS (cm^{-1})	GROUP	WAVENUMBERS (cm^{-1})
-Si-OH	3700-3200; 1030-1000; 910-820	-NH	3350
-Si-NH_2	3600-3300 (doublet); 1530-1510	-C=C-; sp^2 CH stretch	3020
-Si-; $CH=CH_2$	1615-1590; 1420-1390; 1050-1010; 950-920	-CH oop bend	838
-Si-O-Si-	1100-100		
-Si-O-	1062		

Table 12 FT-IR peaks from ref. [230]

10.3.3.3 Energy gap characterization

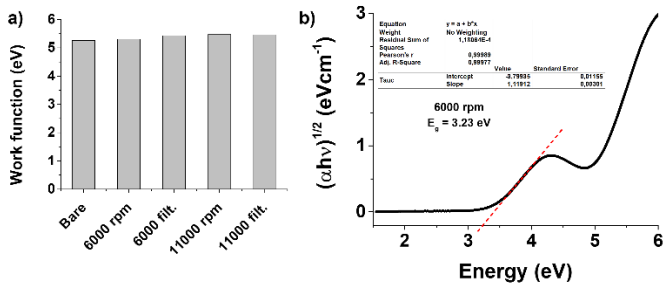

Fig. 72 a) Samples work function estimated by UPS, b) Tauc plot for the estimation of the optical band gap

To further understand materials' surface behaviour, work functions were estimated using Ultraviolet Photoelectron Spectroscopy (UPS). Very similar values of work function were found between the samples, namely from 5.26 to 5.47, probably within the experimental error (Fig. 72a). From the UV/Vis absorption spectrum right after the preparation, it was calculated the optical energy band gap (Fig. 72b) between Valence Band Minimum (VBM) and Conduction Band Minimum (CBM) using a Tauc plot [174] by the formula taken from [175]

$$(\alpha h\nu)^{\frac{1}{\gamma}} = B(h\nu - E_g)$$

where α is is the absorption coefficient ($\alpha = 2.303A \cdot cm^{-1}$), h the Plank constant, ν is the frequency of the incident photon, γ is a parameter that depends on the nature of the electronic transition (in this case for allowed transition could be 0.5 for the indirect and 2 for the direct), B is a constant assumed to be 1 and E_g the energy band gap. E_g was calculated using $\gamma = {}^1/_2$ for the direct electronic transition. The calculated optical band gap is 3.23 eV.

10.3.3.4 Material resistivity (four-point probe)

The obtained resistivity values are shown in Table 13. In Table 14 there are reported experimental values and calculations used to obtain the resistivity parameters. It can be seen large heterogeneity in terms of film thickness and, especially, in terms of sheet resistance. It can be concluded that materials are heterogeneous and seem to be conductive.

SAMPLE	RESISTIVITY ($\Omega \cdot m$)
6000 rpm	14.65 ± 14.76
6000 rpm filtered	$3.58 \cdot 10^{-6} \pm 2.54 \cdot 10^{-6}$
11000 rpm	4.80 ± 7.30
	11.99 ± 42.82
	$1.32 \cdot 10^{-6} \pm 8.62 \cdot 10^{-7}$
11000 rpm filtered	7.12 ± 11.59
	16.62 ± 13.58
	$2.48 \cdot 10^{-6} \pm 1.36 \cdot 10^{-6}$
Bare	0.05 ± 0.02

Table 13 Resistivity values of material thin films estimated from four-point probe technique

SAMPLE	MAX CURRENT	SHEET RESISTANCE (Ω/sq)	THICKNESS (nm)
6000 rpm	10 nA	$2.1 \cdot 10^7$	432, 522, 175 651, 218, 1000 623, 734, 682
		$2.5 \cdot 10^6$	
		$8 \cdot 10^6$	
		$4.2 \cdot 10^7$	
		$5.8 \cdot 10^7$	
		$2.612 \cdot 10^7 \pm 2.3404 \cdot 10^7$	560.66667 ± 258.65953
6000 rpm filtered	100 mA	5	118, 810, 1184 1145, 893, 1307 655, 1078, 1270
		6.15	
		1.1	
		3	
		3.8125 ± 2.22799	940 ± 377.52682
11000 rpm	10 nA	A - $1.5 \cdot 10^7$	345, 373, 320 397, 970, 885 629, 448 452, 580, 1200
	100 mA	B - 3.2	
		B – 1.3	
	10 nA	A - $2.5 \cdot 10^7$	
	100 mA	B – 2.1	
		T - $8 \cdot 10^6 \pm 1{,}151097 \cdot 10^7$	599.90909 ± 293.34909
		A - $2 \cdot 10^7 \pm 7.07107 \cdot 10^7$	
		B – 2.2 ± 0.95394	
11000 rpm filtered	10 nA	A - $2.1 \cdot 10^7$	839, 607, 394 865, 1060, 1298 1527, 1312, 1036 558
	100 mA	B – 4.1	
	10 nA	A - $2.8 \cdot 10^7$	
		A - $3.5 \cdot 10^6$	
	100 mA	B - 2.05	
		B – 2.4	
		B – 1.9	
		T - $7.5 \cdot 10^6 \pm 1.18568 \cdot 10^6$	949.6 ± 365.84247
		A – $1.75 \cdot 10^7 \pm 1.26194 \cdot 10^7$	
		B – 2.6125 ± 1.01355	
Bare	100 nA	$2 \cdot 10^4$	1737, 4346, 2885 2504, 2058
		$1.8 \cdot 10^4$	
		$1.91 \cdot 10^4$	
		$1.81 \cdot 10^4$	
		$1.78 \cdot 10^4$	
		$1.8602 \cdot 10^4 \pm 931.40754$	2706 ± 1015.05049

Table 14 Experimental values of sheet resistances and thicknesses for resistivity calculations

10.3.3.5 XPS characterization

XPS spectra were collected from three different points per each sample. For each sample survey and high-resolution spectra were acquired, the latter for C1s, O1s, Al2p, Si2p, Fe2p, and Mg1s. In Fig. 73a an overlay of the survey spectra is presented for all the different samples, it can be noticed that the exfoliated are overlapping, instead of bare lava (lapilli powder) that is different.

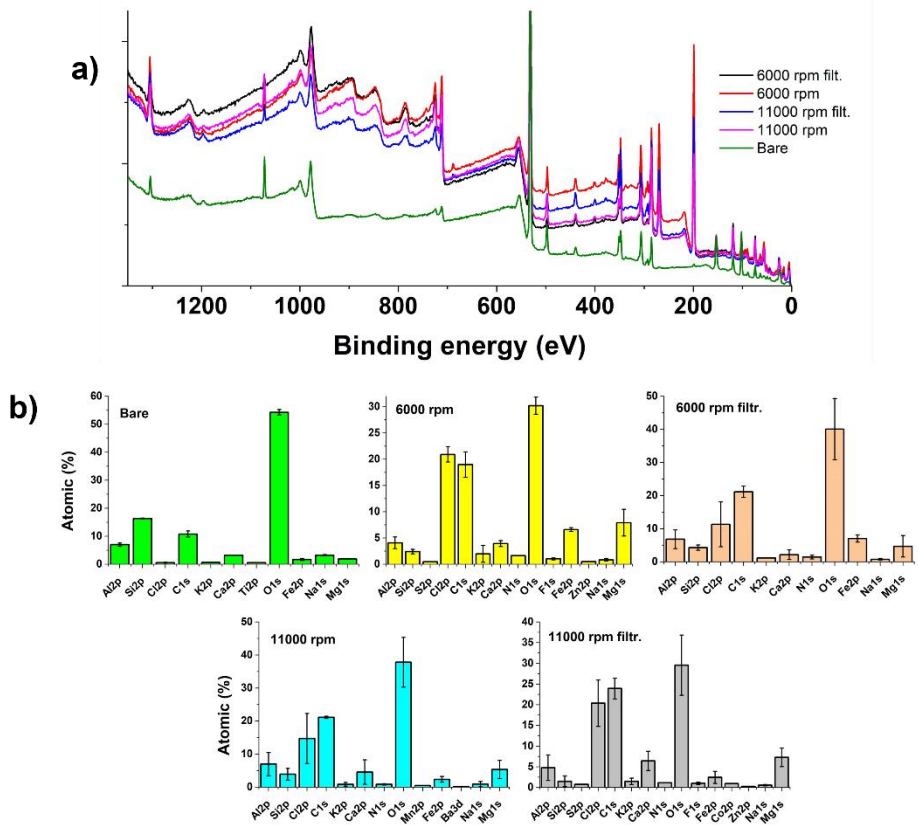

Fig. 73 a) Overlay of XPS survey spectra for LExA samples and bare lava; b) Quantitative XPS determination of LExA and bare lava samples

Three survey spectra per sample allowed statistics on quantitative XPS that are shown in Fig. 73b. As the surveys were not different in peak positions but only in the atomic percentages, it was chosen one representative for the exfoliated (11000 rpm filtered) to plot vs. bare lava for qualitative and quantitative determination (Fig. 74).

The trend of surveys is confirmed by the high-resolution spectra overlay reported in Fig. 75. LExA samples were not subjected to peak shift between them, some are shifted compared to bare lava, but the shape, of course, is different. HR-XPS spectra fitting allowed to show different contributions between bare lava and 11000 rpm filtered (reference for the LExA samples). In Table 15 are reported B.E., attribution, and relative atomic percentage of deconvoluted peaks for both samples. Fitting for Fe2p region is taken from [302]. In Fig. 76 are reported the deconvoluted spectra graphs.

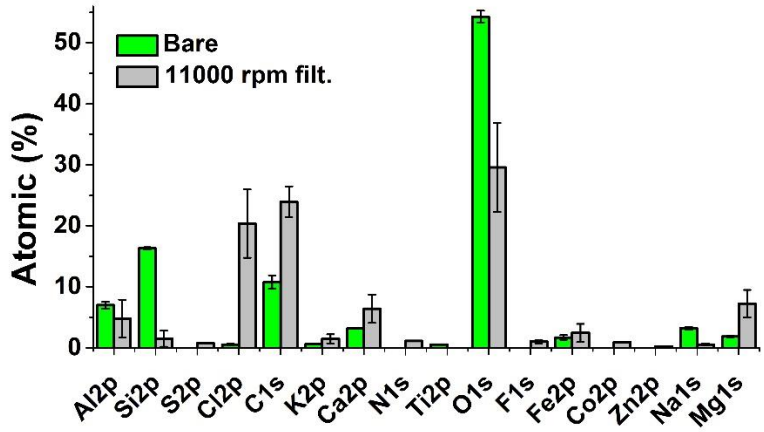

Fig. 74 Quantitative XPS on 11000 rpm filtered and bare lava as the reference

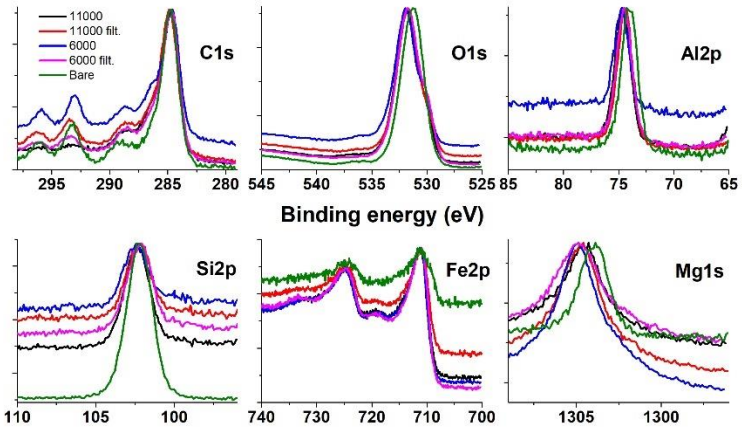

Fig. 75 Overlay of HR-XPS spectra of LExA and bare lava samples

ELEMENT	11000 RPM FILTERED			BARE LAVA		
	PEAK B.E.	ATTRIBUTION	RELATIVE ATOMIC %	PEAK B.E.	ATTRIBUTION	RELATIVE ATOMIC %
Al2p	74.41	Al_2O_3, Al(OH)x	100	74.02	Al_2O_3	100
Si2p	100.19	Si	8.96	101.44	Silicate	22.47
	102.01	Silicate	74.54	102.10	Silicate	17.03
	102.97	Silicate	16.50	102.72	Silicate	60.50
C1s	284.57	C-C, C-H	51.12	284.50	C-C, C-H	64.45
	285.19	C-OH, C-O-C	20.71	285.25	C-OH, C-O-C	10.78
	286.37	C=O	12.07	286.33	C=O	11.34
	287.48	O-C=O	8.51	287.72	O-C=O	5.69
	288.66	Carbonate	7.59	289.13	Carbonate	7.73
O1s	529.89	FeOx	14.67	530.49	FeOx	17.93
	531.32	AlOx, Carbonate	42.92	531.34	AlOx, Carbonate	51.53
	532.24	Silicate	36.45	532.41	Silicate	4.69
	533.51	Water	5.96			
Fe2p	709.02	Pre-peak	1.30	708.55	Pre-peak	2.62
	710.20	Fe2p 3/2	9.24	709.28	Fe2p 3/2	6.98
	711.15		15.48	710.32		9.68
	712.07		17.60	711.51		18.44
	713.16		7.79	713.09		13.51
	714.44	Surface peak	6.12	715.03	Surface peak	5.78
	718.53	Fe2p 3/2 satellite	11.39	171.94	Fe2p 3/2 satellite	7.73
	723.83	Fe2p 1/2	13.60	724.47	Fe2p 1/2	35.25
	725.93		17.49			
Mg1s	1302.60	Mg	21.91	1303.15	MgOx	46.63
	1304.47	MgOx	52.28	1303.86	MgOx	39.04
	1305.53	MgOx, $MgCO_3$	13.23	1304.50	$MgCO_3$	14.33
	1306.86	$MgCO_3$	12.57			

Table 15 XPS peaks chart for 11000 rpm filtered and bare lava samples

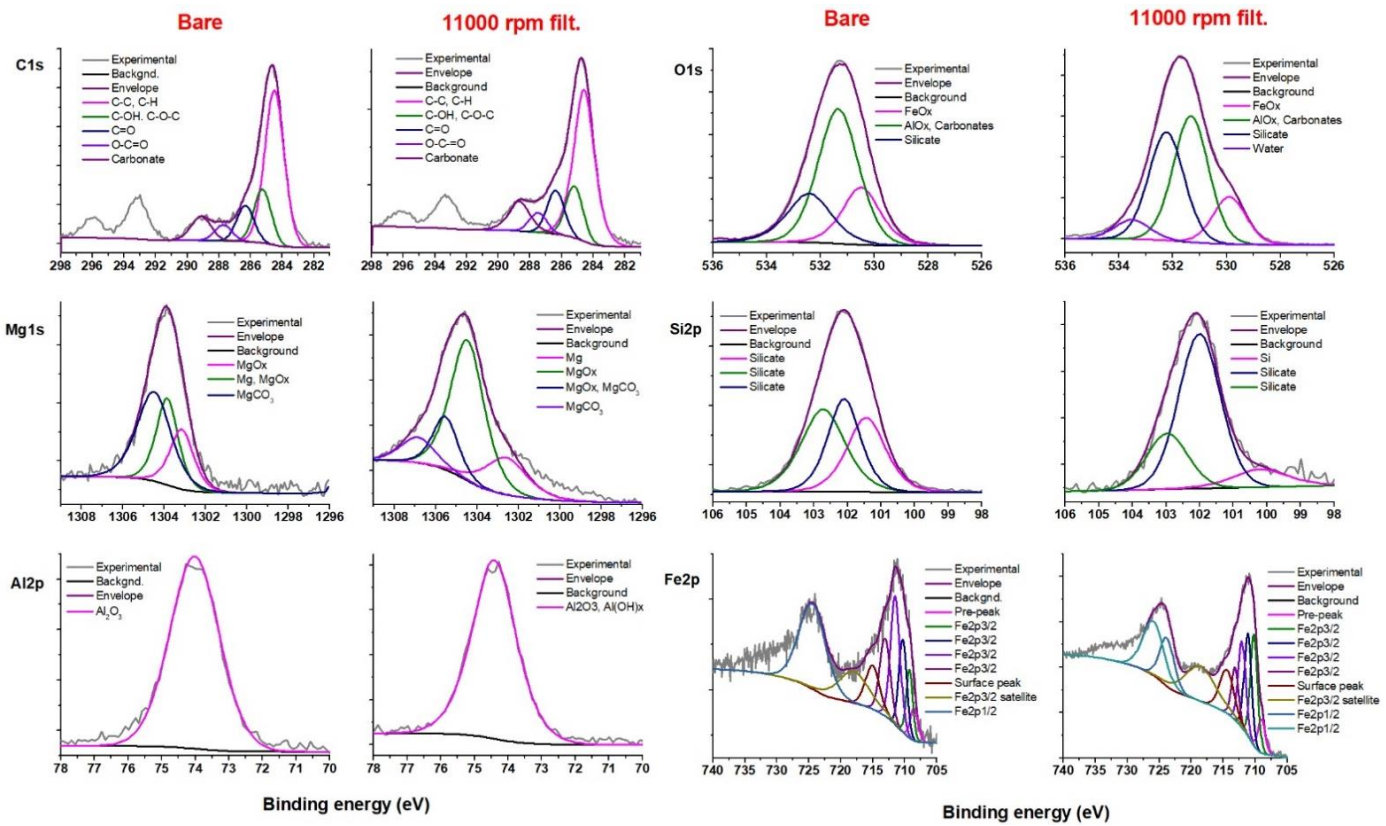

Fig. 76 HR-XPS spectra of 11000 rpm filtered and bare lava sample

10.3.3.6 XRD characterization

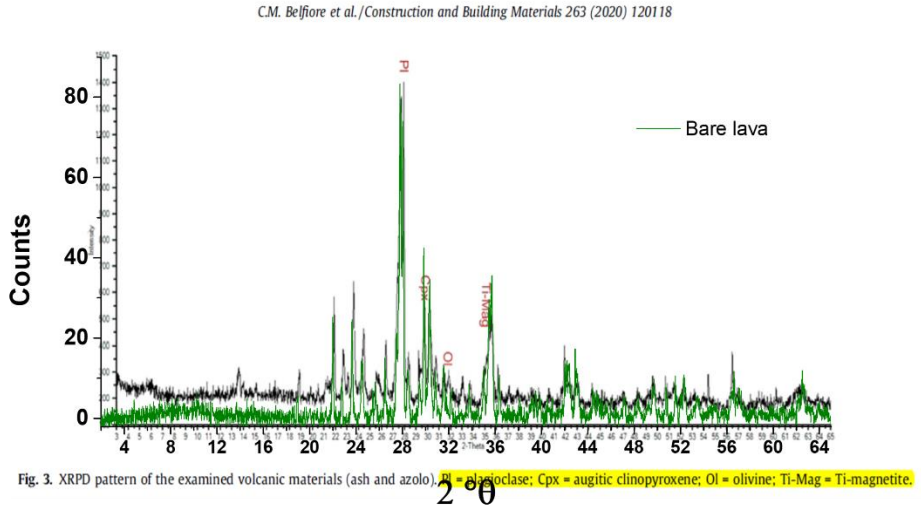

Fig. 77 XRD pattern of bare lava "lapilli" powder (green line) overlayed with literature pattern of volcanic ashes and azolo [303] (black line) reproduced with permission from Elsevier.

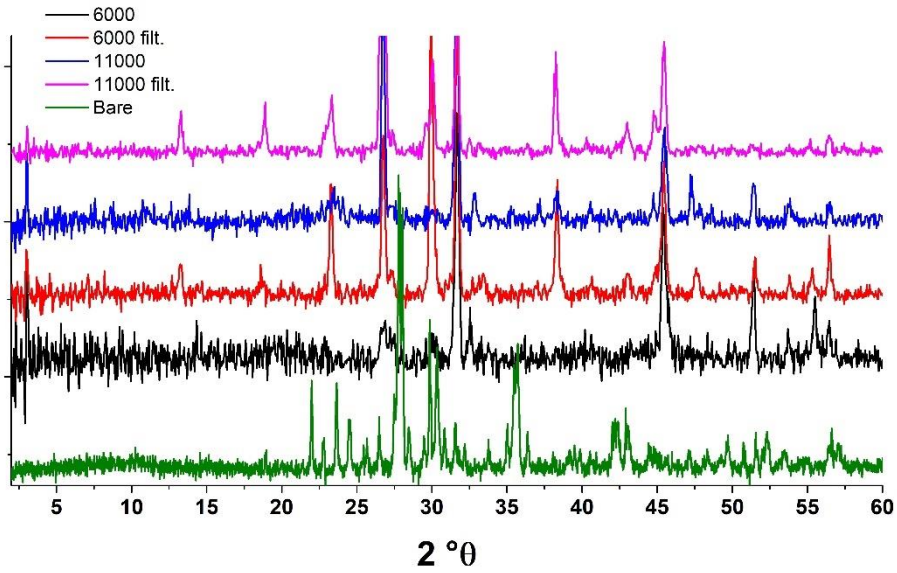

Fig. 78 XRD pattern of LExA samples compared to bare lava

X-Ray powder diffraction pattern of bare lava (lapilli powder) is comparable to one of Mount Etna volcanic ashes and azolo ("a material produced by artificial crashing of trachybalsaltic lava and commonly

employed in the Etnean area as aggregate fraction in the production of building materials such as ceramics and mortars") found in the paper of Belfiore et al [303]. The authors attributed material composition mainly to glass with a low content of crystalline phases given by plagioclaste, augitic clinopyroxene, olivine and Ti-magnetite and only subordinally tachylyte. This minero-petrographic characterization was confirmed by plagioclaste, augitic clinopyroxene, olivine and Ti-magnetite phases individuated in the XRD pattern that is shown in Fig. 77. In that figure is overlayed the experimental pattern acquired from lapilli powder with the literature spectrum. The bare lava XRD pattern is not comparable with LExA samples patterns in Fig. 78, many peaks in fact are missing or shifted. For example, peaks at 2θ = 22°, 26.49°, 35.66°, and 42.15° are not present in the patterns of exfoliated samples, and peaks at 2θ = 23.66°, 27.78°, and 39.53° are shifted. It is also possible to comment that background noise decreases and the sharpness of the peaks increase with the centrifugation speed. The clearest pattern in fact is from 11000 rpm centrifuged and 0.22 μm filtered sample, probably because of the greater homogeneity of the sample.

10.3.3.7 STEM imaging

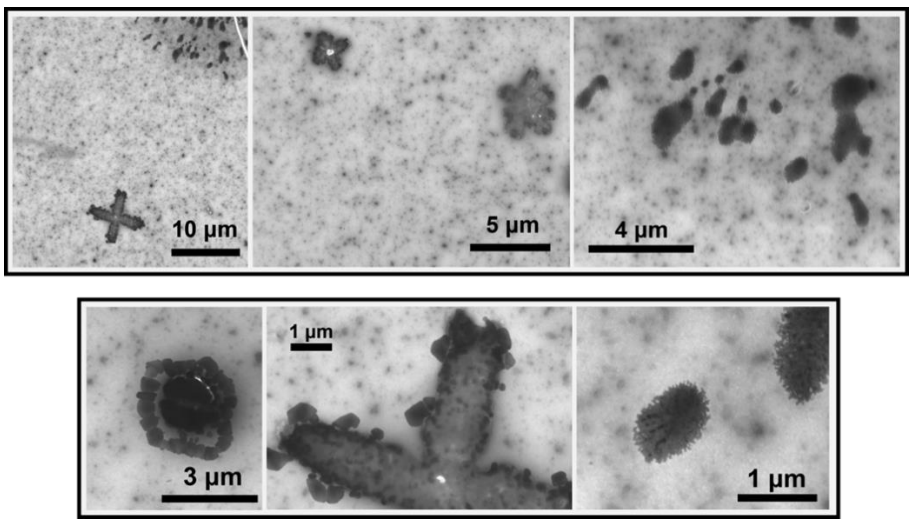

Fig. 79 STEM images on LExA 6000 rpm sample

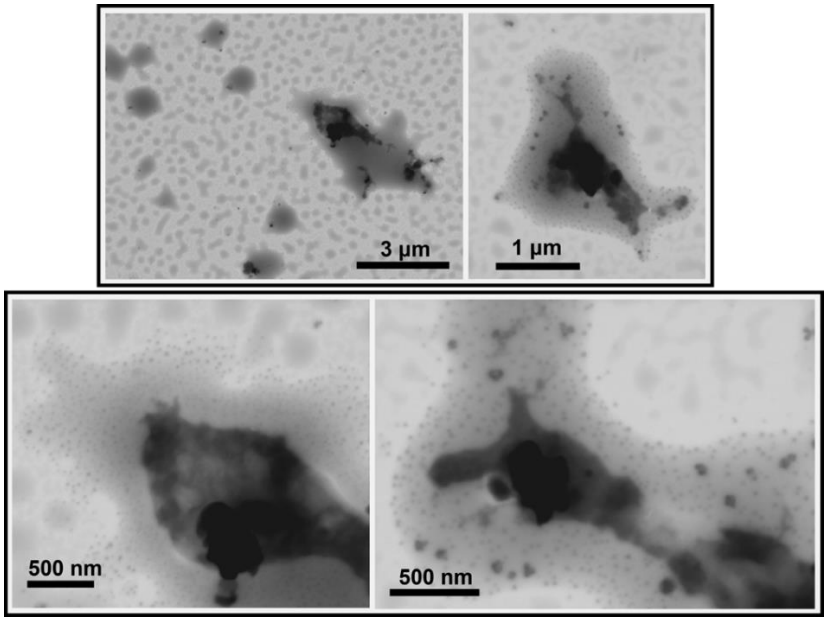

Fig. 80 STEM images on LExA 6000 rpm filtered sample

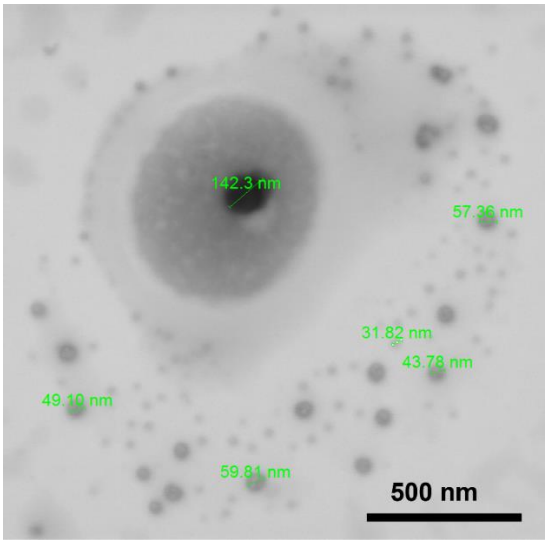

Fig. 81 STEM image with some particle's diameters on LExA 6000 rpm filtered sample

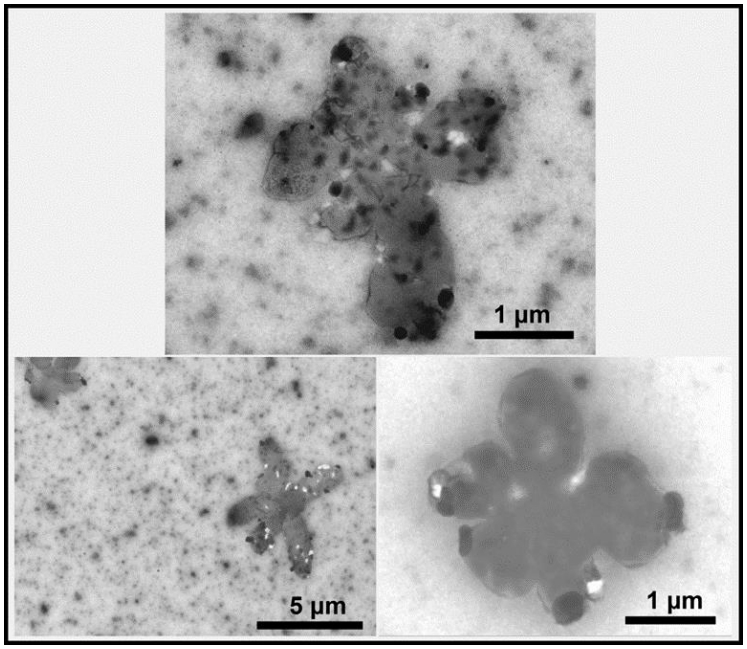

Fig. 82 STEM images on LExA 11000 rpm sample

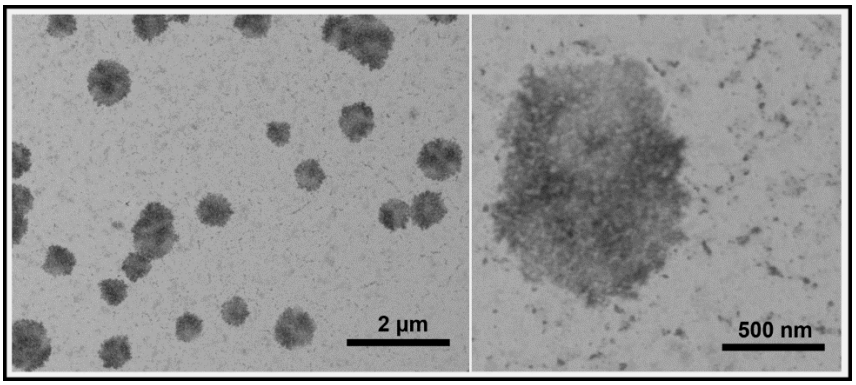

Fig. 83 STEM images on 11000 rpm filtered sample

In Fig. 84 are reported STEM/EDS characterization of the 11000 rpm filtered sample. Composition is heterogeneous, at least 3 different types of nanoparticles were identified: a large amount of indefinite shape ≤ 100-150 nm particles, 500-1000 nm spherical and porous particles and other bigger and irregular structures. Nanostructures are constituted by Silicon (~ 70 %), Carbon (~ 10-20 %), Oxygen (~ 7-9 %) and Aluminium (~ 3-5 %). Chlorine (~ 3-5 %) is present only in the spherical and porous (~ 500-1000 nm) particles.

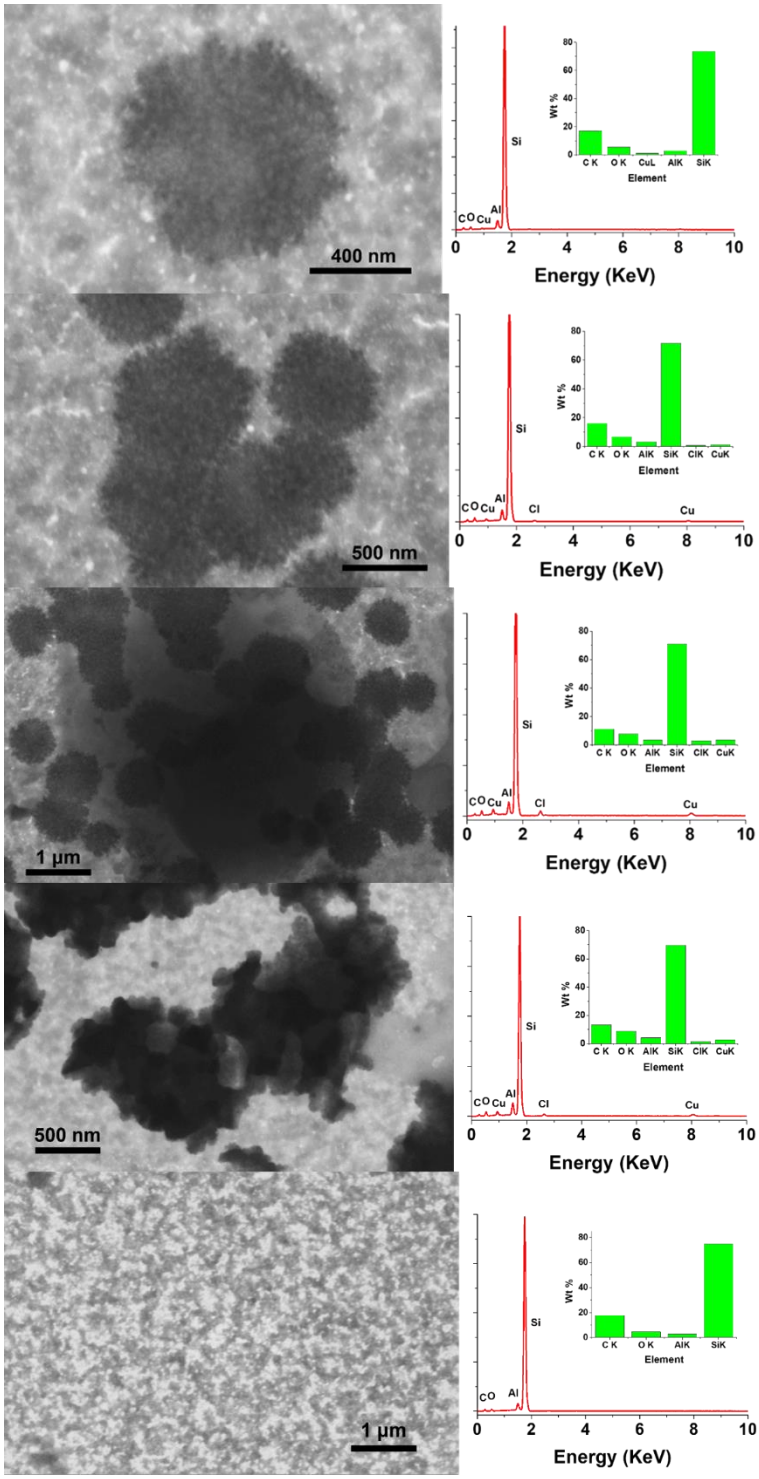

Fig. 84 STEM/EDS characterization on LExA 11000 rpm filtered sample

10.3.4 Surfactant-assisted liquid phase exfoliation

As reported in the material preparation section (vide 2.2.3.2), surfactant-assisted liquid phase exfoliation of lapilli powder was performed with CTAB as surfactant ("LExC") and using both thermal (namely "reflux") and ultrasonication (namely "UW") procedures. Products from both procedures were a "coarse" and a "fine" fraction. Fine fractions were centrifuged and filtered to sort only nanometric scale particles, the procedure was the same for LExA samples. The samples list is reported below.

- LExC reflux coarse
- LExC reflux fine
- LExC reflux fine 6000 rpm
- LExC reflux fine 6000 rpm filtered 0.22 μm

- LExC reflux fine 11000 rpm
- LExC reflux fine 11000 rpm filtered 0.22 μm
- LExC UW coarse
- LExC UW fine
- LExC UW fine 6000 rpm
- LExC UW fine 6000 rpm filtered 0.22 μm

- LExC UW fine 11000 rpm
- LExC UW fine 11000 rpm filtered 0.22 μm

10.3.4.1 UV/Vis characterization

In Fig. 85 there are shown UV/Vis absorption spectra of fine and coarse fractions from both the exfoliation procedures. In ultrapure water particles are in suspension, moreover, there is no clear UV absorption.

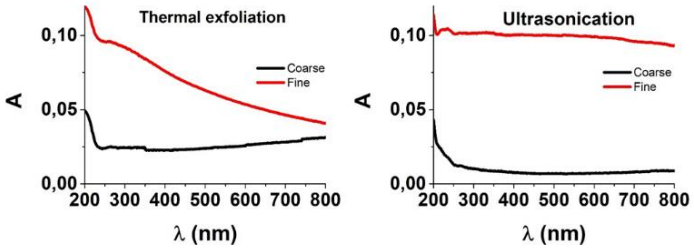

Fig. 85 UV/Vis absorption spectra of fine and coarse fraction of lava CTAB-assisted liquid phase exfoliation. Thermal exfoliation vs. ultrasonication

In Fig. 86 are reported absorption spectra of centrifuged and filtered samples. In this case, although they are diluted, it can be seen the presence of a colloidal dispersion because of the small particles' light scattering visible from the asymptotic absorption trend to UV region. Centrifuged only and centrifuged and filtered samples have two to two similar spectra, the same is for samples coming from the different exfoliation procedures (thermal and ultrasonication). Samples are not luminescent.

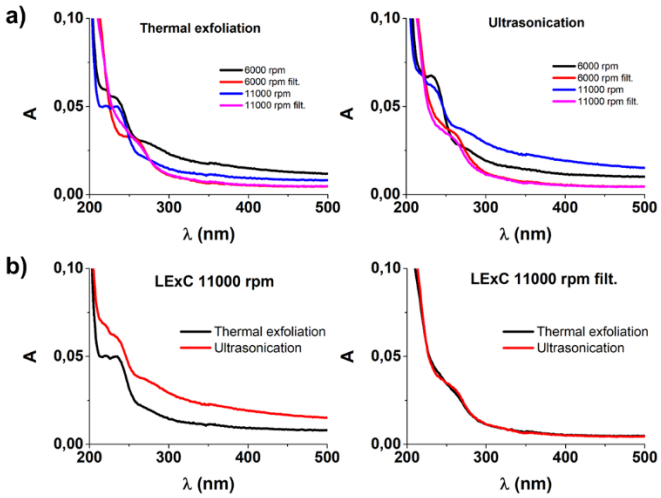

Fig. 86 UV/Vis absorption spectra of centrifuged and filtered samples coming from fine fractions of LExC. a) Thermal exfoliation vs. ultrasonication of all LExC samples; b) Comparison of LExC 11000 rpm sample and 11000 rpm filtered absorption spectra coming from thermal and ultrasonication procedures

10.3.4.2 FT-IR characterization

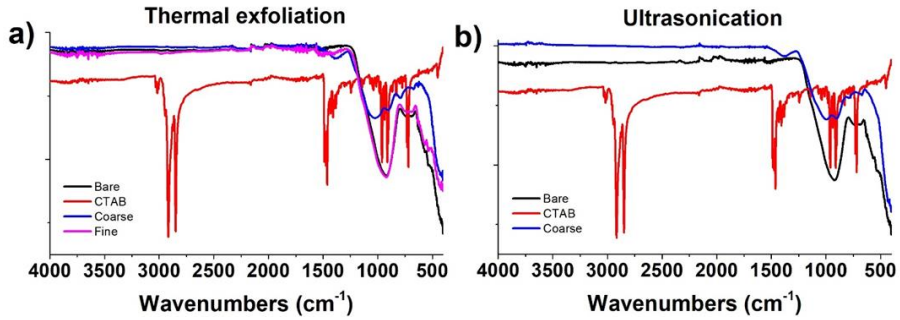

Fig. 87 FT-IR spectra of LExC samples: a) LExC from thermal exfoliation; b) LExC from ultrasonication.

Looking at the FT-IR spectra in Fig. 87 of coarse and fine fractions of thermal (Fig. 87a) and ultrasonication (Fig. 87b) exfoliation there can't be seen significative differences between bare lava (lapilli powder starting material) and the LExC samples.

10.3.4.3 STEM/EDS characterization

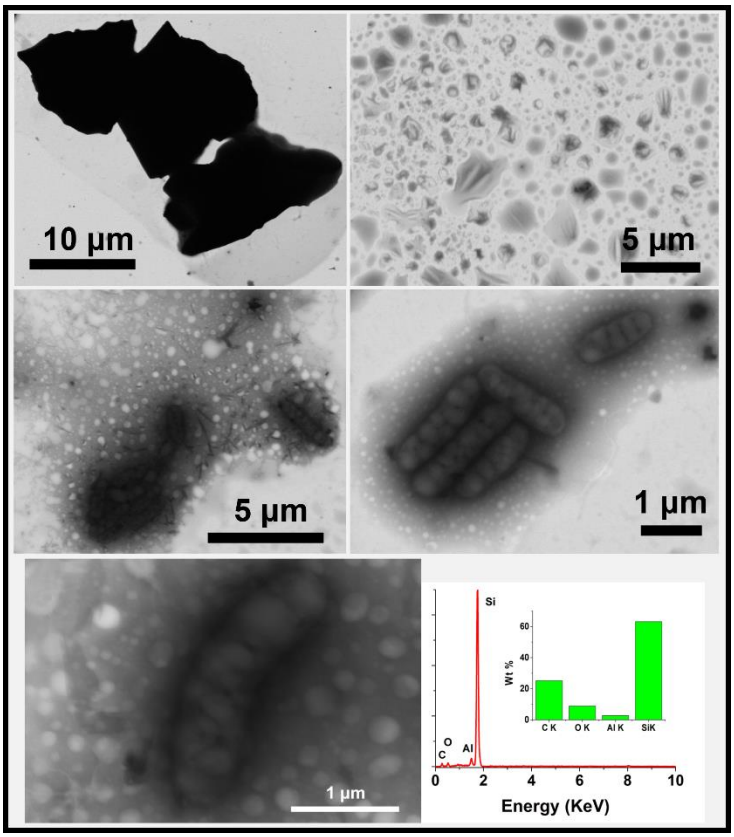

Fig. 88 STEM/EDS characterization on coarse fraction (Thermal)

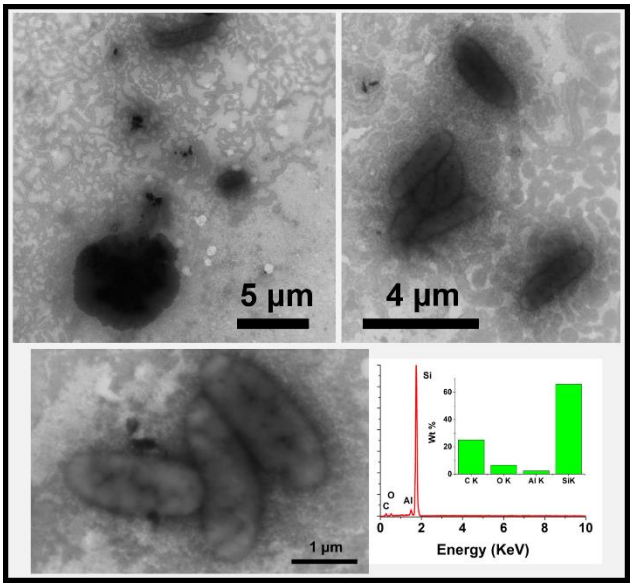

Fig. 89 STEM/EDS characterization on LExC 6000 rpm (Thermal)

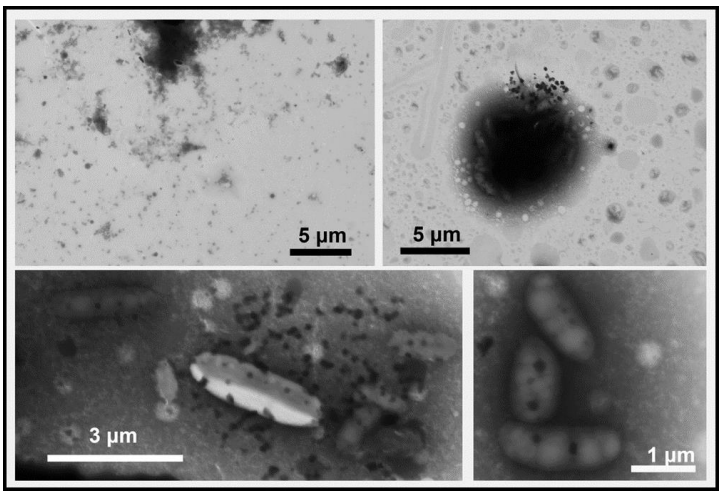

Fig. 90 STEM images on LExC 11000 rpm (Thermal)

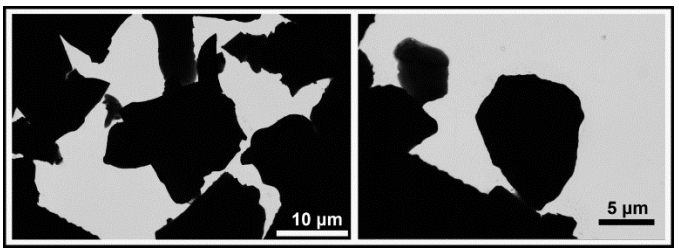

Fig. 91 STEM images on LExC coarse fraction (Ultrasonication)

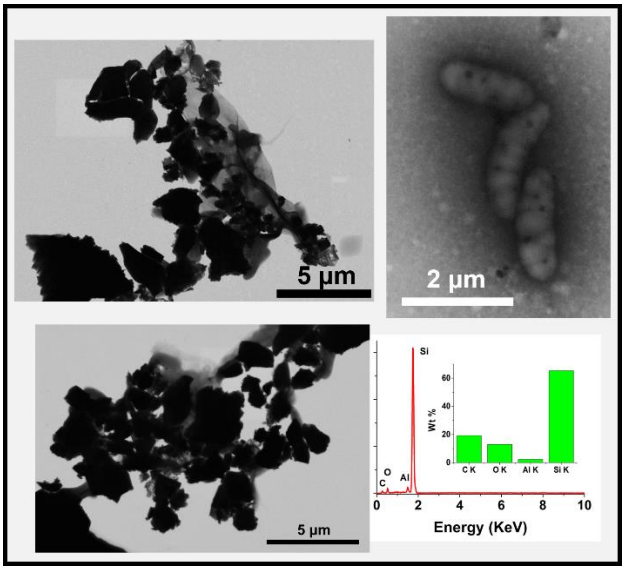

Fig. 92 STEM/EDS characterization on LExC 6000 rpm (Ultrasonication)

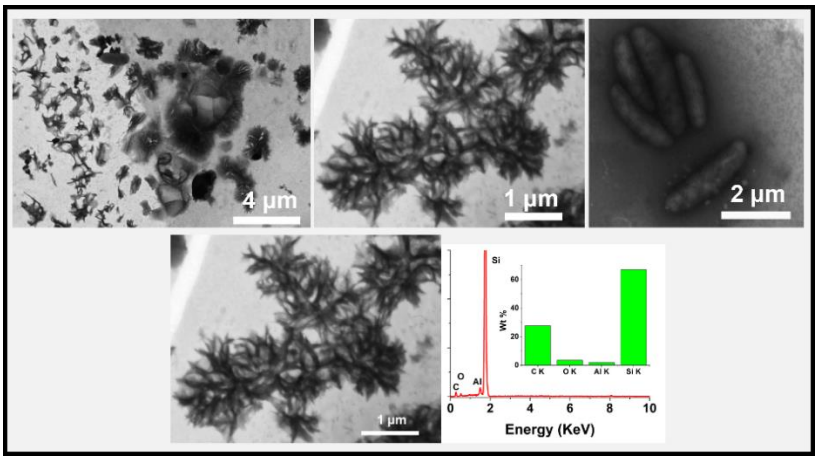

Fig. 93 STEM/EDS characterization on LExC 11000 rpm (Ultrasonication)

10.3.5 Conclusions

Heterogeneous types of silicon oxides nanoparticles were produced via liquid phase exfoliation in acidic medium (LExA) of lava "lapilli" powder; according to the data, in these nanoparticles are embedded metals such as Aluminium, Iron, Magnesium, Calcium and non-metals like Chlorine and Carbon. Considering nanoparticle size, different populations were recognized: the lightest fraction ≤ 100-150 nm with indefinite or approximatively spherical shape, an intermediate fraction between 500 and 1000 nm

constituted by spherical and porous particles, and a heterogeneous group of heavier and irregular structures. The latter group is reasonably constituted by the non-exfoliated/unreacted fraction which have not been separated by centrifugation. Size separation attempted by centrifugation and filtration per steps (6000 rpm, 11000 rpm and 0.22 μm filtration) was effective anyway as it can be seen by STEM imaging and progressive signal definition of the XRD pattern. Investigations performed with UV/Vis and fluorescence spectroscopies, FT-IR spectroscopy and XPS revealed nearly identity between the different centrifugation fractions, but a substantial difference with the starting non-treated material. Liquid exfoliation treatment produced nanoparticles with an identifiable and characteristic spectral pattern. Finally, regardless of the size-related heterogeneity, samples according to four-point probe measurements were conductive. They had a work function, estimated by UPS, of approximately 5.3 eV and an optical band gap, estimated by Tauc plot, of ~ 3.2 eV.

Liquid exfoliated samples produced with the surfactant-assisted method via ultrasonication, and thermal procedures (LExC) were strongly different from LExA. They were difficult to disperse in water and the general appearance was similar to the unreacted material. FT-IR spectra of starting material and LExC samples were, in fact, the same. From a preliminary interpretation, STEM imaging revealed no differences between LExC UW and LExC reflux. It was difficult to find completely covered areas on the TEM grid, probably due to the low dispersibility in water. A lot of aggregates of big particles (5-10 μm) were found, the exact shape of which could not be assessed with STEM, because of the high charging under the electron beam. In every centrifuged sample unusual rod-shaped particles were found, with a length between 1 and 4 μm. Despite issues arisen with the electron beam focusing (maybe due to lower electron density compared to the other particles) the elemental composition was the same as the other structures (C, Al, O, Si). These probably could have been produced thanks to the templating power of CTAB towards tubular/wormlike structures [304, 305], but those are in general one order of magnitude smaller than these.

11. INSTRUMENTS

11.1 Optical spectroscopy

UV/Vis absorption and luminescence spectra were recorded in air-equilibrated solutions or dispersions contained in 1 cm quartz cells.

The UV/Vis spectrophotometers were: Jasco V-560 UV/Vis, Jasco V-570 and V-670 UV/Vis-NIR (Jasco Co., Tokyo, Japan).

Fluorescence steady-state spectrofluorometers were: Agilent Cary Eclipse (Agilent Technologies Inc., Santa Clara, CA – USA), Horiba Jobin-Yvon FluoroMax-P and FluoroLog-2 (mod. F-111) (Horiba Ltd., Kyoto, Japan).

Luminescence lifetimes were determined on an Edinburgh OB900 time-correlated single-photon-counting (Edinburgh Instruments Ltd., Livingston, UK) spectrometer equipped with Hamamatsu PL2 408 nm laser diode (pulse width: 59 ps) (Hamamatsu Photonics K.K., Hamamatsu city, Japan).

- Chapt. 5.2: Jasco V-560, Horiba Jobin-Yvon FluoroMax-P
- Chapt. 6: Jasco V-560, Horiba Jobin-Yvon Spex Fluorolog-2
- Chapt. 7: Jasco V-560, Horiba Jobin-Yvon FluoroMax-P
- Chapt. 8: Jasco V-560, Jasco V-570, Horiba Jobin-Yvon FluoroMax-P, Edinburg OB900.
- Chapt. 9: Jasco V-560
- Chapt. 10: Jasco V-570 UV, Agilent Cary Eclipse.

11.2 Fourier Transform InfraRed spectroscopy (FT-IR)

Fourier Transform Infrared (FT-IR) spectra in Attenuated Total Reflectance (ATR) were acquired with i) Thermo Scientific Nicolet iS50 spectrometer (Thermo Fisher Scientific Inc., Waltham, MA – USA) in the spectral range between 4000 and 400 cm^{-1} (wavenumbers), with a resolution of 4 cm^{-1} and 64 scans per sample and ii) Perkin-Elmer Spectrum Two spectrometer with a diamond ATR single reflection accessory. Transmission FT-IR measurements on silicon-deposited samples were obtained using a

Jasco FTIR 4600LE spectrometer (Jasco Co., Tokyo, Japan) in the spectral range of 560-4000 cm^{-1}, 4 cm^{-1} of resolution and 64 scans per sample.

- Chapt. 5.1: Perkin-Elmer Spectrum Two
- Chapt. 5.2: Jasco 4600LE, Perkin-Elmer Spectrum Two
- Chapt. 6: Jasco 4600LE
- Chapt. 8: Jasco 4600LE, Nicolet iS50
- Chapt. 10: Nicolet iS50

11.3 Raman spectroscopy

Raman spectra were acquired with a Horiba Jobin-Yvon (Horiba Ltd., Kyoto, Japan) LabRAM HR800 micro-Raman spectrometer equipped with 1800 lines/mm grating and a Peltier cooled CCD detector (Horiba, Synapse model). A 3 mW 514.5 nm Ar^+ laser (Spectra-Physics 2060, Newport Corp., CA – USA) was focused onto 1 μm^2 of the samples by a 100X (N.A. = 0.9) objective (Olympus BX41 microscope - Olympus Co., Tokyo, Japan).

Raman measurements were carried out using also a Horiba Raman XploRA coupled with Olympus BX 41 with a laser excitation source at 532 nm (power 0.125 mW cm^{-2}).

- Chapt. 5.1: Horiba XploRA
- Chapt. 5.2: Horiba LabRAM
- Chapt. 8: Horiba LabRAM

11.4 X-Ray Photoelectron Spectroscopy (XPS)

X-Ray Photoelectron Spectroscopy (XPS) was performed on sample dispersions drop-casted on Si/SiO2 slides, by means of a Thermo Scientific K-Alpha X-Ray photoelectron spectrometer (Thermo Fisher Scientific Inc., Waltham, MA – USA) equipped with a monochromatic Al X-Ray source (1.4866 KeV) with 400 μm spot size. The XPS binding energy (BE) scale was calibrated on the C1s peak of adventitious carbon at 284.8 eV.

A PHI 5600 ESCA-Auger spectrometer (Physical Electronics Inc., Chanhassen, MN, USA), equipped with a monochromatic Al-Kα X-ray source, was also used. The XPS binding energy (BE) scale was calibrated on the C 1s peak of adventitious carbon at 285.0 eV.

- Chapt. 5.2: PHI 5600
- Chapt. 6: PHI 5600
- Chapt. 8: PHI 5600
- Chapt. 10: Thermo Scientific K-alpha

11.5 X-Ray Powder Diffraction (XRD)

X-Ray powder diffraction patterns were acquired on thin films drop-casted over Si/SiO2 wafers. There were collected in air and at room temperature with a Bruker D8 Advance diffractometer (Bruker Co., MA - USA) with Cu Kα radiation (λ = 1.54184 Å) and a step size of 0.05 ° at 40 KV and 40 mA in the range of 2θ degrees from 2 ° to 60 °.

- Chapt. 10

11.6 Ultraviolet Photoelectron Spectroscopy (UPS) – Work function

Materials work functions were estimated with a Riken Keiki AC-2 Ultraviolet Photoelectron Spectroscopy (UPS) instrument (Riken Keiki Co. Ltd., Tokyo, Japan) in air and in atmospheric pressure, analysing samples either as powders or as films drop-casted on Si/SiO2 wafers.

- Chapt. 10

11.7 Dynamic Light Scattering (DLS) and Zeta-potential

Nanoparticles hydrodynamic radius and ζ (Zeta) potential were estimated using the dynamic light scattering (DLS) technique with a Malvern Zetasizer Nano ZS90 instrument (Malvern Panalytical Ltd., Malvern, UK) equipped with a 4 mW 632.8 nm He-Ne laser. In order to have statistics each measurement was executed three times collecting mean and standard deviation values.

- Chapt. 5.1
- Chapt. 5.2
- Chapt. 6
- Chapt. 8
- Chapt. 10

11.8 Material resistivity

Film thickness, on samples spray-coated on Si/SiO2 wafers or glass substrates, was measured with a KLA-Tencor Alpha-Step IQ profilometer (KLA-Tencor Co., CA – USA).

Sheet resistance of the films was measured with a Jandel RM3000+ four-point probe test unit (Jandel Eng. Ltd., Leighton Buzzard, UK). Materials resistivities were then calculated by multiplying film thickness by sheet resistance.

- Chapt. 10

11.9 Thermogravimetric and Differential Scanning Calorimetry analyses (TGA/DSC)

Thermogravimetric analysis and Differential Scanning Calorimetry (TGA/DSC) were performed in a Mettler-Toledo TGA/DSC 2 STARe instrument (Mettler Toledo LLC, Columbus, OH – USA). Measurements were executed on Carbon dots powder (from 1 mg to 2.5 mg) both in synthetic air (Air Zero X50S, Air products, Saint Quentin Fallavier, France, from 20.69 % to 21.11 % in Oxygen content) and in pure Nitrogen environments, r starting from 25 °C to 600 °C (5 °C/min).

- Chapt. 5.2

11.10 Microscopy

11.10.1 Scanning Electron Microscopy (SEM) and Scanning Transmission Electron Microscopy (STEM)

Scanning Electron Microscopy (SEM) and Scanning-Transmission Electron Microscopy (STEM) images were obtained with a FEI Quanta FEG 250 instrument (FEI Co., Hillsboro, OR – USA) equipped with a STEM detector and an EDAX AMETEK Octane Elect EDS detector (AMETEK Inc., Berwyn, PA – USA) for Energy Dispersive Spectroscopy (EDS). A SEM EVO MA 10 (Carl Zeiss AG, Oberkochen, Germany) operated at 20 KeV exploiting the Secondary Electron signal (SE mode) in which samples were prior sputter-coated with gold was also used. A ZEISS VP 55 field emission gun scanning electron microscope (FEG-SEM) was also used.

Samples for STEM were deposited on Formvar/Carbon film 400 mesh Copper grids (Agar Scientific Ltd., Stansted, UK).

- Chapt. 8: ZEISS VP55
- Chapt. 9: ZEISS EVO MA 10
- Chapt. 10: FEI Quanta FEG 250

11.10.2 Transmission Electron Microscopy (TEM)

Transmission Electron Microscopy (TEM) analysis was performed in bright field conventional parallel mode with ATEM JEOL JEM 2010 instrument equipped with a 30 mm^2 window energy dispersive X-ray (EDX) spectrometer (JEOL Ltd., Tokyo, Japan).

A JEOL JEM 1400-Plus microscope operated at an accelerating voltage of 120 kV, equipped with GATAN US1000 CCD Camera was also used. Samples were prepared by drop casting of CDs solution on Lacey carbon film coated copper TEM grids.

- Chapt. 5.1: JEOL JEM 1400-Plus
- Chapt. 6: JEOL JEM 2010
- Chapt. 8: JEOL JEM 2010
- Chapt. 9: JEOL JEM 2010

11.10.3 Atomic Force Microscopy (AFM)

AFM images and profiles were acquired by multimode V AFM from Bruker microscope on drop casted diluted CDs solution on silicon substrates.

- Chapt. 5.1: Bruker V AFM

11.10.4 Optical microscopy

An Olympus BX51 fluorescence microscope (Olympus Co., Tokyo, Japan) and a Zeiss Axioscope 5 microscope (Carl Zeiss AG, Oberkochen, Germany) were used for conventional optical microscopy imaging.

- Chapt. 10

11.11 Cyclic Voltammetry (CV)

Cyclic voltammetry (CV) was carried to estimate the HOMO and LUMO energy levels of the CDs and the band gap. The electrochemical measurement was performed by the electrochemical workstation Autolab MSTAT204 Potentiostat/Galvanostat using a three-electrode electrochemical cell with a glassy carbon (3 mm Dia.) working electrode, an Ag/AgCl reference electrode, and a platinum counter electrode (Pt wire) in a 20 mL acetonitrile solution containing 0.1 M tetrabutylammonium hexafluorophosphate ($TBAPF_6$) as the supporting electrolyte and 1 mL of 1 mg/mL CDs solution. Cyclic voltammetry of the sample was run at a scan rate of 50 mV/s at room temperature.

- Chapt. 5.1

12. REFERENCES

1. Giner-Casares, J. J.; Henriksen-Lacey, M.; Coronado-Puchau, M.; Liz-Marzán, L. M., Inorganic nanoparticles for biomedicine: where materials scientists meet medical research. *Materials Today* **2016,** *19* (1), 19-28.
2. Ma, X.; Zhao, Y.; Liang, X.-J., Theranostic Nanoparticles Engineered for Clinic and Pharmaceutics. *Accounts of Chemical Research* **2011,** *44* (10), 1114-1122.
3. Noone, K. M.; Ginger, D. S., Doping for Speed: Colloidal Nanoparticles for Thin-Film Optoelectronics. *ACS Nano* **2009,** *3* (2), 261-265.
4. Araújo, R.; Castro, A. C. M.; Fiúza, A., The Use of Nanoparticles in Soil and Water Remediation Processes. *Materials Today: Proceedings* **2015,** *2* (1), 315-320.
5. Zhang, Q.; Uchaker, E.; Candelaria, S. L.; Cao, G., Nanomaterials for energy conversion and storage. *Chemical Society Reviews* **2013,** *42* (7), 3127-3171.
6. Burda, C.; Chen, X.; Narayanan, R.; El-Sayed, M. A., Chemistry and Properties of Nanocrystals of Different Shapes. *Chemical Reviews* **2005,** *105* (4), 1025-1102.
7. Jain, P. K.; El-Sayed, I. H.; El-Sayed, M. A., Au nanoparticles target cancer. *Nano Today* **2007,** *2* (1), 18-29.
8. Sharma, P.; Brown, S.; Walter, G.; Santra, S.; Moudgil, B., Nanoparticles for bioimaging. *Advances in Colloid and Interface Science* **2006,** *123-126*, 471-485.
9. Couvreur, P., Nanoparticles in drug delivery: Past, present and future. *Advanced Drug Delivery Reviews* **2013,** *65* (1), 21-23.
10. Lucky, S. S.; Soo, K. C.; Zhang, Y., Nanoparticles in Photodynamic Therapy. *Chemical Reviews* **2015,** *115* (4), 1990-2042.
11. Jaque, D.; Martínez Maestro, L.; del Rosal, B.; Haro-Gonzalez, P.; Benayas, A.; Plaza, J. L.; Martín Rodríguez, E.; García Solé, J., Nanoparticles for photothermal therapies. *Nanoscale* **2014,** *6* (16), 9494-9530.
12. Calabrese, G.; Petralia, S.; Franco, D.; Nocito, G.; Fabbi, C.; Forte, L.; Guglielmino, S.; Squarzoni, S.; Traina, F.; Conoci, S., A new Ag-nanostructured hydroxyapatite porous scaffold: Antibacterial effect and cytotoxicity study. *Materials Science and Engineering: C* **2021,** *118*, 111394.
13. Yadid, M.; Feiner, R.; Dvir, T., Gold Nanoparticle-Integrated Scaffolds for Tissue Engineering and Regenerative Medicine. *Nano Letters* **2019,** *19* (4), 2198-2206.
14. Ciofani, G., *Smart Nanoparticles for Biomedicine*. Elsevier: 2018.
15. Hong, G.; Diao, S.; Antaris, A. L.; Dai, H., Carbon Nanomaterials for Biological Imaging and Nanomedicinal Therapy. *Chemical Reviews* **2015,** *115* (19), 10816-10906.
16. Heiligtag, F. J.; Niederberger, M., The fascinating world of nanoparticle research. *Materials Today* **2013,** *16* (7), 262-271.
17. Asha, A. B.; Narain, R., Chapter 15 - Nanomaterials properties. In *Polymer Science and Nanotechnology*, Narain, R., Ed. Elsevier: 2020; pp 343-359.
18. Nunes, D.; Pimentel, A.; Santos, L.; Barquinha, P.; Pereira, L.; Fortunato, E.; Martins, R., 1 - Introduction. In *Metal Oxide Nanostructures*, Nunes, D.; Pimentel, A.; Santos, L.; Barquinha, P.; Pereira, L.; Fortunato, E.; Martins, R., Eds. Elsevier: 2019; pp 1-19.
19. Roduner, E., Size matters: why nanomaterials are different. *Chemical Society Reviews* **2006,** *35* (7), 583-592.
20. Rossetti, R.; Ellison, J. L.; Gibson, J. M.; Brus, L. E., Size effects in the excited electronic states of small colloidal CdS crystallites. *The Journal of Chemical Physics* **1984,** *80* (9), 4464-4469.
21. Malhotra, B. D.; Ali, M. A., Chapter 1 - Nanomaterials in Biosensors: Fundamentals and Applications. In *Nanomaterials for Biosensors*, Malhotra, B. D.; Ali, M. A., Eds. William Andrew Publishing: 2018; pp 1-74.
22. Hulanicki, A.; Glab, S.; Ingman, F., Chemical sensors: definitions and classification. **1991,** *63* (9), 1247-1250.

23. Ebralidze, I. I.; Laschuk, N. O.; Poisson, J.; Zenkina, O. V., Chapter 1 - Colorimetric Sensors and Sensor Arrays. In *Nanomaterials Design for Sensing Applications*, Zenkina, O. V., Ed. Elsevier: 2019; pp 1-39.
24. Viter, R.; Iatsunskyi, I., Chapter 2 - Metal Oxide Nanostructures in Sensing. In *Nanomaterials Design for Sensing Applications*, Zenkina, O. V., Ed. Elsevier: 2019; pp 41-91.
25. Dahman, Y., Chapter 4 - Nanosensors**By Yaser Dahman, Amira Radwan, Boris Nesic, and Jason Isbister. In *Nanotechnology and Functional Materials for Engineers*, Dahman, Y., Ed. Elsevier: 2017; pp 67-91.
26. Barsan, N.; Weimar, U., Conduction Model of Metal Oxide Gas Sensors. *Journal of Electroceramics* **2001,** *7* (3), 143-167.
27. Anzenbacher, J. P.; Lubal, P.; Buček, P.; Palacios, M. A.; Kozelkova, M. E., A practical approach to optical cross-reactive sensor arrays. *Chemical Society Reviews* **2010,** *39* (10), 3954-3979.
28. Jares-Erijman, E. A.; Jovin, T. M., FRET imaging. *Nature Biotechnology* **2003,** *21* (11), 1387-1395.
29. Roda, A.; Mirasoli, M.; Michelini, E.; Di Fusco, M.; Zangheri, M.; Cevenini, L.; Roda, B.; Simoni, P., Progress in chemical luminescence-based biosensors: A critical review. *Biosensors and Bioelectronics* **2016,** *76*, 164-179.
30. Goode, J. A.; Rushworth, J. V. H.; Millner, P. A., Biosensor Regeneration: A Review of Common Techniques and Outcomes. *Langmuir* **2015,** *31* (23), 6267-6276.
31. Guo, X., Surface plasmon resonance based biosensor technique: A review. *Journal of Biophotonics* **2012,** *5* (7), 483-501.
32. Sharma, A.; Majdinasab, M.; Khan, R.; Li, Z.; Hayat, A.; Marty, J. L., Nanomaterials in fluorescence-based biosensors: Defining key roles. *Nano-Structures & Nano-Objects* **2021,** *27*, 100774.
33. Yüce, M.; Kurt, H., How to make nanobiosensors: surface modification and characterisation of nanomaterials for biosensing applications. *RSC Advances* **2017,** *7* (78), 49386-49403.
34. Ghebreyesus, T. A. Urgent health challenges for the next decade. https://www.who.int/news-room/photo-story/photo-story-detail/urgent-health-challenges-for-the-next-decade?utm_source=STAT+Newsletters&utm_campaign=1931cb646b-MR_COPY_02&utm_medium=email&utm_term=0_8cab1d7961-1931cb646b-150708293.
35. Daily briefing: the 13 biggest threats to global health, according to WHO. https://www.advisory.com/daily-briefing/2020/01/15/who-health-challenges.
36. Tay, C. Y.; Setyawati, M. I.; Xie, J.; Parak, W. J.; Leong, D. T., Back to Basics: Exploiting the Innate Physico-chemical Characteristics of Nanomaterials for Biomedical Applications. *Advanced Functional Materials* **2014,** *24* (38), 5936-5955.
37. Kreyling, W., *Nanomedicine : An ESF-European Medical Councils (EMRC) forword look report 2005*. 2005; p 48.
38. Matsumura, Y.; Maeda, H., A New Concept for Macromolecular Therapeutics in Cancer Chemotherapy: Mechanism of Tumoritropic Accumulation of Proteins and the Antitumor Agent Smancs1. *Cancer Research* **1986,** *46* (12_Part_1), 6387-6392.
39. Wu, J. The Enhanced Permeability and Retention (EPR) Effect: The Significance of the Concept and Methods to Enhance Its Application *Journal of Personalized Medicine* [Online], 2021.
40. Alghamdi, M. A.; Fallica, A. N.; Virzì, N.; Kesharwani, P.; Pittalà, V.; Greish, K. The Promise of Nanotechnology in Personalized Medicine *Journal of Personalized Medicine* [Online], 2022.
41. Khan, H. A.; Sakharkar, M. K.; Nayak, A.; Kishore, U.; Khan, A., 14 - Nanoparticles for biomedical applications: An overview. In *Nanobiomaterials*, Narayan, R., Ed. Woodhead Publishing: 2018; pp 357-384.
42. Aflori, M. Smart Nanomaterials for Biomedical Applications—A Review *Nanomaterials* [Online], 2021.

43. Han, X.; Xu, K.; Taratula, O.; Farsad, K., Applications of nanoparticles in biomedical imaging. *Nanoscale* **2019,** *11* (3), 799-819.
44. Fan, Q.; Cheng, K.; Hu, X.; Ma, X.; Zhang, R.; Yang, M.; Lu, X.; Xing, L.; Huang, W.; Gambhir, S. S.; Cheng, Z., Transferring Biomarker into Molecular Probe: Melanin Nanoparticle as a Naturally Active Platform for Multimodality Imaging. *Journal of the American Chemical Society* **2014,** *136* (43), 15185-15194.
45. Yuan, F.; Li, S.; Fan, Z.; Meng, X.; Fan, L.; Yang, S., Shining carbon dots: Synthesis and biomedical and optoelectronic applications. *Nano Today* **2016,** *11* (5), 565-586.
46. Xia, C.; Zhu, S.; Feng, T.; Yang, M.; Yang, B., Evolution and Synthesis of Carbon Dots: From Carbon Dots to Carbonized Polymer Dots. *Advanced Science* **2019,** *6* (23), 1901316.
47. Đorđević, L.; Arcudi, F.; Cacioppo, M.; Prato, M., A multifunctional chemical toolbox to engineer carbon dots for biomedical and energy applications. *Nature Nanotechnology* **2022,** *17* (2), 112-130.
48. Xu, X.; Ray, R.; Gu, Y.; Ploehn, H. J.; Gearheart, L.; Raker, K.; Scrivens, W. A., Electrophoretic Analysis and Purification of Fluorescent Single-Walled Carbon Nanotube Fragments. *Journal of the American Chemical Society* **2004,** *126* (40), 12736-12737.
49. Liu, H.; Ye, T.; Mao, C., Fluorescent Carbon Nanoparticles Derived from Candle Soot. *Angewandte Chemie International Edition* **2007,** *46* (34), 6473-6475.
50. Dey, S.; Govindaraj, A.; Biswas, K.; Rao, C. N. R., Luminescence properties of boron and nitrogen doped graphene quantum dots prepared from arc-discharge-generated doped graphene samples. *Chemical Physics Letters* **2014,** *595-596*, 203-208.
51. Perumal, S.; Atchudan, R.; Edison, T. N. J. I.; Lee, Y. R., Sustainable synthesis of multifunctional carbon dots using biomass and their applications: A mini-review. *Journal of Environmental Chemical Engineering* **2021,** *9* (4), 105802.
52. Wang, J.; Wang, C.-F.; Chen, S., Amphiphilic Egg-Derived Carbon Dots: Rapid Plasma Fabrication, Pyrolysis Process, and Multicolor Printing Patterns. *Angewandte Chemie International Edition* **2012,** *51* (37), 9297-9301.
53. Zheng, Y.; Liu, H.; Li, J.; Xiang, J.; Panmai, M.; Dai, Q.; Xu, Y.; Tie, S.; Lan, S., Controllable Formation of Luminescent Carbon Quantum Dots Mediated by the Fano Resonances Formed in Oligomers of Gold Nanoparticles. *Advanced Materials* **2019,** *31* (30), 1901371.
54. Liu, K.-K.; Song, S.-Y.; Sui, L.-Z.; Wu, S.-X.; Jing, P.-T.; Wang, R.-Q.; Li, Q.-Y.; Wu, G.-R.; Zhang, Z.-Z.; Yuan, K.-J.; Shan, C.-X., Efficient Red/Near-Infrared-Emissive Carbon Nanodots with Multiphoton Excited Upconversion Fluorescence. *Advanced Science* **2019,** *6* (17), 1900766.
55. Zhu, Z.; Cheng, R.; Ling, L.; Li, Q.; Chen, S., Rapid and Large-Scale Production of Multi-Fluorescence Carbon Dots by a Magnetic Hyperthermia Method. *Angewandte Chemie International Edition* **2020,** *59* (8), 3099-3105.
56. Mandal, B.; Sarkar, S.; Sarkar, P., Exploring the electronic structure of graphene quantum dots. *Journal of Nanoparticle Research* **2012,** *14* (12), 1317.
57. Li, Y.; Shu, H.; Niu, X.; Wang, J., Electronic and Optical Properties of Edge-Functionalized Graphene Quantum Dots and the Underlying Mechanism. *The Journal of Physical Chemistry C* **2015,** *119* (44), 24950-24957.
58. Ding, H.; Li, X.-H.; Chen, X.-B.; Wei, J.-S.; Li, X.-B.; Xiong, H.-M., Surface states of carbon dots and their influences on luminescence. *Journal of Applied Physics* **2020,** *127* (23), 231101.
59. Wang, L.; Zhu, S.-J.; Wang, H.-Y.; Qu, S.-N.; Zhang, Y.-L.; Zhang, J.-H.; Chen, Q.-D.; Xu, H.-L.; Han, W.; Yang, B.; Sun, H.-B., Common Origin of Green Luminescence in Carbon Nanodots and Graphene Quantum Dots. *ACS Nano* **2014,** *8* (3), 2541-2547.
60. Sciortino, A.; Cannizzo, A.; Messina, F. Carbon Nanodots: A Review—From the Current Understanding of the Fundamental Photophysics to the Full Control of the Optical Response *C* [Online], 2018.

61. Liu, J.; Li, R.; Yang, B., Carbon Dots: A New Type of Carbon-Based Nanomaterial with Wide Applications. *ACS Central Science* **2020,** *6* (12), 2179-2195.
62. Nocito, G.; Calabrese, G.; Forte, S.; Petralia, S.; Puglisi, C.; Campolo, M.; Esposito, E.; Conoci, S., Carbon Dots as Promising Tools for Cancer Diagnosis and Therapy. *Cancers* **2021,** *13* (9).
63. Shereema, R. M.; Sruthi, T. V.; Kumar, V. B. S.; Rao, T. P.; Shankar, S. S., Angiogenic Profiling of Synthesized Carbon Quantum Dots. *Biochemistry* **2015,** *54* (41), 6352-6356.
64. Dong, X.; Moyer, M. M.; Yang, F.; Sun, Y.-P.; Yang, L., Carbon Dots' Antiviral Functions Against Noroviruses. *Scientific Reports* **2017,** *7* (1), 519.
65. Barras, A.; Pagneux, Q.; Sane, F.; Wang, Q.; Boukherroub, R.; Hober, D.; Szunerits, S., High Efficiency of Functional Carbon Nanodots as Entry Inhibitors of Herpes Simplex Virus Type 1. *ACS Applied Materials & Interfaces* **2016,** *8* (14), 9004-9013.
66. Zheng, D.-W.; Li, B.; Li, C.-X.; Fan, J.-X.; Lei, Q.; Li, C.; Xu, Z.; Zhang, X.-Z., Carbon-Dot-Decorated Carbon Nitride Nanoparticles for Enhanced Photodynamic Therapy against Hypoxic Tumor via Water Splitting. *ACS Nano* **2016,** *10* (9), 8715-8722.
67. Jia, Q.; Ge, J.; Liu, W.; Zheng, X.; Chen, S.; Wen, Y.; Zhang, H.; Wang, P., A Magnetofluorescent Carbon Dot Assembly as an Acidic H2O2-Driven Oxygenerator to Regulate Tumor Hypoxia for Simultaneous Bimodal Imaging and Enhanced Photodynamic Therapy. *Advanced Materials* **2018,** *30* (13), 1706090.
68. Song, J.; Yang, X.; Yang, Z.; Lin, L.; Liu, Y.; Zhou, Z.; Shen, Z.; Yu, G.; Dai, Y.; Jacobson, O.; Munasinghe, J.; Yung, B.; Teng, G.-J.; Chen, X., Rational Design of Branched Nanoporous Gold Nanoshells with Enhanced Physico-Optical Properties for Optical Imaging and Cancer Therapy. *ACS Nano* **2017,** *11* (6), 6102-6113.
69. Azharuddin, M.; Zhu, G. H.; Das, D.; Ozgur, E.; Uzun, L.; Turner, A. P. F.; Patra, H. K., A repertoire of biomedical applications of noble metal nanoparticles. *Chemical Communications* **2019,** *55* (49), 6964-6996.
70. Jain, P. K.; Huang, X.; El-Sayed, I. H.; El-Sayed, M. A., Noble Metals on the Nanoscale: Optical and Photothermal Properties and Some Applications in Imaging, Sensing, Biology, and Medicine. *Accounts of Chemical Research* **2008,** *41* (12), 1578-1586.
71. Nocito, G.; Petralia, S.; Malanga, M.; Béni, S.; Calabrese, G.; Parenti, R.; Conoci, S.; Sortino, S., Biofriendly Route to Near-Infrared-Active Gold Nanotriangles and Nanoflowers through Nitric Oxide Photorelease for Photothermal Applications. *ACS Applied Nano Materials* **2019,** *2* (12), 7916-7923.
72. Sperling, R. A.; Rivera Gil, P.; Zhang, F.; Zanella, M.; Parak, W. J., Biological applications of gold nanoparticles. *Chemical Society Reviews* **2008,** *37* (9), 1896-1908.
73. Sawalha, S.; Silvestri, A.; Criado, A.; Bettini, S.; Prato, M.; Valli, L., Tailoring the sensing abilities of carbon nanodots obtained from olive solid wastes. *Carbon* **2020,** *167*, 696-708.
74. Sawalha, S.; Moulaee, K.; Nocito, G.; Silvestri, A.; Petralia, S.; Prato, M.; Bettini, S.; Valli, L.; Conoci, S.; Neri, G., Carbon-dots conductometric sensor for high performance gas sensing. *Carbon Trends* **2021,** *5*, 100105.
75. Anwar, S.; Ding, H.; Xu, M.; Hu, X.; Li, Z.; Wang, J.; Liu, L.; Jiang, L.; Wang, D.; Dong, C.; Yan, M.; Wang, Q.; Bi, H., Recent Advances in Synthesis, Optical Properties, and Biomedical Applications of Carbon Dots. *ACS Applied Bio Materials* **2019,** *2* (6), 2317-2338.
76. Li, H.; Kang, Z.; Liu, Y.; Lee, S.-T., Carbon nanodots: synthesis, properties and applications. *Journal of Materials Chemistry* **2012,** *22* (46), 24230-24253.
77. Li, M.; Chen, T.; Gooding, J. J.; Liu, J., Review of Carbon and Graphene Quantum Dots for Sensing. *ACS Sensors* **2019,** *4* (7), 1732-1748.
78. Amer, W. A.; Rehab, A. F.; Abdelghafar, M. E.; Torad, N. L.; Atlam, A. S.; Ayad, M. M., Green synthesis of carbon quantum dots from purslane leaves for the

detection of formaldehyde using quartz crystal microbalance. *Carbon* **2021,** *179*, 159-171.
79. Shauloff, N.; Morag, A.; Yaniv, K.; Singh, S.; Malishev, R.; Paz-Tal, O.; Rokach, L.; Jelinek, R., Sniffing Bacteria with a Carbon-Dot Artificial Nose. *Nano-Micro Letters* **2021,** *13* (1), 112.
80. Zhang, J.; Liu, X.; Neri, G.; Pinna, N., Nanostructured Materials for Room-Temperature Gas Sensors. *Advanced Materials* **2016,** *28* (5), 795-831.
81. Hesterberg, T. W.; Bunn, W. B.; McClellan, R. O.; Hamade, A. K.; Long, C. M.; Valberg, P. A., Critical review of the human data on short-term nitrogen dioxide (NO2) exposures: Evidence for NO2 no-effect levels. *Critical Reviews in Toxicology* **2009,** *39* (9), 743-781.
82. Rella, R.; Rizzo, A.; Licciulli, A.; Siciliano, P.; Troisi, L.; Valli, L., Tests in controlled atmosphere on new optical gas sensing layers based on TiO2/metal-phthalocyanines hybrid system. *Materials Science and Engineering: C* **2002,** *22* (2), 439-443.
83. Rella, R.; Serra, A.; Siciliano, P.; Tepore, A.; Valli, L.; Zocco, A., NO2 gas detection by Langmuir-Blodgett films of copper phthalocyanine multilayer structures. *Supramolecular Science* **1997,** *4* (3), 461-464.
84. Rella, R.; Serra, A.; Siciliano, P.; Tepore, A.; Valli, L.; Zocco, A., Effects of NO2 oxidizing gas on a novel phthalocyanine Langmuir-Blodgett thin film. *Thin Solid Films* **1996,** *286* (1), 256-258.
85. Urso, M.; Leonardi, S. G.; Neri, G.; Petralia, S.; Conoci, S.; Priolo, F.; Mirabella, S., Room temperature detection and modelling of sub-ppm NO2 by low-cost nanoporous NiO film. *Sensors and Actuators B: Chemical* **2020,** *305*, 127481.
86. Wang, R.; Li, G.; Dong, Y.; Chi, Y.; Chen, G., Carbon Quantum Dot-Functionalized Aerogels for NO2 Gas Sensing. *Analytical Chemistry* **2013,** *85* (17), 8065-8069.
87. Hu, J.; Zou, C.; Su, Y.; Li, M.; Hu, N.; Ni, H.; Yang, Z.; Zhang, Y., Enhanced NO2 sensing performance of reduced graphene oxide by in situ anchoring carbon dots. *Journal of Materials Chemistry C* **2017,** *5* (27), 6862-6871.
88. Liu, Q.; Zhang, J.; He, H.; Huang, G.; Xing, B.; Jia, J.; Zhang, C., Green Preparation of High Yield Fluorescent Graphene Quantum Dots from Coal-Tar-Pitch by Mild Oxidation. *Nanomaterials* **2018,** *8* (10).
89. Das, P.; Bose, M.; Ganguly, S.; Mondal, S.; Das, A. K.; Banerjee, S.; Das, N. C., Green approach to photoluminescent carbon dots for imaging of gram-negative bacteriaEscherichia coli. *Nanotechnology* **2017,** *28* (19), 195501.
90. Nguyen, V.; Yan, L.; Si, J.; Hou, X., Femtosecond laser-induced size reduction of carbon nanodots in solution: Effect of laser fluence, spot size, and irradiation time. *Journal of Applied Physics* **2015,** *117* (8), 084304.
91. Radhakrishnan, K.; Panneerselvam, P.; Marieeswaran, M., A green synthetic route for the surface-passivation of carbon dots as an effective multifunctional fluorescent sensor for the recognition and detection of toxic metal ions from aqueous solution. *Analytical Methods* **2019,** *11* (4), 490-506.
92. Xue, M.; Zhan, Z.; Zou, M.; Zhang, L.; Zhao, S., Green synthesis of stable and biocompatible fluorescent carbon dots from peanut shells for multicolor living cell imaging. *New Journal of Chemistry* **2016,** *40* (2), 1698-1703.
93. Bandi, R.; Gangapuram, B. R.; Dadigala, R.; Eslavath, R.; Singh, S. S.; Guttena, V., Facile and green synthesis of fluorescent carbon dots from onion waste and their potential applications as sensor and multicolour imaging agents. *RSC Advances* **2016,** *6* (34), 28633-28639.
94. Bettini, S.; Sawalha, S.; Carbone, L.; Giancane, G.; Prato, M.; Valli, L., Carbon nanodot-based heterostructures for improving the charge separation and the photocurrent generation. *Nanoscale* **2019,** *11* (15), 7414-7423.
95. Chen, J.; Liu, J.; Li, J.; Xu, L.; Qiao, Y., One-pot synthesis of nitrogen and sulfur co-doped carbon dots and its application for sensor and multicolor cellular imaging. *Journal of Colloid and Interface Science* **2017,** *485*, 167-174.

96. Choi, J.; Kim, N.; Oh, J.-W.; Kim, F. S., Bandgap engineering of nanosized carbon dots through electron-accepting functionalization. *Journal of Industrial and Engineering Chemistry* **2018,** *65*, 104-111.
97. Zeng, Q.; Shao, D.; He, X.; Ren, Z.; Ji, W.; Shan, C.; Qu, S.; Li, J.; Chen, L.; Li, Q., Carbon dots as a trackable drug delivery carrier for localized cancer therapy in vivo. *Journal of Materials Chemistry B* **2016,** *4* (30), 5119-5126.
98. Litvin, A. P.; Martynenko, I. V.; Purcell-Milton, F.; Baranov, A. V.; Fedorov, A. V.; Gun'ko, Y. K., Colloidal quantum dots for optoelectronics. *Journal of Materials Chemistry A* **2017,** *5* (26), 13252-13275.
99. Kim, H.-J.; Lee, J.-H., Highly sensitive and selective gas sensors using p-type oxide semiconductors: Overview. *Sensors and Actuators B: Chemical* **2014,** *192*, 607-627.
100. Abbas, A.; Tabish, T. A.; Bull, S. J.; Lim, T. M.; Phan, A. N., High yield synthesis of graphene quantum dots from biomass waste as a highly selective probe for Fe3+ sensing. *Scientific Reports* **2020,** *10* (1), 21262.
101. Huang, L.; Wang, Z.; Zhang, J.; Pu, J.; Lin, Y.; Xu, S.; Shen, L.; Chen, Q.; Shi, W., Fully Printed, Rapid-Response Sensors Based on Chemically Modified Graphene for Detecting NO2 at Room Temperature. *ACS Applied Materials & Interfaces* **2014,** *6* (10), 7426-7433.
102. Mao, S.; Lu, G.; Chen, J., Nanocarbon-based gas sensors: progress and challenges. *Journal of Materials Chemistry A* **2014,** *2* (16), 5573-5579.
103. Schroeder, V.; Savagatrup, S.; He, M.; Lin, S.; Swager, T. M., Carbon Nanotube Chemical Sensors. *Chemical Reviews* **2019,** *119* (1), 599-663.
104. Sacco, L.; Forel, S.; Florea, I.; Cojocaru, C.-S., Ultra-sensitive NO2 gas sensors based on single-wall carbon nanotube field effect transistors: Monitoring from ppm to ppb level. *Carbon* **2020,** *157*, 631-639.
105. Chauhan, S. S.; Kumar, D.; Chaturvedi, P.; Rahman, M. R., Highly Sensitive and Stable NO2 Gas Sensors Based on SWNTs With Exceptional Recovery Time. *IEEE Sensors Journal* **2019,** *19* (24), 11775-11783.
106. Park, J.; Kim, Y.; Park, S. Y.; Sung, S. J.; Jang, H. W.; Park, C. R., Band gap engineering of graphene oxide for ultrasensitive NO2 gas sensing. *Carbon* **2020,** *159*, 175-184.
107. Guo, L.; Li, T., Sub-ppb and ultra selective nitrogen dioxide sensor based on sulfur doped graphene. *Sensors and Actuators B: Chemical* **2018,** *255*, 2258-2263.
108. Wu, J.; Tao, K.; Miao, J.; Norford, L. K., Improved Selectivity and Sensitivity of Gas Sensing Using a 3D Reduced Graphene Oxide Hydrogel with an Integrated Microheater. *ACS Applied Materials & Interfaces* **2015,** *7* (49), 27502-27510.
109. Han, T.; Gao, S.; Wang, Z.; Fei, T.; Liu, S.; Zhang, T., Investigation of the effect of oxygen-containing groups on reduced graphene oxide-based room-temperature NO2 sensor. *Journal of Alloys and Compounds* **2019,** *801*, 142-150.
110. Yan, X.; Wu, Y.; Li, R.; Shi, C.; Moro, R.; Ma, Y.; Ma, L., High-Performance UV-Assisted NO2 Sensor Based on Chemical Vapor Deposition Graphene at Room Temperature. *ACS Omega* **2019,** *4* (10), 14179-14187.
111. Llobet, E., Gas sensors using carbon nanomaterials: A review. *Sensors and Actuators B: Chemical* **2013,** *179*, 32-45.
112. Dariyal, P.; Sharma, S.; Chauhan, G. S.; Singh, B. P.; Dhakate, S. R., Recent trends in gas sensing via carbon nanomaterials: outlook and challenges. *Nanoscale Advances* **2021,** *3* (23), 6514-6544.
113. Kumar, P.; Dua, S.; Kaur, R.; Kumar, M.; Bhatt, G., A review on advancements in carbon quantum dots and their application in photovoltaics. *RSC Advances* **2022,** *12* (8), 4714-4759.
114. Wang, R.; Lu, K.-Q.; Tang, Z.-R.; Xu, Y.-J., Recent progress in carbon quantum dots: synthesis, properties and applications in photocatalysis. *Journal of Materials Chemistry A* **2017,** *5* (8), 3717-3734.
115. Zhou, Y.; He, J.; Chen, R.; Li, X., Recent advances in biomass-derived graphene and carbon nanotubes. *Materials Today Sustainability* **2022,** *18*, 100138.

116. Long, C.; Jiang, Z.; Shangguan, J.; Qing, T.; Zhang, P.; Feng, B., Applications of carbon dots in environmental pollution control: A review. *Chemical Engineering Journal* **2021,** *406*, 126848.
117. Kang, C.; Huang, Y.; Yang, H.; Yan, X. F.; Chen, Z. P., A Review of Carbon Dots Produced from Biomass Wastes. *Nanomaterials* **2020,** *10* (11).
118. Sun, X.; Lei, Y., Fluorescent carbon dots and their sensing applications. *TrAC Trends in Analytical Chemistry* **2017,** *89*, 163-180.
119. Sun, Y.; Li, J.; He, D.; Wang, X.; Shi, Y.; Pan, L., Recent progress on performances and mechanisms of carbon dots for gas sensing. *Luminescence* **2022,** *n/a* (n/a).
120. Yu, Z.; Zhang, L.; Wang, X.; He, D.; Suo, H.; Zhao, C. Fabrication of ZnO/Carbon Quantum Dots Composite Sensor for Detecting NO Gas *Sensors* [Online], 2020.
121. Jones, S. S.; Sahatiya, P.; Badhulika, S., One step, high yield synthesis of amphiphilic carbon quantum dots derived from chia seeds: a solvatochromic study. *New Journal of Chemistry* **2017,** *41* (21), 13130-13139.
122. Atchudan, R.; Edison, T. N. J. I.; Lee, Y. R., Nitrogen-doped carbon dots originating from unripe peach for fluorescent bioimaging and electrocatalytic oxygen reduction reaction. *Journal of Colloid and Interface Science* **2016,** *482*, 8-18.
123. Stachowska, J. D.; Murphy, A.; Mellor, C.; Fernandes, D.; Gibbons, E. N.; Krysmann, M. J.; Kelarakis, A.; Burgaz, E.; Moore, J.; Yeates, S. G., A rich gallery of carbon dots based photoluminescent suspensions and powders derived by citric acid/urea. *Scientific Reports* **2021,** *11* (1), 10554.
124. Zhang, Q.; Wang, R.; Feng, B.; Zhong, X.; Ostrikov, K., Photoluminescence mechanism of carbon dots: triggering high-color-purity red fluorescence emission through edge amino protonation. *Nature Communications* **2021,** *12* (1), 6856.
125. Huang, G.; Chen, X.; Wang, C.; Zheng, H.; Huang, Z.; Chen, D.; Xie, H., Photoluminescent carbon dots derived from sugarcane molasses: synthesis, properties, and applications. *RSC Advances* **2017,** *7* (75), 47840-47847.
126. Mewada, A.; Pandey, S.; Shinde, S.; Mishra, N.; Oza, G.; Thakur, M.; Sharon, M.; Sharon, M., Green synthesis of biocompatible carbon dots using aqueous extract of Trapa bispinosa peel. *Materials Science and Engineering: C* **2013,** *33* (5), 2914-2917.
127. Wang, D.; Wang, Z.; Zhan, Q.; Pu, Y.; Wang, J.-X.; Foster, N. R.; Dai, L., Facile and Scalable Preparation of Fluorescent Carbon Dots for Multifunctional Applications. *Engineering* **2017,** *3* (3), 402-408.
128. Mintz, K. J.; Bartoli, M.; Rovere, M.; Zhou, Y.; Hettiarachchi, S. D.; Paudyal, S.; Chen, J.; Domena, J. B.; Liyanage, P. Y.; Sampson, R.; Khadka, D.; Pandey, R. R.; Huang, S.; Chusuei, C. C.; Tagliaferro, A.; Leblanc, R. M., A deep investigation into the structure of carbon dots. *Carbon* **2021,** *173*, 433-447.
129. Jeong, D.-W.; Kim, K. H.; Kim, B. S.; Byun, Y. T., Characteristics of highly sensitive and selective nitric oxide gas sensors using defect-functionalized single-walled carbon nanotubes at room temperature. *Applied Surface Science* **2021,** *550*, 149250.
130. Mäklin, J.; Mustonen, T.; Kordás, K.; Saukko, S.; Tóth, G.; Vähäkangas, J., Nitric oxide gas sensors with functionalized carbon nanotubes. *physica status solidi (b)* **2007,** *244* (11), 4298-4302.
131. Reddeppa, M.; Park, B.-G.; Chinh, N. D.; Kim, D.; Oh, J.-E.; Kim, T. G.; Kim, M.-D., A novel low-temperature resistive NO gas sensor based on InGaN/GaN multi-quantum well-embedded p–i–n GaN nanorods. *Dalton Transactions* **2019,** *48* (4), 1367-1375.
132. Ma, Z.; Yang, K.; Xiao, C.; Jia, L., Electrospun Bi-doped SnO2 porous nanosheets for highly sensitive nitric oxide detection. *Journal of Hazardous Materials* **2021,** *416*, 126118.
133. Barazzouk, S.; Tandon, R. P.; Hotchandani, S., MoO3-based sensor for NO, NO2 and CH4 detection. *Sensors and Actuators B: Chemical* **2006,** *119* (2), 691-694.
134. Cai, Z.-X.; Li, H.-Y.; Yang, X.-N.; Guo, X., NO sensing by single crystalline WO3 nanowires. *Sensors and Actuators B: Chemical* **2015,** *219*, 346-353.

135. Kaur, M.; Kailasaganapathi, S.; Ramgir, N.; Datta, N.; Kumar, S.; Debnath, A. K.; Aswal, D. K.; Gupta, S. K., Gas dependent sensing mechanism in ZnO nanobelt sensor. *Applied Surface Science* **2017,** *394*, 258-266.
136. Chowdhury, N. K.; Bhowmik, B., Micro/nanostructured gas sensors: the physics behind the nanostructure growth, sensing and selectivity mechanisms. *Nanoscale Advances* **2021,** *3* (1), 73-93.
137. Leturcq, R.; Bhusari, R.; Barborini, E., Physical mechanisms underpinning conductometric gas sensing properties of metal oxide nanostructures. *Advances in Physics: X* **2022,** *7* (1), 2044904.
138. Tang, S.; Cao, Z., Adsorption of nitrogen oxides on graphene and graphene oxides: Insights from density functional calculations. *The Journal of Chemical Physics* **2011,** *134* (4), 044710.
139. Salih, E.; Ayesh, A. I. Enhancing the Sensing Performance of Zigzag Graphene Nanoribbon to Detect NO, NO2, and NH3 Gases *Sensors* [Online], 2020.
140. Arunragsa, S.; Seekaew, Y.; Pon-On, W.; Wongchoosuk, C., Hydroxyl edge-functionalized graphene quantum dots for gas-sensing applications. *Diamond and Related Materials* **2020,** *105*, 107790.
141. Liu, C.; Ma, Q.; He, H.; He, G.; Ma, J.; Liu, Y.; Wu, Y., Structure–activity relationship of surface hydroxyl groups during NO2 adsorption and transformation on TiO2 nanoparticles. *Environmental Science: Nano* **2017,** *4* (12), 2388-2394.
142. Nocito, G.; Sciuto, E. L.; Franco, D.; Nastasi, F.; Pulvirenti, L.; Petralia, S.; Spinella, C.; Calabrese, G.; Guglielmino, S.; Conoci, S., Physicochemical Characterization and Antibacterial Properties of Carbon Dots from Two Mediterranean Olive Solid Waste Cultivars. *Nanomaterials* **2022,** *12* (5), 885.
143. Xu, D.; Lin, Q.; Chang, H.-T., Recent Advances and Sensing Applications of Carbon Dots. *Small methods* **2020,** *4* (4), 1900387.
144. Han, M.; Zhu, S.; Lu, S.; Song, Y.; Feng, T.; Tao, S.; Liu, J.; Yang, B., Recent progress on the photocatalysis of carbon dots: Classification, mechanism and applications. *Nano Today* **2018,** *19*, 201-218.
145. Stepanidenko, E. A.; Ushakova, E. V.; Fedorov, A. V.; Rogach, A. L., Applications of Carbon Dots in Optoelectronics. *Nanomaterials* **2021,** *11* (2), 364.
146. Peng, Z.; Miyanji, E. H.; Zhou, Y.; Pardo, J.; Hettiarachchi, S. D.; Li, S.; Blackwelder, P. L.; Skromne, I.; Leblanc, R. M., Carbon dots: promising biomaterials for bone-specific imaging and drug delivery. *Nanoscale* **2017,** *9* (44), 17533-17543.
147. Su, W.; Wu, H.; Xu, H.; Zhang, Y.; Li, Y.; Li, X.; Fan, L., Carbon dots: a booming material for biomedical applications. *Materials Chemistry Frontiers* **2020,** *4* (3), 821-836.
148. Kasouni, A.; Chatzimitakos, T.; Stalikas, C., Bioimaging Applications of Carbon Nanodots: A Review. *C* **2019,** *5* (2).
149. Calabrese, G.; De Luca, G.; Nocito, G.; Rizzo, M. G.; Lombardo, S. P.; Chisari, G.; Forte, S.; Sciuto, E. L.; Conoci, S., Carbon Dots: An Innovative Tool for Drug Delivery in Brain Tumors. *International Journal of Molecular Science* **2021,** *22* (21), 11783.
150. Baker, S. N.; Baker, G. A., Luminescent Carbon Nanodots: Emergent Nanolights. *Angewandte Chemie International Edition* **2010,** *49* (38), 6726-6744.
151. Namdari, P.; Negahdari, B.; Eatemadi, A., Synthesis, properties and biomedical applications of carbon-based quantum dots: An updated review. *Biomedicine & Pharmacotherapy* **2017,** *87*, 209-222.
152. Lim, S. Y.; Shen, W.; Gao, Z., Carbon quantum dots and their applications. *Chemical Society Reviews* **2015,** *44* (1), 362-381.
153. Macairan, J.-R.; de Medeiros, T. V.; Gazzetto, M.; Yarur Villanueva, F.; Cannizzo, A.; Naccache, R., Elucidating the mechanism of dual-fluorescence in carbon dots. *Journal of Colloid and Interface Science* **2022,** *606*, 67-76.
154. Meng, W.; Bai, X.; Wang, B.; Liu, Z.; Lu, S.; Yang, B., Biomass-Derived Carbon Dots and Their Applications. *ENERGY & ENVIRONMENTAL MATERIALS* **2019,** *2* (3), 172-192.

155. Mintz, K. J.; Zhou, Y.; Leblanc, R. M., Recent development of carbon quantum dots regarding their optical properties, photoluminescence mechanism, and core structure. *Nanoscale* **2019,** *11* (11), 4634-4652.
156. Wareing, T. C.; Gentile, P.; Phan, A. N., Biomass-Based Carbon Dots: Current Development and Future Perspectives. *ACS Nano* **2021,** *15* (10), 15471-15501.
157. Doula, M. K.; Moreno-Ortego, J. L.; Tinivella, F.; Inglezakis, V. J.; Sarris, A.; Komnitsas, K., Chapter 2 - Olive mill waste: recent advances for the sustainable development of olive oil industry. In *Olive Mill Waste*, Galanakis, C. M., Ed. Academic Press: 2017; pp 29-56.
158. Xue, M.; Zou, M.; Zhao, J.; Zhan, Z.; Zhao, S., Green preparation of fluorescent carbon dots from lychee seeds and their application for the selective detection of methylene blue and imaging in living cells. *Journal of Materials Chemistry B* **2015,** *3* (33), 6783-6789.
159. Shi, L.; Zhao, B.; Li, X.; Zhang, G.; Zhang, Y.; Dong, C.; Shuang, S., Eco-friendly synthesis of nitrogen-doped carbon nanodots from wool for multicolor cell imaging, patterning, and biosensing. *Sensors and Actuators B: Chemical* **2016,** *235*, 316-324.
160. Zhao, Y.; Duan, J.; He, B.; Jiao, Z.; Tang, Q., Improved charge extraction with N-doped carbon quantum dots in dye-sensitized solar cells. *Electrochimica Acta* **2018,** *282*, 255-262.
161. Algarra, M.; Orfãos, L. d.; Alves, C. S.; Moreno-Tost, R.; Pino-González, M. S.; Jiménez-Jiménez, J.; Rodríguez-Castellón, E.; Eliche-Quesada, D.; Castro, E.; Luque, R., Sustainable Production of Carbon Nanoparticles from Olive Pit Biomass: Understanding Proton Transfer in the Excited State on Carbon Dots. *ACS Sustainable Chemistry & Engineering* **2019,** *7* (12), 10493-10500.
162. Nekoueian, K.; Amiri, M.; Sillanpää, M.; Marken, F.; Boukherroub, R.; Szunerits, S., Carbon-based quantum particles: an electroanalytical and biomedical perspective. *Chemical Society Reviews* **2019,** *48* (15), 4281-4316.
163. Dong, X.; Liang, W.; Meziani, M. J.; Sun, Y.-P.; Yang, L., Carbon dots as potent antimicrobial agents. *Theranostics* **2020,** *10* (2), 671-686.
164. Franco, D.; Calabrese, G.; Petralia, S.; Neri, G.; Corsaro, C.; Forte, L.; Squarzoni, S.; Guglielmino, S.; Traina, F.; Fazio, E.; Conoci, S., Antimicrobial Effect and Cytotoxic Evaluation of Mg-Doped Hydroxyapatite Functionalized with Au-Nano Rods. *Molecules* **2021,** *26* (4).
165. Hajipour, M. J.; Fromm, K. M.; Akbar Ashkarran, A.; Jimenez de Aberasturi, D.; Larramendi, I. R. d.; Rojo, T.; Serpooshan, V.; Parak, W. J.; Mahmoudi, M., Antibacterial properties of nanoparticles. *Trends in Biotechnology* **2012,** *30* (10), 499-511.
166. Leonardi, A. A.; Lo Faro, M. J.; Irrera, A., Biosensing platforms based on silicon nanostructures: A critical review. *Analytica Chimica Acta* **2021,** *1160*, 338393.
167. Sun, B.; Wu, F.; Zhang, Q.; Chu, X.; Wang, Z.; Huang, X.; Li, J.; Yao, C.; Zhou, N.; Shen, J., Insight into the effect of particle size distribution differences on the antibacterial activity of carbon dots. *Journal of Colloid and Interface Science* **2021,** *584*, 505-519.
168. Xin, Q.; Shah, H.; Nawaz, A.; Xie, W.; Akram, M. Z.; Batool, A.; Tian, L.; Jan, S. U.; Boddula, R.; Guo, B.; Liu, Q.; Gong, J. R., Antibacterial Carbon-Based Nanomaterials. *Advanced Materials* **2019,** *31* (45), 1804838.
169. Al-Jumaili, A.; Alancherry, S.; Bazaka, K.; Jacob, M. V., Review on the Antimicrobial Properties of Carbon Nanostructures. *Materials* **2017,** *10* (9).
170. Karahan, H. E.; Wiraja, C.; Xu, C.; Wei, J.; Wang, Y.; Wang, L.; Liu, F.; Chen, Y., Graphene Materials in Antimicrobial Nanomedicine: Current Status and Future Perspectives. *Advanced Healthcare Materials* **2018,** *7* (13), 1701406.
171. Zou, X.; Zhang, L.; Wang, Z.; Luo, Y., Mechanisms of the Antimicrobial Activities of Graphene Materials. *Journal of the American Chemical Society* **2016,** *138* (7), 2064-2077.

172. Zhang, X.; Wang, J.; Liu, J.; Wu, J.; Chen, H.; Bi, H., Design and preparation of a ternary composite of graphene oxide/carbon dots/polypyrrole for supercapacitor application: Importance and unique role of carbon dots. *Carbon* **2017,** *115*, 134-146.
173. Holub, J.; Santoro, A.; Lehn, J.-M., Electronic absorption and emission properties of bishydrazone [2 × 2] metallosupramolecular grid-type architectures. *Inorganica Chimica Acta* **2019,** *494*, 223-231.
174. Tauc, J.; Grigorovici, R.; Vancu, A., Optical Properties and Electronic Structure of Amorphous Germanium. *Physica Status Solidi b* **1966,** *15* (2), 627-637.
175. Makuła, P.; Pacia, M.; Macyk, W., How To Correctly Determine the Band Gap Energy of Modified Semiconductor Photocatalysts Based on UV–Vis Spectra. *The Journal of Physical Chemistry Letters* **2018,** *9* (23), 6814-6817.
176. Wei, S.; Yin, X.; Li, H.; Du, X.; Zhang, L.; Yang, Q.; Yang, R., Multi-Color Fluorescent Carbon Dots: Graphitized sp2 Conjugated Domains and Surface State Energy Level Co-Modulate Band Gap Rather Than Size Effects. *Chemistry – A European Journal* **2020,** *26* (36), 8129-8136.
177. Bing, W.; Sun, H.; Yan, Z.; Ren, J.; Qu, X., Programmed Bacteria Death Induced by Carbon Dots with Different Surface Charge. *Small* **2016,** *12* (34), 4713-4718.
178. Nocito, G.; Puntoriero, F.; Conoci, S.; Galletta, M.; Nastasi, F. In *A New Carbon Dots-Eu(III) Complex as Red Emitting pH-Sensor*, Sensors and Microsystems, Cham, 2023//; Di Francia, G.; Di Natale, C., Eds. Springer International Publishing: Cham, 2023; pp 67-72.
179. Sun, Y.-P.; Zhou, B.; Lin, Y.; Wang, W.; Fernando, K. A. S.; Pathak, P.; Meziani, M. J.; Harruff, B. A.; Wang, X.; Wang, H.; Luo, P. G.; Yang, H.; Kose, M. E.; Chen, B.; Veca, L. M.; Xie, S.-Y., Quantum-Sized Carbon Dots for Bright and Colorful Photoluminescence. *Journal of the American Chemical Society* **2006,** *128* (24), 7756-7757.
180. Petralia, S.; Sciuto, E. L.; Di Pietro, M. L.; Zimbone, M.; Grimaldi, M. G.; Conoci, S., An innovative chemical strategy for PCR-free genetic detection of pathogens by an integrated electrochemical biosensor. *Analyst* **2017,** *142* (12), 2090-2093.
181. de Silva, A. P.; Gunaratne, H. Q. N.; Gunnlaugsson, T.; Huxley, A. J. M.; McCoy, C. P.; Rademacher, J. T.; Rice, T. E., Signaling Recognition Events with Fluorescent Sensors and Switches. *Chemical Reviews* **1997,** *97* (5), 1515-1566.
182. Wegner, H. A., Molecular Switches. Second Edition. Edited by Ben L. Feringa and Wesley R. Browne. *Angewandte Chemie International Edition* **2012,** *51* (10), 2281-2281.
183. Balzani, V.; Credi, A.; Venturi, M., *Molecular Devices and Machines – A Journey into the Nano World*. Wiley-VCH Verlag GmbH & Co. KGaA: 2003.
184. Prodi, L., Luminescent chemosensors: from molecules to nanoparticles. *New Journal of Chemistry* **2005,** *29* (1), 20-31.
185. Giannetto, A.; Nastasi, F.; Puntoriero, F.; Bella, G.; Campagna, S.; Lanza, S., Fast transport of HCl across a hydrophobic layer over macroscopic distances by using a Pt(ii) compound as the transporter: micro- and nanometric aggregates as effective transporters. *Dalton Transactions* **2021,** *50* (4), 1422-1433.
186. Cordaro, M.; Mineo, P.; Nastasi, F.; Magazzù, G., Facile synthesis of boronic acids on a BODIPY core with promising sensitivity towards polyols. *RSC Advances* **2014,** *4* (83), 43931-43933.
187. Kumar, R.; Sharma, A.; Singh, H.; Suating, P.; Kim, H. S.; Sunwoo, K.; Shim, I.; Gibb, B. C.; Kim, J. S., Revisiting Fluorescent Calixarenes: From Molecular Sensors to Smart Materials. *Chemical Reviews* **2019,** *119* (16), 9657-9721.
188. Carbonaro, C. M.; Corpino, R.; Salis, M.; Mocci, F.; Thakkar, S. V.; Olla, C.; Ricci, P. C., On the Emission Properties of Carbon Dots: Reviewing Data and Discussing Models. *C* **2019,** *5* (4).
189. Miao, S.; Liang, K.; Zhu, J.; Yang, B.; Zhao, D.; Kong, B., Hetero-atom-doped carbon dots: Doping strategies, properties and applications. *Nano Today* **2020,** *33*, 100879.

190. Zhou, Y.; Sharma, S. K.; Peng, Z.; Leblanc, R. M., Polymers in Carbon Dots: A Review. *Polymers* **2017,** *9* (2).
191. Ding, H.; Zhou, X.; Qin, B.; Zhou, Z.; Zhao, Y., Highly fluorescent near-infrared emitting carbon dots derived from lemon juice and its bioimaging application. *Journal of Luminescence* **2019,** *211*, 298-304.
192. Ye, Z.; Tang, R.; Wu, H.; Wang, B.; Tan, M.; Yuan, J., Preparation of europium complex-conjugated carbon dots for ratiometric fluorescence detection of copper(ii) ions. *New Journal of Chemistry* **2014,** *38* (12), 5721-5726.
193. Liu, J.; Ge, X.; Sun, L.; Wei, R.; Liu, J.; Shi, L., Light modulation (vis-NIR region) based on lanthanide complex-functionalized carbon dots. *RSC Advances* **2016,** *6* (53), 47427-47433.
194. Sabbatini, N.; Guardigli, M.; Lehn, J.-M., Luminescent lanthanide complexes as photochemical supramolecular devices. *Coordination Chemistry Reviews* **1993,** *123* (1), 201-228.
195. Sun, Y.-L.; Feng, X.; Guo, N.; Wang, L.-Y.; Li, R.-F.; Bai, R.-F., A novel europium coordination polymer based on mixed carboxylic acid ligands: Synthesis, structure and luminescence. *Inorganic Chemistry Communications* **2016,** *67*, 90-94.
196. Saha, K.; Agasti, S. S.; Kim, C.; Li, X.; Rotello, V. M., Gold Nanoparticles in Chemical and Biological Sensing. *Chemical Reviews* **2012,** *112* (5), 2739-2779.
197. Ziegler, C.; Eychmüller, A., Seeded Growth Synthesis of Uniform Gold Nanoparticles with Diameters of 15–300 nm. *The Journal of Physical Chemistry C* **2011,** *115* (11), 4502-4506.
198. Amendola, V.; Pilot, R.; Frasconi, M.; Maragò, O. M.; Iatì, M. A., Surface plasmon resonance in gold nanoparticles: a review. *Journal of Physics: Condensed Matter* **2017,** *29*, 203002.
199. Su, K. H.; Wei, Q. H.; Zhang, X.; Mock, J. J.; Smith, D. R.; Schultz, S., Interparticle Coupling Effects on Plasmon Resonances of Nanogold Particles. *Nano Letters* **2003,** *3* (8), 1087-1090.
200. Lu, Z.; Giles, L. W.; Teo, B. M.; Tabor, R. F., Carbon dots as a 'green' reagent to produce shape and size controlled gold nanoparticles for application in pollutant degradation. *Colloid and Interface Science Communications* **2022,** *46*, 100571.
201. Anastas, P.; Eghbali, N., Green Chemistry: Principles and Practice. *Chemical Society Reviews* **2010,** *39* (1), 301-312.
202. Raveendran, P.; Fu, J.; Wallen, S. L., Completely "Green" Synthesis and Stabilization of Metal Nanoparticles. *Journal of the American Chemical Society* **2003,** *125* (46), 13940-13941.
203. Arcudi, F.; Đorđević, L.; Prato, M., Design, Synthesis, and Functionalization Strategies of Tailored Carbon Nanodots. *Accounts of Chemical Research* **2019,** *52* (8), 2070-2079.
204. Zheng, X. T.; Ananthanarayanan, A.; Luo, K. Q.; Chen, P., Glowing Graphene Quantum Dots and Carbon Dots: Properties, Syntheses, and Biological Applications. *Small* **2015,** *11* (14), 1620-1636.
205. Dreaden, E. C.; Alkilany, A. M.; Huang, X.; Murphy, C. J.; El-Sayed, M. A., The golden age: gold nanoparticles for biomedicine. *Chemical Society Reviews* **2012,** *41* (7), 2740-2779.
206. Hutton, G. A. M.; Martindale, B. C. M.; Reisner, E., Carbon dots as photosensitisers for solar-driven catalysis. *Chemical Society Reviews* **2017,** *46* (20), 6111-6123.
207. Yoo, D.; Park, Y.; Cheon, B.; Park, M.-H., Carbon Dots as an Effective Fluorescent Sensing Platform for Metal Ion Detection. *Nanoscale Research Letters* **2019,** *14* (1), 272.
208. Choi, D.; Jang, D.-J., Photodeposition of gold nanoparticles on silica nanospheres using carbon dots as excellent electron donors. *New Journal of Chemistry* **2018,** *42* (18), 14717-14720.
209. Lu, Q.; Deng, J.; Hou, Y.; Wang, H.; Li, H.; Zhang, Y.; Yao, S., Hydroxyl-rich C-dots synthesized by a one-pot method and their application in the preparation of noble metal nanoparticles. *Chemical Communications* **2015,** *51* (33), 7164-7167.

210. Ansi, V. A.; P, S., P.; Raveendran, P.; Renuka, N. K., Table sugar derived carbon dot—A promising green reducing agent. *Materials Research Bulletin* **2021,** *139*, 111284.
211. Wang, X.; Long, Y.; Wang, Q.; Zhang, H.; Huang, X.; Zhu, R.; Teng, P.; Liang, L.; Zheng, H., Reduced state carbon dots as both reductant and stabilizer for the synthesis of gold nanoparticles. *Carbon* **2013,** *64*, 499-506.
212. Mehta, A.; D, P.; Thakur, A.; Basu, S., Enhanced photocatalytic water splitting by gold carbon dot core shell nanocatalyst under visible/sunlight. *New Journal of Chemistry* **2017,** *41* (11), 4573-4581.
213. Liu, P.; Wang, L.; Zhao, K.; Liu, Z.; Cao, H.; Ye, S.; Liang, G., High luminous efficiency Au@CDs for sensitive and label-free electrochemiluminescent detection of circulating tumor cells in serum. *Sensors and Actuators B: Chemical* **2020,** *316*, 128131.
214. Nozaki, T.; Kakuda, T.; Pottathara, Y. B.; Kawasaki, H., A nanocomposite of N-doped carbon dots with gold nanoparticles for visible light active photosensitisers. *Photochemical & Photobiological Sciences* **2019,** *18* (5), 1235-1241.
215. Emam, A. N.; Loutfy, S. A.; Mostafa, A. A.; Awad, H.; Mohamed, M. B., Cytotoxicity, biocompatibility and cellular response of carbon dots–plasmonic based nanohybrids for bioimaging. *RSC Advances* **2017,** *7* (38), 23502-23514.
216. Perez-Lloret, M.; Fraix, A.; Petralia, S.; Conoci, S.; Tafani, V.; Cutrone, G.; Vargas-Berenguel, A.; Gref, R.; Sortino, S., One-Step Photochemical Green Synthesis of Water-Dispersible Ag, Au, and Au@Ag Core–Shell Nanoparticles. *Chemistry - A European Journal* **2019,** *25* (64), 14638-14643.
217. Marin, M. L.; McGilvray, K. L.; Scaiano, J. C., Photochemical Strategies for the Synthesis of Gold Nanoparticles from Au(III) and Au(I) Using Photoinduced Free Radical Generation. *Journal of the American Chemical Society* **2008,** *130* (49), 16572-16584.
218. Mäsing, F.; Mardyukov, A.; Doerenkamp, C.; Eckert, H.; Malkus, U.; Nüsse, H.; Klingauf, J.; Studer, A., Controlled Light-Mediated Preparation of Gold Nanoparticles by a Norrish Type I Reaction of Photoactive Polymers. *Angewandte Chemie International Edition* **2015,** *54* (43), 12612-12617.
219. Jara, N.; Milán, N. S.; Rahman, A.; Mouheb, L.; Boffito, D. C.; Jeffryes, C.; Dahoumane, S. A., Photochemical Synthesis of Gold and Silver Nanoparticles—A Review. *Molecules* **2021,** *26* (15), 4585.
220. Guo, A.; Fu, Y.; Wang, G.; Wang, X., Diameter effect of gold nanoparticles on photothermal conversion for solar steam generation. *RSC Advances* **2017,** *7* (8), 4815-4824.
221. Dong, W.; Zhou, S.; Dong, Y.; Wang, J.; Ge, X.; Sui, L., The preparation of ethylenediamine-modified fluorescent carbon dots and their use in imaging of cells. *Luminescence* **2015,** *30* (6), 867-871.
222. Zheng, M.; Liu, S.; Li, J.; Qu, D.; Zhao, H.; Guan, X.; Hu, X.; Xie, Z.; Jing, X.; Sun, Z., Integrating Oxaliplatin with Highly Luminescent Carbon Dots: An Unprecedented Theranostic Agent for Personalized Medicine. *Advanced Materials* **2014,** *26* (21), 3554-3560.
223. Liu, W.; Li, C.; Ren, Y.; Sun, X.; Pan, W.; Li, Y.; Wang, J.; Wang, W., Carbon dots: surface engineering and applications. *Journal of Materials Chemistry B* **2016,** *4* (35), 5772-5788.
224. Yan, F.; Jiang, Y.; Sun, X.; Bai, Z.; Zhang, Y.; Zhou, X., Surface modification and chemical functionalization of carbon dots: a review. *Microchimica Acta* **2018,** *185* (9), 424.
225. Enustun, B. V.; Turkevich, J., Coagulation of Colloidal Gold. *Journal of the American Chemical Society* **1963,** *85* (21), 3317-3328.
226. Martin, B.; Sedelmeier, J.; Bouisseau, A.; Fernandez-Rodriguez, P.; Haber, J.; Kleinbeck, F.; Kamptmann, S.; Susanne, F.; Hoehn, P.; Lanz, M.; Pellegatti, L.; Venturoni, F.; Robertson, J.; Willis, M. C.; Schenkel, B., Toolbox study for application of hydrogen peroxide as a versatile, safe and industrially-relevant green oxidant in continuous flow mode. *Green Chemistry* **2017,** *19* (6), 1439-1448.

227. Zhu, S.; Meng, Q.; Wang, L.; Zhang, J.; Song, Y.; Jin, H.; Zhang, K.; Sun, H.; Wang, H.; Yang, B., Highly Photoluminescent Carbon Dots for Multicolor Patterning, Sensors, and Bioimaging. *Angewandte Chemie International Edition* **2013,** *52* (14), 3953-3957.
228. Sudolská, M.; Dubecký, M.; Sarkar, S.; Reckmeier, C. J.; Zbořil, R.; Rogach, A. L.; Otyepka, M., Nature of Absorption Bands in Oxygen-Functionalized Graphitic Carbon Dots. *The Journal of Physical Chemistry C* **2015,** *119* (23), 13369-13373.
229. Ji, Y.; Yang, X.; Ji, Z.; Zhu, L.; Ma, N.; Chen, D.; Jia, X.; Tang, J.; Cao, Y., DFT-Calculated IR Spectrum Amide I, II, and III Band Contributions of N-Methylacetamide Fine Components. *ACS Omega* **2020,** *5* (15), 8572-8578.
230. Pavia, D. L.; Lampman, G. M.; Kriz, G. S.; Vyvyan, J. R., *Introduction to spectroscopy, Fourth edition*. Brooks/Cole Cengage learning: 2009.
231. He, D.; Peng, Z.; Gong, W.; Luo, Y.; Zhao, P.; Kong, L., Mechanism of a green graphene oxide reduction with reusable potassium carbonate. *RSC Advances* **2015,** *5* (16), 11966-11972.
232. Júnior, Z. S. S.; Botta, S. B.; Ana, P. A.; França, C. M.; Fernandes, K. P. S.; Mesquita-Ferrari, R. A.; Deana, A.; Bussadori, S. K., Effect of papain-based gel on type I collagen - spectroscopy applied for microstructural analysis. *Scientific Reports* **2015,** *5* (1), 11448.
233. Chuntonov, L.; Kumar, R.; Kuroda, D. G., Non-linear infrared spectroscopy of the water bending mode: direct experimental evidence of hydration shell reorganization? *Physical Chemistry Chemical Physics* **2014,** *16* (26), 13172-13181.
234. Link, S.; El-Sayed, M. A., Size and Temperature Dependence of the Plasmon Absorption of Colloidal Gold Nanoparticles. *The Journal of Physical Chemistry B* **1999,** *103* (21), 4212-4217.
235. Wang, C.; Astruc, D., Nanogold plasmonic photocatalysis for organic synthesis and clean energy conversion. *Chemical Society Reviews* **2014,** *43* (20), 7188-7216.
236. Millstone, J. E.; Park, S.; Shuford, K. L.; Qin, L.; Schatz, G. C.; Mirkin, C. A., Observation of a Quadrupole Plasmon Mode for a Colloidal Solution of Gold Nanoprisms. *Journal of the American Chemical Society* **2005,** *127* (15), 5312-5313.
237. Cao, L.; Jennings, M. C.; Puddephatt, R. J., Amine–Amide Equilibrium in Gold(III) Complexes and a Gold(III)–Gold(I) Aurophilic Bond. *Inorganic Chemistry* **2007,** *46* (4), 1361-1368.
238. Rao, X.; Tatoulian, M.; Guyon, C.; Ognier, S.; Chu, C.; Abou Hassan, A., A Comparison Study of Functional Groups (Amine vs. Thiol) for Immobilizing AuNPs on Zeolite Surface. *Nanomaterials* **2019,** *9* (7), 1034.
239. Pustovit, V. N.; Shahbazyan, T. V., Fluorescence quenching near small metal nanoparticles. *Journal of Physical Chemistry* **2012,** *136* (20), 204701.
240. Jiang, K.; Smith, D. A.; Pinchuk, A., Size-Dependent Photothermal Conversion Efficiencies of Plasmonically Heated Gold Nanoparticles. *The Journal of Physical Chemistry C* **2013,** *117* (51), 27073-27080.
241. Shahbazi, M.-A.; Faghfouri, L.; Ferreira, M. P. A.; Figueiredo, P.; Maleki, H.; Sefat, F.; Hirvonen, J.; Santos, H. A., The versatile biomedical applications of bismuth-based nanoparticles and composites: therapeutic, diagnostic, biosensing, and regenerative properties. *Chemical Society Reviews* **2020,** *49* (4), 1253-1321.
242. Min, J.; Choi, K. Y.; Dreaden, E. C.; Padera, R. F.; Braatz, R. D.; Spector, M.; Hammond, P. T., Designer Dual Therapy Nanolayered Implant Coatings Eradicate Biofilms and Accelerate Bone Tissue Repair. *ACS Nano* **2016,** *10* (4), 4441-4450.
243. Lin, M.-C.; Chen, C.-C.; Wu, I. T.; Ding, S.-J., Enhanced antibacterial activity of calcium silicate-based hybrid cements for bone repair. *Materials Science and Engineering: C* **2020,** *110*, 110727.
244. Xu, C.; Cao, Y.; Lei, C.; Li, Z.; Kumeria, T.; Meka, A. K.; Xu, J.; Liu, J.; Yan, C.; Luo, L.; Khademhosseini, A.; Popat, A.; He, Y.; Ye, Q., Polymer–Mesoporous Silica Nanoparticle Core–Shell Nanofibers as a Dual-Drug-Delivery System for Guided Tissue Regeneration. *ACS Applied Nano Materials* **2020,** *3* (2), 1457-1467.

245. Gong, T.; Xie, J.; Liao, J.; Zhang, T.; Lin, S.; Lin, Y., Nanomaterials and bone regeneration. *Bone Research* **2015,** *3* (1), 15029.
246. Köse, S.; Kankilic, B.; Gizer, M.; Ciftci Dede, E.; Bayramli, E.; Korkusuz, P.; Korkusuz, F., Stem Cell and Advanced Nano Bioceramic Interactions. In *Novel Biomaterials for Regenerative Medicine*, Chun, H. J.; Park, K.; Kim, C.-H.; Khang, G., Eds. Springer Singapore: Singapore, 2018; pp 317-342.
247. Shao, R.; Quan, R.; Zhang, L.; Wei, X.; Yang, D.; Xie, S., Porous hydroxyapatite bioceramics in bone tissue engineering: current uses and perspectives. *Journal of the Ceramic Society of Japan* **2015,** *123* (1433), 17-20.
248. Henderson, B.; Nair, S. P., Hard labour: bacterial infection of the skeleton. *Trends in Microbiology* **2003,** *11* (12), 570-577.
249. Darouiche, R. O., Treatment of Infections Associated with Surgical Implants. *New England Journal of Medicine* **2004,** *350* (14), 1422-1429.
250. Busscher Henk, J.; van der Mei Henny, C.; Subbiahdoss, G.; Jutte Paul, C.; van den Dungen Jan, J. A. M.; Zaat Sebastian, A. J.; Schultz Marcus, J.; Grainger David, W., Biomaterial-Associated Infection: Locating the Finish Line in the Race for the Surface. *Science Translational Medicine* **2012,** *4* (153), 153rv10-153rv10.
251. Wright, J. A.; Nair, S. P., Interaction of staphylococci with bone. *International Journal of Medical Microbiology* **2010,** *300* (2), 193-204.
252. Lew, D. P.; Waldvogel, F. A., Osteomyelitis. *The Lancet* **2004,** *364* (9431), 369-379.
253. Xiong, J.; Li, Y.; Hodgson, P. D.; Wen, C. e., In vitro osteoblast-like cell proliferation on nano-hydroxyapatite coatings with different morphologies on a titanium-niobium shape memory alloy. *Journal of Biomedical Materials Research Part A* **2010,** *95A* (3), 766-773.
254. Ge, X.; Ren, C.; Ding, Y.; Chen, G.; Lu, X.; Wang, K.; Ren, F.; Yang, M.; Wang, Z.; Li, J.; An, X.; Qian, B.; Leng, Y., Micro/nano-structured TiO2 surface with dual-functional antibacterial effects for biomedical applications. *Bioactive Materials* **2019,** *4*, 346-357.
255. Sedelnikova, M. B.; Komarova, E. G.; Sharkeev, Y. P.; Ugodchikova, A. V.; Tolkacheva, T. V.; Rau, J. V.; Buyko, E. E.; Ivanov, V. V.; Sheikin, V. V., Modification of titanium surface via Ag-, Sr- and Si-containing micro-arc calcium phosphate coating. *Bioactive Materials* **2019,** *4*, 224-235.
256. Huang, B.; Tan, L.; Liu, X.; Li, J.; Wu, S., A facile fabrication of novel stuff with antibacterial property and osteogenic promotion utilizing red phosphorus and near-infrared light. *Bioactive Materials* **2019,** *4*, 17-21.
257. Ge, X.; Leng, Y.; Bao, C.; Xu, S. L.; Wang, R.; Ren, F., Antibacterial coatings of fluoridated hydroxyapatite for percutaneous implants. *Journal of Biomedical Materials Research Part A* **2010,** *95A* (2), 588-599.
258. Ge, X.; Zhao, J.; Esmeryan, K. D.; Lu, X.; Li, Z.; Wang, K.; Ren, F.; Wang, Q.; Wang, M.; Qian, B., Cicada-inspired fluoridated hydroxyapatite nanostructured surfaces synthesized by electrochemical additive manufacturing. *Materials & Design* **2020,** *193*, 108790.
259. Su, Y.; Cockerill, I.; Zheng, Y.; Tang, L.; Qin, Y.-X.; Zhu, D., Biofunctionalization of metallic implants by calcium phosphate coatings. *Bioactive Materials* **2019,** *4*, 196-206.
260. Jung, W. K.; Koo, H. C.; Kim, K. W.; Shin, S.; Kim, S. H.; Park, Y. H., Antibacterial activity and mechanism of action of the silver ion in Staphylococcus aureus and Escherichia coli. *Applied and environmental microbiology* **2008,** *74* (7), 2171-8.
261. Baker, C.; Pradhan, A.; Pakstis, L.; Pochan, D. J.; Shah, S. I., Synthesis and Antibacterial Properties of Silver Nanoparticles. *Journal of Nanoscience and Nanotechnology* **2005,** *5* (2), 244-249.
262. Sim, W.; Barnard, R. T.; Blaskovich, M. A. T.; Ziora, Z. M., Antimicrobial Silver in Medicinal and Consumer Applications: A Patent Review of the Past Decade (2007–2017). *Antibiotics* **2018,** *7* (4), 93.

263. Quing, Y.; Cheng, L.; Li, R.; Liu, G.; Zhang, Y.; Tang, X.; Wang, J.; Liu, H.; Qin, Y., Potential antibacterial mechanism of silver nanoparticles and the optimization of orthopedic implants by advanced modification technologies. *Int J Nanomedicine* **2018,** *13*, 3311-3327.
264. Castiglioni, S.; Cazzaniga, A.; Locatelli, L.; Maier, J. A. M., Silver Nanoparticles in Orthopedic Applications: New Insights on Their Effects on Osteogenic Cells. *Nanomaterials* **2017,** *7* (6), 124.
265. Khalandi, B.; Asadi, N.; Milani, M.; Davaran, S.; Abadi, A. J. N.; Abasi, E.; Akbarzadeh, A., A Review on Potential Role of Silver Nanoparticles and Possible Mechanisms of their Actions on Bacteria. *Drug Res (Stuttg)* **2017,** *11* (02), 70-76.
266. Jin, J.-C.; Wu, X.-J.; Xu, J.; Wang, B.; Jiang, F.; Liu, Y. J. B. s., Ultrasmall silver nanoclusters: Highly efficient antibacterial activity and their mechanisms. *Biomaterials Science* **2017,** *5* 2, 247-257.
267. Pal, S.; Tak, Y. K.; Song, J. M., Does the Antibacterial Activity of Silver Nanoparticles Depend on the Shape of the Nanoparticle? A Study of the Gram-Negative Bacterium *Escherichia coli*. *Applied and environmental microbiology* **2007,** *73* (6), 1712-1720.
268. Martínez-Castañón, G. A.; Niño-Martínez, N.; Martínez-Gutierrez, F.; Martínez-Mendoza, J. R.; Ruiz, F., Synthesis and antibacterial activity of silver nanoparticles with different sizes. *Journal of Nanoparticle Research* **2008,** *10* (8), 1343-1348.
269. Alt, V., Antimicrobial coated implants in trauma and orthopaedics–A clinical review and risk-benefit analysis. *Injury* **2017,** *48* (3), 599-607.
270. Li, G.; Qin, S.; Zhang, D.; Liu, X., Preparation of antibacterial degummed silk fiber/nano-hydroxyapatite/polylactic acid composite scaffold by degummed silk fiber loaded silver nanoparticles. *Nanotechnology* **2019,** *30* (29), 295101.
271. Ciobanu, G.; Ilisei, S.; Luca, C., Hydroxyapatite-silver nanoparticles coatings on porous polyurethane scaffold. *Materials Science and Engineering: C* **2014,** *35*, 36-42.
272. Versace, D.-L.; Ramier, J.; Grande, D.; Andaloussi, S. A.; Dubot, P.; Hobeika, N.; Malval, J.-P.; Lalevee, J.; Renard, E.; Langlois, V., Versatile Photochemical Surface Modification of Biopolyester Microfibrous Scaffolds with Photogenerated Silver Nanoparticles for Antibacterial Activity. *Advanced Healthcare Materials* **2013,** *2* (7), 1008-1018.
273. Manjari Mishra, P.; Kumar Sahoo, S.; Kumar Naik, G.; Parida, K., Biomimetic synthesis, characterization and mechanism of formation of stable silver nanoparticles using Averrhoa carambola L. leaf extract. *Materials Letters* **2015,** *160*, 566-571.
274. Petralia, S.; Ventimiglia, G., Photodecorated Surface with Nanoparticles: Versatile Substrates for Technology Applications. *BioNanoScience* **2018,** *8* (2), 609-616.
275. Petralia, S.; Barbuzzi, T.; Ventimiglia, G., Polymerase chain reaction efficiency improved by water soluble β-cyclodextrins capped platinum nanoparticles. *Materials Science and Engineering: C* **2012,** *32* (4), 848-850.
276. Calabrese, G.; Giuffrida, R.; Forte, S.; Salvatorelli, L.; Fabbi, C.; Figallo, E.; Gulisano, M.; Parenti, R.; Magro, G.; Colarossi, C.; Memeo, L.; Gulino, R., Bone augmentation after ectopic implantation of a cell-free collagen-hydroxyapatite scaffold in the mouse. *Scientific Reports* **2016,** *6* (1), 36399.
277. Calabrese, G.; Giuffrida, R.; Forte, S.; Fabbi, C.; Figallo, E.; Salvatorelli, L.; Memeo, L.; Parenti, R.; Gulisano, M.; Gulino, R., Human adipose-derived mesenchymal stem cells seeded into a collagen-hydroxyapatite scaffold promote bone augmentation after implantation in the mouse. *Scientific Reports* **2017,** *7* (1), 7110.
278. Barbera, L.; De Plano, L. M.; Franco, D.; Gattuso, G.; Guglielmino, S. P. P.; Lando, G.; Notti, A.; Parisi, M. F.; Pisagatti, I., Antiadhesive and antibacterial properties of pillar[5]arene-based multilayers. *Chemical Communications* **2018,** *54* (72), 10203-10206.
279. Zagami, R.; Franco, D.; Pipkin, J. D.; Antle, V.; De Plano, L.; Patanè, S.; Guglielmino, S.; Monsù Scolaro, L.; Mazzaglia, A., Sulfobutylether-β-

cyclodextrin/5,10,15,20-tetrakis(1-methylpyridinium-4-yl)porphine nanoassemblies with sustained antimicrobial phototherapeutic action. *International Journal of Pharmaceutics* **2020,** *585*, 119487.
280. Calabrese, G.; Giuffrida, R.; Fabbi, C.; Figallo, E.; Lo Furno, D.; Gulino, R.; Colarossi, C.; Fullone, F.; Giuffrida, R.; Parenti, R.; Memeo, L.; Forte, S., Collagen-Hydroxyapatite Scaffolds Induce Human Adipose Derived Stem Cells Osteogenic Differentiation In Vitro. *PLOS ONE* **2016,** *11* (3), e0151181.
281. Giuffrida, S.; Ventimiglia, G.; Sortino, S., Straightforward green synthesis of "naked" aqueous silver nanoparticles. *Chemical Communications* **2009,** (27), 4055-4057.
282. Giuffrida, S.; Ventimiglia, G.; Petralia, S.; Conoci, S.; Sortino, S., Facile Light-Triggered One-Step Synthesis of Small and Stable Platinum Nanoparticles in an Aqueous Medium from a β-Cyclodextrin Host–Guest Inclusion Complex. *Inorganic Chemistry* **2006,** *45* (2), 508-510.
283. Abbaszadegan, A.; Ghahramani, Y.; Gholami, A.; Hemmateenejad, B.; Dorostkar, S.; Nabavizadeh, M.; Sharghi, H., The Effect of Charge at the Surface of Silver Nanoparticles on Antimicrobial Activity against Gram-Positive and Gram-Negative Bacteria: A Preliminary Study. *Journal of Nanomaterials* **2015,** *2015*, 720654.
284. Quinteros, M. A.; Cano Aristizábal, V.; Dalmasso, P. R.; Paraje, M. G.; Páez, P. L., Oxidative stress generation of silver nanoparticles in three bacterial genera and its relationship with the antimicrobial activity. *Toxicology in Vitro* **2016,** *36*, 216-223.
285. Lee, W.; Kim, K.-J.; Lee, D. G., A novel mechanism for the antibacterial effect of silver nanoparticles on Escherichia coli. *BioMetals* **2014,** *27* (6), 1191-1201.
286. Hackenberg, S.; Scherzed, A.; Kessler, M.; Hummel, S.; Technau, A.; Froelich, K.; Ginzkey, C.; Koehler, C.; Hagen, R.; Kleinsasser, N., Silver nanoparticles: Evaluation of DNA damage, toxicity and functional impairment in human mesenchymal stem cells. *Toxicology Letters* **2011,** *201* (1), 27-33.
287. Carlson, C.; Hussain, S. M.; Schrand, A. M.; K. Braydich-Stolle, L.; Hess, K. L.; Jones, R. L.; Schlager, J. J., Unique Cellular Interaction of Silver Nanoparticles: Size-Dependent Generation of Reactive Oxygen Species. *The Journal of Physical Chemistry B* **2008,** *112* (43), 13608-13619.
288. Cheng, X.; Zhang, W.; Ji, Y.; Meng, J.; Guo, H.; Liu, J.; Wu, X.; Xu, H., Revealing silver cytotoxicity using Au nanorods/Ag shell nanostructures: disrupting cell membrane and causing apoptosis through oxidative damage. *RSC Advances* **2013,** *3* (7), 2296-2305.
289. Akter, M.; Sikder, M. T.; Rahman, M. M.; Ullah, A. K. M. A.; Hossain, K. F. B.; Banik, S.; Hosokawa, T.; Saito, T.; Kurasaki, M., A systematic review on silver nanoparticles-induced cytotoxicity: Physicochemical properties and perspectives. *Journal of Advanced Research* **2018,** *9*, 1-16.
290. Liu, Z.; Fu, S.; Liu, X.; Narita, A.; Samorì, P.; Bonn, M.; Wang, H. I., Small Size, Big Impact: Recent Progress in Bottom-Up Synthesized Nanographenes for Optoelectronic and Energy Applications. *Advanced Science* **2022,** *9* (19), 2106055.
291. Clocchiatti, R.; Condomines, M.; Guénot, N.; Tanguy, J.-C., Magma changes at Mount Etna: the 2001 and 2002–2003 eruptions. *Earth and Planetary Science Letters* **2004,** *226* (3), 397-414.
292. Viccaro, M.; Calcagno, R.; Garozzo, I.; Giuffrida, M.; Nicotra, E., Continuous magma recharge at Mt. Etna during the 2011–2013 period controls the style of volcanic activity and compositions of erupted lavas. *Mineralogy and Petrology* **2015,** *109* (1), 67-83.
293. Giordano, D.; Russell, J. K.; González-García, D.; Bersani, D.; Dingwell, D. B.; Del Negro, C., Raman Spectroscopy from Laboratory and Proximal to Remote Sensing: A Tool for the Volcanological Sciences. *Remote sensing* **2020,** *12* (5), 805.
294. Su, D. S.; Chen, X.-W., Natural Lavas as Catalysts for Efficient Production of Carbon Nanotubes and Nanofibers. *Angewandte Chemie International Edition* **2007,** *46* (11), 1823-1824.

295. Su, D. S.; Chen, X.; Liu, X.; Delgado, J. J.; Schlögl, R.; Gajović, A., Mount-Etna-Lava-Supported Nanocarbons for Oxidative Dehydrogenation Reactions. *Advanced Materials* **2008,** *20* (19), 3597-3600.
296. Zhu, X.; Song, T.; Lv, Z.; Ji, G., High-efficiency and low-cost α-Fe2O3 nanoparticles-coated volcanic rock for Cd(II) removal from wastewater. *Process Safety and Environmental Protection* **2016,** *104*, 373-381.
297. Nicolosi, V.; Chhowalla, M.; Kanatzidis Mercouri, G.; Strano Michael, S.; Coleman Jonathan, N., Liquid Exfoliation of Layered Materials. *Science* **2013,** *340* (6139), 1226419.
298. Ali, F.; Reinert, L.; Levêque, J.-M.; Duclaux, L.; Muller, F.; Saeed, S.; Shah, S. S., Effect of sonication conditions: Solvent, time, temperature and reactor type on the preparation of micron sized vermiculite particles. *Ultrasonics Sonochemistry* **2014,** *21* (3), 1002-1009.
299. Li, W.; Zhang, M.; Zhang, J.; Han, Y., Self-assembly of cetyl trimethylammonium bromide in ethanol-water mixtures. *Frontiers of Chemistry in China* **2006,** *1* (4), 438-442.
300. Janica, I.; Del Buffa, S.; Mikołajczak, A.; Eredia, M.; Pakulski, D.; Ciesielski, A.; Samorì, P., Thermal insulation with 2D materials: liquid phase exfoliated vermiculite functional nanosheets. *Nanoscale* **2018,** *10* (48), 23182-23190.
301. Lee, S. M.; Tiwari, D., Organo and inorgano-organo-modified clays in the remediation of aqueous solutions: An overview. *Applied Clay Science* **2012,** *59-60*, 84-102.
302. Grosvenor, A. P.; Kobe, B. A.; Biesinger, M. C.; McIntyre, N. S., Investigation of multiplet splitting of Fe 2p XPS spectra and bonding in iron compounds. *Surface and Interface Analysis* **2004,** *36* (12), 1564-1574.
303. Belfiore, C. M.; Amato, C.; Pezzino, A.; Viccaro, M., An end of waste alternative for volcanic ash: A resource in the manufacture of ceramic tiles. *Construction and Building Materials* **2020,** *263*, 120118.
304. Das, N. C.; Cao, H.; Kaiser, H.; Warren, G. T.; Gladden, J. R.; Sokol, P. E., Shape and Size of Highly Concentrated Micelles in CTAB/NaSal Solutions by Small Angle Neutron Scattering (SANS). *Langmuir* **2012,** *28* (33), 11962-11968.
305. Lin, Z.; Cai, J. J.; Scriven, L. E.; Davis, H. T., Spherical-to-Wormlike Micelle Transition in CTAB Solutions. *The Journal of Physical Chemistry* **1994,** *98* (23), 5984-5993.